Functional Characterization of the Candidate Colorectal Cancer Gene *CNOT1*

A DISSERTATION
SUBMITTED TO THE FACULTY OF THE GRADUATE SCHOOL OF THE UNIVERSITY OF MINNESOTA

By

Lei Zhao

IN PARTIAL FULFILLMENT OF THE REQUIREMENTS FOR THE DEGREE OF DOCTOR OF PHILOSOPHY

Thesis Advisors: Robert Cormier, Ph.D.
and Patricia Scott, Ph.D.

December 2013

Acknowledgements

First and foremost, I would like to acknowledge my thesis advisors, Drs. Robert Cormier and Patricia Scott, for their continuous support of my PhD study and mentorship on this thesis research project. I could not have imagined having better advisors and mentors for my PhD studies than them.

I gratefully acknowledge my committee chair Dr. Lester Drewes for the instructions on my research and the organization of my thesis defense. I also would like to thank other members of my committee, Dr. David Largaespada, Dr. Matthew Andrews, Dr. Kendall Wallace, and Dr. Lynne Bemis for their helpful guidance and support throughout the course of this research.

I also would like to thank my lab members: Annette Rod, Elaine Than, and Mike Madden for their friendship and help during the past four years.

My special thanks go to my wife Yanjun Wu for her dedication, love and persistent confidence in me. I could not have done this without her.

Finally, I want to thank the NIH and Whiteside Institute for Clinical Research for providing the financial support for this study.

Dedication

This thesis is dedicated to my family who has always been supporting me. This dissertation is simply impossible without the support from my wife Yanjun Wu and my parents. To them I dedicate this dissertation.

Abstract

Cnot1 was identified as a candidate colorectal cancer (CRC) gene in multiple *Sleeping Beauty*-based screens. Multiple somatic mutations in *CNOT1* in CRC have been documented. Depletion of *CNOT1* in the SW480 CRC cell line resulted in a dramatic decrease in cell viability, suggesting that *CNOT1* may act as an oncogene. CNOT1 is a scaffold of the CCR4-NOT complex, which regulates mRNA expression at several levels. Examination of global gene expression in *CNOT1*-depleted SW480 cells revealed dramatically increased expression of *TXNIP*, which can initiate apoptotic pathways in response to extreme endoplasmic reticulum (ER) stress. We hypothesized that CNOT1 might protect cell viability by limiting *TXNIP* expression. In support of this idea that upregulation of *TXNIP* was responsible for decreased cell viability seen in *CNOT1*-depleted cells, we found that enforced expression of *TXNIP* in HEK293 cells resulted in decreased cell viability. Also, analysis of *TXNIP* expression in parallel with cell apoptosis in *CNOT1* depleted cells revealed that upregulation of *TXNIP* occurs well before a measurable increase in cell apoptosis, suggesting that elevated *TXNIP* may contribute to apoptosis seen in *CNOT1*-depleted cells. To substantiate this connection we investigated the mechanism by which CNOT1 regulates *TXNIP* levels. We found that depletion of *CNOT8*, a deadenylase subunit of the CCR4-NOT complex, also results in decreased cell viability and increased *TXNIP* expression. Further, *CNOT1* depletion results in increased *TXNIP* mRNA stability. These results argue that CNOT1 limits *TXNIP* expression via regulation of mRNA deadenylation and stability. TXNIP is activated to promote apoptosis by extreme ER stress in part by means of relief of *miR-17*-mediated degradation of *TXNIP* mRNA. In support of this, we found that *miR-17* overexpression downregulates *TXNIP* mRNA in SW480 cells. We also found that limiting *TXNIP* expression increases cell viability under condition of ER stress. CNOT1 acts as an adapter between the miRNA RISC and deadenylase subunits of the CNOT complex. Thus, we hypothesized that increased activity of CNOT1 may facilitate the degradation of *TXNIP* by *miR-17*. Further analyses suggested that CNOT1 might limit ER stress and activation of the unfolded protein response (UPR) pathways. Based on the results above, we proposed the following model. As cancer cells are often subject to extreme stresses, increased activity of CNOT1 may protect against the effects of severe ER stress through directly limiting *TXNIP* transcript levels and preventing ER stress leading to apopotsis, thus conferring a growth advantage to cancer cells.

Table of Contents

CHAPTER

List of Tables

Chapter 1

Chapter 2

Chapter 4

Appendices

List of Figures

Chapter 1

Chapter 2

Appendices

Abbreviations

3'UTR	3' untranslated region
APC	Adenomatous polyposis coli
ARE	AU-rich elements
ASK-1	apoptosis signaling kinase-1
ATF6	activating transcription factor-6
BMP	Bone morphogenetic proteins
CBC	crypt-base-columnar
CHOP	C/EBP homologous protein
CIS	Common Insertion Site
CNOT1	CCR4-NOT transcription complex, subunit 1
CNOT8	CCR4-NOT transcription complex, subunit 8
CRC	Colorectal cancer
CRCLM	CRC liver metastasis
DDT	Dichloro-diphenyl-trichloroethane
EMT	Epithelial-mesenchymal transition
ER	Endoplasmic reticulum
ER	Estrogen receptor
FAP	Familial adenomatous polyposis
FFPE	Formalin-fixed and paraffin-embedded
FKMF	Fragments per kilobase of exon per Million Fragments mapped
GEO	Gene expression omnibus
GI	Gastrointestinal
GSEA	Gene set enrichment analysis
HNPCC	Hereditary non-polyposis colorectal cancer
IL-1β	Interleukin 1β
IPA	Ingenuity pathway analysis
IR	Inverted repeats
IRE1	Inositol requiring enzyme 1
ISC	Intestinal stem cell
K-RAS	Kirsten rat sarcoma viral oncogene homolog
KCNQ1	Potassium voltage-gated channel, KQT-like subfamily, member1
KO	Knockout
LM-PCR	Ligation-mediated pcr
LOH	Loss of heterozygosity
LQTS	Long QT Syndrome
LRP5	Low-density lipoprotein receptor-related protein 5
LSL	Lox-STOP-Lox
LTR	Long terminal repeat

Min	Multiple intestinal neoplasia
MMR	Mis-match repair
MMTV	Mouse mammary tumor virus
MSCV	Murine stem cell virus
MSI	Microsatellite instability
MTT	(3-(4,5-dimethylthiazol-2-yl)-2,5-diphenyltetrazolium bromide, a yellow tetrazole
NCCN	National comprehensive cancer network
NES	Normalized enrichment score
NOTCH	NOTCH homolog 1, translocation-associated (Drosophila)
OS	Overall survival
PABP	Poly(A)-binding proteins
PARN	Poly(A)-specific ribonuclease
PERK	PKR-like eukaryotic initiation factor 2a kinase
PI3K	Phosphatidylinositol 3-Kinase
PTEN	Phosphatase and tensin homologue
RBP	RNA binding protein
RIDD	Regulated IRE1-dependent decay
RISC	RNA-induced silencing complex
RTK	Receptor tyrosine kinase
SB	Sleeping beauty
SD	Splice donor
sXBP1	Spliced X-box binding protein-1
TA	Transit-amplifying
TCGA	The cancer genome atlas
TLR	Toll-like receptor
TXNIP	Thioredoxin-interacting protein
UPR	Unfolded protein response
WNT	Wingless-type
WT	Wild-type
XBP1	X-box binding protein-1

Chapters 1-4 are the basis of the following manuscript in preparation:

Zhao, L., Zhang, Y., Silverstein, K., Starr, T.K., Rod, A., Liu, Y., Largaespada, D.L., Cormier, R.T. and Scott, P.M. Functional characterization of the candidate colorectal cancer gene *CNOT1*. 2013 *In preparation to be submitted to Cell Death & Differentiation.*

Personal Contribution. Zhao, L contributed to design of research. Zhao, L performed the cellular and molecular biology studies including studies of: CNOT1 role in cell viability, role of TXNIP in cell viability, regulation of *TXNIP* by CNOT1, and role of the Unfolded Protein Response. In addition Zhao, L isolated RNA samples for Illumina microarrays and RNA Sequencing. Zhao, L carried out analysis of these studies, including carrying out IPA and GSEA analyses and statistical analysis.

Chapter 1

Introduction

Epidemiology and Challenges in Colorectal Cancer Treatment

Colorectal cancer (CRC) is the third most common cancer in men (663,000 cases) and the second in women (571,000 cases) worldwide. About 608,000 deaths from CRC were estimated to occur worldwide, accounting for 8% of all cancer deaths, making it the fourth most common cause of death from cancer (Ferlay *et al*., 2010). In the United States, CRC is the third leading cause of cancer death accounting for 142,820 new cases and 50,830 deaths in the year 2012 (Siegel *et al*., 2013). In China, the incidence rate of CRC is relatively lower than western countries. However, the rate has increased dramatically in recent years partially due to the changes in lifestyle and environmental pollution. In 2008, China reported 220,000 new cases and 109,000 deaths from CRC, the highest number to date in each category of CRC. These statistics highlight the significant impact of CRC on our society and thus the importance of new diagnostic and therapeutic tools for this cancer.

Up to 95% of all CRCs are gland-forming adenocarcinomas derived from the crypt epithelium (Parkin *et al*., 2001). Other types of malignancy account for the remaining 5% of CRC, including mucinous tumors, signet ring tumors, adenosquamous carcinoma, and undifferentiated carcinoma (Jessurun *et al*., 1999). CRC often causes no symptoms until it reaches an advanced stage. Symptoms may be present, but are nonspecific and vague, including a change in bowel habits, weight loss, abdominal pain, hematochezia, melena, fatigue and weakness (Benedix *et al*., 2010). The diagnosis of CRC is usually made on the basis of histopathology of surgical or biopsy specimens. Imaging, including CT and MRI scans of the abdomen and pelvis and lung, is used to accurately stage patients. CRC tissues are usually graded as well-, moderately- and poorly-differentiated based on how closely the tumor cells resemble normal epithelial cells. Once the diagnosis of CRC is made, the disease should be staged. Accurate staging

leads to both proper management and prognostic significance for the patient. The two most common staging systems to define the extent of invasion of CRC are the Dukes' and the TNM staging system. In the TNM staging system, patients are stratified according to the depth of tumor penetration (T), number of positive lymph nodes (N) and extent of distant metastasis (M) (Edge *et al*., 2009). Although pathological staging is useful in determining the treatment strategy and predicting the prognosis of CRC patients, it has some disadvantages. For example it cannot distinguish stage II patients who will relapse from those who will be cured by surgery alone. A novel staging system integrating the genetic changes in specific cancers may be more effective in selecting therapy and predicting prognosis (Eschrich *et al*., 2005).

The last decade has witnessed new strategies for the diagnosis and treatment of CRC which have improved patient survival. All treatment decisions are determined on an individual basis based on the stage, differentiation, pathological type of cancer as well as patient's age, general health, and other medical conditions. Surgery, radiation, chemotherapy or a combination of these approaches are among the options available to treat patients with CRC. Surgery is the most common treatment for all stages of CRC and is the only potentially curative treatment (Lee *et al*., 2007). Chemotherapy is widely used for treatment of stage III CRC post-surgically to prevent the recurrence of disease. It can also be used as the primary therapy for advanced CRC when surgery is not indicated (NCCN 2012). The use of adjuvant chemotherapy in stage II disease remains unclear and controversial (André *et al*., 2004). Surgery alone is the predominant therapy for stage II CRC patients as large clinical trails have not demonstrated a significant benefit to a surgery plus chemotherapy regimen in treating stage II disease. However, up to 25% of stage II CRC patients rapidly relapse following surgery alone therapy. Thus, there is a subset of stage II patients who would benefit by more aggressive therapy. This highlights the importance of genetic studies to distinguish this group of high-risk patients from low risk patients. The options for treatment of advanced disease are still limited. Even given the most effective regimen, 50% of stage III patients relapse (NCCN 2012). For stage IV patients, the situation is even worse. The overall survival is only around two years following treatment with surgery combined with standard FOLFOX chemotherapy and

bevacizumab (NCCN 2012). These limitations and challenges in CRC management highlight the importance of research, especially genetic research, in improving outcomes in CRC patients, for example, in the identification of biomarkers for further stratifying patients and as targets for emerging novel therapeutic strategies.

The Biology of the Human Intestinal Tract

The human intestinal tract extends from the stomach, the small intestine, and proceeds to the large intestine, and terminates at the anus. The small intestine is composed of the duodenum, jejunum and ileum, and is about 20-25 feet long on average, and is the site where most of the digestion and absorption of nutrients is carried out. The large intestine, about 5 feet long, consists of the caecum with appendix extension; the ascending, transverse, descending and sigmoid colon; and the rectum. The large intestine is horseshoe shaped and extends around the small intestine. A major physiological function of the large intestine is to absorb water from the remaining indigestible food matter and temporarily store waste matter. Besides nutrient digestion and absorption, the intestinal tract, in particular the large intestine, also plays important roles in immunological defense, water homeostasis, and entero-endocrine signaling, and other functions.

The intestinal wall is composed of four layers, which are the serosa, muscularis, submucosa and mucosa from outside to inside (intestinal lumen). Each layer has different tissues and functions. The serosa layer consists of connective tissue and acts as a covering for the digestive tube. The muscularis layer surrounds the submucosa and is responsible for intestinal peristalsis. Rich in vessels like arteries, veins, lymphatics and nerves, the submucosa layer provides the intestine with blood supply and is the location of a varaiety of non-epitheliual cells (*e.g*., fibroblasts, cells of the innate and adaptive immune systems) that comprise the intestinal stroma. The mucosa is the innermost layer of the intestinal tract which is lined by absorptive and secretory epithelium. The epithelium consists of a simple columnar epithelium layer with millions of “crypts of Lieberkuhn” that are finger-like invaginations of the epithelium into the underlying connective tissue (Figure 3). There are four classes of terminally differentiated cells in

small intestinal crypts. The enterocytes, the most abundant cell type in the intestinal epithelium, are absorptive cells while the other three classes are all secretory: goblet cells secrete mucus; enteroendocrine cells are smaller and secrete various gut hormones (peptides and catecholamines) that regulate numerous important biological processes; and Paneth cells secrete digestive enzymes, growth factors and especially diverse host defense (antimicrobial) proteins such as α-defensins, secretory phospholipase A2 and various proinflammatory cytokines (e.g. TNF-α, IL-1β) to protect the constantly renewing crypt from harmful invaders. The composition of cell types in the colon is similar to that of the small intestine, except for the absence of villi and Paneth cells.

All types of terminally differentiated cells originate from the differentiation of progeny of intestinal stem cells (ISCs) which are located at the base of the crypt in both the small and large intestine. In the small intestine, ISCs are interspersed with Paneth cells (Sato *et al*., 2011). Under normal conditions, the intestinal epithelial cells are renewed every 2-7 days, which is fueled by stem cells (Figure 4, Medema *et al*., 2011). ISCs are responsible for generating the entire crypt-villus structure. In the small intestine, Paneth cells migrate downward to reside at the bottom of the crypt and live for 6-8 weeks. Slightly higher up the crypt are the transit amplifying (TA) cells and committed progenitor cells that undergo differentiation into the enterocytes, goblet cells, and enteroendocrine cells as they migrate from the base of the crypt towards the lumen. When the migration of these differentiated cells reaches the villus tip (small intestine) or intercrypt table (colon), they undergo apoptosis and are shed into the intestinal lumen.

There are two hypothetical models of stem cells in the intestine (Clevers *et al*., 2013). The "+4 model" refers to a common intestinal stem cell origin at position 4-5, directly above the Paneth cell compartment. Potten *et al.* showed that the radiation-sensitive, label-retaining +4 cells were actively proliferating with 24 hour cell cycles. The other model is termed as "the stem cell zone model" which is based on the finding that the crypt base is not solely populated by postmitotic Paneth cells. Instead, a population of slender crypt-base-columnar (CBC) cells was wedged between the Paneth cells located at position 1-5, which were radiation-sensitive but not label-retaining and were called

intestinal stem cells (Cheng and Leblond, 1974). Although the identity of intestinal stem cells is still controversial, it is agreed that intestinal stem cells reside in a niche that provides them with essential signals from important morphogenetic pathways such as WNT, NOTCH, and BMP (Figure 5, Heath JK 2010, Crosnier *et al*., 2006, Reya and Clevers 2005).

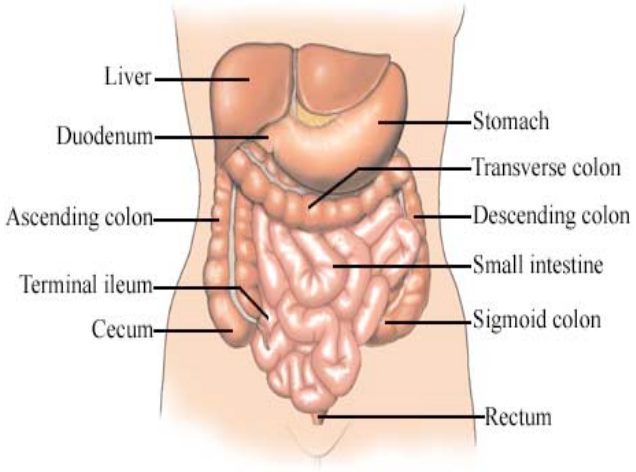

Figure 1. The anatomy of the gastrointestinal tract. (Nucleus Medical Art, Inc. 2008)

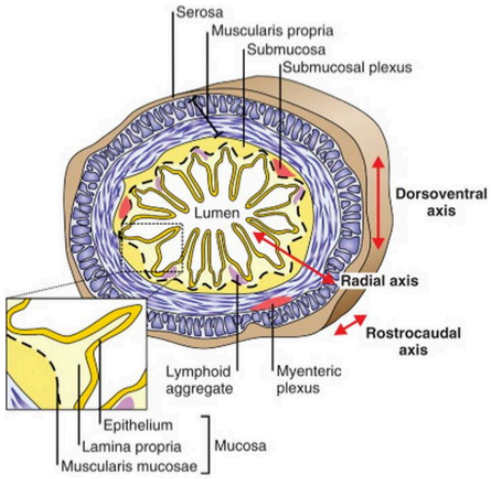

Figure 2. The multi-layered organization of the mature GI tract. (Heath JK 2010).

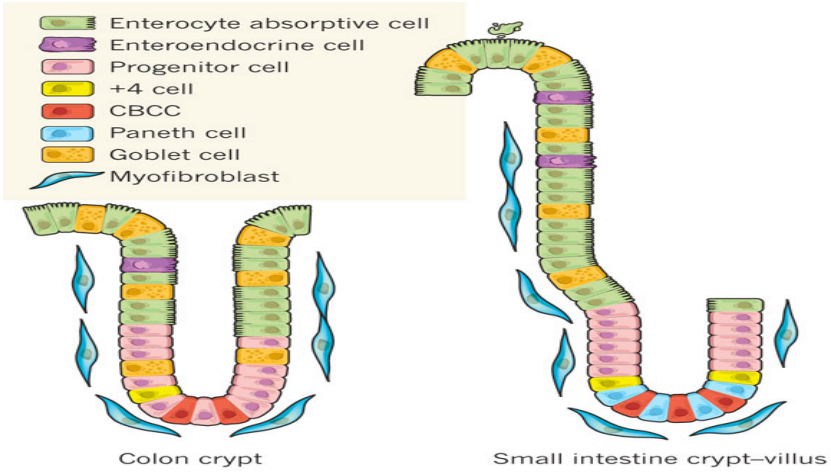

Figure 3. The organization of the small intestinal crypt-villus and the colon crypt. Both the colon crypt (left) and the small intestinal crypt (right) are shown. (Medema and Vermeulen, 2011).

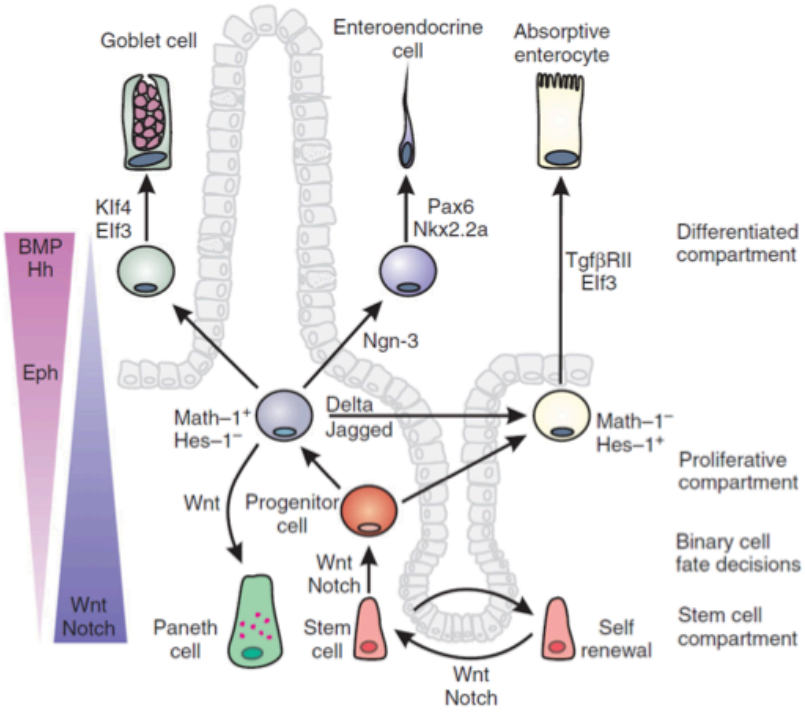

Figure 4. Organization of the intestinal epithelium and the crypts of Lieberkühn and cell lineage determination in the intestinal epithelium. (Heath JK 2010).

Important Signaling Pathways in Intestinal Crypt Renewal

Specifically, several key regulatory signals have been reported to be involved in intestinal stem cell renewal and differentiation, including the WNT, bone morphogenetic protein (BMP), and NOTCH pathways (Heath JK, 2010, Reya and Clevers, 2005). Furthermore, evidence suggests there is a close interaction between several key pathways in directing intestinal epithelial stem cell renewal and differentiation (Figure 4).

WNT Signaling Pathway

WNT signaling is crucial in controlling cell proliferation/regeneration in the intestinal epithelium and the maintenance of intestinal stem cells (Polakis, 2007). WNT proteins are extracellular glycoproteins produced by epithelial cells in the crypt, which bind the Frizzled and the low density lipoprotein receptor-related protein 5 (Lrp5) receptors on the surface of intestinal epithelial cells. β-catenin is the key effector of the canonical WNT signaling pathway. In the absence of WNT binding, cytoplasmic β-catenin levels are normally kept low through continuous degradation, which is controlled by the APC/Axin/CK1/GSK3 destruction complex. This complex binds to newly synthesized β-catenin and phosphorylates it, thereby targeting phosphorylated β-catenin for ubiquitination-mediated proteolysis. When WNT proteins bind to the Frizzled/LRP receptor complex at the cell surface, the destruction complex is inactivated, resulting in the accumulation of β-catenin in the cytoplasm. The accumulated β-catenin then translocates into the nucleus to bind with Tcf/Lef transcription factors, leading to transcriptional activation of important target genes involved in cell proliferation and oncogenesis such as *Cyclin D1* and *c-MYC* (Komiya *et al*., 2008, Cadigan *et al*., 2012). The expression level of components of the WNT signaling is highest at the bottom of intestinal crypts. Canonical WNT signaling plays a major role in maintaining intestinal stem cell fate and stimulating progenitor cell proliferation (Reya and Clevers, 2005). For example, in *Tcf4*$^{-/-}$ mice, the proliferating compartment between the villi was entirely absent, suggesting an essential role for Wnt in maintenance of crypt progenitors (Korinek *et al*., 1998). Dysregulation of the WNT signaling pathway was shown to cause aberrant proliferation of colonic crypts and is the rate-limiting step in CRC development. For

example, in 80% of CRCs both *APC* alleles are inactivated. Furthermore, mutations in other canonical WNT pathway components have also been observed in CRC. For example, somatic mutations in *AXIN1* (Jin *et al*., 2003) and the *TCF4* transcription factor have been observed in a subset of CRCs (Angus-Hill *et al*., 2011). Activating mutations in the *β-catenin* gene (*CTNNB1*) that protect the protein from APC-mediated degradation are also observed in CRC and adenomas (Kaler *et al*., 2012).

NOTCH Signaling Pathway

Another important signaling pathway for intestinal homeostasis and differentiation is the NOTCH signaling pathway. NOTCH signaling mediates cell-cell interactions in animal development and is known to regulate the proliferation and differentiation of intestinal stem cells. Mammals express four transmembrane Notch receptors (Notch1-4) and five canonical transmembrane ligands (Delta-like [DLL] 1,3, and 4, Jagged-1, 2) (Espinoza *et al*., 2013). In canonical NOTCH signaling, when NOTCH receptors bind to their ligands expressed on neighboring cells, this initiates proteolytic cleavage of the receptors by α-secretase and γ-secretase to release NOTCH receptors' intracellular domain (NICD). The cleaved receptors then translocate into the nucleus and form complexes with RBP-jκ and induce transcriptional activation of NOTCH target genes such as transcription factor hairy/enhancer of split (*Hes1*) which is important for NOTCH induced repression of differentiation. Knockout of *Hes1* in intestinal tumor cells in *Apc*-mutant mice was reported to reduce tumor cell proliferation, while promoting differentiation toward epithelial lineages (Ueo *et al*., 2012). Crucial components of the NOTCH signaling pathway have been shown to localize to the proliferative zone of the intestinal crypts but only weakly in the intestinal villi (Jensen *et al*., 2000, Riccio *et al*., 2008). NOTCH signaling promotes progenitor cells' differentiation into the absorptive cell lineage rather than the secretory cell lineage (Jensen *et al*., 2000, Riccio *et al*., 2008) through inhibition of the transcription factor *atonal homolog 1* (*Atoh1*) which appears to be required for secretory cell differentiation (VanDussen and Samuelson, 2010). Thus, disruption of NOTCH signaling results in increased *Atoh1* expression and secretory cell hyperplasia, whereas hyperactive NOTCH

signaling results in decreased *Atoh1* expression and increased numbers of absorptive enterocytes (VanDussen *et al*., 2012). Importantly, NOTCH signaling does not act alone but interacts with other key signaling pathways, such as WNT signaling, to promote functional signaling networks required for development and tissue homeostasis. In addition, there may be a cross-talk between the Notch and RAS signaling pathways, in which RAS activating mutations can activate Notch signaling while Notch activation is required for RAS-mediated transformation (Saif and Chu, 2010). NOTCH signaling also has been shown to be a key participant in epithelial-to-mesenchymal transition (EMT) that is an important process for metastatic disease (Saad *et al.,* 2010).

BMP Signaling Pathway

The bone morphogenetic protein (BMP) pathway, originally identified as factors inducing cartilage and bone formation, also has been shown to play a key role in gastrointestinal cell development and in maintaining tissue homeostasis (Itoh *et al*., 2000). BMPs belong to the transforming growth factor beta (TGFβ) superfamily, which share intracellular signaling through the SMAD proteins. The action of BMP is mediated by type 1 (BMPRI) and type 2 (BMPR2) serine/threonine kinase receptors. In the canonical BMP pathway, the binding of BMP to BMPRI results in activation of BMPRI, leading to phosphorylation of SMAD proteins (SMAD1, SMAD5 and SMAD8). The phosphorylated BMP-SMADs form a complex with a co-SMAD (SMAD4) and translocate into the nucleus. Once in the nucleus, the SMAD complex cooperates with other transcription factors to modulate target gene expression. BMP signaling within the intestine is quite complex as BMPs and their receptors are expressed in both epithelial and mesenchymal compartments. It has been suggested that BMP2 and BMP4, expressed by the mesenchymal cells, can halt proliferation at the crypt-villus border, as BMPs are active at the top of the crypt where differentiation occurs. Though also produced at the crypt base, they are kept in check by BMP inhibitors such as Noggin. BMP signaling has been reported to antagonize WNT signaling along the crypt-villus axis to inhibit intestinal stem cell activation and expansion. This signaling pathway has also been shown to be involved in lineage fate decisions of secretory cells (He *et al*., 2004, Derynck *et al*.,2003).

The human adult colonic epithelium undergoes perpetual regeneration fueled by intestinal epithelial stem cells and progenitor cells, which is a highly coordinated process regulated by different signaling pathways. Disrruption of the signaling pathways critical for stem cell renewal may result in a series of diseases in GI tract, including CRC.

Hereditary and Sporadic CRC

CRC can be subdivided into hereditary or sporadic cancers depending on the presence or absence of familial genetic predisposition. Around 30% of diagnosed CRC are considered to be hereditary, while the majority of the CRC cases (70%) occur in sporadic forms (Figure 5, Lynch *et al*., 2003).

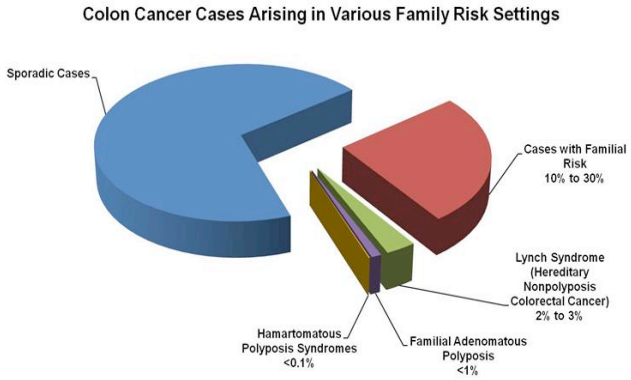

Figure 5. The fraction of colon cancer cases that arise in various family risk settings. (Burt, 2000)

Hereditary CRC

Around 30% of the diagnosed CRC cases are considered to be hereditary, including dominantly inherited CRC syndromes, such as Familial Adenomatous Polyposis (FAP), Hereditary Non Polyposis Colorectal Cancer (HNPCC), and MUTYH Associated Polyposis (MAP), which together account for 5-10% of cases and CRC in patients from families with familial susceptibility (~25-30% of cases) (Chapelle *et al*., 2004).

FAP is an autosomal dominant syndrome which causes 0.5-1.0% of CRCs and affects approximately 1 in 10,000 births (Fearon *et al*., 2011, Rustgi *et al*., 2007). FAP

patients usually carry germline mutations in *APC*, typically frameshift or nonsense mutations. FAP is characterized by hundreds to thousands of adenomas in the colon and rectum, which start to appear in the patient's second decade of life. Some of these adenomas inevitably progress to adenocarcinoma and metastatic disease unless the patient undergoes prophylactic colectomy. Hence, FAP patients are recommended have endoscopic screening from 10 years old. Genetic studies of FAP led to understanding the role of *APC* somatic mutations in also causing sporadic CRCs.

Also known as Lynch syndrome, HNPCC is an autosomal dominant condition which causes ~2-5% of CRCs and is a genetically heterogeneous disease (Fearon, *et al*., 2011). HNPCC patients have germline mutations in genes involved in DNA mismatch repair (MMR), with the majority of known HNPCC mutations being found in the genes *MSH2* and *MLH1*. Tumors from HNPCC patients also often contain microsatellite instability (MSI). There is a more rapid transition from adenomatous lesion to carcinoma compared to sporadic cancers, as affected cells accumulate mutations swiftly due to impaired DNA repair mechanisms. HNPCC patients have an 80% lifetime risk of developing CRC that typically develop in patients in their 40's, compared with an average incidence age for sporadic CRC in the 60's. HNPCC also increases the risk of other cancers such as gastric, ovarian, endometrial, renal and hepatobiliary cancers (Johns Hopkins Medicine CRC).

Genetic Alterations in Sporadic CRC

The majority of CRC (~70%) is considered sporadic, reflecting no (or very little) family history of the disease. Sporadic CRC are different from dominant hereditary syndrome forms in that they arise from an accumulation of somatic mutations in rate-limiting tumor suppressor genes and oncogenes rather than inheriting germline mutations (Rustgi *et al*., 2007). Both sporadic and inherited CRC emerge from normal colonic epithelium as a result of a sequence of genetic mutations and genomic alterations (including epigenetic changes) that lead to uncontrolled cell division and tumor formation. Identification of the genetic abnormalities that accumulate in a step-wise manner has led to the well-known model of the adenoma-carcinoma sequence initially

characterized by Fearon and Vogelstein (Figure 6, Fearon *et al*., 1990). This model describes the stepwise progression from normal glandular epithelial cells to benign neoplasia (adenoma) to carcinoma and eventually metastatic cancer and correlates specific genetic events with evolving tissue morphology. In the model that accounts for ~80% of CRC, mutations in the *APC* gene result in the activation of WNT signaling, which promotes the formation of small adenomas in the form of polyps. Subsequent mutations in *KRAS, BRAF, P53,* and other genes promote the progression to carcinomas, and finally additional mutations drive tumor metastasis (Walther *et al*., 2009). As discussed below, many additional mutations that confer a selective advantage for tumor growth are required for the development of a CRC. The progression from adenoma to invasive carcinoma can take years or even decades (Walther *et al*., 2009). This concept not only provides an excellent model to study the genetics of invasive cancer, but also affords a means of preventing CRC by endoscopic removal of precursor lesions (Jass *et al*., 2007).

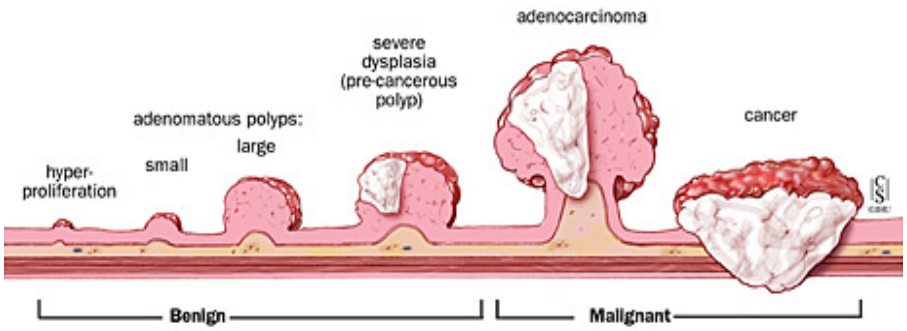

Figure 6. Schematic representation of the Vogelstein model of colonic carcinogenesis. (Johns Hopkins Medicine CRC)

Identification and characterization of genes that drive cancer processes are critical for the development of cancer diagnostic and therapeutic modalities. Over the past three decades, molecular genetic studies have revealed some critical mutations at high frequency underlying the pathogenesis of the sporadic and inherited forms of CRC, including *APC, K-RAS,* and *TP53*.

APC has been reported to be involved in multiple critical cellular functions. The best-established role for APC in CRC is as a major negative regulator of the canonical WNT signaling pathway. Germline mutations in *APC* play a key role in FAP. More than 95% of known mutations in *APC* in FAP patients are frameshift or nonsense mutations that lead to premature truncation of protein synthesis (Segditsas *et al*., 2006). FAP individuals who inherit germline mutations in *APC* develop thousands of colorectal adenomas by their teens with the inevitable progression of some of these to carcinoma, unless the intestine is surgically resected (Kinzler and Vogelstein, 1996). In addition to the role in FAP, *APC* plays a very prominent role in sporadic CRC. Loss of function mutations in *APC* occur in over 80% of sporadic CRC (Kinzler and Vogelstein, 1996). Nearly all somatic mutations lead to premature truncation of the APC protein (Segditsas *et al*., 2006). Somatic *APC* mutations are an early and rate-limiting event in the development of most adenomas (Powell *et al*., 1992). The inactivation of both alleles of the *APC* gene can be detected in most of the intestinal tumors at early stages of development (Powell *et al*., 1992), in agreement with Knudson's two hit hypothesis. However, accumulated mutations in additional genes are required for progression of the early lesions to cancer.

Activating mutations in *K-RAS (Kirsten rat sarcoma viral oncogene homolog)*, a member of the RAS family of proto-oncogenes, represent a second genetic alteration which occurs early in the evolution towards intestinal cancer (Plesec *et al*., 2009). The RAS family of small-G proteins function as molecular switches downstream of multiple receptor tyrosine kinase (RTK) growth factor receptors, such as the epidermal growth factor receptor (EGFR) family (Malumbres *et al*., 2003, Zhao *et al*., 2008). The product of the proto-oncogene *K-RAS* is involved in transduction of the MAPK (mitogen activated protein kinase) signaling pathway. *K-RAS* mutations in specific codons occur in approximately 40% of CRC and lead to the constitutive activation of the RAS/RAF/MEK/ERK signaling pathway, resulting in the transduction of signals involved in cell proliferation and apoptosis inhibition and thus, contributing to malignant transformation (Kim and Lance, 1997). *K-RAS* mutations contribute to colorectal adenoma progression but are not required for adenoma initiation, which is supported by

the fact that *K-RAS* mutations are found in at least 50% of colorectal adenomas larger than 1 cm and in carcinomas (Vogelstein *et al*., 1988). *K-RAS* mutations occur after *APC* mutations in the adenoma-to-carcinoma progression sequence, but are still a relatively early event in tumorigenesis. Acquired *K-RAS* mutations are maintained throughout carcinogenesis, as evidenced by the concordance of *K-RAS* mutation status in primary and metastatic colorectal cancer (Artale *et al*., 2008).

The *phosphatase and tensin homologue (PTEN)* gene codes for a lipid phosphatase which functions as a negative regulator of the phosphoinositide-3-kinase (PI3K)/ v-akt murine thymoma viral oncogene homolog 1 (AKT) pathway. The loss of *PTEN*, which occurs through different mechanisms, probably acts to enhance effects downstream of the K-RAS protein via PIP3-mediated activation of AKT that acts on downstream anti-apoptotic factors and the mTOR pathway, resulting in persistent oncogenic signaling (Cully *et al*., 2006, Chalhoub *et al*., 2009). Germline *PTEN* mutations are found in Cowden syndrome, leading to hyperactivity of the mTOR pathway, and an increased risk of some benign GI tumors but not an elevated risk of CRC (Hobert *et al*., 2009). Some studies suggest that PTEN protein expression may be lost in 15-20% of CRCs (Laurent-Puig *et al*., 2009). Other studies indicate that loss of PTEN protein expression measured by IHC occurs in 30% to 45% of CRCs (Loupakis *et al*., 2009).

Loss of heterozygosity (LOH) is a key mechanism for inactivating one allele of certain tumor suppressor genes in cancer. Approximately 70% of CRCs are characterized by loss of the short arm of chromosome 17 (17p) (Fearon *et al*., 1990, Vogelstein *et al*., 1988). LOH at this locus correlates with the transition from benign adenoma to invasive cancer (Vogelstein *et al*., 1988, Baker *et al*., 1990). The *TP53* gene is thought to be the main target of 17p LOH (Baker *et al*., 1990). In addition to 17p LOH, the function of *TP53* may be lost due to intrachromosomal somatic mutations. Approximately 85% of *TP53* mutations in CRC are missense defects, which most often occur at codons 175, 245, 248, 273, and 282 (Wood *et al*., 2007, Baker *et al*., 1990). The few nonsense and frameshift mutants encode a truncated TP53 product. TP53 is regarded as the "guardian

of the genome" due to its functions in cell-cycle checkpoints at the G1/S and G2/M boundaries, in promoting apoptosis, and in restricting angiogenesis (Vousden *et al*., 2009). *TP53* mutations and LOH of *TP53* alterations have been reported in 4-26% of adenomas, approximate 50% of *in situ* carcinomas, and in 50-75% of adenocarcinoma (Kaserer *et al*., 2000). This result is indicative of the central role of loss of TP53 function in the adenoma to carcinoma transition. Selection for *TP53* mutations in CRC may be due in part to the loss of TP53 function in regulating key target genes, including *p21, BAX,* and *MDM2* (Vousden *et al*., 2009). Loss of function in TP53 may facilitate continued growth and the acquisition of invasive properties in the face of stresses, including DNA-strand breakage, telomere erosion, hypoxia, and reduced nutrient exposure, that might otherwise severely limit tumor cell survival and maintenance at the adenoma-carcinoma transition.

However, these documented high frequency mutations do not completely explain all CRCs, since more mutations need to be acquired in addition to these high frequency mutations in the progression to highly invasive carcinomas. Moreover, some CRCs lack these high frequency mutations. Therefore, genome-wide analyses of somatic mutations in CRC were performed to obtain a deeper understanding of genetic alterations in CRC. The first genome-scale study of somatic mutations in CRC was conducted by the Vogelstein group at Johns Hopkins University (Wood *et al*., 2007). They identified a small population of genes that were frequently mutated in CRCs. These were called “mountains”, including genes such as *APC, KRAS, and TP53*. Surprisingly, their study identified a much larger population of genes mutated at a lower frequency, hence the term “hills” (Figure 7, Wood *et al*. 2007). They then analyzed the influence of the low frequency mutations in signaling pathways by determining whether the genes within specific pathways were mutated more often than predicted by chance. They found that 38 pathways were preferentially mutated in CRC. Within the 38 pathways, many of them were involved in the PI3K signaling. Additional pathways altered in CRC were related to cell adhesion, the cytoskeleton, and the extracellular matrix. These findings suggest that tumor growth in individual human CRCs may be driven by some genes that are mutated at a low frequency though affecting important signaling pathways.

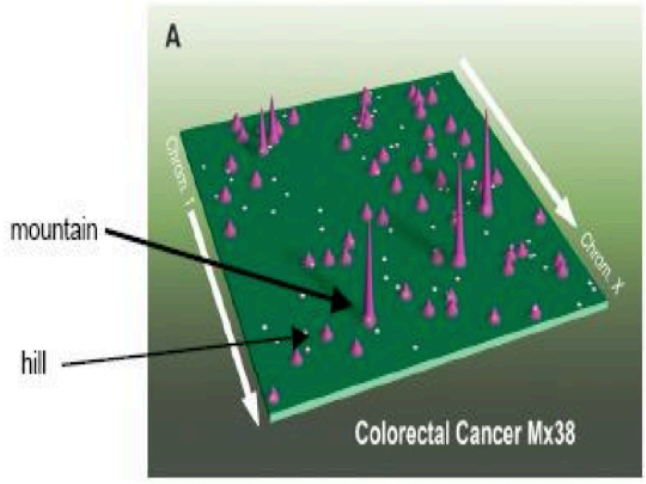

Figure 7. Human colorectal cancer genome landscape. (Wood *et al*. 2007).

To identify a more complete list of genes dysregulated in CRC, large-scale exome and genome sequencing studies of human CRCs have been conducted by multiple groups (Cancer Genome Atlas Network 2012, Han *et al*., 2013, Schee *et al*., 2013). These studies have revealed that there are hundreds to thousands of DNA alterations in the average CRC genome, and that there are roughly 80–100 genes that are commonly altered by non-synonymous mutations, and roughly 15 mutations in candidate 'driver' genes per cancer genome. Somatic mutations can be classified as either driver mutations or passenger mutations. Driver mutations confer a growth advantage to the cells carrying them in the neoplastic process and are positively selected for during tumorigenesis. They reside, by definition, in the subset of genes known as 'cancer genes' that are causally implicated in cancer development. Passenger mutations provide no positive or negative selective advantage to the tumor but are retained by chance during repeated rounds of cell division and clonal expansion (Grady *et al*., 2013, Wood *et al*., 2007). However, the 'passengers' can be converted into 'drivers' under certain selective environments, such as chemotherapy (Roche-Lestienne *et al*., 2002, Mullighan *et al*., 2008). The number of driver mutations in an individual cancer is a central conceptual parameter of cancer development, but is not well established. On the basis of age-incidence statistics it has been suggested that common adult epithelial cancers such as breast, colorectal and prostate cancers require 5-7 rate-limiting events, possibly equating to drivers, whereas

cancers of the haematological system may require fewer (Stratton *et al*., 2009). These estimates are supported by experimental studies which show that engineering changes in the functions of at least 5 or 6 genes in normal primary human cells are necessary to convert them into cancer cells (Schinzel *et al*., 2008). However, recent analyses of somatic mutation data from cancers indicate that the number of drivers might be as many as 20 driver mutations in individual cancers (Beerenwinkel *et al*., 2007). Ultimately, direct estimates of the number of drivers in individual cancers will be provided by identifying all the cancer genes and systematically measuring the prevalence of genomic mutations and epigenetic alterations in them.

While identifying the whole constellation of genomic abnormalities is significant, identifying those that are cancer drivers is even more meaningful. It appears that most somatic mutations in cancer genomes are likely passenger events (Greenman *et al*., 2007). A major challenge to all systematic mutation screens will, therefore, be to distinguish the driver mutations hidden within a much larger number of passenger mutations within the human cancer genome (Voidonikolas *et al*., 2009). Researchers have been tackling this challenge by improving experimental conditions and developing more sophisticated statistical models and functional analysis strategies. Performing an unbiased forward genetic screen in mice provides the tools to generate tumors and analyze their genetic composition, while reducing the background of passenger mutations. A successful strategy for such a genetic screen has been developed using the *Sleeping Beauty* transposon system to induce tumors in transgenic mice (Starr *et al*., 2011).

Sleeping Beauty Transposon-Based Forward Genetic Screens

The *Sleeping Beauty (SB)* transposon system is composed of a Sleeping Beauty transposase and a synthetic DNA transposon. The resurrected transposase gene was named "*Sleeping Beauty*" because it was brought back to activity from a long evolutionary silencing (Ivics *et al*., 1997). It was re-constructed from extinct (fossil) transposase sequences belonging to the Tc1/mariner class of transposons found in the genomes of salmonid fish, which have been inactive for more than 10 million years due to accumulated mutations (Doak *et al*., 1994, Radice *et al*., 1994). The transposon

component of the *SB* system was isolated from the genome of another salmonid fish, *Tanichthys albonubes*. The transposon was designed with an expression cassette of interest flanked by inverted repeat/direct repeat (IR/DR) sequences of about 340 base pairs each. Similar to other Tc1/mariner-type transposases, the SB transposase catalyzes the excision of DNA sequences within the IRs and the reintegration of this sequence into a recipient DNA in a cut-and-paste manner. *SB* transposons integrate nearly randomly into chromosomes at TA-dinucleotide base pairs, making it act as an effective tool for random mutagenesis, although the sequences flanking the TAs may influence the probability of integration at a given site (Figure 8, Geurts *et al*., 2006). As a result, DNA cargo in a chromosomally integrated transposon can be expressed over the lifetime of a cell.

The *SB* transposon system has several advantages over other mutagenesis systems. First, transposition efficiency of the SB transposase is greatly enhanced, enabling highly efficient transgenic integration and expression (Mates *et al*., 2009, Grabundzija *et al*., 2010). Second, *SB*-based vectors are likely superior in safety for two main reasons. *SB* shows a random genomic insertion profile without overt preference for integrating into genes and their transcriptional regulatory regions (Grabundzija *et al*., 2010, Ammar *et al*., 2012). In addition, the IRs sequence of *SB* vectors has negligible enhancer/promoter activity (Moldt *et al*., 2007, Walisko *et al*., 2008). Third, there are no *SB*-related sequences in mammalian genomes, thereby precluding potential cross-mobilization between endogenous and exogenously introduced transposons (Newman *et al*., 2008).

Since the *SB* transposon system can mediate efficient integration and stable long-term expression of a precisely defined DNA sequence, over the past decade, this system has been widely used in studying functional genomics, insertional mutagenesis, transgenesis, and somatic gene therapy.

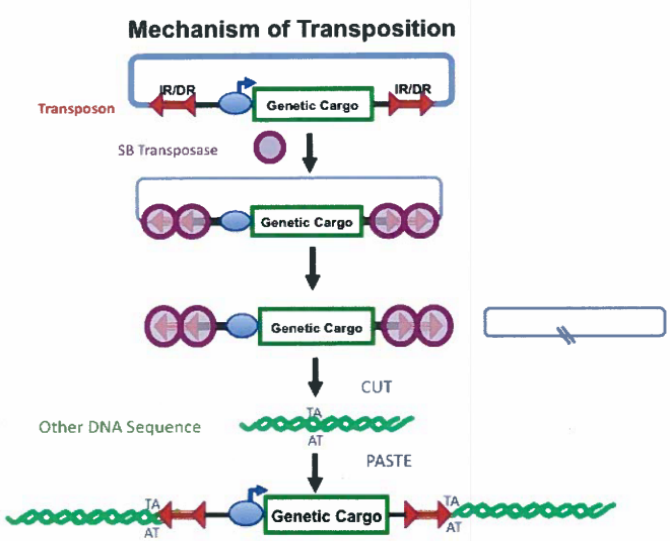

Figure 8. Mechanism of *SB*-mediated transposition. (by Perryhackett on Wikipedia)

Large scale sequencing of cancer genomes has revealed a vast array of somatic mutations in breast, colon, lung and pancreatic cancers (Wood *et al*., 2007, Ding *et al*., 2008, Jones *et al*., 2008). Distinguishing driver mutations from passenger mutations which are in a much larger number within the human cancer genome has been a major task for biologists. The *SB* transposon-based unbiased forward genetic screen in mice provides a tool to generate tumors and identify potential driver mutations, while reducing the background of passenger mutations, because the tumor formation process could select and enrich for the driver mutations.

An *SB*-based screen is initiated by breeding mice carrying *SB* transposon and transposase transgenes together. Further, tissue-specific expression of the transposon can be achieved using conditional expression alleles of the transposase that are activated by a tissue specific Cre recombinase. In addition, the system can be used in mice of differential susceptibility to sporadic cancers. For example, this permits the identification of genes important for tumor development in wildtype mice but also permits the identification of genes that cooperate with known cancer genes, such as *APC*. The mutagenic *SB* transposon was designed to create both loss- and gain-of-function mutations similar to those that drive tumorigenesis in sporadic human cancers. Recent modifications to the system using an inducible, tissue-specific transposase under the

control of a tissue-specific *Cre recombinase* allele have been shown to produce a wide range of epithelial-derived carcinomas (Dupuy *et al*., 2009) and tissue-specific cancers including GI neoplasms (Starr *et al*., 2009). Tumors from these mice are isolated and genomic DNA is extracted. Next generation sequencing is then used to identify transposon insertion sites in the tumors and bioinformatics tools are employed to identify high frequency common insertion sites (CIS) (Starr *et al*., 2009). A CIS is defined by analyzing transposon insertions in many tumors and identifying genomic loci that contain transposon insertions at a higher rate than would be expected by chance. The presence of a CIS indicates that a transposon-mediated mutation in that locus probably has contributed to tumor development. By analyzing the genes within the CIS, one can identify candidate cancer genes which need to be further validated by biological investigations. Cancer genetic fingerprints are obtained that can be characterized by networks of interacting cancer-gene mutations. These genes can be queried in relevant human cancers (Hackett *et al*., 2013). The process of devising and executing a forward genetic screen using the *SB* transposon system to identify candidate cancer genes is illustrated in Figure 9.

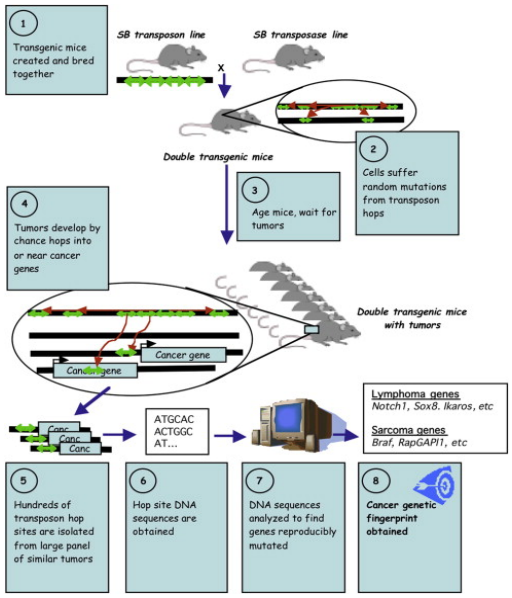

Figure 9. Using *SB* system for cancer gene screens in mice. (Hackett *et al*., 2013)

Due to the characteristics of the *SB* system, there are several advantages of using the *SB* system to identify candidate cancer genes. First, the transposon can easily be located in the genome because its sequence is known. Second, transposition can be directed to almost any cell type. Third, the transposon is capable of introducing both gain- and loss-of-function mutations (Bergemann *et al*., 2012).

The *SB* transposon-based screens have been successful in a number of studies that yielded lists of CIS genes which are potential cancer genes in colon (Starr *et al*., 2009, March *et al*., 2011), liver (O'Donnell *et al*., 2012), pancreatic (Pérez-Mancera *et al*., 2012) and skin (Quintana *et al*., 2013) cancers. Following functional characterization will be helpful in understanding the roles of these novel candidate cancer genes in different types of cancers. In addition, the use of this technique may lead to the eventual design of new therapies aimed to eliminate the results of these specific genetic mutations.

The CCR4-NOT (CNOT) Complex and CNOT1

Cnot1 (Table1) and other subunits of the CNOT complex, including *Cnot2, Cnot4, Cnot6, Cnot6l,* and *Cnot8*, were identified as CIS associated candidate cancer genes in CRC and other types of cancers in multiple *SB* screens in mice (Koso *et al*., 2012, March *et al*., 2011, Pérez–Mancera *et al*., 2012, Rahrmann *et al*., 2013, Starr *et al*., 2009, Starr *et al*., 2011, Wu *et al*., 2012). The updated information of CIS candidate genes in all published *SB*-based screens in different cancer types is available on the website of the Candidate Cancer Gene Database (CCGD) which is maintained by Dr. Starr's group at the University of Minnesota (http://ccgd-starrlab.oit.umn.edu/search.php).

The CNOT complex is a multicomponent complex evolutionarily conserved from yeast to human, which has a crucial role in regulation of gene expression at multiple levels (Collart *et al*., 2004). To date, the structural components and dynamics of this complex are still not completely known. The human CNOT complex is thought to be composed of 11 subunits (Figure 10, Boland *et al*., 2013). CNOT1 functions as a modular scaffold to provide binding sites for other CNOT subunits. Deadenylation is one of the main functions of the CNOT complex. The CNOT complex contains four deadenylases,

CNOT6 and its paralog CNOT6L, and CNOT7 and its paralog CNOT8, which are categorized into the exonuclease–endonuclease–phosphatase (EEP) and Asp-Glu-Asp-Asp (DEDD) families of nucleases based on their nuclease domains (Lau *et al*., 2009). All four deadenylases have deadenylation activity. Different deadenylase subunits have been shown to have various target genes and deadenylases of the same category have partial redundancy in function (Lau *et al*., 2009). The conserved core of the CNOT complex consists of two major modules: a catalytic module comprising the middle region of CNOT1 and two deadenylases (CNOT6 or CNOT6L, and CNOT7 or CNOT8), and the NOT module which minimally consists of the CNOT1 C-terminal region, CNOT2 and CNOT3. The integration of additional subunits has been shown, including CNOT4, CNOT5, CNOT9, CNOT10 and CNOT11 (Boland *et al*., 2013). The catalytic module is responsible for the deadenylation of specific mRNAs. The precise function of the NOT module remains largely unclear. It has been shown to regulate the stability and activity of the catalytic module and plays a crucial role in the recruitment of the CNOT complex to mRNAs by microRNAs (Wahle *et al*., 2013). In addition to the role in mRNA deadenylation/degradation, the CNOT complex is also involved in the transcriptional repression of nuclear receptor-mediated transcription in a ligand-dependent manner via CNOT1 and CNOT2 (Winkler *et al.,* 2006). The CNOT complex also plays a role in protein ubiquitination/degradation via the CNOT4 subunit with an E3 ligase activity (Collart *et al*., 2004). Furthermore, the CNOT complex is associated with various other functions in cells, such as translational repression (Cooke *et al*., 2010), DNA repair (Mulder *et al*., 2005) and histone methylation (Mulder *et al*., 2007). Given the diverse activities associated with the CNOT complex, it plays a role in a wide range of biological processes, including cell proliferation, apoptosis, oogenesis and embryogenesis, spermatogenesis, bone formation and energy metabolism (Collart *et al*., 2012).

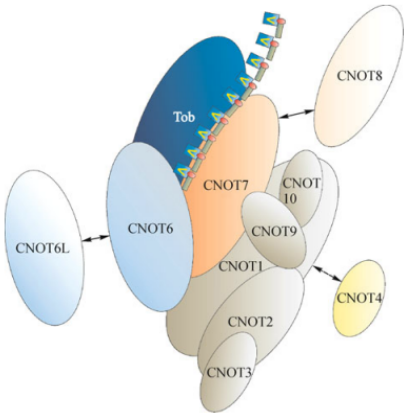

Figure 10. A proposed model for the human CCR4-NOT complex. (Bartlam *et al*., 2010)

Cnot1 (Table1, Figure 11) was identified as a CIS candidate cancer gene in CRC and other types of cancers in multiple *SB* screens in mice (Koso *et al*., 2012, March *et al*., 2011, Pérez–Mancera *et al*., 2012, Rahrmann *et al*., 2013, Starr *et al*., 2011).

Cancer Type	Study
Colorectal Cancer	Starr *et al*., 2011
Colorectal Cancer	March *et al*., 2011
Pancreatic Cancer	Pérez–Mancera *et al*., 2012
Nervous System Cancer	Koso *et al*., 2012
Nervous System Cancer	Rahrmann *et al*., 2013

Table 1. *Cnot1* was identified as CIS candidate cancer gene by multiple *SB* screens.

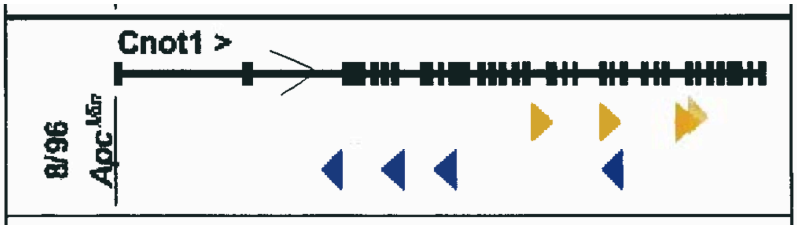

Figure 11. Map of *SB* insertions in *Cnot1* in Apc^{Min} screen. (Starr *et al*., 2011) Yellow and blue markers represent sites of transposon insertions on the same and opposite direction of *Cnot1* gene, respectively, in GI tumors.

The human *CNOT1* gene is located over 100kb on the long arm of chromosome 16 at position 16q21. *CNOT1* mRNA has three splicing variants, NM_016284.4,

NM_206999.2, and NM_001265612.1, encoding three protein isoforms NP_057368.3, NP_996882.1 and NP_001252541.1, respectively (Table 2). The variant NM_016284.4 (*CNOT1L*) encodes for the longest isoform of 2376 amino acids (aa) (Figure 13). The variant NM_206999.2 (*CNOT1S*) differs in the 3' UTR compared to variant NM_016284.4. The encoded isoform NP_996882.1 is 1551aa and has a distinct C-terminus. The variant NM_001265612.1 (*CNOT1M*) uses an alternate splice site in the coding region, but maintains the reading frame, encoding an isoform NP_001252541.1 that is 2371aa.

Transcript variant	mRNA length (nt)	Protein isoform	Protein length (aa)	Abbrevation
NM_016284.4	8476	NP_057368.3	2376	CNOT1L
NM_206999.2	5221	NP_996882.1	1551	CNOT1S
NM_001265612.1	8461	NP_001252541.1	2371	CNOT1M

Table 2. Splicing variants and protein isoforms of *CNOT1*.

Multiple somatic mutations in *CNOT1* in different types of cancers, in particular CRC, have been documented by several projects. The COSMIC database documented 49 mutations in *CNOT1* among 610 cases (8%). In the TCGA database, *CNOT1* mutations were identified in 11 out of 212 cases (5.2%) (Cancer Genome Atlas Network, 2012). In a study by Seshagiri *et al* (Seshagiri *et al*., 2012), *CNOT1* mutations were identified in 9 out of 72 cases (12.5%) (Figure 12). Some mutations, such as R1733H and R1640Q, occurred multiple times. For all three databases, *CNOT1* is mutated most frequently in CRC. Most of these mutations are missense mutations and no specific cluster or hotspot was observed. The high *CNOT1* mutation rate in CRC suggests a correlation of *CNOT1* genetic alteration with CRC development.

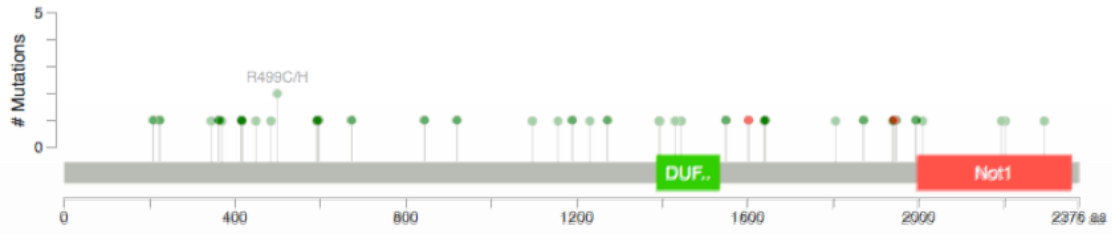

Figure 12. Mutations in *CNOT1* identified in CRC samples by TCGA and Seshagiri *et al.*

The longest CNOT1 isoform is composed of 2376 amino acids which can be divided into N-terminal, middle and C-terminal regions. The CNOT1 N terminus consists of two HEAT-repeat domains. The CNOT1 middle region contains a MIF4G domain and a domain of unknown function (DUF3819). The CNOT1 C terminus contains the NOT1 superfamily homology (SH) domain (Figure 13).

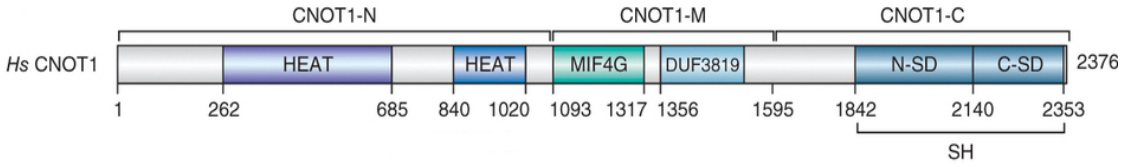

Figure 13. Diagrams of CNOT1 with N-terminal, middle and C-terminal regions. (Boland *et al*., 2013)

CNOT1 is essential for the assembly of the complete CNOT complex (Boland *et al*., 2013). The N terminus of CNOT1 provides binding sites for the CNOT10–CNOT11 module with functions that are largely unknown (Boland *et al*., 2013). The catalytic module comprising deadenylases centers on the middle region of CNOT1, which is critical for deadenylation of specific mRNAs. For example, the MIF4G domain (residues 1093-1317) in middle region of CNOT1 binds to CNOT7 directly through a pre-formed interface and leaves the CNOT7 catalytic site fully accessible to RNA substrates (Petit *et al*., 2012). The the middle region of CNOT1 is also important for interaction with RNA binding proteins. For example, residues 800-1015 of CNOT1 are critical for binding with the ZFP36 ring finger protein (ZFP36). Disruption of the ZFP36-CNOT1 interaction impairs mRNA deadenylation *in vitro* and *in vivo* (Fabian *et al*., 2013). The C terminus of CNOT1 is the scaffold of the NOT module which minimally consists of CNOT2 and CNOT3. The NOT module has been shown to regulate the stability and activity of the catalytic module and play a crucial role in the recruitment of the CNOT complex to mRNAs by microRNAs (Wahle *et al*., 2013). GW182, a RISC complex component, directly binds to the CNOT1 C terminal domain to recruit the CNOT deadenylase complex (Fabian *et al*., 2011).

Due to the central role of CNOT1 in the integrity and function of the CNOT complex, disruption of CNOT1 has been shown to attenuate deadenylation mediated by the CNOT complex (Ito *et al*., 2011, Fabian *et al*., 2013, Boland *et al*., 2013). Biological functions of CNOT1 have not been well studied, in particular in cancer. Some studies showed that depletion of *CNOT1* could cause significant apoptotic cell death in a caspase-4 dependent manner in Hela cells (Ito *et al*., 2011). Depletion of another CNOT subunit, *CNOT2*, also has been shown to cause cell apoptosis (Sonnichsen *et al*., 2005, Ito *et al*., 2011). Deadenylase CNOT6L is required for cell proliferation via regulation of mRNA levels of the cell cycle inhibitor $p27^{Kip}$ (Morita *et al*., 2007). CNOT7 and CNOT8 are important for cell proliferation in MCF7 breast cancer cells (Aslam *et al*., 2009). These results suggest that the integrity and the deadenylation function of the CNOT complex are critical for cell survival. Futhermore, CNOT1 mediates repression of estrogen receptor α (ERα)- and retinoid X receptor (RXR)-mediated transcription via direct recruitment of the CNOT complex to hormone-regulated promoters. In support of this notion, knockdown of *CNOT1* by siRNA results in induction of ERα target genes, *TFF1* and *c-MYC*, in MCF-7 cells (Winkler *et al*., 2006).

Moreover, the disrupted deadenylation function of the CNOT complex can cause up-regulated mRNA levels of a large group of genes (Aslam *et al*., 2009). When these mRNAs are translated in the endoplasmic reticulum (ER), it may cause overproduction of proteins, inducing a cellular stress condition called ER stress. This is supported by an Ito *et al* study showing that depletion of *CNOT1* and *CNOT2* in Hela cells can cause activation of unfolded protein response (UPR) pathways, which is a cellular response to ER stress (Ito *et al*., 2011).

Mechanisms of mRNA Decay

One of the main functions of the CCR4-NOT complex and CNOT1 is regulation of mRNA deadenylation and turnover. Control of mRNA decay is a fundamentally important step in determining the amount of protein produced from the mRNA by translation. Microarray analyses have revealed that 40-50% of changes in gene expression in response to cellular signals occurs at the level of mRNA stability, allowing

rapid regulation of gene expression in response to different cellular conditions (Fan *et al*., 2002, Cheadle *et al*., 2005). Polyadenylation and deadenylation of an mRNA transcript are key processes that regulate its stability and degradation.

During the process of maturation, almost all eukaryotic precursor mRNAs undergo cleavage/polyadenylation at their 3' ends, with the exception of histone mRNAs, which are cleaved but not polyadenylated (Gilmartin *et al*., 2005). During transcription, the mRNA transcript is cleaved at a site 10-30 nucleotides downstream of the poly(A) signal (AAUAAA), and then a poly(A) tail of 200-300 nucleotides long is added to the 3' end by polyadenylate polymerase. The poly(A) tail and the poly(A)-binding proteins (PABPs) bound to it aid in protecting mRNAs from degradation by exonucleases (Mandel *et al*., 2008).

In eukaryotes the 5’ cap and the 3’ poly(A) tail interact with the cytoplasmic proteins eIF4E and PABPs, respectively, to protect the transcript from exonucleases and to enhance translation initiation. To initiate decay, either one of these two structures must be compromised. Decay of most mRNAs is initiated by shortening of the poly(A) tail at the 3’ end, referred to as deadenylation (Shyu *et al*., 1991). The deadenylation process is considered as the rate-limiting step and is also the most efficient step in controlling mRNA decay (Decker and Parker, 1993). Many cellular factors and mechanisms are devoted to modulating the rate of deadenylation, including deadenylases which carry out the deadenylation of target mRNAs. There are three main categories of eukaryotic deadenylases, including the PAN2-PAN3 complex, the CNOT complex and the PARN (poly(A)-specific ribonuclease), each with unique properties (Yamashita *et al*. 2005). The CNOT complex has been described above. PAN is a heterodimeric complex consisting of catalytic PAN2 and regulatory PAN3 subunits (Uchida *et al*., 2004). It was reported that mammalian PAN2-PAN3 carries out the initial shortening of the tail of a *β-globin* reporter transcript from the usual 200 nucleotides to a length of ~80 nucleotides (Yamashita *et al*. 2005). At this point, the deadenylation is handed over to the CNOT complex. Whether PAN2-PAN3 has a role in deadenylating all mRNAs in higher eukaryotes is still unclear as it seems likely that this function can be carried out by other

deadenylases (Yamashita *et al*. 2005). PARN has cap-dependent deadenylase activity, i.e., its processivity is enhanced by the presence of a 5'cap and inhibited by cap-binding proteins (Balatsos *et al*., 2006). PARN is essential for embryogenesis in many higher eukaryotes including mammals. For example, PARN was reported to be implicated in the mass deadenylation of maternal mRNAs in *Xenopus laevis* oocytes during maturation (Korner *et al*., 1998). Following deadenylation, two mechanisms can degrade an mRNA: the 5'-to-3' and 3'-to-5' exonucleolytic degradation pathways. In the 5'-to-3' pathway, the 5' cap is removed by the DCP1–DCP2 complex which is involved in early steps of poly(A) tail metabolism. Following decapping, the 5'-3' exoribonuclease 1 (XRN1) degrades the mRNA transcript (Fenger-Gron *et al*., 2005). Alternatively, the deadenylated mRNA can be degraded in the 3'-to-5' direction by the exosome, a multi-subunit complex that consists of 6 core subunits proteins with RNase activity. Following 3'-to-5' decay, the 5' cap on the remaining oligomer is hydrolyzed by the scavenger decapping enzyme DcpS (Garneau *et al*., 2007). These two pathways are not mutually exclusive and both are involved in the decay of unstable mRNAs in mammalian cells (Figure 14).

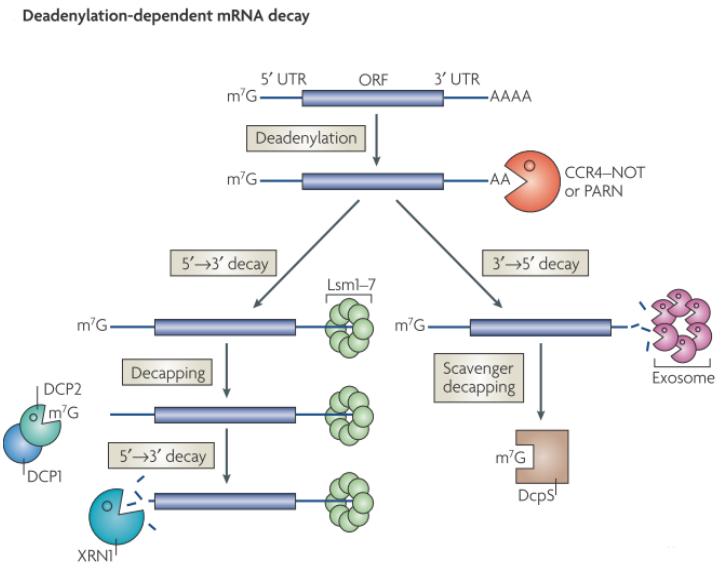

Figure 14. Mechanisms of normal mRNA degradation. (Garneau *et al*., 2007)

mRNA deadenylation/decay represents an important checkpoint for regulation of post-transcriptional gene expression. The mRNA deadenylation determinants are found predominantly in the 3'UTR, such as AU-rich elements (ARE) and microRNA target sites (Sandberg *et al*., 2008), but they are also found in the 5' UTR and coding regions.

About 12% of mammalian mRNAs, especially those encoding cytokines, proto-oncogenes and transcription factors, bear important regulatory ARE signals in their 3'UTRs (Khabar *et al*., 2005). The AREs typically contain one or several AUUUA pentamer repeats within a U-rich region of the 3'UTR. Both the AREs sequences and the flanking sequences can influence the overall effect on mRNA stability (Stoecklin *et al*., 2003). RNA binding proteins (RBPs) can bind to the ARE element to regulate ARE-mediated mRNA decay by either inhibiting or activating deadenylation (Barreau *et al*., 2006). RBPs are key components in RNA metabolism, regulating the temporal, spatial and functional dynamics of RNAs (Barreau *et al*., 2006). Most mRNAs are associated with multiple RBPs, while a RBP can bind to multiple mRNA targets, suggesting the potential for a multidimensional network of post-transcriptional regulation of RNA metabolism. RBPs play diverse roles in mRNA decay. Some RBPs accelerate decay of target mRNA transcripts through promoting deadenylation, including ZFP36, butyrate response factor 1 (BRF1), AU-rich binding factor 1 (AUF1) and KH-type splicing regulatory protein (KSRP). To promote deadenylation of target mRNA transcripts RBPs can recruit the CNOT complex to target transcripts to carry out the removal of the poly(A) tail. In this process, CNOT1 provides a platform that recruits other subunits of the CNOT complex, including deadenylase subunits, to target transcripts (Sandler *et al*., 2011). For example, Nanos2 plays a key role in the sexual differentiation of germ cells through regulating the expression levels of several important genes, such as *Sycp3*, *Stra8* and *Dazl*. It can bind to the CNOT1 protein directly, in turn recruiting the deadenylase subunits to the Nanos2-RNA complex to execute deadenylation of these mRNAs (Suzuki *et al*., 2010). PUM1 can promote *HMOX1* mRNA deadenylation through binding to its ARE and recruiting the CNOT complex (Miller *et al*., 2011). ZFP36 is an RNA binding zinc-finger protein which binds the ARE of *TNF-α* mRNA and accelerates its degradation through recruiting the CNOT complex (Sandler *et al*., 2011). The disruption of the

interaction between RBPs and the CNOT complex may interrupt RBP-mediated mRNA degradation. For example, the depletion of *CNOT1* by siRNA could result in a dramatically decreased decay of *globin*-ARE reporter mRNA by ZFP36 (Sandler *et al*., 2011). The defects in RNA metabolism caused by aberrations in RBP-mediated mRNA decay contribute to a broad spectrum of human disorders including cancer (Dean *et al*., 2004). Besides the CNOT complex the deadenylase PARN is also involved in ZFP36-directed deadenylation *in vitro* (Lin *et al*., 2007). On the other hand, ELAV like RNA binding protein 1 (ELAVL1) can stabilize mRNAs containing AREs in their 3'UTR, such as *c-fos, GM-CSF* and *EGF*, by blocking the recruitment of deadenylases or the exosome (Fan *et al*., 1998).

MicroRNAs (miRNAs) are a large family of single-stranded small non-coding RNA molecules (~22 nucleotides in length) found in plants and animals, which function in transcriptional and post-transcriptional regulation of gene expression. The human genome may encode over 1000 miRNAs, which may target about 60% of mammalian genes (Friedman *et al*., 2009). miRNAs are encoded by the eukaryotic genome from either their own genes or from introns or even exons of other genes. miRNA genes can be transcribed as independent units, or, in some cases, together with its host gene, providing a means for coupled regulation of both the miRNA and protein-coding gene (Lee *et al*., 2004). In the canonical maturation pathways, miRNA genes are transcribed by either RNA polymerase II or RNA polymerase III into primary miRNA transcripts (pri-miRNA) which are usually capped and polyadenylated and spliced (Lee *et al*., 2004). The pri-miRNA is next endonucleolytically cleaved by the nuclear microprocessor complex Drosha–DGCR8 in the nucleus to produce a hairpin structure of about 70 nucleotides, termed a precursor-miRNA (pre-miRNA). The pre-miRNA is then exported from the nucleus by the Exportin-5–Ran-GTP complex to the cytoplasm. In the cytoplasm, the pre-miRNA hairpin is cleaved by the RNase III enzyme Dicer in a complex with the double-stranded RNA-binding protein TRBP, yielding an imperfect miRNA:miRNA* duplex about 22 nucleotides in length (Lund *et al*., 2006). Although either strand of the duplex may potentially act as a functional miRNA, only the functional strand of the mature

miRNA is loaded together with Argonaute (Ago) proteins into the RNA-induced silencing complex (RISC), whereas the passenger strand is degraded (Figure 15).

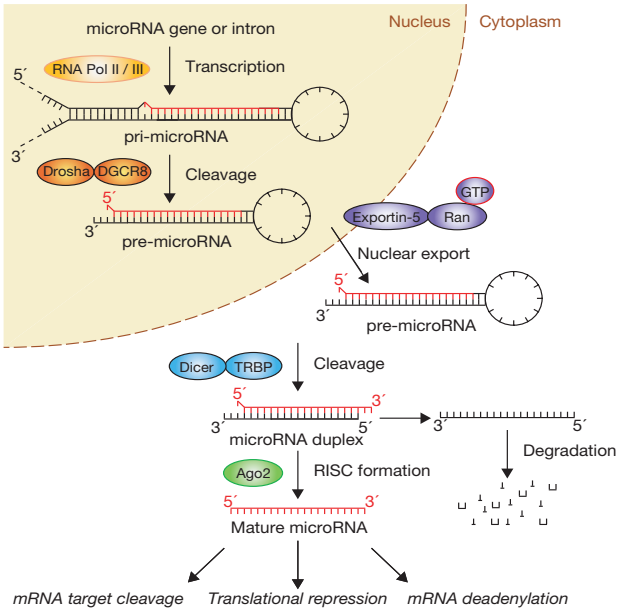

Figure 15. The canonical pathway of microRNA processing. (Winter *et al*., 2009)

miRNAs result in gene silencing either through translational repression and/or degradation of target mRNAs (Eulalio *et al*., 2008). These two mechanisms may represent two distinct independent pathways: the ability of miRNAs to expedite deadenylation does not depend on decreased translation; in some cases translational repression by miRNAs require a poly(A) tail (Wu *et al*., 2006). miRNAs accomplish their regulatory function through the RISC complex. miRISCs facilitate degradation of miRNA targeted mRNAs via deadenylation followed by Dcp1-Dcp2 complex-directed decapping, and subsequent exonucleolytic digestion (Chen *et al*., 2009). The core RISC contains at a minimum a specificity-determining miRNA, an Ago protein bound to miRNA, and a GW182 protein. Target recognition by a RISC is determined mainly by the base-pairing between the 5' portion of the miRNA and the 3'UTR of target mRNAs (Bartel *et al*., 2009). Ago proteins bind the mature miRNA and facilitates its interaction with a target mRNA. Some Ago proteins, such as Ago2, can cleave target transcripts directly by their PIWI domain when the match-up of miRNA with target mRNA is

perfect, such as in the case of miR-196 downregulating the *HOXB8* mRNA (Soraya *et al*., 2004). However, the vast majority of miRNAs are only partially complimentarity with the 3'UTR of their targets, so in most cases, Ago has to recruit additional proteins to achieve translational repression and mRNA decay (Bartel *et al*., 2009). Generally, Ago proteins recruit GW182 proteins to miRNA-targeted mRNAs in which the C-terminal region of Ago directly binds to the GW-rich regions of GW182 in the N terminal (Takimoto *et al*., 2009). Three GW182 paralogs exist in vertebrates (TNRC6A/GW182, TNRC6B, and TNRC6C) (Eulalio *et al*., 2009). The binding of the RISC to the target transcript can result in the recruitment of deadenylation factors mediated by GW182 (Fabian *et al*., 2011). Human GW182 proteins recruit the PAN2-PAN3 and the CNOT complexes through direct interactions with PAN3 and CNOT1 by the middle and C-terminal regions of the silencing domains, respectively. Therefore, GW182 proteins provide a docking platform through which deadenylase complexes gain access to the poly (A) tail of miRNA targets to promote their deadenylation. In this process, CNOT1 mediates the interactions between GW182 and the additional subunits of the CNOT complex that provides a major contribution to miRNA-mediated mRNA degradation (Piao *et al*., 2010). The CNOT complex recruited by GW182 can also act to repress translation initiation (Pasquinelli *et al*., 2012). Thus we hypothesized that the genetic alterations in *CNOT1* may impair the miRNA-mediated post-transcriptional regulation of genes, contributing to the development of CRC. Supporting this idea, knockdown of *CNOT8* and *CNOT1* expression and the overexpression of CCR4 or CAF1 mutants could significantly reduce miRNA-mediated deadenylation and mRNA decay, but not translational repression (Piao *et al*., 2010, Fabian *et al*., 2009). The PAN2-PAN3 complex has also been shown to be involved in but not essential for degradation of miRNA targets, as inactivation of the PAN2-PAN3 complex slows down the initial deadenylation, but deadenylation and decay still occur, minimally affecting miRNA target levels at steady state (Chen *et al*., 2009). How and if PARN is involved in miRNA-mediated deadenylation still remains to be established.

ER Stress and the Unfolded Protein Response

The CNOT complex and CNOT1 are widely involved in RBP- and miRNA-mediated mRNA deadenylation/decay. Therefore, the disruption of the function of the CNOT complex and CNOT1 may lead to an altered gene expression profile. In addition, an enlarged pool of mRNAs may be translated in the endoplasmic reticulum (ER). In the ER the nascent polypeptides are folded into specific tertiary structures essential to their functions. When the requirement for proper folding of nascent polypeptides exceeds the protein folding capacity of the ER, unfolded or misfolded proteins will accumulate in the ER lumen, inducing a situation termed ER stress. When ER stress occurs, cells will activate an elaborate adaptive response known as the unfolded protein response (UPR) (Ron, *et al*., 2007). In eukaryotic cells, canonical branches of the UPR are mediated by three ER membrane-associated proteins, PKR-like eukaryotic initiation factor 2a kinase (PERK), inositol requiring enzyme 1α (IRE1α), and activating transcription factor-6 (ATF6) (Tsai *et al*., 2010) (Figure16). In a ‘‘stress-free’’ ER, these three trans-membrane proteins are bound by a chaperone, glucose-regulated protein, 78kDa (GRP78/BiP), in their intraluminal domains and rendered inactive. Accumulation of improperly folded proteins in the ER results in the dissociation of GRP78/BiP away from these UPR sensors (Bertolotti *et al*., 2000). This event leads to oligomerization and activation of PERK and IRE1α and translocation of ATF6 to the Golgi apparatus where it is processed into an active transcription factor, resulting in the activation of a series of downstream signaling events (Ron *et al*, 2007). Together these three arms of the UPR can mitigate ER stress by reducing protein synthesis, facilitating protein degradation, and increasing production of protein folding chaperones, which helps cells to restore homeostasis.

The IRE1α pathway is the oldest branch of the UPR in an evolutionary sense. The endoribonuclease activity of IRE1α cleaves a 26 base-pair segment from the mRNA of the *X-box binding protein-1 (XBP1)*, creating an alternative message that is translated into the spliced active form of the transcription factor sXBP1 (Calfon *et al*., 2002). sXBP1, alone or in conjunction with ATF6, launches a transcriptional program to produce chaperones and proteins involved in ER biogenesis, phospholipid synthesis, and ER-associated protein degradation (ERAD). Thus, sXBP1 activates one of the major pathways for enhancing the folding capacity of the ER to deal with ER stress.

Hyperactivated IRE1α has been reported to increase *TXNIP* mRNA stability by reducing levels of *miR-17*, a *TXNIP* destabilizing microRNA. In turn, elevated TXNIP protein activates the NLRP3 inflammasome, causing procaspase-1 cleavage and interleukin 1β (IL-1β) secretion (Lerner *et al*., 2012).

Under ER stress, ATF6 translocates to the Golgi apparatus, where it is processed by Golgi proteases (S1P, S2P) to release the active transcription factor. Activated ATF6 then moves to the nucleus and functions as a transcription factor to promote the transcription of genes containing ER stress elements (ERSE), UPR elements (UPRE), and cAMP response elements (CRE) in their promoters. As a result, ERAD and production of the ER degradation-enhancing mannosidase-like protein (EDEM) are boosted by these events, facilitating clearance and degradation of misfolded proteins from the ER lumen. Furthermore, ATF6 can upregulate *XBP1* mRNA transcription levels. Currently, ATF6 and sXBP1 are viewed as the predominant regulators of the transcriptional response programs triggered by the activation of the UPR (Tsai, *et al*., 2010).

Activation of the third arm of the UPR through PERK results in phosphorylation of eIF2α (eukaryotic translational initiation factor 2α) at serine 51, which converts eIF2α to a competitor of eIF2b, resulting in reduced global protein synthesis. In addition, this branch of the UPR can also lead to activation of activating transcription factor-4 (ATF4), nuclear erythroid 2 p45-related factor 2 (NRF2), and nuclear factor kappa b (NF-κB) through several distinct mechanisms. ATF4 is produced through enhanced translation and induces expression of genes involved in apoptosis (*CHOP, C/EBP homologous protein*), ER redox control (*ERO1, endoplasmic reticulum oxidoreductin*), and glucose metabolism (*GCK, glucokinase*). One consequence of ER stress is the accumulation of reactive oxygen species (ROS) that promotes a state of oxidative stress. The UPR has incorporated an antioxidant defense system via activation of the NRF2 and ATF4 transcription factors, coordinating the convergence of ER stress with oxidative stress signaling, and orchestrating the transcription program of the antioxidant response element-dependent genes, including *hemeoxygenase-1 (HMOX1), thioredoxin reductase 1 (TXNRD1),* and *the glutathione S-transferases (GSTP1)*.

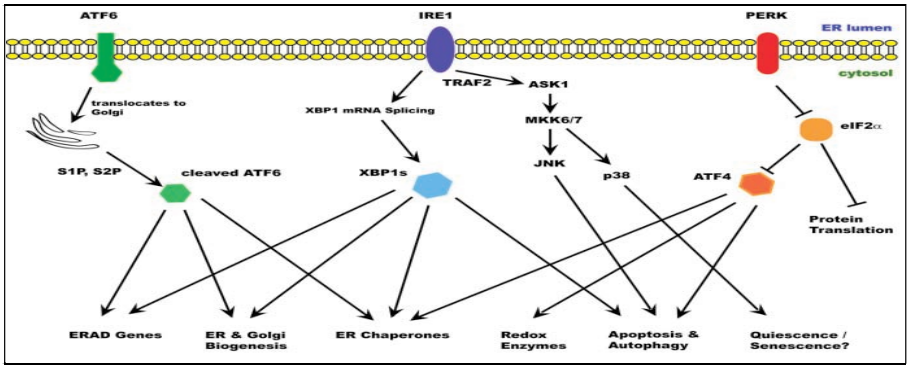

Figure 16. Unfolded protein response in mammalian cells. (Schönthal *et al*., 2011)

Through activation of these three UPR pathways, cells can deal with a moderate level of ER stress and restore homeostasis. However, the UPR does not always result in successful alleviation of ER stress and reestablishment of a functional equilibrium in the ER. When driven by severe or prolonged stress signals, the UPR can also induce cell apoptosis through several mechanisms (Tabas *et al*., 2011). The IRE1α mediated UPR pathway is a critical lever in the UPR that controls commitment to cell death or promotes survival (Ron *et al*., 2007). IRE1α leads to activation of the apoptosis signaling kinase 1 (ASK1) and downstream kinases through binding TRAF2, leading to activation of the c-Jun N-terminal kinase (JNK) pro-apoptotic signaling pathway that promotes apoptosis by switching on the pro-apoptotic B-cell CLL/lymphoma 2 (BCL-2) family proteins BCL2-associated X protein (BAX) and BCL2-antagonist/killer 1 (BAK) (Zong *et al*., 2003). IRE1α also has been reported to upregulate thioredoxin-interacting protein (*TXNIP*) levels by reducing levels of *miR-17*. In turn, elevated TXNIP protein activates a series of pro-apoptotic pathways, such as activation of interleukin-1 beta (IL-1β) (Lerner *et al*., 2012). In addition，IRE1α can also induce the preferential degradation of a pool of mRNAs through a mechanism known as regulated IRE1-dependent decay (RIDD) (Hollien *et al*., 2009). Hyper activation of the PERK pathway can induce expression of *CHOP*, a pro-apoptotic transcription factor, which regulates the transcription of *BCL2* family members and other pro-apoptotic genes (Zinszner *et al*., 1998). In addition, activation of both the PERK and IRE1α pathways lead to activation of the NF-κB signaling pathway (Tam *et al*., 2012).

There is evidence that chronic ER stress and activation of the UPR are important in the pathogenesis of a number of diseases, including cancer, neurodegenerative diseases, diabetes, and inflammatory disease (Hosoi *et al*., 2010, Lerner *et al*., 2012). Some cancer cells, unlike normal cells, harbor a chronically activated protective module of ER stress components in order to manage intensified protein synthesis or to adapt to hostile microenvironmental conditions, such as hypoglycemia, hypoxia, acidosis, or chemotherapy, which are known triggers of ER stress (Luo *et al*., 2013). The genetic alterations resulting in better management of ER stress in tumor cells may confer growth advantage to cancer cells and contribute to cancer progression. Therefore, we hypothesize that the increased activity of CNOT1 may help cancer cells to limit the production of proteins in the ER, thus reducing the levels of ER stress.

In accordance with the previously described balance of this cellular system, two opposing approaches are offered in order to therapeutically target ER stress. On the one hand, experimental efforts are aimed at supporting pro-survival modules and/or blocking the pro-apoptotic components in order to increase cellular survival. For example, in type 2 diabetes where chronic ER stress may lead to the destruction of pancreatic β-cells, controlling ER stress may help to protect β-cells and delay the development of diabetes (Lerner *et al*., 2012). On the other hand, efforts to further aggravate pre-existing ER stress and enhance pro-apoptotic processes could be beneficial in the case of malignant neoplasms. For example, deterioration of chronic ER stress in cancer cells by therapeutic reagents may induce ER stress mediated cell apoptosis selectively in tumor cells which have higher levels of ER stress than normal cells (Schönthal *et al*., 2011).

Thioredoxin-Interacting Protein (TXNIP)

When unfolded proteins accumulate to irremediably high levels within the ER, the UPR becomes hyperactivated to cause programmed cell death. TXNIP that is rapidly induced by IRE1α is a critical node in this ‘‘terminal UPR.’’ *TXNIP* was originally identified in HL-60 leukemia cells treated with 1,25-dihydroxyvitamin D3 and was termed as *vitamin D up-regulated protein 1 (VDUP1)* (Chen *et al*. 1995). This gene encodes for an inhibitor of the antioxidant protein Thioredoxin (TRX), which directly

interacts with TRX and blocks its reducing activity and inhibits the interaction between TRX and other factors, such as ASK-1 and PAG (Junn, *et al*., 2000). TXNIP is also reported to exert functions through redox independent mechanisms. TXNIP has been reported to be involved in multiple cellular processes, including cell growth and apoptosis (Jeon, *et al*., 2005), metabolic regulation (Patwari, *et al*., 2009), and inflammatory response (Zhou, *et al*., 2010). *TXNIP* expression is regulated by multiple mechanisms, such as glucose, HDACs, KLFs, and PPARs. Its expression is also upregulated by various cellular stresses, including ER stress, oxidative stress, and irradiation (Han *et al*., 2003). Further, NRF2, an important transcription factor known to regulate anti-oxidant responses, also upregulates *TXNIP* expression levels (Adair-Kirk *et al*., 2008). As described before, *TXNIP* levels are also upregulated by activation of IRE1α that destabilizes *miR-17*.

As a tumor suppressor, TXNIP has been reported to cause cell cycle arrest and apoptosis. To induce cell growth arrest, TXNIP translocates to the nucleus where it regulates cell proliferation by multiple mechanisms, including increasing the stability of the cell cycle inhibitor $p27^{kip}$, upregulating levels of the CDK inhibitor p16, and reducing RB phosphorylation (Jeon *et al*., 2005). TXNIP can also promote apoptosis through redox-dependent and -independent mechanisms. Thioredoxin (TRX) inhibits apoptosis via inhibiting ASK1 and PTEN (Saitoh *et al*., 1998). TXNIP inhibits the interaction between TRX and ASK1, relieving the constitutive inhibition of ASK1 and the released ASK1 induces apoptosis through activation of the JNK and p38 signaling pathways (Tobiume *et al*., 2001). A recent report described how TXNIP promotes NLR family, pyrin domain containing 3 (NLRP3) inflammasome activation and IL-1β maturation that can lead to apoptosis in response to different cellular stresses (Zhou, *et al*., 2010).

TXNIP has been identified as a novel tumor suppressor based on its effects on regulating both cell growth and death (Han *et al*., 2003, Goldberg *et al*., 2003). TXNIP has dramatically reduced expression in multiple tumors including renal, breast, lung, gastric, colon, and hepatocellular carcinoma (Cadenas *et al*., 2010， Dutta *et al*., 2005, Takahashi *et al*., 2002). The enforced expression of TXNIP inhibited the proliferation of

cancer cells including gastric cancer, and promyelocytic leukemia, and suppressed tumor growth and metastasis in transplantation models (Han *et al*., 2003， Wang *et al*., 2002， Goldberg *et al*., 2003). TXNIP has also been shown to play an important role in several pathologic conditions besides cancer, including diabetes, cardiovascular disease, and chronic inflammation.

It has been shown that *miR-17* destabilizes *TXNIP* mRNA (Lerner *et al*., 2012). miRNAs recruit the CNOT complex through direct binding to CNOT1 to deadenylate target mRNAs. Therefore, we hypothesize that increased activity of CNOT1 as well as the CNOT complex may contribute to the regulation of *TXNIP* levels by *miR-17*.

Summary

Identification of driver mutations in CRC is important in overcoming the challenges in CRC management and improving patients' outcome. In the hundreds of DNA mutations in each CRC genome, only a small portion are driver mutations, whereas most of them are passenger mutations. Therefore, a major challenge in CRC genetic studies is to distinguish driver mutations hidden within a much larger number of passenger mutations. To identify candidate CRC driver mutations, we performed a *Sleeping Beauty* transposon-based forward genetic screen in mice and we found a list of CIS candidate CRC genes. One of the top CIS candidates is *Cnot1* which encodes for the scaffold factor of the CNOT complex that is a multicomponent complex widely involved in post-transcriptional gene expression regulation. One of the main functions of the CNOT complex is regulation of mRNA deadenylation which is the rate-limiting step and the most efficient step in controlling mRNA decay. RBPs and miRNAs can recruit the CNOT complex to target transcripts to promote deadenylation of target mRNA through direct binding to CNOT1. Aberrations in the deadenylation function of the CNOT complex have been shown to cause altered gene expression profiles and reduced cell viability. Furthermore, multiple somatic mutations have been documented in CRC by the TCGA and COSMIC databases. Based on the *SB*-based screens, somatic mutations and function of the CNOT complex, we hypothesize that genetic alterations in *CNOT1* may contribute to CRC development through affecting deadenylation of mRNA transcripts.

Notably, the functions of CNOT1 and the CNOT complex in cancer development have not been adequately studied. Therefore the objective of this study is to characterize *CNOT1* in the development of CRC and investigate the underlying mechanisms.

Chapter 2

Results

Loss of *CNOT1* Results in Decreased Cell Viability

Cnot1 was identified as a candidate colorectal cancer (CRC) gene in the Apc^{Min} (Starr *et al*., 2011) and $LSL\text{-}p53^{R270H}$ (Starr T.K., unpublished data) *Sleeping Beauty* (SB)-based screens. To determine the contribution of genetic alterations in *CNOT1* to CRC we evaluated cell viability in *CNOT1*-depleted SW480 human CRC cell line and a non-intestinal cell line HEK293. The SW480 cell line is *APC* deficient as it lacks one allele and has a truncating mutation at position 1338. This APC status is similar to the status of Apc in most adenomas formed in the Apc^{Min} mouse strain used in the original *SB* screens that identified *Cnot1* as a CIS associated candidate CRC gene. Apc^{Min} mice carry an inactivating germline mutation in one allele and the second allele is inactivated in most adenomas. For these studies SW480 and HEK293 cells were transfected twice, 48 hours apart, with either a pool of four siRNA oligos targeting distinct regions in the *CNOT1* mRNAs, or a non-targeting control siRNA, or transfection reagent only (mock transfected), or not transfected. The effectiveness of depletion was confirmed by qRT-PCR (Figure 17A). *CNOT1* expression was reduced to 35% and 33% of the expression levels in control SW480 cells and HEK293 cells, respectively. Cell viability was evaluated daily for 6 days after the second transfection using the MTT assay. Over the 6-day interval, depletion of *CNOT1* by siRNA resulted in a dramatic decrease in cell viability in SW480 cells (Figure 17B) as well as HEK293 cells (Figure 17C).

To examine the means by which *CNOT1* depletion causes decreased cell viability we examined the levels of apoptosis in *CNOT1*-depleted SW480 cells using an Annexin V fluorescein isothiocyanate (AV-FITC) and propidium iodide (PI) double staining flow cytometry assay, where AV-FITC staining identifies cells in the early stages of apoptosis which have undergone translocation of phosphatidylserine to the external surface of the plasma membrane lipid but still have intact plasma membranes and thus are impervious

to PI staining. AV-FITC-PI staining was determined on day 6 (3 days after the first transfection) and day 7 (1 day after the second transfection). No changes in apoptosis were seen on day 6 but on day 7 *CNOT1* depletion resulted in a greater than two fold increase in apoptosis, from 7 to 19% of total cell population, with a corresponding decrease in unstained live cells from 78 to 64% (Figure 18A, B and C). These results show that depletion of *CNOT1* causes decreased cell viability in SW480 and HEK293 cells and increased apoptotic cell death in SW480 cells.

A.

Cell line	Relative *CNOT1* mRNA levels
SW480	35.89± 3.09%
HEK293	33.81± 0.99%

B. C.

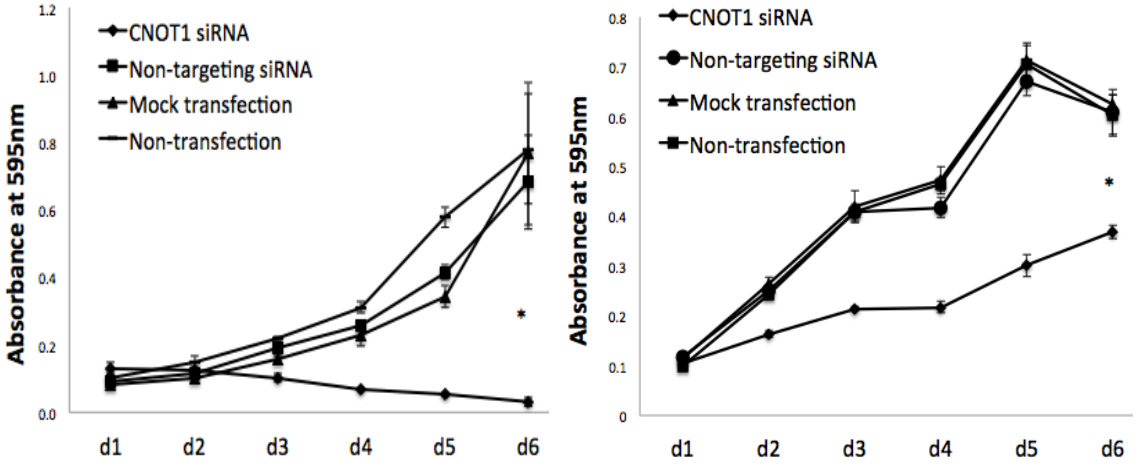

Figure 17. *CNOT1* depletion leads to decreased cell viability in transformed cell lines SW480 and HEK293. (A) Cells at 70% confluence were transfected with siRNA oligos targeting *CNOT1*, non-targeting siRNA, transfection reagent only (mock transfected), or not transfected, twice, 48 hours apart, at a final concentration of 50 nM. *CNOT1* levels were determined by qRT-PCR. Relative *CNOT1* mRNA levels represent the expression of *CNOT1* in *CNOT1* siRNA-treated cells relative to control siRNA treated. Values represent the average of three (SW480) or two (HEK293) experiments ± SD. (B and C) Cells were plated at 5000 (SW480) or 2500 (HEK293) cells per well in triplicate in 96 well plates 24 hours after the second transfection. Cell

viability was measured by MTT assay on days 1-6 after the second transfection. (B) SW480 cells. (C) HEK293 cells. Each data point represents mean ± SD of three replicates from a representative experiment. Significance of differences in cell viability on day 6 was determined by one-way ANOVA. * = $p < 0.05$ between *CNOT1* and all controls.

A.

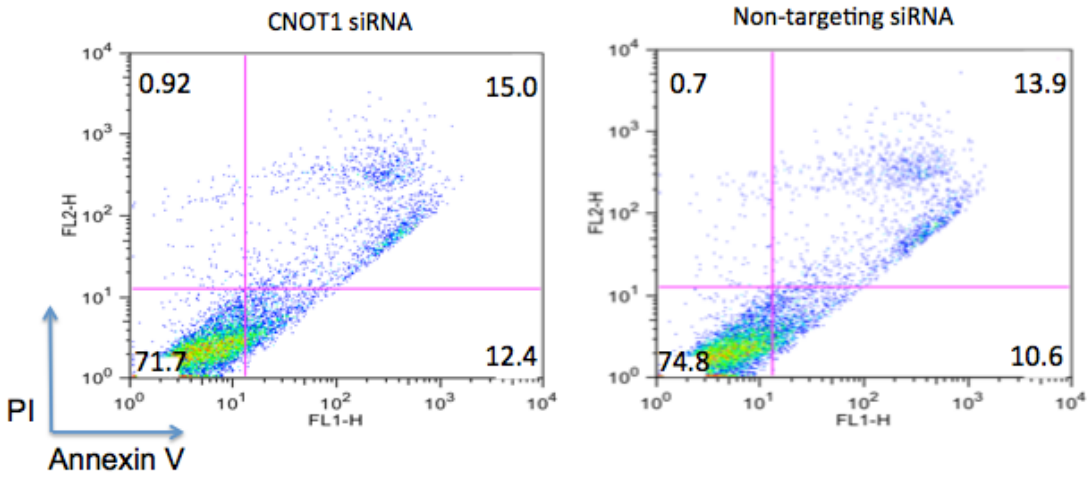

B.

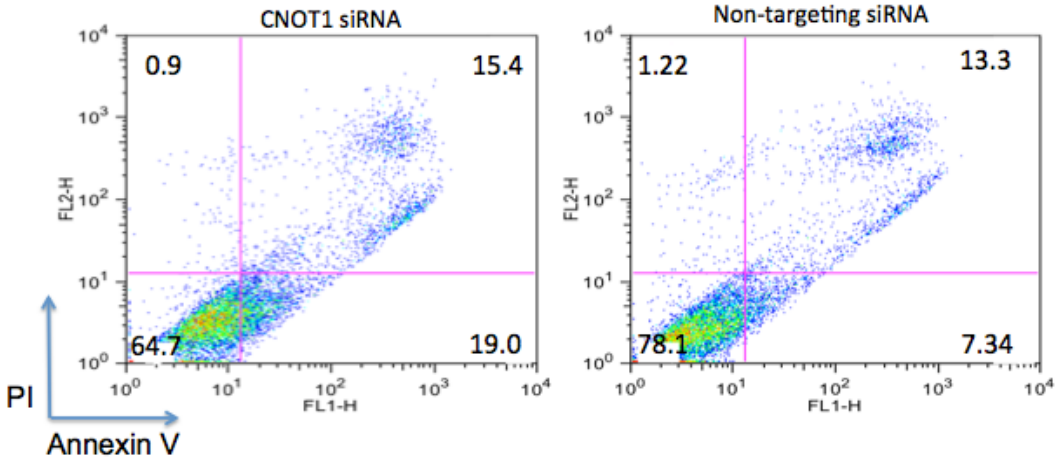

C.

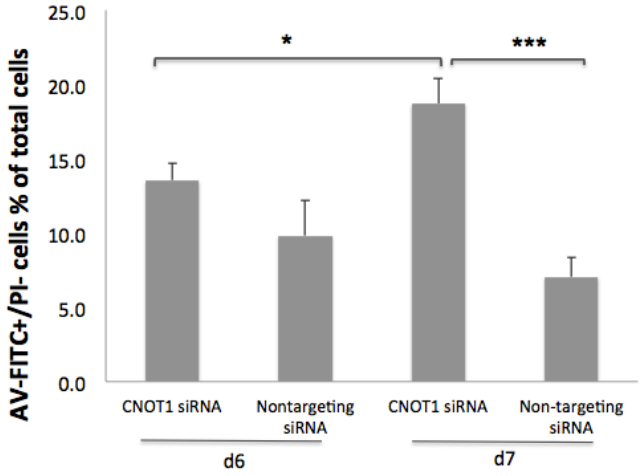

Figure 18. *CNOT1* depletion leads to increased apoptosis in SW480 cells. SW480 cells were transfected with siRNA oligos targeting *CNOT1* or non-targeting siRNA as in Figure 17. Cell apoptosis was determined by an annexin V fluorescein isothiocyanate (AV-FITC) and propidium iodide (PI) double staining flow cytometry assay at 72 hours (day 6) after the first transfection and at 24 hours (day 7) after the second transfection. (A and B) Representative dot plots of AV-FITC-PI staining in SW480 cells on day 6 (A) and day 7 (B). The number in each quadrant indicates the percentage of cells stained with specific combination of dyes. Lower right quadrant represents cells stained by AV-FITC alone that are early apoptotic cells. (C) Quantitative analysis showing AV-FITC stained apoptotic cells as percent of total cells. Values represent mean ± SD of three independent experiments. Significance of differences was determined by one-way ANOVA. ***=$p < 0.001$, * = $p < 0.05$.

Loss of *CNOT1* Results in Extensive Changes in Gene Expression

CNOT1 is a member of the CCR4-NOT complex, which regulates mRNA expression at several levels. Therefore, to begin to determine the means by which *CNOT1* depletion might promote decreased cell viability we examined global gene expression in *CNOT1*-depleted SW480 cells using an Illumina Human HT-12 v4 BeadChip array. High quality total RNA was isolated from *CNOT1*-depleted and control SW480 cells. RNA Integrity Number (RIN) values were ≥ 9.8 (Figure 19A). qRT-PCR confirmed 90% knockdown of *CNOT1* mRNA levels (Figure 19B). Analysis of gene expression identified 266 genes with statistically significant, greater than or equal to two-fold,

change in gene expression. Of these 183 (69%) were up-regulated and 83 (31%) were down-regulated (Figure 19C, Table 4). Expression levels of five top changing genes, *TXNIP, DKK1, EMP1, BTG1* and *IGFBP3*, were confirmed by qRT-PCR to validate the results of the microarray (Figure 19D). Ingenuity Pathway Analysis (IPA) was used to identify pathways and processes associated with changes in gene expression in *CNOT1*-depleted cells. IPA analysis generated three networks with scores of 10 or more. These networks represent molecules interacting with protein products of genes that change expression in *CNOT1*-depleted cells. The functions associated with these networks are associated with tumor morphology, cellular growth and proliferation, cellular death and survival and cell development consistent with an effect of *CNOT1* depletion on cell viability (Figure 20A, B, C and D, Figure 33).

A.

Sample name	RIN
CNOT1 1a 03232012	10
OT3 1b 03232012	10
CNOT1 2a 03292012	9.8
OT3 2b 03292012	10
CNOT1 3a 05082012	10
OT3 3b 05082012	10

B.

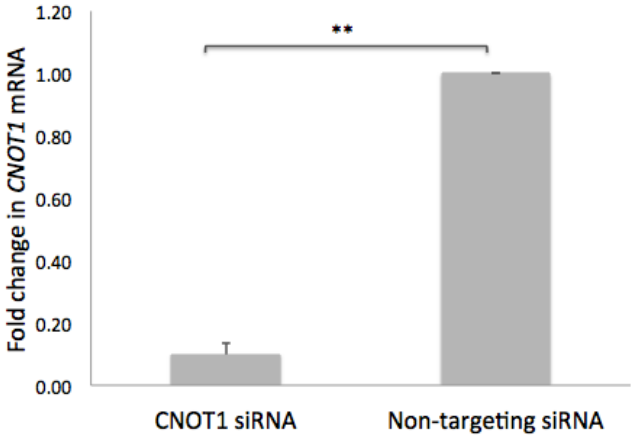

C.

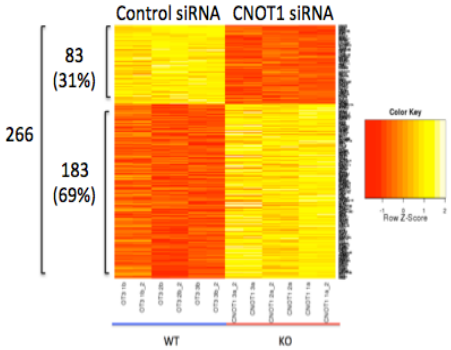

D.

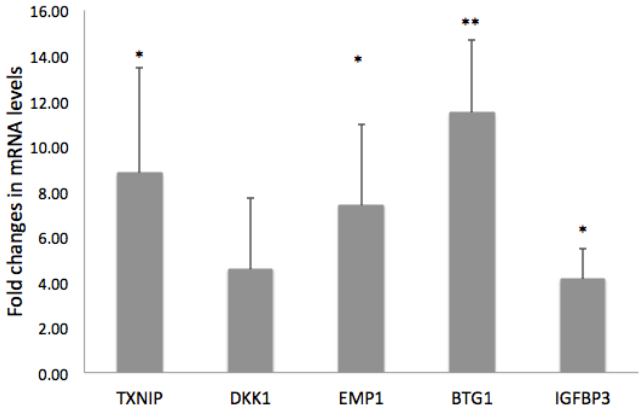

Figure 19. Depletion of *CNOT1* in SW480 cells causes an altered gene expression profiles. SW480 cells were transfected with either *CNOT1* siRNA or a non-targeting siRNA control at 50 nM final concentrations, twice, 48 hours apart. Total RNA was extracted 72 hours after the second transfection from three pairs of biological replicates of *CNOT1*-depleted and non-targeting control treated SW480 cells and hybridized to an Illumina Human HT-12 v4 BeadChip array to determine the gene expression profile. To improve reproducibility each of the 6 independent RNA samples was hybridized twice. (A) The integrity of RNA samples was determined using an Agilent Bioanalyzer Lab-on-a-chip system to generate an RNA Integrity Number (RIN) representing the ratio of 28S/18S RNA as well as other features. All samples met the standard of quality with a RIN > 8. OT3 = non-targeting control siRNA. (B) Validation of knockdown of *CNOT1* in RNA samples by qRT-PCR. (C) Heatmap presentation of the 266 genes showing significant differences in expression (fold change ≥ 2, $p<0.05$) between *CNOT1*-depleted and control cells. Relative gene expression is shown as Z-score. Genes are shown on the Y-axis and siRNA treatments on the X-axis. The quality control and normalization were performed using the R-based package: *lumi* and *limma*. (D) The results of the array analysis were validated via measuring the mRNA levels of five of the genes with highest fold changes in the microarray by qRT-PCR. For all qRT-PCR assays, values represent mean ± SD of three independent experiments. Statistical significance was determined by a *t*-test. ** = $p < 0.01$, * = $p < 0.05$.

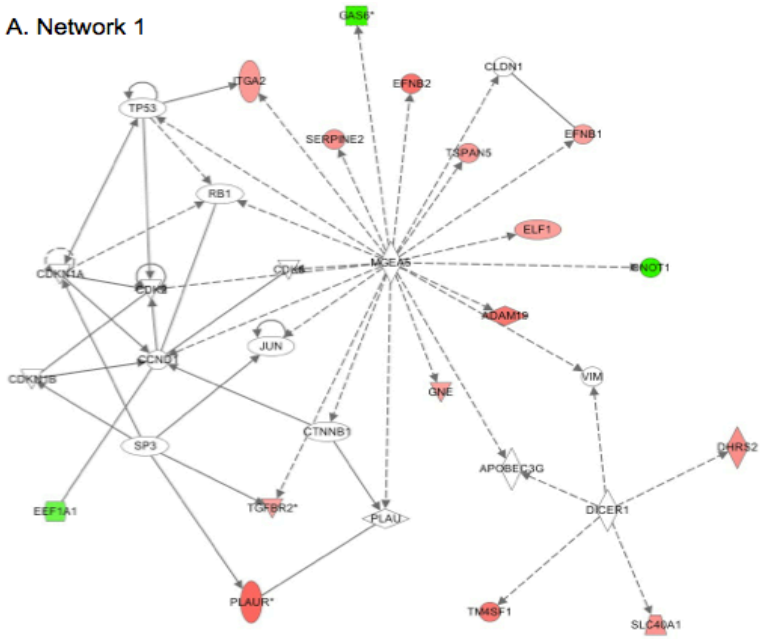

B. Network 2

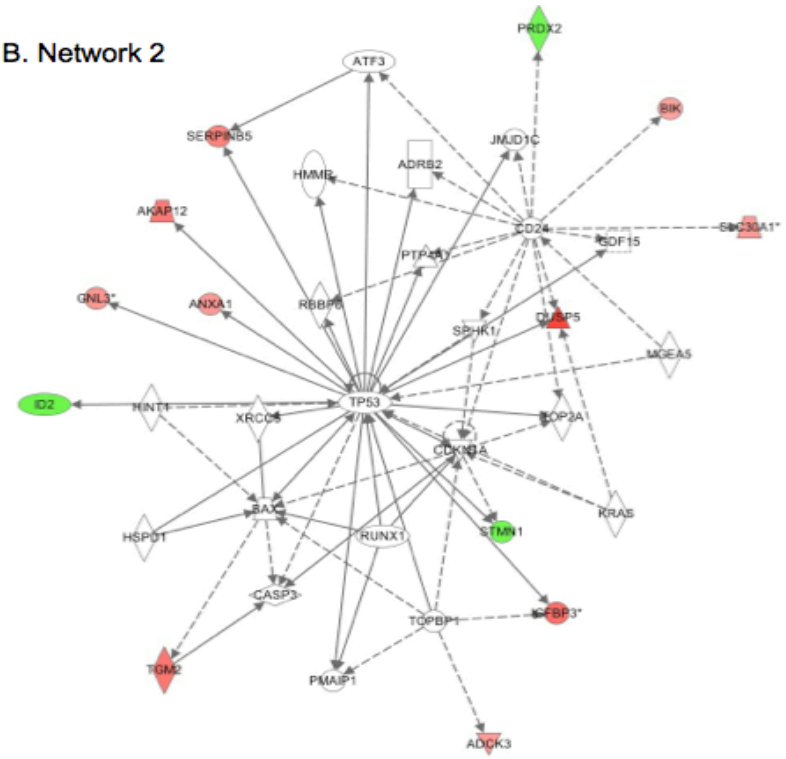

C. Network 3

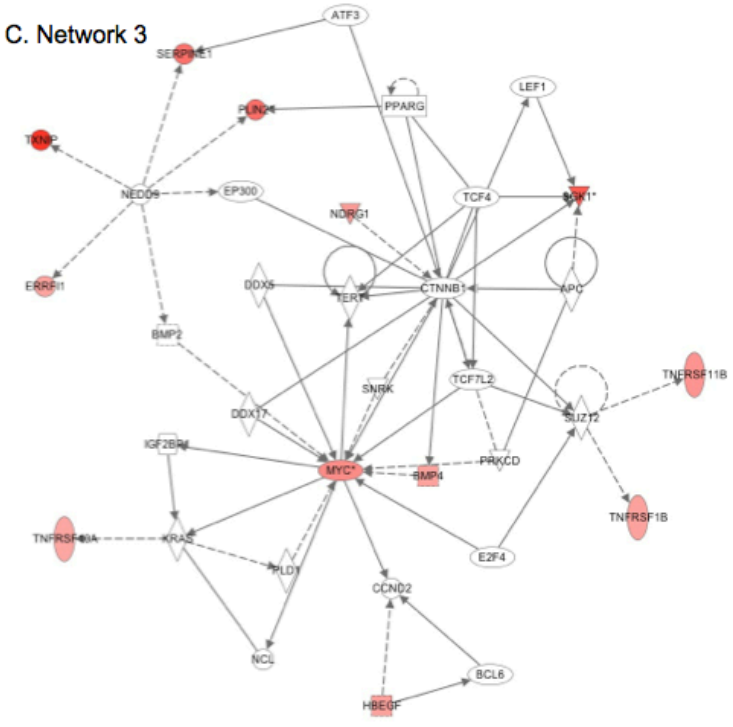

D.

ID	Network Functions	Score
1	Tumor Morphology, Cellular Development, Cellular Growth and Proliferation	17
2	Cell death and Survival, Tumor Morphology, Cellular Growth and Proliferation	12
3	Cellular Development, Cellular Growth and Proliferation, Cell death and Survival	10

Figure 20. IPA analysis of gene expression in *CNOT1*-depleted SW480 cells. Networks based on genes that change expression in *CNOT1*-depleted cells (Network Eligible molecules) were generated by Ingenuity Pathway Analysis (IPA). The three top scoring networks are shown (A, B and C). The score is calculated using the Fishers Exact Test to determine the likelihood of the network containing a given number of Network Eligible molecules by chance. The score = -log (Fisher's Exact test result). (D) The functions and scores of the three networks are shown.

CRC Liver Metastases With High *CNOT1* Expression Levels Show Upregulation Of Proliferation Related Genes

To determine if these changes are relevant to human cancers we analyzed gene expression in 20 human CRC liver metastasis samples and 5 unrelated normal samples. High quality RNA was isolated from flash frozen tissue using RNAIceLater (Ambion) and RNeasy (Qiagen) kits. This RNA was sequenced by the University of Minnesota BioMedical Genomics Center using the Illumina HiSeq 2000 platform. Sequence was assembled and analyzed by Dr. Ying Zhang at the University of Minnesota Supercomputing Institute. Fragments per kilobase of exon per million fragments (FPKM) gene expression values were obtained. Levels of *CNOT1* expression vary by 3-fold among the metastasis samples. Levels in the normal samples fall around the average of the normal samples with all normal samples falling within two standard deviations. To identify genes whose expression correlated with highest levels and lowest levels of *CNOT1* expression we used Geneset Enrichment Analysis (GSEA) (Subramanian *et al*., 2005). The three samples with highest *CNOT1* expression were designated *CNOT1*-Hi and the three samples with lowest *CNOT1* expression were designated *CNOT1*-Lo. A

complete ranked expression dataset was generated in which genes were ranked according to ratio of expression in *CNOT1*-Hi samples to *CNOT1*-Lo samples (*CNOT1*-Hi/*CNOT1*-Lo). This ranked dataset was compared to genesets derived from Merlos-Suárez (Merlos-Suárez *et al*., 2011). Merlos-Suárez *et al* sorted mouse intestinal crypt cells based on expression of EphB2 to define gene programs for normal crypt cell populations. Genes enriched in $EphB2^{Hi}$ cells defined the intestinal stem cell (ISC) signature. Genes expressed at equal levels in $EphB2^{Hi}$ and $EphB2^{Med}$ defined a proliferation signature. Genes differentially expressed in $EphB2^{Lo}$ cells defined a late progenitor, transit amplifying population. We found that genes in the proliferation geneset were enriched in the *CNOT1*-Hi samples while *CNOT1*-Lo genes were not enriched in any of the three crypt populations (Figure 21A, Table 5A). The *CNOT1*-Hi/*CNOT1*-Lo dataset was also compared to genesets of candidate CRC genes identified by *SB* transposon mutagenesis of mouse intestine (Figure 21B an C, Table 5B and C). It was found that genes up-regulated in *CNOT1*-Hi tumors, but not in *CNOT1*-Lo tumors were enriched in candidate cancer genes (CIS genes) identified by *Sleeping Beauty* mutagenesis. These results are consistent with *in vitro* results in which loss of *CNOT1* resulted in decreased cell viability. However, three metastasis samples had *CNOT1* expression levels significantly lower than normal samples. As the anchor protein of a multifunctional complex CNOT1 may potentially regulate many cellular processes. The fact that both *CNOT1*-Hi and *CNOT1*-Lo are found in metastasis samples but associated with different expression patterns suggests that CNOT1 affect on CRC may differently dependent on genetic context.

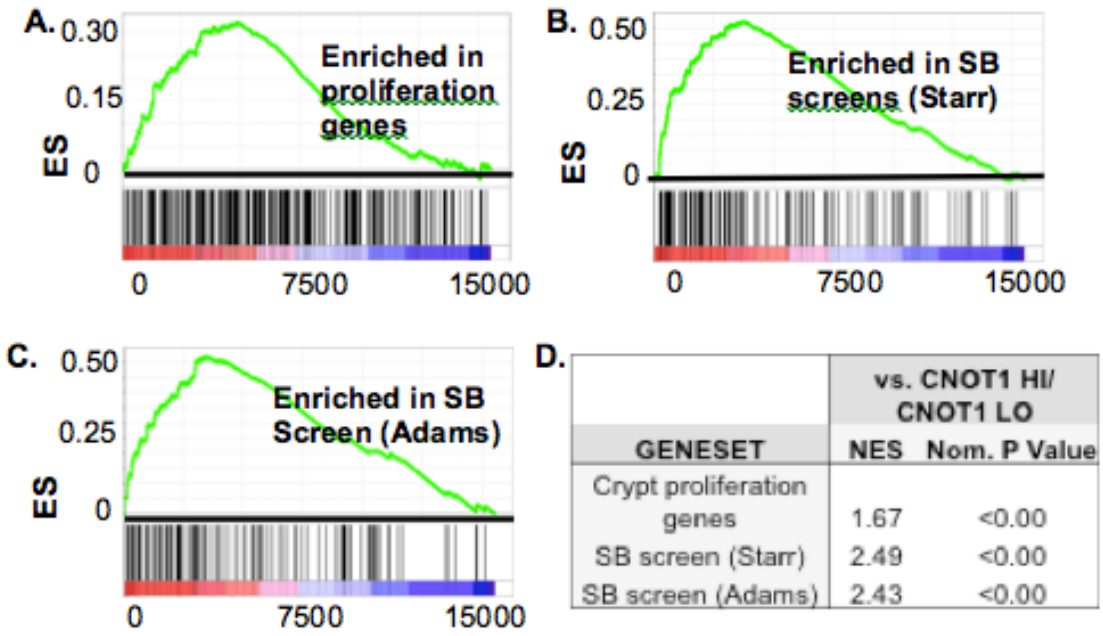

GENESET	vs. CNOT1 HI/ CNOT1 LO NES	Nom. P Value
Crypt proliferation genes	1.67	<0.00
SB screen (Starr)	2.49	<0.00
SB screen (Adams)	2.43	<0.00

Figure 21. Geneset Enrichment Analysis of human metastasis CRC samples. *CNOT1*-Hi/*CNOT1*-Lo expression dataset (see text for details) was analyzed for enrichment in crypt proliferation genes and CRC candidate cancer genes identified by *SB* screens. Genesets consist of: (A) genes differentially expressed in proliferating crypt cells (Merlos-Suárez *et al*., 2011); (B) top CIS-associated genes identified in a wild-type background (Starr *et al*., 2009), in an Apc^{Min} background (Starr *et al*., 2011), and a p53-mutant background (Starr T.K., unpublished data); (C) top 200 CIS-associated genes identified in *SB* screen using a 120 k window (March *et al*., 2011). (D) Normalized enrichment score (NES) and nominal *p* value (Nom. *p* value) are shown for each comparison.

CNOT1 Limits the mRNA Expression Levels of *TXNIP* in SW480 and HEK293 Cell Lines.

Because of connections seen between *CNOT1*-Hi expression and cancer-related phenotypes, we chose to investigate the mechanism by which *CNOT1* expression protects cell viability. Microarray analysis revealed dramatically increased expression of *Thioredoxin-interacting protein (TXNIP)* (7.45-fold). *TXNIP* has been identified as a tumor suppressor in human breast, colon, lung and liver cancers through inhibition of cell proliferation and arrest of the cell cycle at G_0/G_1 phase and its expression is decreased in several cancers including CRC (Jeon, *et al*., 2005, Han *et al*., 2003, Goldberg *et al*., 2003,

Zhou, *et al*., 2010, Sheth *et al*., 2006). In addition, in pancreatic beta cells, activation of TXNIP by oxidative or ER stress initiates apoptotic pathways (Lerner *et al*., 2012, Zhou *et al*., 2010, Oslowski *et al*., 2012). As cancer cells are often subject to extreme stresses we hypothesized that *CNOT1* might protect cell viability by limiting *TXNIP* expression. In accordance with the array results *CNOT1* depletion results in increased *TXNIP* expression by qRT-PCR in *CNOT1*-depleted SW480 cells and HEK293 cells (8.8 and 2.85 fold, respectively) (Figure 22 A and B). Increased expression of *TXNIP* in SW480 cells was detected as early as 2 days after the first siRNA transfection (Table 3). In addition, overexpression of the longest *CNOT1* transcript variant (NM_00126561, *CNOT1*L) in HEK293 cells results in a decrease in *TXNIP* expression to about 70% of controls (Figure 22C). These results indicate that CNOT1 limits *TXNIP* mRNA levels in these two cell lines.

A.

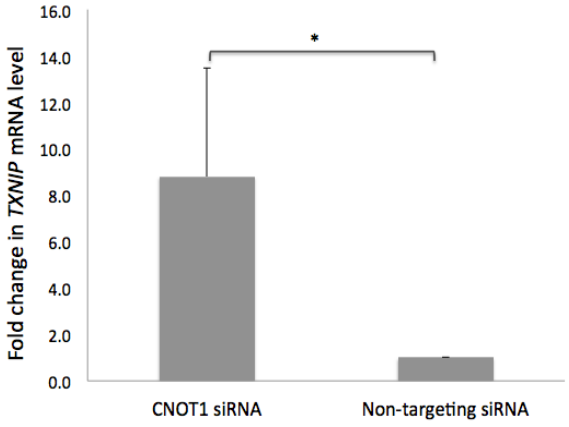

B.

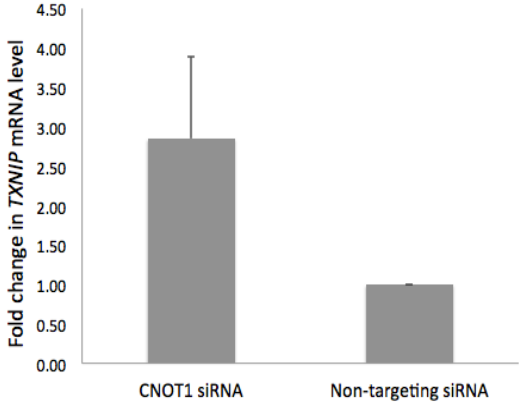

C.

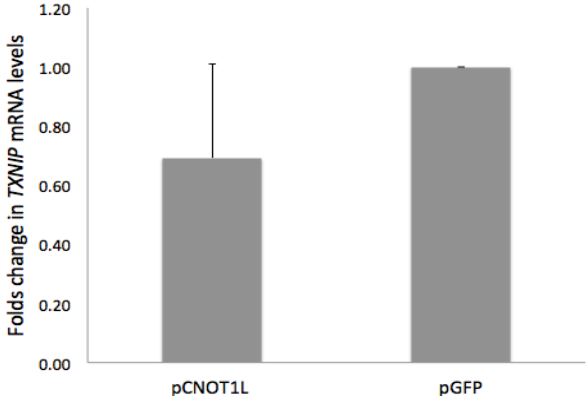

Figure 22. CNOT1 limits *TXNIP* mRNA levels in SW480 and HEK293 cell lines. (A) *TXNIP* mRNA expression levels in RNA samples used for the microarray assay were determined by qRT-PCR. (B) *TXNIP* mRNA levels in HEK293 cells depleted for *CNOT1* were determined by qRT-PCR. HEK293 cells were transfected with either *CNOT1* siRNA or a non-targeting siRNA control as described in Figure 17. Total RNA was extracted 48 hours after the second transfection and subjected to qRT-PCR to determine *TXNIP* levels. (C) HEK293 cells were transfected with plasmids encoding *CNOT1*L (NM_016284.4) or a control plasmid encoding green fluorescent protein (GFP). 48 hours after transfection RNA samples were isolated and *TXNIP* mRNA levels were determined by qRT-PCR. Values in (A), (B), (C) represent mean ± SD of 3, 2, 4 independent experiments, respectively. Significance of differences was calculated by a *t*-test. * = $p < 0.05$.

Increased *TXNIP* Levels are Linked to CNOT1-Mediated Apoptosis

To determine if CNOT1-mediated up-regulation of *TXNIP* might be responsible for decreased cell viability seen in *CNOT1*-depleted cells, we examined the effect of overexpression of TXNIP on cell viability. For these experiments a plasmid encoding TXNIP was transiently overexpressed in HEK293 cells. Control cells were transfected with a GFP-encoding plasmid in the same vector. Transfection efficiency was estimated to be 60%. *TXNIP* mRNA expression was increased by 7.5-fold 48 hours after transfection (Figure 23A). In a parallel experiment, cells were evaluated for cell viability by MTT assay. Viability was decreased to about 50% that of control cells at 72 hours (Figure 23B). To test this relationship further, we deterimined whether elevated *TXNIP* levels occurred before apoptosis in *CNOT1*-depleted cells. Compilation of data shown in Figures 18A, 18B and 22A indicates that upregulation of *TXNIP* mRNA expression is detected as early as 2 days (day 5) after the first transfection. However, detectable increases in apoptosis do not occur until the first day (day 7) after the second transfection (Table 3). This result is consistent with CNOT1 mediating cell viability by regulating *TXNIP* levels. To summarize, depletion of *CNOT1* results in increased apoptosis, decreased cell viability and increased levels of *TXNIP* in SW480 and HEK293 cells. Increased levels of *TXNIP* result in decreased cell viability in HEK293 cells. Finally, *CNOT1* depletion in SW480 cells results in increased *TXNIP* levels before increased

apoptosis and decreased cell viability. Taken together, these results suggest that CNOT1 protects cell viability at least in part by limiting *TXNIP* expression.

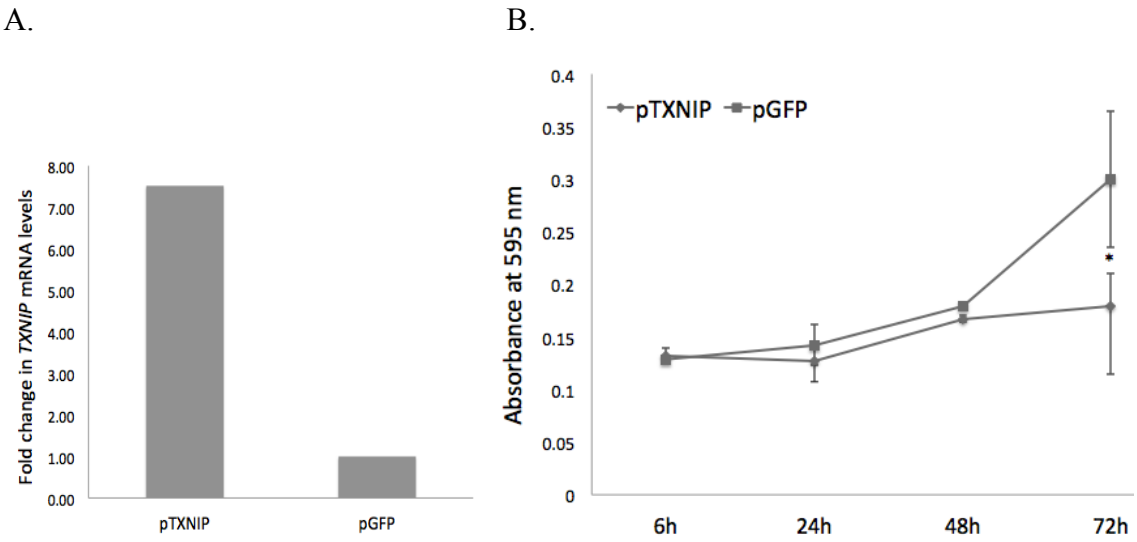

Figure 23. Overexpression of TXNIP reduces SW480 cell viability. HEK 293 cells were transiently transfected with plasmids encoding either TXNIP or GFP as a control. (A) Total RNA was isolated 48 hours after transfection and *TXNIP* mRNA levels were determined by qRT-PCR. (B) Transfected cells were plated at 2 x 10^4 cells per well in triplicate in 96 well plates. Cell viability was measured by MTT assay on 6 hours to 72 hours after transfection. Viability is shown as absorbance at 595 nm. Each data point represents mean ± SD of three replicates from one representative experiment of two. Significance of differences in cell viability at 72 hours was determined by a *t*-test. * = $p < 0.05$.

	d3	d4	d5	d6	d7	d9
Transfection	1st tfx.			2nd tfx		
CNOT1 fold change		0.11	0.13	0.17		0.1
TXNIP fold change		0.81	6.04	2.9	4.37	8.8
Apoptosis fold change				No change	Increase	

Table 3. Time course study of a correlation between *CNOT1* depletion, upregulated *TXNIP* and cell apoptosis. Compilation of results of *CNOT1* depletion in SW480 cells taken from Figures 17A, *CNOT1* depletion; 17B, cell viability; 18C, apoptosis; and 22A, *TXNIP* mRNA levels. Fold change = level in *CNOT1*-depleted cells/level in non-targeting control treated cells. Results are shown relative to a timeline of the *CNOT1* siRNA depletion protocol.

Identification of CNOT1 Isoforms and CCR4-NOT Subunits Involved in *TXNIP* Regulation

We then investigated the mechanism by which CNOT1 regulates *TXNIP* levels. Human cells express three *CNOT1* transcript variants with translated protein products (See details in **Introduction**). The two longest forms (*CNOT1L*, NM_016284.4 and *CNOT1M*, NM_001265612.1) contain a C-terminal NOT domain with binding sites for several potentially biologically relevant interactors, such a CNOT2, CNOT3, and CNOT5. To determine which of these variants contribute to cell viability in SW480 cells, primers were designed to specifically distinguish between the two long forms (*CNOT1L* and *M*) and the short form (*CNOT1S*). qRT-PCR analysis of SW480 cells revealed that one or both of the long forms are virtually the only form expressed in these cells (98%), while the short form makes up no more than 2% of overall *CNOT1* mRNA expression (Figure 24A). In addition, the short form is almost undetectable in CRC liver metastasis and normal colon samples, suggesting that one or both of the long forms are the biologically relevant form in the colon (Figure 24B). Importantly, expression of the shortest isoform (CNOT1S) resulted in increased *TXNIP* expression (Figure 24C). This result suggests that some part of the C-terminal region unique to the CNOT1L and/or CNOT1M isoforms contributes to downregulation of *TXNIP*. As CNOT1 acts as part of a larger complex CNOT1S may act as a dominant negative by sequestering essential subunits.

Because CNOT1 is part of the CCR4-NOT complex and because the full range of configurations of this complex is not known (Chen *et al*., 2011) we determined if knockdown of other CCR4-NOT subunits would also decrease cell viability and increase *TXNIP* levels. We focused on CNOT2, which is also a core member of the CCR4-NOT and which has also been identified as a candidate CRC gene in *SB* screens, and on the four deadenylase subunits because deadenylation leading to mRNA degradation is the best characterized mechanism of CCR4-NOT mediated gene regulation. Analysis of SW480 cells depleted for *CNOT2*, and the deadenylase subunits *CNOT6, 6L, 7* and *8* (Figure 24D) indicated that while cell viability was decreased in cells depleted for each of these subunits (CNOT6 not measured), *TXNIP* levels were elevated only in *CNOT8*-depleted cells (7.07 fold) (Figure 24E). These results suggest that CNOT1 works with

CNOT8 to regulate *TXNIP* levels. In addition, they suggest that CNOT1 will be found to regulate cell viability by additional pathways involving interactions with other CCR4-NOT subunits.

A.

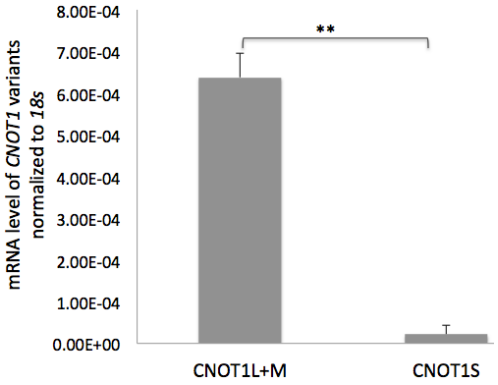

B.

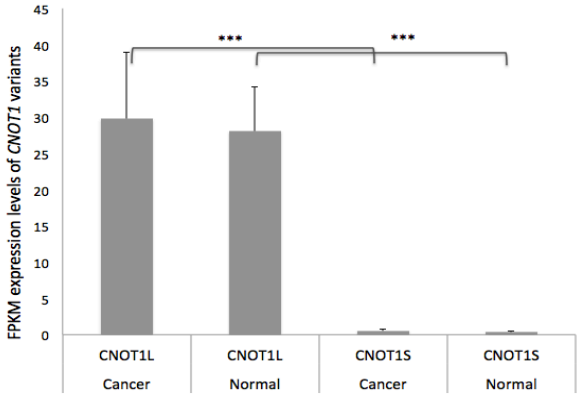

C.

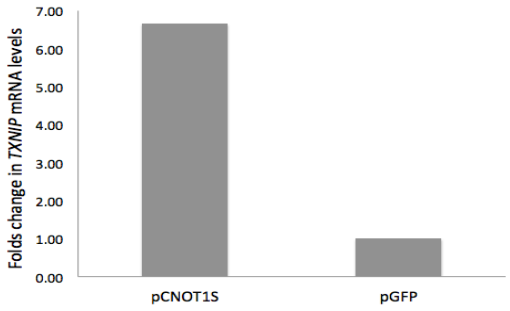

D.

Gene	mRNA levels	Cell viability
CNOT2	35.55±17.05%	38.30±16.32%
CNOT6	15.89%	NA
CNOT6L	19.38±7.85%	34.11±1.87%
CNOT7	17.05±5.21%	62.89±1.05%
CNOT8	54.27±5.07%	33.53±9.94%

E.

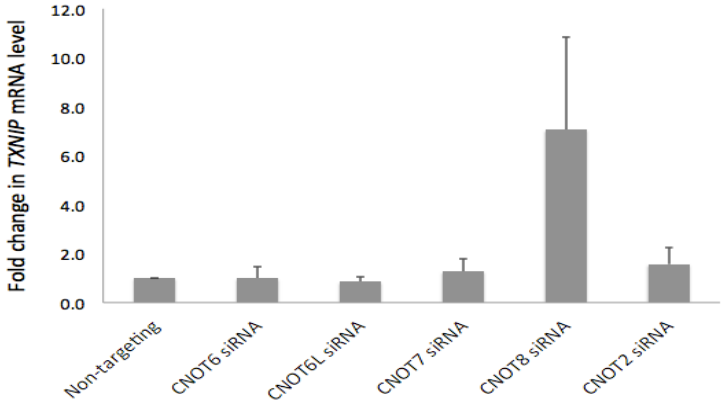

Figure 24. Identification of CNOT1 isoforms and CCR4-NOT subunits involved in *TXNIP* regulation. (A) *CNOT1* variants expressed in untreated SW480 cells were determined by qRT-

PCR using primers designed to distinguish between the two long isoforms, *CNOT1L* and *CNOT1M* (NM_016284.4 and NM 001265612.1) and the short isoform *CNOT1S* (NM_206999.2). Values represent mean ± SD of three independent experiments. Significance of differences was calculated by a *t*-test. ** = $p < 0.01$. (B) FPKM (fragments per kilobase of exon per million fragments mapped) expression levels of *CNOT1L* and *CNOT1S* in 20 liver metastasis of stage IV human CRCs and 5 normal colonic tissues. Values represent mean ± SD of each group of samples. Significance of differences was calculated by one-way ANOVA. *** = $p < 0.001$. (C) Expression of *TXNIP* was determined in cells overexpressing *CNOT1S*. HEK 293 cells were transfected with plasmids encoding either CNOT1S or GFP as a control. Total RNA was isolated at 48 hours after transfection and probed for *TXNIP* levels by qRT-PCR. Values represent result of one experiment. (D) SW480 cells were transfected with siRNA oligos targeting *CNOT2*, *6, 6L, 7, 8*, or non-targeting siRNA, twice, 48 hours apart, at a final concentration of 50 nM. Total RNA was extracted 72 hours after the second transfection and depletion of target genes was determined by qRT-PCR. Relative mRNA level = level of indicated subunit in subunit-specific siRNA-treated cells/control siRNA treated. On day 1 after the second transfection SW480 cells were plated at 2,500 cells per well in triplicate in 96 well plates. Cell viability was measured by MTT assay on day 6 after the second transfection. Relative cell viability represents = absorbance at 595 nm of cells treated with indicated siRNA/cells treated with non-targeting control. Results represent at least two experiments except for CNOT6 (one experiment, no MTT assay). (E) *TXNIP* expression levels were determined by qRT-PCR in SW480 cells depleted for *CNOT2*, and the deadenylase subunits *CNOT6, 6L, 7,* and *8*. Values represent mean ± SD of at least two experiments except for CNOT6 (one experiment). Significance of difference was calculated by a *t*-test.

CNOT1 Limits *TXNIP* mRNA Levels Through Decreasing mRNA Stability

As CCR4-NOT subunits with deadenylase activity, such as CNOT8, can initiate mRNA degradation, we pursued the idea that CNOT1 regulates *TXNIP* mRNA stability. *CNOT1*-depleted and control SW480 cells were treated with Actinomycin D to block transcription and *TXNIP* mRNA levels were determined by qRT-PCR for 2 hours. This study showed that *TXNIP* levels were significantly higher in *CNOT1*-depleted cells after 2-hour exposure to Actinomycin D (Figure 25) indicating that *TXNIP* mRNA stability is enhanced in the absence of CNOT1.

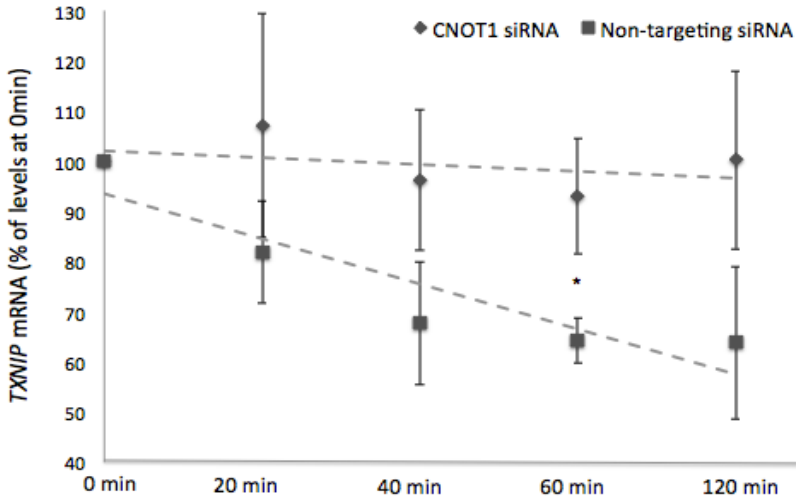

Figure 25. CNOT1 limits *TXNIP* mRNA levels through decreasing mRNA stability. SW480 cells were transfected with either *CNOT1* siRNA or control siRNA. Actinomycin D was added at a final concentration of 5 μg/ml 72 hours after one siRNA transfection. Total mRNA was isolated at indicated intervals from 0 to 120 mininutes after treatment. *TXNIP* mRNA levels were determined by qRT-PCR. The *TXNIP* mRNA levels at each time point are shown as the percentage of *TXNIP* mRNA levels at 0 minute. Values represent mean ± SD of three independent experiments. The best-fit line is shown as a dotted line. Significance of difference was calculated by a *t*-test at 60 minutes and 120 mininutes. * = $p < 0.05$.

3'UTR Binding Proteins ZFP36 (TTP), PUM1, PUM2 and CELF1 (CUGBP1) Are Not Involved in CNOT1-Mediated Regulation of *TXNIP*.

CNOT1 commonly regulates mRNA stability by acting as an adapter between 3'UTR binding factors and deadenylase subunits of the CCR4-NOT complex. CNOT1 has been reported to interact with the 3'UTR binding proteins ZFP36, PUM1 and PUM2 (Fabian *et al*., 2013, Van Etten *et al*., 2012), which mediate deadenylation and degradation of targeted mRNAs. In addition *Pum1, Pum2* and *Celf1*, another 3'UTR binding protein, were identified as candidate colorectal cancer genes in *SB* screens (Starr *et al*., 2009, Starr *et al*., 2011). To determine if these 3'UTR binding proteins were involved in CNOT1 regulation of *TXNIP*, *TXNIP* levels were determined in SW480 cells depleted for each protein. Depletion of each of these proteins results in less than two-fold increase in *TXNIP* (Figure 26A and B) suggesting that these 3'UTR binding proteins are

not involved in CNOT1-mediated regulation of *TXNIP*. 3'UTR binding proteins often bind AU rich motifs in the 3'UTR to target mRNAs for deadenylation and decay. Examination of the number and locations of conserved ARE motifs in the *TXNIP* mRNA transcript using a bioinformatics tool (ARESite 1.0 http://rna.tbi.univie.ac.at/cgi-bin/ARESite.cgi) identified only one ARE motif (ATTTA) in the 3'UTR of *TXNIP* mRNA (1934-1938 nt). As mRNAs targeted by RBPs usually contain multiple sites, the lack of ARE sites may account for the result that *TXNIP* mRNA is not regulated by these 3'UTR binding proteins.

A.

Gene	mRNA levels
ZFP36	74.07±17.04%
PUM1	60.03%
PUM2	15.76%
CELF1	46.16%

B.

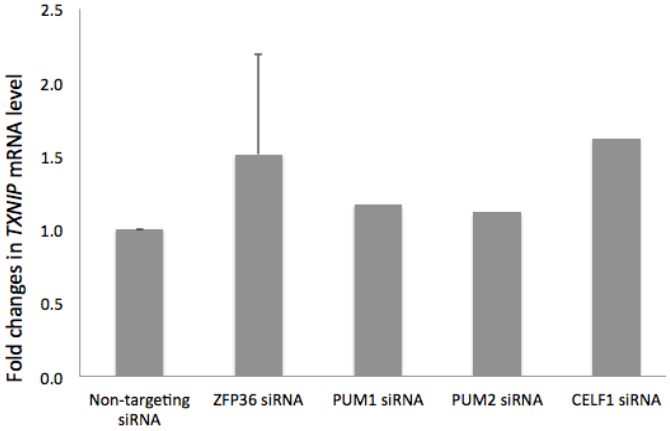

Figure 26. 3'UTR binding proteins ZFP36, PUM1, PUM2 and CELF1 are not involved in CNOT1-mediated regulation of *TXNIP*. SW480 cells were transfected with siRNA oligos targeting indicated 3'UTR binding proteins or non-targeting siRNA, twice, 48 hours apart, at a final concentration of 50 nM. (A) Relative mRNA levels of targeted genes. Relative mRNA level = levels of indicated RBPs in RBP siRNA-treated cells/control siRNA treated. (B) *TXNIP* mRNA levels in SW480 cells depleted for indicated RNA binding proteins. The values represent result of one experiment, except for ZNF36, which represents mean ± SD of two experiments. Significance of differences was calculated by a *t*-test.

miR-17 Downregulates *TXNIP* mRNA Levels

CNOT1 also interacts as an adapter between TNRC6A (GW182) of the microRNA RISC complex and CCR4-NOT deadenylase subunits, thus facilitating microRNA-mediated mRNA degradation. *TXNIP* has been reported to be degraded by

miR-17 suggesting that CNOT1 may facilitate *miR-17*-mediated degradation of *TXNIP*. However, *miR-17* regulates *TXNIP* expression in a cell specific fashion. For instance, it is active in pancreatic beta cells but not in macrophages. The role of microRNAs in *TXNIP* mRNA stability in CRC cells is unknown so we first sought to determine if *miR-17* regulates *TXNIP* in SW480 cells. In initial studies *miR-17* was found to be present in SW480 cells (Figure 27A) and overexpression of a *miR-17* mimic in SW480 cells resulted in a 31% decrease in levels of *TXNIP* mRNA. mRNA levels of two other *miR-17* targets, which like *TXNIP* are upregulated in CNOT1 depleted cells, *HBP1* (Li *et al*., 2011) and *TGFBR2* (Dews *et al*., 2010), were decreased by 30% and 49%, respectively (Figure 27B). In addition, *TXNIP* levels were reduced by more than 50% in HEK293 cells transfected with the *miR-17* mimic (Figure 27C). Results of these studies suggested that *miR-17* downregulates *TXNIP* levels in SW480 and HEK293 cell lines.

These results support a model in which CNOT1 regulates *TXNIP* expression post-transcriptionally by facilitating the deadenylase activity of CNOT8. This CCR4-NOT complex may be recruited to the 3'UTR of *TXNIP* mRNA via interaction with a miRNA RISC complex containing *miR-17*.

A.

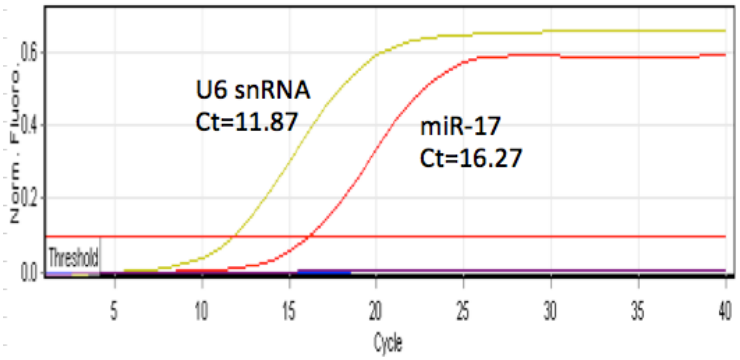

B. C.

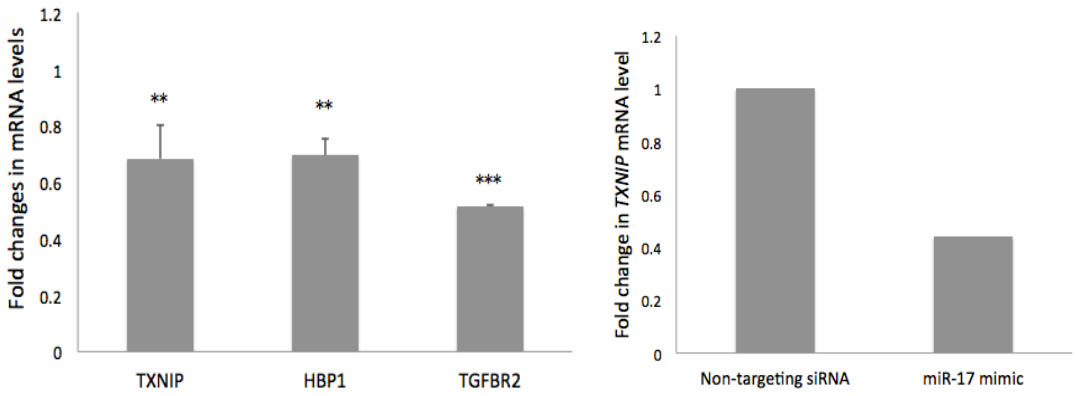

Figure 27. *miR-17* downregulates *TXNIP* mRNA levels. (A) Amplification curve showing amplification of endogenous *miR-17* and *U6* snRNA from SW480 cells using qRT-PCR. Ct (cycle threshold) = the number of cycles required for the fluorescent signal to cross the threshold (0.1 in this case). Total RNA including small RNAs was isolated using a miRNeasy Mini Kit (Qiagen). RNA was then transcribed to cDNA and ligated with universal adaptors using a miScript II RT Kit (Qiagen). Expression levels of mature *miR-17* and *U6* snRNA (internal control, abundant in most type of cells) were measured by qRT-PCR using a miScript SYBR Green PCR Kit with a miScript universal primer and specific primer for *miR-17* and *U6* from the miScript Primer Assay Plate (Qiagen). (B and C) SW480 and HEK293 cells were transfected with either *miR-17* mimic oligos or non-targeting siRNA control at 5nM final concentration. Total RNA was extracted 24 hours after transfection and probed for known targets of *miR-17* by qRT-PCR. Values represent ratio of mRNA expression in *miR-17* mimic treated cells relative to non-targeting control treated cells. (B) Expression levels of three known mirR-17 targets, *TXNIP*, *HBP1* and *TGBR2*, in SW480 cells. Values represent mean ± SD of two independent experiments. Significance of difference was calculated by a *t*-test. *** = $p < 0.001$, ** = $p < 0.01$. (C) Expression levels of *TXNIP* in HEK293 cells. Values represent result from one experiment.

TXNIP and CNOT1 Are Associated with the Unfolded Protein Response (UPR).

TXNIP and the UPR. TXNIP is activated to promote apoptosis by cellular conditions such as oxidative stress and extreme endoplasmic reticulum (ER) stress. Accumulation of unfolded proteins in the ER results in ER stress and activation of the unfolded protein response (UPR). Moderate ER stress leads to activation of an adaptive UPR, which initiates several pathways that decrease general translation and increase transcription and translation of factors to increase ER folding capacity. However, under

conditions of extreme stress the UPR initiates pathways leading to cell death, a process known as terminal UPR. It has recently been reported that activation of TXNIP can promote the switch from adaptive to terminal UPR. Further, this activation takes place in part by means of relief of *miR-17*-mediated degradation of *TXNIP* mRNA. Thus, CNOT1-mediated downregulation of *TXNIP* expression may contribute to protection from terminal UPR pathways.

To test this idea we first determined if the UPR contributed to apoptosis in SW480 cells. Cells were treated with different concentrations of tunicamycin, a potent pharmacological inducer of ER stress and the UPR, from 0.05 µg/ml to 1.0 µg/ml over a time period of 96 hours and cell viability was evaluated by MTT assay at intervals of 24 hours (Figure 28A). This experiment revealed that treatment with tunicamycin results in a dose and time dependent decrease in cell viability in SW480 cells. To confirm that treatment with tunicamycin can induce ER stress and activate UPR pathways, we also measured mRNA levels of genes involved in UPR signaling. We found that *GRP78/Bip, sXBP1, ATF6, PERK* and *XBP1* mRNA levels showed at least two fold upregulation in SW480 cells treated with tunicamycin at 0.25 µg/ml for 6 hours (Figure 28B). This result suggested that tunicamycin could induce decreased cell viability through activation of UPR signaling.

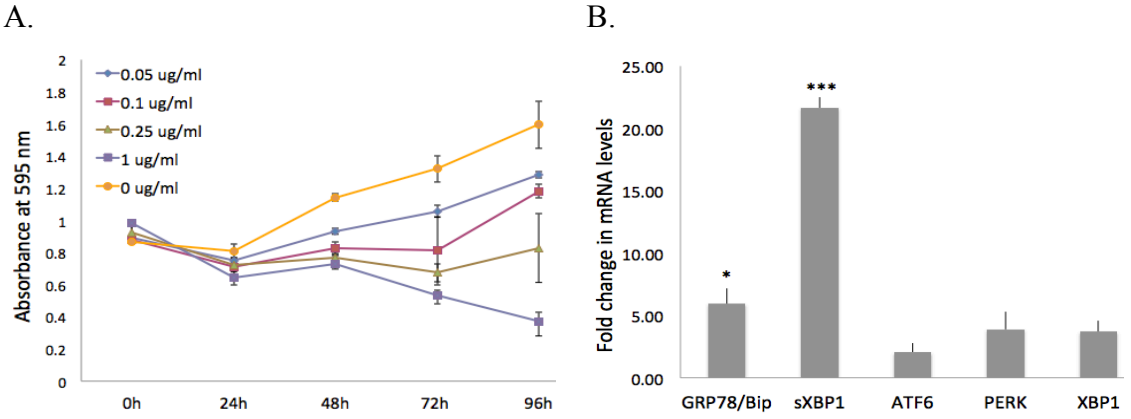

Figure 28. Tunicamycin induces decreased cell viability and activation of UPR signaling in SW480 cells. (A) SW480 cells were plated at 2 X 10^4 cells per well in triplicate in 96 well plates. Cells were treated with tunicamycin at 0.05 µg/ml to 1.0 µg/ml and cell viability was measured

by MTT assay over a time period of 96 hours at intervals of 24 hours. Each data point represents mean ± SD of three replicates from an MTT assay. (B) SW480 cells at 70% confluence were treated with tunicamycin at 0.25 µg/ml for 6 hours. Total RNA was extracted and measured for mRNA expression levels of indicated genes. Values represent mean ± SD of two experiments. Significance of differences was determined by a *t*-test. *** = $p < 0.001$, * = $p < 0.05$.

To determine if TXNIP is involved in the response to UPR in SW480 cells we first examined the effect of tunicamycin treatment on *TXNIP* expression. Treatment with tunicamycin at 0.25 µg/ml for 6 hours resulted in upregulated *TXNIP* levels (Figure 29A) consistent with a role for TXNIP in the UPR in these cells. We then examined cell viability in cells treated with a moderate dose (0.1 µg/ml) of tunicamycin. *TXNIP*-depleted cells showed increased viability compared to control cells (Figure 29B) suggesting that TXNIP promotes the terminal UPR pathway in these cells.

A. B.

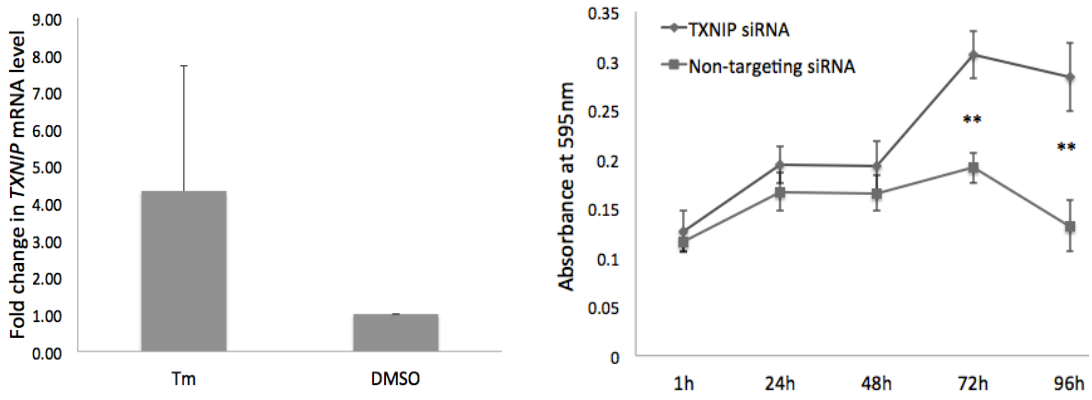

Figure 29. TXNIP plays a role in the UPR in SW480 cells. (A) SW480 cells were treated with tunicamycin of 0.25 µg/ml for 6 hours. Total RNA was isolated and analyzed by RT-qPCR to determine *TXNIP* expression levels. Values represent mean ± SD of two experiments. Significance of differences was calculated by a *t*-test. (B) SW480 cells were transfected with either siRNA targeting *TXNIP* or control siRNA twice 48 hours apart. Cells were plated at 5000 cells per well in triplicate in 96 well plates 24 hours after the second transfection. Cells were treated with tunicamycin at 0.1 µg/ml and cell viability was measured by MTT assay over a time period of 96 hours as indicated. Each data point represents mean ± SD of three replicates from

one experiment. Significance of differences in cell viability was determined at 72 hour and 96 hour by a *t*-test. ** = $p < 0.01$.

CNOT1 and the UPR. To determine if CNOT1 also plays a role in the UPR in SW480 cells we examined expression of mRNAs upregulated during the UPR. qRT-PCR analysis revealed that mRNA levels of genes involved in all three pathways of the UPR are upregulated in *CNOT1*-depleted SW480 cells (Figure 30A), such as *sXBP1* (IRE1α pathway), *PERK*, *ATF4* and *DDIT3* (*CHOP)* (PERK pathway), and *ATF6*, *XBP1*(ATF6 pathway). It is important to note that only changes in mRNA levels were examined. To gain a full picture of the effect of CNOT1 on these pathways we will need to examine translational and post-translational regulation.

To determine if CNOT1 might be involved in apoptotic pathways initiated by TXNIP activation we examined expression of *IL8* and *NFKB1* and found that their levels were increased in *CNOT1*-depleted cells consistent with a model in which CNOT1 acts through TXNIP (Figure 30B).

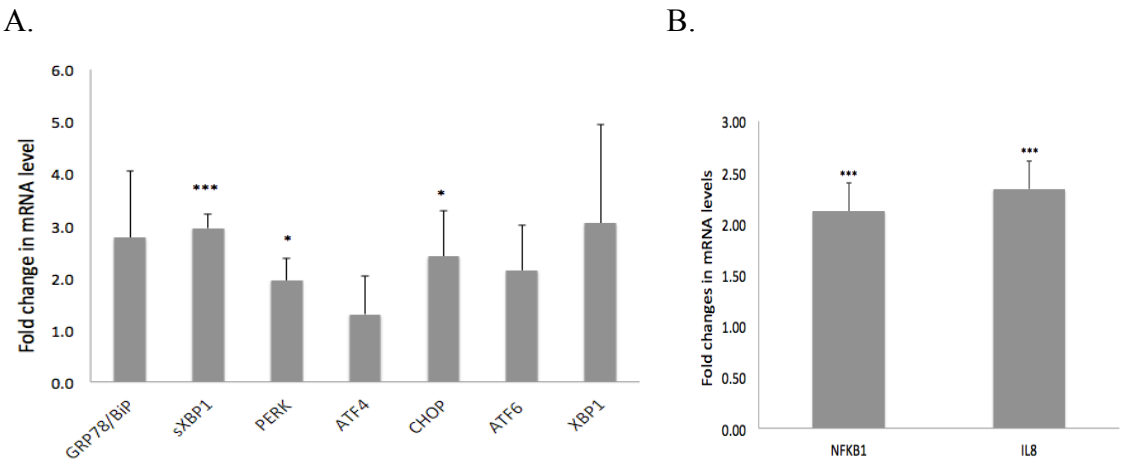

Figure 30. Depletion of *CNOT1* results in ER stress and activation of UPR pathways. (A) Quantification of mRNA expression levels of genes involved in UPR pathways in SW480 depleted for *CNOT1* by qRT-PCR. (B) mRNA expression levels of *NFKB1* and *IL8* in SW480 depleted for *CNOT1*. Values represent mean ± SD of three independent experiments. Significance of differences was calculated by a *t*-test. *** = $p < 0.001$, * = $p < 0.05$.

To further characterize the role of CNOT1 in the unfolded protein response we performed GSEA to analyze the altered gene expression profile following *CNOT1* depletion. A complete ranked expression dataset was generated in which genes were ranked according to ratio of expression in *CNOT1*-depleted cells to control treated cells. Genesets were compiled to represent gene expression in adaptive UPR or terminal UPR. GSEA revealed significant overlap with a group of mRNAs associated with response to extreme UPR known as Regulated IRE-1 Dependent Decay (RIDD) genes. These included RIDD genes degraded in mouse liver (So *et al*., 2012) and in pancreatic beta cells (Han *et al*., 2009) in response to extreme ER stress. Transcripts down-regulated in *CNOT1*-depleted cells were enriched in genes down-regulated in response to extreme ER stress, suggesting that downregulation of CNOT1 promotes RIDD and therefore *CNOT1* expression is protective (Figure 31A, Table 6). In addition, comparison with the Molecular Signatures Database geneset collection of cellular components (MsigDB C5 CC, http://www.broadinstitute.org/gsea/msigdb/collections.jsp#C5) revealed that four of the five most enriched genesets consisted of plasma membrane localized components and thus transcripts that would be translated and processed in the ER (Figure 31B, Table 7). This result suggests that CNOT1 may also protect the cell from the UPR by limiting transcript levels. Together these results suggest that CNOT1 may protect against the effects of ER stress by mechanisms in addition to *TXNIP* regulation.

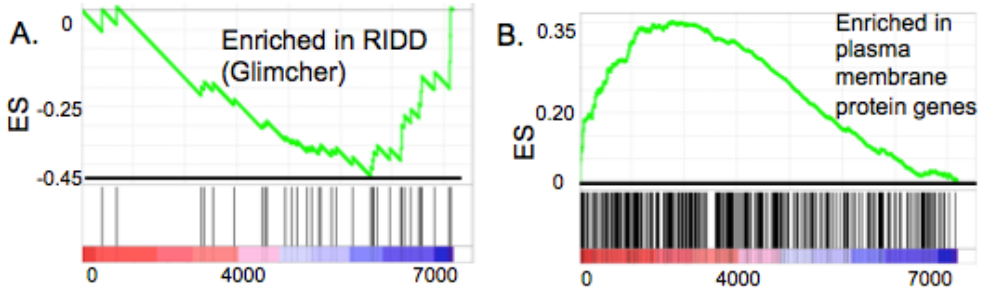

C.

	vs. *CNOT1*-depleted array	
GENESET	**NES**	**Nom. P Value**
RIDD genes (So *et al*)	-1.99	<0.001
Plasma membrane protein genes	2.02	<0.001

Figure 31. CNOT1 is involved in ER stress and activation of UPR pathways. Gene set enrichment analysis (GSEA) of gene expression profile in SW480 cells depleted for *CNOT1*. Ranked *CNOT1* expression data set (see text) was analyzed for enrichment in UPR-related genesets. (A) Representative enrichment plot of genesets compiled from gene expression studies of adaptive and terminal responses to the UPR. Shown is RIDD geneset from So *et al* (So *et al*., 2012). (B) Representative enrichment plot analysis of genesets found in MsigDB C5 CC collection, consisting of genes expressed in specific cellular components. Shown is enrichment plot for the GO geneset 'PLASMA_MEMBRANE_PART'. (C) Normalized enrichment score (NES) and nominal *p* value (Nom. *p* value) are shown for each comparison.

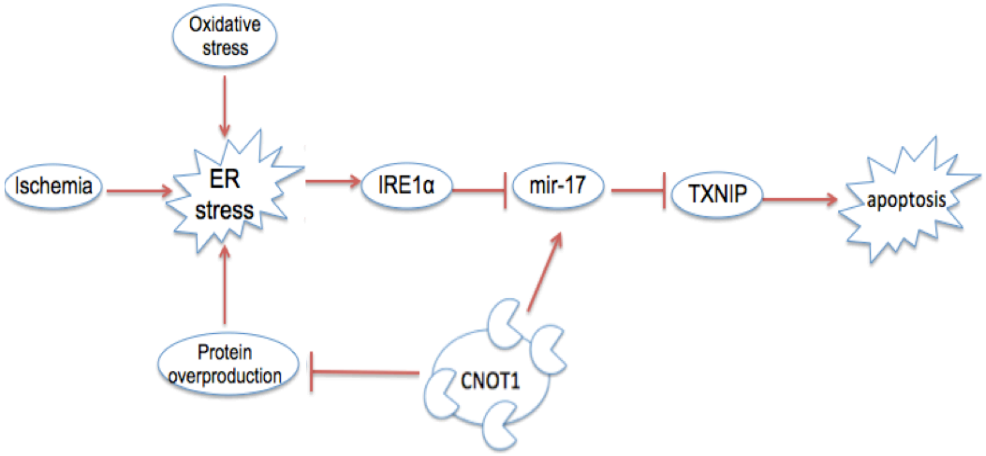

Figure 32. A model for roles of CNOT1 in regulating cell viability.

To summarize, these studies demonstrate that depletion of *CNOT1* in the human CRC cell line SW480 results in decreased cell viability, increased apoptosis and increased *TXNIP* levels. Increased *TXNIP* levels in HEK293 cells resulted in decreased cell viability. In addition, in *CNOT1*-depleted SW480 cells, elevation of *TXNIP* levels occurs before an increase in apoptosis. These results suggest that decreased cell viability in *CNOT1*-depleted cells is due to increased *TXNIP* levels. To further test this idea we will examine the effect of co-expression and co-depletion of *CNOT1* and *TXNIP*. Further, our data indicate that CNOT1 destabilizes *TXNIP* mRNA possibly through *miR-17*-mediated degradation involving CNOT8 deadenylase. To test this idea we will examine 3'UTR reporter activity.

In pancreatic beta cells elevation of *TXNIP* levels occurs in response to extreme ER stress and leads to apoptosis. As increased *TXNIP* levels occur through post-transcriptional stabilization, *CNOT1* expression may protect from and *CNOT1* depletion may exacerbate the effects of extreme ER stress and the terminal unfolded protein response in SW480 cells. In support of this idea, depletion of *TXNIP* in SW480 cells protects against tunicamycin-induced cell death suggesting that CNOT1-mediated limitation of *TXNIP* may be protective. In support of a role for CNOT1, mRNAs from each of the major UPR pathways are upregulated in *CNOT1*-depleted cells. In addition, analysis of gene expression in *CNOT1*-depleted cells suggests that CNOT1 may limit the UPR by other mechanisms as well.

A model based on these results is shown in Figure 32. This model predicts that CNOT1 activity protects cell viability by limiting the effects of the terminal UPR. Severe cellular conditions, such as protein overprocduction and oxidative stress, cause ER stress and activate UPR pathways. Under terminal, non-remediable ER stress, hyperactivation of IRE1α results in uregulated *TXNIP* expression, which in turn, activates apoptotic signaling pathways. CNOT1 activity may protect against the effects of severe ER stress through directly limiting *TXNIP* transcript levels. In addition, CNOT1 activity may limit the pool of mRNA to be translated in the ER.

However, two major gaps need to be filled. (1) Evidence that increased activity of CNOT1 can prevent cell apoptosis under severe ER stress, such as treatment with tunicamycin, needs to be provided. (2) We also need to show increased TXNIP activity is the cause of increased apoptosis in *CNOT1*-depleted cells and that limiting TXNIP activity can improve cell viability in these cells. As cancer cells are often subject to extreme stresses due to harsh growth conditions or enhanced protein production, increased activity of CNOT1 may protect cancer cells from apoptosis through this mechanism and confer growth advantage to cancer cells.

Supplemental Information:

Table 4. List of 266 genes showing significant upregulated (A) and downregulated (B) expression levels in SW480 cells depleted for *CNOT1*.

(A) Upregulated Genes:

Gene Symbol	log fold change	n fold change
TXNIP	2.896508483	7.44622
DKK1	2.35158454	5.10385
DUSP5	2.150944437	4.44118
EMP1	2.096157218	4.27569
NA	1.973349402	3.92679
NRP1	1.96182098	3.89553
TNFRSF6B	1.923383113	3.79312
IL1RAPL1	1.918700003	3.78082
LYPD6B	1.915699299	3.77297
SGK1	1.88472168	3.69282
S100P	1.863698467	3.63939
STEAP1	1.812791333	3.51321
BTG1	1.771000055	3.41290
PLAUR	1.762770283	3.39349
ZNF365	1.7489493	3.36114
MUC13	1.714169268	3.28108
PLIN2	1.6600699	3.16032
PROCR	1.654243386	3.14758
SERPINE1	1.648272383	3.13458
GPRC5A	1.643272601	3.12374
IGFBP3	1.637889705	3.11210
HAVCR2	1.629860019	3.09483
EFNB2	1.624880988	3.08417
LYPD6B	1.6078959	3.04807
IGFBP3	1.574230479	2.97777
ADAM19	1.567745266	2.96441
TM4SF1	1.565727169	2.96027
TNFRSF6B	1.563680091	2.95607
TGM2	1.56321117	2.95511
LPAR5	1.547263062	2.92262
ZBED2	1.522691159	2.87327
AKAP12	1.52109659	2.87009

POLR1C	1.50002564	2.82848
PLAUR	1.498237703	2.82497
FZD9	1.48279479	2.79490
TMEM22	1.482594424	2.79451
SGK1	1.476720245	2.78315
C2orf49	1.471895329	2.77386
CD58	1.453009577	2.73779
NA	1.448875551	2.72995
NRP1	1.43272506	2.69956
COL7A1	1.419252403	2.67447
MMD	1.411019172	2.65925
SERPINB5	1.410881657	2.65900
SGK1	1.405235672	2.64861
POLR1C	1.404352218	2.64699
F2RL1	1.386263215	2.61401
UCN2	1.368591711	2.58218
BCAR3	1.368519302	2.58205
PRDM1	1.367655949	2.58051
KLF9	1.359572662	2.56609
CD58	1.354648683	2.55735
NA	1.349074792	2.54749
F2RL1	1.341613134	2.53435
KLF2	1.328770538	2.51189
CDKN2B	1.327136363	2.50904
MYC	1.322388951	2.50080
EDAR	1.322030806	2.50018
ZNF296	1.316873858	2.49126
PELO	1.313247411	2.48500
PTRH2	1.312743744	2.48414
DNAJB9	1.309275207	2.47817
DHRS2	1.300894478	2.46382
MYC	1.300779098	2.46362
DEPDC7	1.299956801	2.46222
IFRD1	1.292732494	2.44992
UBE2H	1.276342691	2.42224
TRIB1	1.266021197	2.40497
IFRD1	1.263630497	2.40099
PLIN2	1.261534137	2.39751
HIST1H2BD	1.261314556	2.39714
LMO2	1.257296455	2.39047

ICAM2	1.254362976	2.38562
SERPINE2	1.253807761	2.38470
DKK4	1.244804631	2.36986
NOP2	1.244625355	2.36957
TNFRSF6B	1.243115008	2.36709
DEPDC7	1.23948181	2.36114
HEY2	1.235810152	2.35514
KRT81	1.231054712	2.34739
FRAT2	1.225722218	2.33872
SLC40A1	1.219612857	2.32884
TNFRSF11B	1.21452103	2.32064
TANC1	1.213628042	2.31920
AKIRIN2	1.212223406	2.31694
KANSL2	1.211242518	2.31537
VASN	1.211055295	2.31507
RGL1	1.210689082	2.31448
GZMB	1.202988495	2.30216
GNL3	1.198410379	2.29487
FAM216A	1.197542091	2.29349
HES7	1.195248472	2.28984
HS3ST3A1	1.192675668	2.28576
YRDC	1.191016461	2.28314
CST1	1.18858886	2.27930
KIAA0895	1.185541336	2.27449
KCTD14	1.184888387	2.27346
ARHGEF3	1.184740405	2.27322
PHLDA1	1.177206928	2.26139
TMEM177	1.175174863	2.25820
TM4SF19	1.174174787	2.25664
KRT6A	1.167536766	2.24628
RNF149	1.165157634	2.24258
RNASE1	1.164472224	2.24151
ANXA1	1.160708624	2.23567
ITGA2	1.15583959	2.22814
NDRG1	1.155667332	2.22787
TSPAN5	1.155568505	2.22772
NOP16	1.152421033	2.22287
SLC30A1	1.151151774	2.22091
ATG16L1	1.144311522	2.21041
NOP16	1.139920452	2.20369

ITGA5	1.137479692	2.19996
IRF1	1.135474794	2.19691
GTF2B	1.132604331	2.19254
RN28S1	1.132534635	2.19244
GJB3	1.132510918	2.19240
S100A3	1.12691402	2.18391
GJB4	1.126536321	2.18334
ARHGEF2	1.123660666	2.17899
LGR6	1.123615779	2.17892
ADCK3	1.121741223	2.17609
GPRC5C	1.117589583	2.16984
TNFRSF21	1.110188935	2.15874
SRPK2	1.110075426	2.15857
LRRN4	1.109654821	2.15794
RCL1	1.107295885	2.15441
ECE2	1.107189669	2.15426
WFDC3	1.105573451	2.15184
PDE8B	1.104913843	2.15086
BRIX1	1.103104365	2.14816
MRPS30	1.102410059	2.14713
NGDN	1.098735412	2.14167
GTPBP4	1.097972613	2.14054
CXorf38	1.093019097	2.13320
IRF9	1.092852582	2.13295
ELF1	1.088877751	2.12709
EFNB1	1.085619757	2.12229
NA	1.080680745	2.11503
HBEGF	1.077663741	2.11062
NA	1.0726737	2.10333
BRIX1	1.072631123	2.10327
BMP4	1.066868563	2.09488
GNE	1.064478369	2.09141
TNFRSF1B	1.062264226	2.08821
PHLDB2	1.062150174	2.08804
C15orf39	1.061062307	2.08647
SLC52A3	1.058176403	2.08230
TPST2	1.053237269	2.07518
BIK	1.052793952	2.07454
PCGF1	1.050910242	2.07184
ERRFI1	1.049601191	2.06996

NA	1.047888796	2.06750
GEMIN4	1.046831838	2.06599
KRT80	1.043820483	2.06168
GRWD1	1.043588185	2.06135
TIPARP	1.041089411	2.05778
PHLDB2	1.040286765	2.05664
DYRK2	1.038949974	2.05473
SLC30A1	1.038818451	2.05454
LARP6	1.036906679	2.05182
ESM1	1.032017112	2.04488
NGDN	1.031984235	2.04483
CLPX	1.031922469	2.04475
MAOA	1.031648332	2.04436
NA	1.031440349	2.04406
GNL3	1.030186706	2.04229
ATG16L1	1.027767688	2.03887
KCNK6	1.026330093	2.03684
SERPINH1	1.025405705	2.03553
NAA30	1.023109618	2.03229
SLC16A6	1.020905652	2.02919
NOLC1	1.019195294	2.02679
ITPRIPL2	1.017698402	2.02469
IFFO1	1.015243453	2.02124
SMAGP	1.01417318	2.01975
FAT1	1.014064792	2.01959
NA	1.013732904	2.01913
PLCXD1	1.012174234	2.01695
TGFBR2	1.006768665	2.00941
RIOK2	1.005436348	2.00755
TGFBR2	1.005031254	2.00699
TNFRSF10A	1.002916451	2.00405

(B) Downregulated Genes:

Gene Symbol	log fold change	n fold change
NOTUM	-1.000398452	0.49986
CAPNS1	-1.001472128	0.49949
DPM3	-1.00613552	0.49788
MYO1D	-1.007438581	0.49743
PNPLA7	-1.008982297	0.49690

NA	-1.009959309	0.49656
ACAT2	-1.011950446	0.49588
FRG1B	-1.016104068	0.49445
PRDX5	-1.018125981	0.49376
ACTA2	-1.019750865	0.49320
LRRC26	-1.022477331	0.49227
GUSB	-1.024492829	0.49158
NBPF10	-1.026236051	0.49099
C9orf86	-1.02854056	0.49021
LARP1	-1.028968038	0.49006
PRDX2	-1.029784963	0.48978
NA	-1.034871243	0.48806
ATP5G2	-1.039293116	0.48657
STMN1	-1.039295822	0.48656
MT2A	-1.039511988	0.48649
ZNF358	-1.041108951	0.48595
CCDC3	-1.042282209	0.48556
BLOC1S1	-1.044234985	0.48490
TMEM139	-1.046606621	0.48411
PHPT1	-1.049034528	0.48329
SWI5	-1.054176634	0.48157
RRM2	-1.055679283	0.48107
NA	-1.056466049	0.48081
DUT	-1.062637917	0.47876
DGCR6L	-1.06420164	0.47824
PRDX5	-1.065571077	0.47778
ID2	-1.084708887	0.47149
EEF1A1	-1.085389656	0.47126
HES6	-1.086841283	0.47079
COL18A1	-1.088102123	0.47038
NA	-1.089487748	0.46993
NA	-1.09305909	0.46877
CHMP3	-1.095295069	0.46804
NOTUM	-1.095386954	0.46801
ESPN	-1.097498842	0.46733
LYPD5	-1.100455961	0.46637
NEBL	-1.1127466	0.46241
ANAPC11	-1.113088303	0.46230
NA	-1.126632316	0.45798

TNNC1	-1.127174225	0.45781
SLC48A1	-1.129260008	0.45715
CHMP3	-1.135397638	0.45521
BCL7C	-1.14512003	0.45215
DGCR6	-1.147594581	0.45138
ASPSCR1	-1.151948655	0.45002
LAMA5	-1.153491384	0.44954
TMSB15B	-1.156822818	0.44850
NA	-1.172094204	0.44378
ITGAE	-1.177191077	0.44221
DUT	-1.17874924	0.44173
LSM4	-1.180022421	0.44134
RARRES2	-1.18033437	0.44125
TMSB15B	-1.181507537	0.44089
TSTD1	-1.183928672	0.44015
NA	-1.187084934	0.43919
SPC24	-1.187984996	0.43892
SLC25A23	-1.197016162	0.43618
C1orf86	-1.205394913	0.43365
C11orf51	-1.215371146	0.43066
C9orf142	-1.221651257	0.42879
NA	-1.225679708	0.42760
HMGB3	-1.230032617	0.42631
DGCR6	-1.259765955	0.41761
ANAPC11	-1.262579478	0.41680
RPS23	-1.279880514	0.41183
PDXK	-1.287642434	0.40962
GCHFR	-1.298126329	0.40665
NA	-1.305968633	0.40445
MAL2	-1.323249611	0.39963
AGRN	-1.341449303	0.39462
SKA2	-1.349357812	0.39247
C18orf56	-1.368946242	0.38717
NUDT14	-1.378213468	0.38469
GAS6	-1.503109748	0.35279
GAS6	-1.508886578	0.35138
TCEA3	-1.57567094	0.33549
PXMP2	-1.636131507	0.32172
CNOT1	-2.549125461	0.17086

ID	Molecules in Network	Score
1	↑**ADAM19**, APOBEC3G, CCND1, CDK2, CDK5, CDKN1A, CDKN1B, CLDN1, ↓**CNOT1**, CTNNB1, ↑**DHRS2**, DICER1, ↓**EEF1A1**, ↑**EFNB1**, ↑**EFNB2**, ↑**ELF1**, ↓**GAS6***, ↑**GNE**, ↑**ITGA2**, JUN, MGEA5, PLAU, ↑**PLAUR***, RB1, ↑**SERPINE2**, ↑**SLC40A1**, SP3, ↑**TGFBR2***, ↑**TM4SF1**, TP53, ↑**TSPAN5**, VIM	17
2	↑**ADCK3**, ADRB2, ↑**AKAP12**, ↑**ANXA1**, ATF3, BAX, ↑**BIK**, CASP3, CD24, CDKN1A, ↑**DUSP5**, GDF15, ↑**GNL3***, HINT1, HMMR, HSPD1, ↓**ID2**, ↑**IGFBP3***, JMJD1C, KRAS, MGEA5, PMAIP1, ↓**PRDX2**, PTP4A1, RBBP6, RUNX1, ↑**SERPINB5**, ↑**SLC30A1***, SPHK1, ↓**STMN1**, ↑**TGM2**, TOP2A, TOPBP1, TP53, XRCC6	12
3	APC, ATF3, BCL6, BMP2, ↑**BMP4**, CCND2, CTNNB1, DDX5, DDX17, E2F4, EP300, ↑**ERRFI1**, ↑**HBEGF**, IGF2BP1, KRAS, LEF1, ↑**MYC***, NCL, ↑**NDRG1**, NEDD9, PLD1, ↑**PLIN2***, PPARG, PRKCD, ↑**SERPINE1**, ↑**SGK1***, SNRK, SUZ12, TCF4, TCF7L2, TERT, ↑**TNFRSF10A**, ↑**TNFRSF11B**, ↑**TNFRSF1B**, ↑**TXNIP**	10

Figure 33. Molecules in top three gene networks in IPA shown in Figure 20. Names in bold represent genes that change expression in *CNOT1*-depleted cells. Unbold represent interacting genes. Arrows show direction of change.

Table 5. Core genes enriched in *CNOT1*-HI/*CNOT1*-LO.

(A) Genes differentially expressed in proliferating intestinal crypts (Merlos-Suarez *et al*., 2011).

NAME	PROBE	RANK IN GENE LIST	RANK METRIC SCORE	RUNNING ES	CORE ENRICHMENT
row_0	ZNRF3	58	1.5959	0.0111	Yes
row_1	POLR1E	188	1.2693	0.0145	Yes
row_2	BCKDHB	239	1.2092	0.0226	Yes
row_3	ZC3H7B	256	1.1874	0.0326	Yes
row_4	CYP39A1	267	1.1748	0.0430	Yes
row_5	POLA1	430	1.0580	0.0423	Yes
row_6	BARD1	448	1.0437	0.0509	Yes
row_7	FADS1	536	0.9853	0.0544	Yes
row_8	HAUS6	577	0.9663	0.0608	Yes
row_9	MYB	587	0.9618	0.0693	Yes
row_10	MDN1	636	0.9364	0.0749	Yes
row_11	TSPAN12	642	0.9346	0.0833	Yes
row_12	GEN1	751	0.8938	0.0846	Yes
row_13	NCAPD2	777	0.8853	0.0912	Yes
row_14	TUBB	797	0.8779	0.0982	Yes
row_15	NDE1	833	0.8654	0.1040	Yes
row_16	GTSE1	834	0.8652	0.1121	Yes
row_17	CEP192	851	0.8588	0.1191	Yes

row_18	KIF24	1073	0.7982	0.1120	Yes
row_19	TXNDC16	1118	0.7851	0.1165	Yes
row_20	SGOL2	1176	0.7697	0.1200	Yes
row_21	PUS7	1181	0.7683	0.1269	Yes
row_22	GLS2	1219	0.7601	0.1316	Yes
row_23	CKAP2L	1239	0.7536	0.1374	Yes
row_24	TBC1D4	1250	0.7518	0.1438	Yes
row_25	DACH1	1289	0.7422	0.1482	Yes
row_26	DNA2	1309	0.7364	0.1539	Yes
row_27	GEMIN4	1312	0.7354	0.1606	Yes
row_28	CELSR2	1317	0.7346	0.1672	Yes
row_29	FTSJD1	1329	0.7314	0.1734	Yes
row_30	MCM5	1332	0.7304	0.1801	Yes
row_31	TTPA	1369	0.7198	0.1844	Yes
row_32	CASC5	1420	0.7098	0.1878	Yes
row_33	LIG1	1633	0.6709	0.1802	Yes
row_34	SCML2	1649	0.6692	0.1854	Yes
row_35	CEP76	1654	0.6672	0.1914	Yes
row_36	CENPI	1728	0.6526	0.1927	Yes
row_37	PCK2	1768	0.6454	0.1962	Yes
row_38	ALMS1	1808	0.6355	0.1996	Yes
row_39	MCM8	1851	0.6288	0.2027	Yes
row_40	RRM2	1875	0.6239	0.2071	Yes
row_41	PIP4K2B	1904	0.6188	0.2110	Yes
row_42	CP110	1955	0.6120	0.2135	Yes
row_43	RPUSD2	2032	0.6002	0.2141	Yes
row_44	MYC	2034	0.6002	0.2196	Yes
row_45	MCM7	2082	0.5933	0.2221	Yes
row_46	DUS4L	2180	0.5806	0.2212	Yes
row_47	CCNF	2274	0.5656	0.2204	Yes
row_48	DSN1	2339	0.5547	0.2214	Yes
row_49	CDCA2	2344	0.5537	0.2263	Yes
row_50	MPHOSPH9	2356	0.5514	0.2307	Yes
row_51	ZBTB16	2381	0.5480	0.2343	Yes
row_52	BRCA1	2467	0.5356	0.2337	Yes
row_53	MELK	2485	0.5320	0.2376	Yes
row_54	DCK	2548	0.5229	0.2384	Yes
row_55	KIF18B	2557	0.5214	0.2428	Yes
row_56	KLHL23	2596	0.5176	0.2451	Yes
row_57	KBTBD6	2612	0.5153	0.2489	Yes

row_58	TUBE1	2723	0.4975	0.2464	Yes
row_59	RPP40	2736	0.4959	0.2502	Yes
row_60	ZNF367	2747	0.4943	0.2542	Yes
row_61	TPX2	2771	0.4912	0.2573	Yes
row_62	INCENP	2829	0.4828	0.2581	Yes
row_63	KIF20B	2874	0.4770	0.2596	Yes
row_64	PFAS	2961	0.4659	0.2584	Yes
row_65	XRCC2	3117	0.4461	0.2524	Yes
row_66	SMC2	3130	0.4442	0.2557	Yes
row_67	ZNF275	3132	0.4438	0.2598	Yes
row_68	WDR35	3136	0.4428	0.2638	Yes
row_69	TSGA14	3145	0.4418	0.2674	Yes
row_70	SGOL1	3160	0.4397	0.2706	Yes
row_71	PRR11	3181	0.4373	0.2734	Yes
row_72	WDR76	3184	0.4368	0.2773	Yes
row_73	KIFC1	3220	0.4319	0.2791	Yes
row_74	DIAPH3	3228	0.4303	0.2826	Yes
row_75	KIF11	3293	0.4220	0.2824	Yes
row_76	KIAA0649	3301	0.4211	0.2859	Yes
row_77	NFATC2	3319	0.4188	0.2887	Yes
row_78	RFC3	3322	0.4187	0.2925	Yes
row_79	SHCBP1	3327	0.4184	0.2961	Yes
row_80	ASPM	3335	0.4170	0.2996	Yes
row_81	SLC7A2	3386	0.4117	0.3001	Yes
row_82	CLSPN	3433	0.4043	0.3009	Yes
row_83	HMMR	3462	0.4005	0.3028	Yes
row_84	TOPBP1	3492	0.3967	0.3046	Yes
row_85	CHEK1	3604	0.3841	0.3009	Yes
row_86	GSTCD	3622	0.3809	0.3034	Yes
row_87	POLE2	3733	0.3679	0.2996	Yes
row_88	TRIM37	3745	0.3661	0.3023	Yes
row_89	NRM	3779	0.3621	0.3035	Yes
row_90	FIGNL1	3820	0.3570	0.3042	Yes
row_91	RAD18	3826	0.3562	0.3072	Yes
row_92	NCAPH	3831	0.3550	0.3103	Yes
row_93	BLM	3866	0.3523	0.3114	Yes
row_94	KIF4A	4061	0.3300	0.3017	Yes
row_95	LMNB1	4075	0.3290	0.3039	Yes
row_96	HAUS5	4102	0.3263	0.3053	Yes
row_97	TAF4B	4154	0.3209	0.3049	Yes

row_98	MYBL2	4161	0.3203	0.3075	Yes
row_99	PLK4	4168	0.3191	0.3101	Yes
row_100	ESPL1	4199	0.3153	0.3111	Yes
row_101	ZNF473	4210	0.3141	0.3134	Yes
row_102	ESCO2	4265	0.3083	0.3127	Yes
row_103	ATAD5	4349	0.2978	0.3101	Yes
row_104	TCF19	4371	0.2956	0.3115	Yes
row_105	BCL7A	4383	0.2944	0.3135	Yes
row_106	MCM4	4458	0.2851	0.3113	Yes
row_107	NEIL3	4518	0.2788	0.3101	Yes
row_108	NCAPG2	4525	0.2782	0.3123	Yes
row_109	ATAD2	4556	0.2745	0.3129	Yes
row_110	TMEM107	4560	0.2743	0.3152	Yes
row_111	AURKA	4580	0.2720	0.3165	Yes
row_112	FAM54A	4603	0.2687	0.3176	Yes
row_113	BUB1	4677	0.2613	0.3153	Yes
row_114	KIF18A	4682	0.2607	0.3174	Yes
row_115	PALB2	4720	0.2571	0.3174	Yes
row_116	ANLN	4777	0.2505	0.3161	Yes
row_117	DKC1	4796	0.2484	0.3172	Yes
row_118	PSIP1	4809	0.2468	0.3187	Yes
row_119	NUSAP1	4832	0.2433	0.3196	Yes
row_120	POLD1	4833	0.2433	0.3219	Yes

(B) CIS-associated genes identified in *SB* screens by Starr *et al.* (Starr *et al*., 2009, Starr *et al*., 2011, Starr T.K., unpublished data).

NAME	PROBE	RANK IN GENE LIST	RANK METRIC SCORE	RUNNING ES	CORE ENRICH-MENT
row_0	CNOT1	31	1.8093	0.0220	Yes
row_1	MKLN1	230	1.2179	0.0253	Yes
row_2	ATF2	232	1.2174	0.0414	Yes
row_3	INO80D	237	1.2098	0.0572	Yes
row_4	LMO7	244	1.2050	0.0729	Yes
row_5	CDK12	252	1.1907	0.0882	Yes
row_6	SMG1	271	1.1719	0.1026	Yes
row_7	ELF1	281	1.1665	0.1175	Yes
row_8	RREB1	314	1.1414	0.1306	Yes
row_9	PUM2	330	1.1241	0.1446	Yes
row_10	RAD50	350	1.1132	0.1581	Yes

row_11	SND1	452	1.0393	0.1654	Yes
row_12	PUM1	454	1.0387	0.1791	Yes
row_13	EXOC2	499	1.0067	0.1896	Yes
row_14	PPP4R2	526	0.9901	0.2011	Yes
row_15	UGGT1	550	0.9791	0.2126	Yes
row_16	PBRM1	569	0.9711	0.2243	Yes
row_17	GMDS	580	0.9652	0.2365	Yes
row_18	INPP5D	616	0.9466	0.2468	Yes
row_19	ATP8B1	649	0.9321	0.2571	Yes
row_20	STAG1	696	0.9174	0.2663	Yes
row_21	ROCK2	698	0.9170	0.2784	Yes
row_22	CNOT4	725	0.9033	0.2887	Yes
row_23	MKL2	791	0.8793	0.2962	Yes
row_24	UBAP2	876	0.8506	0.3020	Yes
row_25	UBN2	1049	0.8030	0.3015	Yes
row_26	TM9SF2	1130	0.7812	0.3067	Yes
row_27	ANKRD11	1197	0.7652	0.3125	Yes
row_28	MLL3	1222	0.7590	0.3211	Yes
row_29	KCTD20	1283	0.7440	0.3270	Yes
row_30	PDZD8	1285	0.7434	0.3369	Yes
row_31	DACH1	1289	0.7422	0.3465	Yes
row_32	SETD5	1337	0.7293	0.3532	Yes
row_33	RSF1	1346	0.7278	0.3623	Yes
row_34	STXBP5	1497	0.6961	0.3618	Yes
row_35	CDK8	1519	0.6913	0.3696	Yes
row_36	NSD1	1522	0.6907	0.3787	Yes
row_37	RASGRF1	1546	0.6868	0.3863	Yes
row_38	XPO7	1591	0.6768	0.3924	Yes
row_39	ZNRF2	1699	0.6589	0.3942	Yes
row_40	MYO5B	1726	0.6528	0.4012	Yes
row_41	ZNF48	1795	0.6386	0.4052	Yes
row_42	TPP2	1892	0.6202	0.4072	Yes
row_43	PDCD6IP	1930	0.6150	0.4130	Yes
row_44	MAPK8	1954	0.6121	0.4196	Yes
row_45	ARID2	1973	0.6097	0.4266	Yes
row_46	CASP8	2004	0.6042	0.4326	Yes
row_47	GSK3B	2008	0.6039	0.4405	Yes
row_48	ZCCHC7	2052	0.5985	0.4456	Yes
row_49	ESCO1	2120	0.5883	0.4491	Yes
row_50	PAN3	2221	0.5740	0.4502	Yes

row_51	UHRF2	2349	0.5527	0.4493	Yes
row_52	PTPRK	2355	0.5515	0.4563	Yes
row_53	SNX4	2376	0.5487	0.4623	Yes
row_54	RASEF	2415	0.5425	0.4670	Yes
row_55	MOBKL2B	2416	0.5424	0.4742	Yes
row_56	FUBP1	2544	0.5233	0.4729	Yes
row_57	PIK3R1	2655	0.5081	0.4725	Yes
row_58	ANKRD17	2684	0.5044	0.4774	Yes
row_59	NOTCH1	2739	0.4953	0.4804	Yes
row_60	MAN1A2	2794	0.4879	0.4834	Yes
row_61	SORT1	2922	0.4721	0.4814	Yes
row_62	TNPO3	2964	0.4653	0.4849	Yes
row_63	APC	2968	0.4648	0.4909	Yes
row_64	FNBP1L	2971	0.4645	0.4969	Yes
row_65	ARHGAP5	3009	0.4595	0.5006	Yes
row_66	KCNQ1	3018	0.4588	0.5062	Yes
row_67	ERBB2IP	3118	0.4459	0.5057	Yes
row_68	AP1AR	3168	0.4389	0.5083	Yes
row_69	TDRKH	3178	0.4377	0.5136	Yes
row_70	CLTC	3300	0.4212	0.5113	Yes
row_71	TNKS	3412	0.4086	0.5095	Yes
row_72	DMXL1	3420	0.4068	0.5144	Yes
row_73	SIPA1L1	3458	0.4016	0.5174	Yes
row_74	RNF111	3557	0.3888	0.5162	Yes
row_75	CSNK2A1	3573	0.3871	0.5203	Yes
row_76	CFTR	3645	0.3780	0.5207	Yes
row_77	TRIM33	3669	0.3764	0.5242	Yes

(C) CIS-associated genes identified in a *SB* screen by March *et al* (March *et al*., 2011)**.**

NAME	PROBE	RANK IN GENE LIST	RANK METRIC SCORE	RUNNING ES	CORE ENRICH-MENT
row_0	LRP5	22	1.9433	0.0295	Yes
row_1	CNOT1	31	1.8093	0.0577	Yes
row_2	BIRC6	116	1.4012	0.0745	Yes
row_3	NEDD4	132	1.3770	0.0954	Yes
row_4	LRIG1	148	1.3435	0.1158	Yes
row_5	PRKCA	202	1.2556	0.1324	Yes
row_6	PCF11	311	1.1427	0.1435	Yes

row_7	RREB1	314	1.1414	0.1615	Yes
row_8	ITGA6	339	1.1207	0.1778	Yes
row_9	NIPBL	395	1.0834	0.1914	Yes
row_10	PUM1	454	1.0387	0.2042	Yes
row_11	GMDS	580	0.9652	0.2114	Yes
row_12	MLL5	614	0.9470	0.2243	Yes
row_13	ATP8B1	649	0.9321	0.2369	Yes
row_14	ROCK2	698	0.9170	0.2484	Yes
row_15	NRIP1	894	0.8449	0.2491	Yes
row_16	ATAD2B	936	0.8326	0.2597	Yes
row_17	LGR4	944	0.8304	0.2724	Yes
row_18	PIP5K1B	946	0.8303	0.2856	Yes
row_19	DENND4C	973	0.8245	0.2970	Yes
row_20	ARID1B	1147	0.7759	0.2981	Yes
row_21	EML4	1245	0.7525	0.3037	Yes
row_22	ITFG3	1262	0.7494	0.3146	Yes
row_23	GTF2IRD1	1288	0.7430	0.3248	Yes
row_24	BAZ2B	1302	0.7381	0.3357	Yes
row_25	TLK1	1381	0.7167	0.3420	Yes
row_26	USP6NL	1477	0.7000	0.3470	Yes
row_27	NSD1	1522	0.6907	0.3551	Yes
row_28	NUP98	1571	0.6818	0.3628	Yes
row_29	ASXL1	1735	0.6515	0.3626	Yes
row_30	SLC25A20	1790	0.6403	0.3692	Yes
row_31	CTNND1	1829	0.6317	0.3768	Yes
row_32	SETD2	1918	0.6162	0.3809	Yes
row_33	ARID2	1973	0.6097	0.3871	Yes
row_34	GSK3B	2008	0.6039	0.3945	Yes
row_35	WAPAL	2204	0.5766	0.3910	Yes
row_36	PAN3	2221	0.5740	0.3990	Yes
row_37	WDR33	2236	0.5715	0.4072	Yes
row_38	PDXDC1	2251	0.5689	0.4154	Yes
row_39	RRBP1	2314	0.5584	0.4202	Yes
row_40	DDX6	2342	0.5540	0.4273	Yes
row_41	PTPRK	2355	0.5515	0.4352	Yes
row_42	ATRX	2476	0.5342	0.4359	Yes
row_43	PIK3R1	2655	0.5081	0.4324	Yes
row_44	ANKRD17	2684	0.5044	0.4386	Yes
row_45	MPP5	2785	0.4889	0.4399	Yes
row_46	MAN1A2	2794	0.4879	0.4472	Yes

row_47	ATP2A2	2841	0.4813	0.4518	Yes
row_48	VPS24	2916	0.4727	0.4545	Yes
row_49	ZFHX3	2948	0.4674	0.4599	Yes
row_50	SDC1	2967	0.4652	0.4662	Yes
row_51	APC	2968	0.4648	0.4736	Yes
row_52	FNBP1L	2971	0.4645	0.4808	Yes
row_53	CAPRIN1	3004	0.4601	0.4860	Yes
row_54	ARHGAP5	3009	0.4595	0.4931	Yes
row_55	KCNQ1	3018	0.4588	0.4999	Yes
row_56	FAM116A	3043	0.4550	0.5055	Yes
row_57	ERBB2IP	3118	0.4459	0.5078	Yes
row_58	GAB1	3194	0.4355	0.5099	Yes
row_59	NFIB	3211	0.4331	0.5157	Yes
row_60	ACVR1B	3347	0.4161	0.5136	Yes
row_61	MYOM1	3383	0.4121	0.5178	Yes
row_62	SYNCRIP	3427	0.4059	0.5215	Yes

Table 6. Core RIDD genes enriched in *CNOT1*-depleted SW480 cells (So *et al*., 2012)**.**

NAME	PROBE	RANK IN GENE LIST	RANK METRIC SCORE	RUNNING ES	CORE ENRICHMENT
row_19	COL18A1	5581	-0.082292341	-0.4058358	Yes
row_20	BTBD1	5619	-0.083633006	-0.38739416	Yes
row_21	DERA	5641	-0.084373057	-0.36650765	Yes
row_22	PAPOLA	5705	-0.087333411	-0.35065457	Yes
row_23	FDPS	5961	-0.09705963	-0.3588861	Yes
row_24	SLC27A5	6177	-0.108391821	-0.3583285	Yes
row_25	ABCA2	6183	-0.108704239	-0.3283367	Yes
row_26	FADS1	6184	-0.108723998	-0.29764056	Yes
row_27	PTPRF	6232	-0.11189945	-0.27261585	Yes
row_28	BOLA3	6366	-0.120483741	-0.2571854	Yes
row_29	IDI1	6518	-0.130967647	-0.2413104	Yes
row_30	RNF130	6563	-0.13481155	-0.20939767	Yes
row_31	TM7SF2	6566	-0.135234132	-0.17149644	Yes
row_32	PMVK	6816	-0.162154734	-0.16051117	Yes
row_33	TPP1	7127	-0.245197475	-0.13460472	Yes
row_34	BLOC1S1	7129	-0.246350572	-0.06519217	Yes
row_35	PXMP2	7145	-0.261100173	0.006428248	Yes

Table 7. Plasma membrane localized components (PLASMA_MEMBRANE_PART) enriched in *CNOT1*-depleted SW480 cells.

	PROBE	RANK IN GENE LIST	RANK METRIC SCORE	RUNNING ES	CORE ENRICHMENT
1	GPRC5A	11	0.466	0.0112	Yes
2	PROCR	12	0.463	0.024	Yes
3	EFNB2	13	0.46	0.0367	Yes
4	STEAP1	16	0.434	0.0484	Yes
5	SLC40A1	28	0.378	0.0572	Yes
6	F2RL1	29	0.377	0.0676	Yes
7	GZMB	43	0.354	0.0755	Yes
8	ITGA2	53	0.331	0.0833	Yes
9	TM4SF1	55	0.328	0.0922	Yes
10	ITGA5	56	0.327	0.1013	Yes
11	MMD	62	0.322	0.1094	Yes
12	ICAM2	70	0.311	0.117	Yes
13	HBEGF	79	0.306	0.1243	Yes
14	KCNK6	80	0.306	0.1327	Yes
15	SLC16A6	103	0.285	0.1374	Yes
16	TNFSF10	139	0.266	0.1396	Yes
17	EFNB1	162	0.258	0.1435	Yes
18	ITGA1	180	0.252	0.148	Yes
19	SLC20A2	251	0.229	0.1441	Yes
20	ZAP70	252	0.229	0.1504	Yes
21	EPHA4	258	0.227	0.156	Yes
22	EGFR	262	0.226	0.1618	Yes
23	SLC31A2	274	0.222	0.1663	Yes
24	GPRC5C	299	0.217	0.1688	Yes
25	CD24	305	0.215	0.174	Yes
26	KCNN4	307	0.215	0.1798	Yes
27	GPER	308	0.215	0.1857	Yes
28	LAT	322	0.212	0.1896	Yes
29	CCR7	323	0.212	0.1955	Yes
30	PRRG1	354	0.207	0.1968	Yes
31	IFNGR1	358	0.206	0.2021	Yes
32	CD55	410	0.196	0.2001	Yes
33	ACVR1	414	0.195	0.205	Yes
34	GJB2	447	0.191	0.2056	Yes
35	RCE1	452	0.19	0.2103	Yes
36	RGMB	459	0.189	0.2146	Yes
37	CD33	469	0.188	0.2185	Yes

38	TLR4	494	0.185	0.2201	Yes
39	MALL	521	0.181	0.2213	Yes
40	ZYX	526	0.181	0.2257	Yes
41	TRIP6	530	0.18	0.2303	Yes
42	TNFRSF1A	535	0.18	0.2346	Yes
43	CCR3	538	0.18	0.2393	Yes
44	SLC25A13	539	0.18	0.2443	Yes
45	BCAR1	546	0.179	0.2483	Yes
46	EFNA4	600	0.172	0.2454	Yes
47	TRIM27	603	0.172	0.2498	Yes
48	TACSTD2	617	0.17	0.2526	Yes
49	IL27RA	634	0.169	0.255	Yes
50	ACVR1B	644	0.168	0.2583	Yes
51	CD97	675	0.164	0.2584	Yes
52	EPHA2	698	0.162	0.2597	Yes
53	PRNP	718	0.16	0.2613	Yes
54	SLC7A2	721	0.16	0.2655	Yes
55	ATP6V0A4	745	0.158	0.2665	Yes
56	TRPM2	769	0.156	0.2674	Yes
57	CXCR4	793	0.153	0.2683	Yes
58	ADORA2B	819	0.151	0.2688	Yes
59	VIPR1	864	0.148	0.2665	Yes
60	GPR35	886	0.146	0.2675	Yes
61	SLC19A1	912	0.144	0.2678	Yes
62	NTSR1	913	0.144	0.2718	Yes
63	PDZD2	916	0.144	0.2755	Yes
64	SLC2A8	930	0.143	0.2775	Yes
65	IFNGR2	931	0.143	0.2815	Yes
66	P2RY2	937	0.143	0.2847	Yes
67	IL28RA	940	0.143	0.2884	Yes
68	LAT2	949	0.142	0.2911	Yes
69	ORAI1	953	0.142	0.2946	Yes
70	CTLA4	958	0.141	0.2979	Yes
71	DCBLD2	959	0.141	0.3018	Yes
72	EFNA1	985	0.139	0.302	Yes
73	ROR2	987	0.139	0.3057	Yes
74	CCRL2	993	0.138	0.3087	Yes
75	ABCA1	1027	0.136	0.3077	Yes
76	SLC7A7	1040	0.135	0.3097	Yes
77	BST2	1047	0.134	0.3125	Yes

78	CD83	1053	0.134	0.3155	Yes
79	IL2RB	1061	0.133	0.3181	Yes
80	MC1R	1068	0.133	0.3209	Yes
81	GZMA	1069	0.133	0.3246	Yes
82	CAV1	1076	0.133	0.3274	Yes
83	STOM	1105	0.131	0.3269	Yes
84	SYTL2	1116	0.13	0.3291	Yes
85	SLMAP	1118	0.13	0.3325	Yes
86	AXIN1	1126	0.13	0.3351	Yes
87	IL4R	1132	0.13	0.3379	Yes
88	VCL	1161	0.128	0.3374	Yes
89	TM4SF5	1193	0.126	0.3363	Yes
90	PAG1	1199	0.125	0.3391	Yes
91	LCK	1272	0.12	0.3319	Yes
92	CLDN3	1273	0.12	0.3352	Yes
93	ITGB7	1285	0.119	0.3369	Yes
94	CLDN23	1350	0.116	0.3308	Yes
95	KCNK1	1362	0.115	0.3324	Yes
96	SORBS1	1364	0.115	0.3354	Yes
97	LDLR	1376	0.115	0.337	Yes
98	SLC46A1	1378	0.114	0.34	Yes
99	BTN2A1	1388	0.114	0.3418	Yes
100	PSMG1	1395	0.114	0.3441	Yes
101	LYN	1399	0.114	0.3468	Yes
102	SLC4A11	1466	0.11	0.3402	Yes
103	CXADR	1489	0.109	0.34	Yes
104	LAPTM5	1496	0.109	0.3421	Yes
105	LYPD3	1505	0.108	0.3439	Yes
106	ABCB4	1519	0.107	0.345	Yes
107	ARRB1	1608	0.103	0.335	Yes
108	CD52	1609	0.103	0.3378	Yes
109	CAPRIN1	1617	0.102	0.3397	Yes
110	STX4	1620	0.102	0.3422	Yes
111	CLDN11	1638	0.101	0.3425	Yes
112	ERBB3	1671	0.1	0.3406	Yes
113	NCSTN	1677	0.1	0.3426	Yes
114	MAEA	1681	0.1	0.3449	Yes
115	LAMB1	1691	0.099	0.3464	Yes
116	OXTR	1697	0.099	0.3484	Yes
117	PTPRJ	1708	0.098	0.3496	Yes

118	KL	1732	0.098	0.349	Yes
119	TMEM11	1750	0.097	0.3492	Yes
120	PODXL2	1754	0.097	0.3514	Yes
121	SLC16A3	1764	0.097	0.3527	Yes

Chapter 3

Discussion

Cnot1 was identified as a candidate CRC cancer gene in multiple *Sleeping Beauty*-based screens. In addition, a high incidence of *CNOT1* somatic mutations in CRC has been documented by several projects including the COSMIC database (http://cancer.sanger.ac.uk/cancergenome/projects/cosmic/), TCGA (Cancer Genome Atlas Network, 2012) and, Seshagiri *et al*., 2012, providing evidence for a correlation between genetic alterations in *CNOT1* and CRC. To determine the contribution of genetic alterations in *CNOT1* to CRC we evaluated cell viability in *CNOT1*-depleted SW480 CRC cell line and the non-cancerous HEK293 cell line. Depletion of *CNOT1* resulted in a dramatic decrease in cell viability in both cell lines (Figure 17), and increased cell apoptosis in SW480 cells (Figure 18), suggesting that *CNOT1* might act as an oncogene.

In support of this role, CNOT1 limits expression of *TXNIP* which has been identified as a tumor suppressor in several cancers, including colorectal cancer. The enforced expression of *TXNIP* inhibits proliferation of cancer cells and suppresses tumor growth and metastasis in transplantation models (Han *et al*., 2003， Wang *et al*., 2002， Goldberg *et al*., 2003). In addition, activation of TXNIP initiates apoptotic pathways under some cell stress conditions, including extreme ER stress through multiple mechanisms including activation of ASK1-induced apoptotic pathways and maturation of IL-1β (Tobiume *et al*., 2001, Zhou, *et al*., 2010). Two results suggest that CNOT1 may protect cell viability by means of limiting *TXNIP* levels. First, in HEK293 cells depletion of *CNOT1* leads to increased *TXNIP* levels, while overexpression of *TXNIP* leads to decreased cell viability. Second, in *CNOT1*-depleted SW480 cells, upregulation of *TXNIP* precedes increased apoptosis and decreased cell viability (Table 3).

Our data argue that CNOT1 limits TXNIP expression by facilitating post-transcriptional degradation as we found that *TXNIP* mRNA transcripts were significantly stabilized after *CNOT1* knockdown. CNOT1-mediated destabilization likely involves

CNOT8-mediated deadenylation as depletion of *CNOT8* caused decreased cell viability and increased expression of *TXNIP* (Figure 24E). *TXNIP* mRNA levels are limited by *miR-17* in pancreatic beta cells. We have found that *miR-17* regulates *TXNIP* levels in SW480 and HEK293 cells as well. Given that CNOT1 binds GW182 and acts as an adapter between the miRNA RISC complex and CCR4-NOT deadenylase subunits, this result suggests that CNOT1 may limit *TXNIP* expression by facilitating *miR-17*-mediated *TXNIP* mRNA degradation.

TXNIP mRNA levels are upregulated in response to extreme ER stress. Increased TXNIP activity can, in turn, initiate pro-apoptotic signaling pathways. Upregulation of TXNIP following depletion of *CNOT1* suggests that CNOT1 may be involved in the unfolded protein response to ER stress as well. In support of this idea depletion of *CNOT1* in SW480 cells results in upregulated transcripts of genes involved in all three UPR pathways such as *sXBP1* (IRE1α pathway), *PERK*, *ATF4* and *DDIT3* (PERK pathway), and *ATF6*, *XBP1* (ATF6 pathway) (Figure 30A) (see Figure 16 in introduction describing the three UPR pathways). It is important to note that only changes in mRNA transcripts levels of these genes were examined. To gain a full picture of the effect of *CNOT1* depletion on these pathways we will need to examine translational and post-translational regulation.

Moreover, the disrupted deadenylation function of the CNOT complex can cause upregulated mRNA levels of a large group of genes (Aslam *et al*., 2009). When these mRNAs are translated in the ER, it may cause overproduction of proteins in the ER, inducing ER stress and activation of UPR pathways. This is supported by an Ito *et al* study showing that depletion of *CNOT1* in Hela cells can cause ER stress and activation of UPR pathways (Ito *et al*., 2011). We examined global gene expression in *CNOT1*-depleted SW480 cells using a microarray assay. 266 genes showed a significant alteration in mRNA expression levels and 2/3 of them were upregulated, consistent with the idea that CNOT1-mediated degradation plays a major role in these cells and that *CNOT1* depletion could result in an enlarged mRNA pool. In support of this idea, GSEA comparison of microarray data with the Molecular Signatures Database geneset collection

of cellular components (MsigDB C5 CC, http://www.broadinstitute.org/gsea/msigdb/collections.jsp#C5) revealed that four of the five most enriched genesets consisted of plasma membrane localized components and thus transcripts that would be translated and processed in the ER (Figure 31B, Table 7), suggesting that CNOT1 may help in limiting protein production in the ER.

Under moderate ER stress the only known target of IRE1 alpha RNase activity is the *XBP1* transcript. However, under extreme ER stress IRE1 alpha RNase becomes less specific. This is thought to lead to degradation of *miR-17* and thus upregulation of *TXNIP* (see introduction for details). In addition, under extreme stress IRE1 alpha RNase activity degrades a pool of RNAs in a process known as Regulated IRE1 alpha Dependent Decay (RIDD). Decay of these mRNAs is a well-characterized part of the terminal UPR. GSEA of global gene expression changes revealed that transcripts downregulated in *CNOT1*-depleted SW480 cells were enriched in genes downregulated in response to extreme ER stress (RIDD genes), suggesting that downregulation of *CNOT1* promotes RIDD and therefore *CNOT1* expression is protective against terminal UPR (Figure 31A, Table 6).

Based on these studies we will determine if CNOT1 is required for *miR-17*-mediated degradation by determining if depletion of *CNOT1* can ablate the effect of overexpression of *miR-17*.

In sum, these results suggest a model in which CNOT1 protects cell viability by protecting cells against ER stress by raising the bar for activation of the apoptotic UPR pathways both by limiting *TXNIP* expression and possibly by regulating expression of other pools of mRNAs. Cancer cells are commonly subject to increased levels of ER stress. Thus increased CNOT1 activity may provide a selective advantage to cancer cells by making it more difficult to activate the UPR apoptotic pathway under high stress conditions, such as severe ER stress. Thus, this model suggests a mechanism by which *CNOT1* may act as an oncogene.

Although our data are supportive of this model, several key experiments remain to be done to fill the gaps. (1) To determine if increased TXNIP activity contributes to

increased apoptosis in *CNOT1*-depleted cells we will need to examine the effect of co-depletion of *CNOT1* and *TXNIP* on cell viability and apoptosis. If *CNOT1*-depletion promotes apoptosis by increasing TXNIP activity, then apoptosis will be reduced when *TXNIP* is depleted together with *CNOT1* depletion. (2) Several experiments will be conducted to further investigate the mechanism of CNOT1-mediated destabilization of *TXNIP* mRNA transcripts. mRNA stability is commonly regulated through interactions of complexes containing 3'UTR binding factors, adapters and deadenylases with the 3'UTR region of the target mRNA transcript. To determine if CNOT1 regulates *TXNIP* mRNA stability through the *TXNIP* 3'UTR we will examine the effect of *CNOT1* depletion on expression of a luciferase reporter construct containing the 3'UTR of *TXNIP*. To determine if *miR-17*-mediated regulation of *TXNIP* involves CNOT1 we will co-transfect SW480 cells with both *miR-17* mimics and *CNOT1* siRNA to investigate whether depletion of *CNOT1* reduces the effect of overexpression of *miR-17* on *TXNIP* mRNA levels. (3) Finally to determine if CNOT1 is protective against severe ER stress we will look at the response to induction of ER stress on cells depleted for or overexpressing *CNOT1* to determine if *CNOT1* depletion results in increased cell death and overexpression is protective and improving cell viability under severe ER stress.

Although these *in vitro* studies point to a role for *CNOT1* as an oncogene in CRC, the actual role in *in vivo* cancers is likely to be more complex. As the scaffold for the CCR4-NOT complex CNOT1 is likely involved in most or all functions of the complex in addition to deadenylation, such as transcriptional regulation, chromatin modification and ubiquitin-mediated proteolysis (Bartlam *et al*., 2010). In addition, as an adapter mediating mRNA degradation by several 3'UTR binding factors, including miRNAs and RNA binding proteins, CNOT1 can potentially influence expression of a large group of genes, which is supported by the microarray data. Therefore, the roles of CNOT1 in CRC are likely to depend on the context of a specific tumor, including other genetic alterations, stage of tumor development and interactions between the cancer and its microenvironment.

Our data suggest that CNOT1 interaction with additional CNOT subunits also plays a role in regulating *TXNIP* levels. The shortest isoform of CNOT1, CNOT1S, lacks a NOT domain that is important for interaction with CNOT 2, CNOT3 and CNOT5 (Boland *et al*., 2013). Unlike the long isoform of CNOT1 (CNOT1L) overexpression of *CNOT1S* results in increased expression of *TXNIP* mRNA levels, suggesting that one or more of these subunits may also be important to *TXNIP* regulation by CNOT1.

In addition, depletion of *CNOT 6L* and *7* results in decreased cell viability but little or no increase in *TXNIP* levels, indicating that the CNOT complex can support cell viability by mechanisms other than *TXNIP* regulation.

Finally, in *SB* screens insertions into *CNOT1* are found in both orientations (Figure 11). This pattern is often associated with inactivation of a tumor suppressor gene. However, it could indicate that either activation or inactivation of a specific gene could contribute to development of CRC depending on site of insertion and the context of other genetic alterations. Two pieces of data from our work suggest that this might be the case. First, overexpression of *CNOT1S* has the opposite effect as overexpression of *CNOT1L* (Figure 24C), suggesting that the specific domains affected by a genetic alteration will influence the effect of CNOT1 on gene regulation. Second, analysis of human CRC liver metastases reveals both CNOT1 high expressers and CNOT1 low expressers, with different gene expression profiles (Figure 21), suggesting that genetic context will influence which alterations in *CNOT1* provide selective advantage to cancer cells.

Together, although our *in vitro* studies suggest a role for *CNOT1* as an oncogene in CRC through protecting cells from severe ER stress-induced cell apoptosis via limiting *TXNIP* levels and limiting mRNA transcripts to be translated in the ER, we should note that CNOT1 might contribute to CRC through additional mechanisms. The following experiments are designed to further investigate the role of genetic alteration in *CNOT1* in CRC. (1) Perform *in vivo* studies in a mouse model carrying a conditional knockout allele of *CNOT1* in wildtype or Apc^{Min} backgrounds to investigate the effect of *CNOT1* deficiency on intestinal tumor phenotypes. (2) Evaluate the effect of somatic mutations in *CNOT1* on oncogenic phenotypes, assembly of the CNOT complex and deadenylation of

target mRNA transcripts in *in vitro* studies. Furthermore, we may carry out *in vivo* studies by producing transgenic mice bearing the *CNOT1* mutations which show strong phenotypes in cell line based studies. (3) Evaluate the role of *CNOT1* in maintenance of colonic epithelial stem cells. The CNOT complex has been reported to influence other aspects of cancer development. For example, Cnot1, Cnot2 and Cnot3 were reported to play critical roles in maintaining mouse and human embryonic stem cell (ESC) identity and inhibiting ESC differentiation into the extraembryonic lineages via repressing the expression of early trophectoderm transcription factors such as *Cdx2* (Zheng *et al*., 2012). CRC is thought to arise from stem cells that lie in the base of colonic crypts. Factors that affect normal stem cell activity also affect development of cancer stem cells so that the role of *CNOT1* and other members of the CCR4-NOT complex in ES cells may also reflect a role in CRC. In particular, the unfolded protein response is required for differentiation of progenitor cells from stem cells in the normal colon epithelium (Heijmans *et al*., 2013), suggesting that factors that limit the unfolded protein response may support stem cell activity. Organoid culture can be used to model stem cell activity and study differentiation of colonic crypts. Therefore we will investigate the role of *CNOT1* and the CNOT complex in stem cell activity using this system.

Chapter 4

Material and Methods

Reagents

Tunicamycin and Actinomycin D were obtained from Sigma Aldrich (St. Louis, MO, USA). Stocks were prepared in DMSO at 1mg/ml and stored at -20˚C. Dimethyl sulfoxide (DMSO), Dithiothreitol (DTT) and β-Mercaptoethanol (β-ME) were purchased from Sigma Chemical Co. (St. Louis, MO, USA). RNasin was obtained from Promega (Madison, WI, USA).

Cell Culture

SW480 and HEK 293 cells were purchased from American Type Culture Collection (ATCC). Cells were maintained in DMEM supplemented with 10% FBS, 2 mmol/L glutamine, and incubated in a humidified atmosphere of 95% air and 5% CO_2 at 37°C.

RNA Isolation

RNA isolation from cell culture. Total RNA was extracted from cell cultures using an RNeasy kit (Qiagen) according to manufacturer's directions for isolation of cytoplasmic RNA with an added DNA digestion step. Cells growing in a monolayer on culture dishes were harvested using Trypsin-EDTA 0.25% at 37°C and centrifuged at 300 x g for 3 minutes. The plasma membrane was lysed by addition of 175 µl ice cold RLN buffer (50 mM Tris-HCl pH 8.0, 140 mM NaCl, 1.5 mM $MgCl_2$, 0.5% (v/v) NP-40, DEPC H2O) supplemented with 1000 U/ml RNasin and 1 mM DTT on ice for 5 minutes. Lysate was centrifuged at 300 x g for 2 minutes at 4˚C to remove nuclei and debris, followed by addition of RLT (guanidine thiocyanate) buffer supplemented with 10 U/ml β-mercaptoethanol and 100% ethanol. Sample was applied to column and washed with RW1 buffer. DNase digestion was carried by incubation with 240 unit of RNase free

DNase (Qiagen) for 15 minutes at room temperature. After washes with RPE buffer, RNA was eluted with 30 µl elution buffer. RNA was stored at -80°C.

RNA isolation from human fresh frozen tissue. Samples obtained during resection of human CRC liver metastases or CRC were flash frozen in liquid nitrogen and processed by the University of Minnesota Biological Procurement Network (BioNet). Total RNA was isolated from 20 fresh frozen CRC liver metastasis samples and 5 fresh frozen normal colon tissues. Tissues were transferred from liquid nitrogen to precooled RNAlater-ICE (Ambion, Foster City, CA, USA) at -80°C for 30 minutes followed by transfer to -20°C for at least 48 hours to inactivate endogenous RNase activities. Immediately before RNA isolation, tissue in RNAlaterICE was placed in 3 ml of RLT buffer supplemented with β-mercaptoethanol at 10 µl/ml. The tissue was then homogenized using an IKA ultra-Turrax T25 digital homogenizer (Fisher Scientific, Waltham, MA, USA). Tissue lysates were centrifuged at 300 x g for 5 minutes and supernatants were transferred to new 1.5 ml tubes. RNA isolation was then conducted using an RNeasy Mini Kit (Qiagen) following the manufacturer's directions with an added DNase digestion step starting after the RLT addition step. RNA was stored at -80°C.

Plasmid Construction

Plasmids encoding various open reading frames were obtained from Open Biosystems (Thermo Scientific).

To construct a plasmid expressing the short form of CNOT1 (encoded by NM_206999.2) Open Biosystems clone #5266600 encoding *CNOT1S* ORF (BC040523) in a pBluescriptR vector was digested with Not1 and Apa1 and inserted between the corresponding restriction sites on a pcDNA3 vector (Life Technologies) to generate pcDNA3-CNOT1S. To construct a plasmid expressing the longest form of CNOT1 (CNOT1L) (encoded by NM_016284.4) pcDNA3-CNOT1S was combined with a fragment obtained from OpenBiosystems clone #3913601 encoding a partial *CNOT1L* ORF (BC0234317) in a pCMV-SPORT6 vector. To add the 3' region of *CNOT1L* to *CNOT1S* to generate a full length *CNOT1L* plasmid both plasmids were digested with

Cla1 and Apa1 and the Cla1-Apa1 fragment from the partial *CNOT1L* plasmid was inserted into the pcDNA3-CNOT1S plasmid. To construct a plasmid expressing *TXNIP* (NM_006472.4) Open Biosystems clone #7939547 encoding the *TXNIP* ORF (BC093702) in a pCR4-TOPO vector was digested with EcoR1 and inserted in the EcoR1 restriction sites of pcDNA3 vector to generate pcDNA3-TXNIP. Orientation was determined by Sanger sequencing. Plasmids were prepared using a QIAprep Spin Miniprep Kit (Qiagen) following the manufacturer's protocol.

DNA and RNA Quantification and Integrity Analysis

DNA and RNA quantity and purity was analyzed using a Nanodrop 2000 spectrophotometer (NanoDrop, ThermoScientific) to measure absorbance (A) at a range of concentrations. DNA concentration = A_{260} x 50 µg/µl. RNA concentration = A_{260} x 40 µg/µl. The ratio of the A_{260} nm/A_{280} nm values allows the assessment of nucleic acid purity. Pure preparations of DNA will have a 260/280 ratio > 1.8. RNA samples are considered to be pure if the absorbance ratio is close to 2.0. For Illumina gene expression array analysis and Illumina RNA sequence analysis, RNA integrity was assessed by capillary electrophoresis using an Agilent BioAnalyzer 2100 (Agilent Technologies). An RNA integrity number (RIN) was generated for each sample representing 28S/18S ribosomal RNA detection as well as other parameters. All the samples met the standard of quality with a RIN > 8.

qRT-PCR

cDNA synthesis. For each experimental sample 1.5 µg RNA was converted to cDNA with random nonomer primers (IDT) and recombinant Omniscript Reverse Transcriptase using the Omniscript RT kit (Qiagen) according to manufacturer's instructions. Each reaction consisted of 2 µl of 10 X RT buffer, 2 µl of 50 mM dNTPs, 4 µl of random nonomer primers, 0.25 µl of RNasin RNase inhibitor (Promega) and 1 µl of Omniscript Reverse Transcriptase, 1.5 µg RNA and H2O sufficient for final volume of 20 µl. Reactions were incubated at 65°C for 60 minutes, 72°C for 10 minutes, 85°C for 5 minutes. cDNA was stored at -20°C until needed.

qPCR. Target cDNAs and 18S ribosomal DNA were amplified from cDNA by PCR. Real-time PCR reactions were carried out in 10 µl using 2 µl cDNA from a 10 X dilution of the 20 µl RT reaction (equivalent to 15 ng reverse transcribed RNA) for target genes and a 100 X dilution for 18S rRNA, 500 nM each primer, 5 µl LightCycler480 SYBR Green 1 Master Mix (Roche Applied Science). PCRs were performed on a LightCycler® 480 System (Roche Diagnostics) in 96 well plates using the amplification protocol: 1 cycle of preincubation, 5 minutes at 95°C; 45 cycles of amplification each consisting of denaturation at 95°C for 5 seconds, annealing at 60°C for 5 seconds and elongation at 72°C for 10 seconds; 1 cycle melting at 95°C for 5 seconds, 65°C for 1 minutes, heating to 97°C; 1 cycle cooling at 40°C for 30 seconds. Water was used as a template for negative control amplifications for each PCR run. All reactions were performed in duplicate. Standards were generated by reverse transcription of total RNA from untreated cells followed by PCR amplification to generate template DNA of the same sequence as target genes or 18S gene PCR product. Serial dilutions of template DNA were amplified in parallel with experimental samples and used to generate a standard curve for each gene. Data were analyzed using Roche LightCycler® 480 software and CP's calculated using the Absolute Quantification-Second Derivative Maximum method. The standard curve was used to determine efficiency of PCR amplification (E) for each gene. "Relative mRNA levels" represent the relative expression of a target gene in corresponding siRNA-treated cells to expression in control siRNA-treated cells. Target gene expression was normalized to 18S rRNA levels and relative mRNA levels were calcµlated as described by Pfaffl (Pfaffl M.W., 2001): relative mRNA levels = $([E_{target}]^{\Delta CPtarget(control-treated)})/([E_{ref}]^{\Delta CPref(control-treated)})$. Primers used in RT-PCR are shown below (Table 8).

Table 8. Primers used in qRT-PCR.

Gene	Forward primer	Reverse primer
18s	CGCCGCTAGAGGTGAAATTCTT	CAGTCGGCATCGTTTATGGTC
AFT6	ATGTCTCCCCTTTCCTTATATGGT	AAGGCTTGGGCTGAATTGAA
ATF4	CCACCATGGCGTATTAGGGG	TGCTGAATGCCGTGAGAAGC
BTG1	TCTCCAAGTTTCTCCGCACC	GGTAACCCGATCCCTTGCAT

CDX2	ACTACAGTCGCTACATCACCA	GAAGACACCGGACTCAAGGG
CHOP	GGTGGCAGCGACAGAGCCAAA	ACTCAGCTGCCATCTCTGCAGTT
CNOT1	CTTTCA ACCCCCAATCAGACC	AGGTTTCATCTTACTCTGCTGGA
CNOT1 long	GAGGCCTACCAAAGCTCCTG	TGTGCATACATAGGCCACCC
CNOT1 total	TCCCTGCAGTGAATAACGACC	CCACACCTGAGACAAGTCCG
CNOT2	CTTAACGAACATTCACATTAGGGATA	CTTCACCATATCGGCCAAGT
CNOT6	GTGGCCTGATGCCTTACACGAA	CCAGAGGGCCCAGGATGCCTA
CNOT6L	AGCAGAGGAGGTAGCCAATGGGA	AGGTGCAGCGCTGTCAAGTGT
CNOT7	CCCTCACTATGCCAGCGGCAA	ACCACACCTGGAAACTCGGTGTC
CNOT8	GGGCCTGCGCTTACCGGAAA	TCCACAAGTGCTGCAGGCATCC
CELF1	GCGCAGCATCTGTGTGGGGA	GGGTGGAGGCTGCTCAGGGT
DKK1	GGCGGGAATAAGTACCAGACC	CGAGACAGATTTGCACGCC
EMP1	ACCATGGAGAAGGGAAACCG	ATAGCCGTGGTGATACTGCG
GRP78/Bip	AAGCTGTAGCGTATGGTGCT	GTTTGGTCATGACACCTCCCA
HBP1	CGACCAGTCCACAAAGTCCA	GAGGGCGTGCATAGGAATGT
IGFBP3	TAAAGACAGCCAGCGCTACA	ATTTCTCTACGGCAGGGACC
IL8	TTTTGCCAAGGAGTGCTAAAGA	AACCCTCTGCACCCAGTTTTC
$p27^{kip}$	TAGCGGAGCAATGCGCAGGAA	ACCGGCATTTGGGGAACCGTC
PERK	ATGAGACAGAGTTGCGACCG	TGGATGACACCAAGGAACCG
PUM1	ACGGATTCGAGGCCACGTCC	TGGCCATCTAGTTCCCGAACCAT
PUM2	AGCTCTTGCATTAGAATCTCGGGGA	TGGTGAGAAGCTCCCCATGCAGT
sXBP1	CTGAGTCCGCAGCAGGTGC	TTGTCCAGAATGCCCAACAGG
TGFBR2	CCCCTGTGTCGAAAGCATGA	TCACACACCATCTGGATGCC
ZFP36	TCCCACTCTCGGCCGACACC	GATGGCACGGGCACGTCAGG
TXNIP	TCCCACTCTCGGCCGACACC	GATGGCACGGGCACGTCAGG
XBP1	GGGGAATGAAGTGAGGCCAG	TTGTCCAGAATGCCCAACAGG

Transfection Protocols

DNA plasmid transfection. HEK 293 cells were plated at 7.5 x 10^5 cells/dish into 6 cm dishes or 2 x 10^4 cells/well in 96 well plates. 24 hours later, cells were transfected with pcDNA3-CNOT1S, pcDNA3-CNOT1L, pcDNA3-TXNIP or a pcDNA3-GFP plasmid using Lipofectamine LTX with Plus reagent (Invitrogen) according to the manufacturer's protocol. For a 6 cm dish, 4 µg of plasmid was added to 4 µl PLUS reagent in 200 µl of OptiMEM. The plasmid solution was mixed with 12 µl Lipofectamine LTX reagent in 200 µl OptiMEM. The 400 µl reaction was then added to the cells.

siRNA transfection. SW480 cells and HEK 293 cells at 70% confluence were transfected twice, unless otherwise noted, 48 hours apart, with short interfering RNA oligonucleotides (siRNA oligos) targeting a specific gene or with a non-targeting control siRNA, at a final concentration of 50 nmol/L, using Lipofectamine 2000 transfection reagent (Life Technologies). Oligo targeting *CNOT1* was obtained from Dharmacon: *CNOT1* On-TARGETplus SMARTPool. Control siRNA oligo was also obtained from Dharmacon: OnTARGETplus Non-targeting siRNA # 3. siRNA oligos targeting other genes were obtained from Qiagen: Hs_*CDX2*_6_HP siRNA, Hs_*CNOT2*_10_HP siRNA, Hs_*CNOT6*_3_HP siRNA, Hs_*CNOT6L*_4_HP siRNA, Hs_*CNOT7*_4_HP siRNA, Hs_*CNOT8*_5_HP siRNA, Hs_*CELF1*_1_HP siRNA，Hs_*PUM1*_6_HP siRNA, Hs_*PUM2*_4_HP siRNA, Hs_*ZFP36*_6_HP siRNA, Hs_*TXNIP*_6_HP siRNA.

Transfection of *miR-17* mimic. SW480 cells and HEK 293 cells at 70% confluence were transfected once with an *miR-17* mimic (Qiagen, Syn-hsa-*miR-17*-5p miScript miRNA Mimic) or with a non-targeting control siRNA (Dharmacon, OnTARGETplus Non-targeting siRNA # 3) at a final concentration of 5 nmol/L, using Lipofectamine 2000 transfection reagent (Life Technologies).

Illumina Beadchip Microarray

SW480 cells were transfected twice, 48 hours apart, with *CNOT1* siRNA or with a non-targeting control siRNA. Three experiments were done to achieve three biological replicates for each treatment. Total RNA was extracted from cells as described. Six samples of total RNA, 2 μg per sample, were submitted to the University of Minnesota BioMedical Genomics Center for microarray analysis. All samples had RIN > 8. 1 ug of total RNA was converted to biotinylated, antisense cRNA using the Illumina TotalPrep-96 RNA Amplification Kit (Life Technologies), and 1500 ng of biotin-labeled cRNA was hybridized onto an Illumina HumanHT-12 v4 Expression BeadChip (Illumina). Hybridized Beadchips were scanned with an Illumina iScan scanner. Raw intensity data was extracted from iScan scan image files using GenomeStudio software (Illumina), $\log_2$ transformed, and normalized. Microarray raw data was analyzed by Dr. Ying Zhang at the University of Minnesota Supercomputing Institute using the R package: *lumi* and

limma according to the manufacturer's protocol. Differential gene expression between *CNOT1* siRNA and control siRNA transfected cells was assessed by a statistical linear model analysis using the bioconductor package *limma*, in which an empirical Bayes method was used to moderate the standard errors of the estimated log-fold changes of gene expression. The moderated *t*-statistic *p* values derived from the *limma* analysis were further adjusted for multiple testing by Benjamini and Hochberg's method to control false discovery rate (FDR).

Illumina RNA Sequencing

Total RNA isolated from fresh frozen human CRC liver metastasis and normal colon samples was sequenced by the University of Minnesota BioMedical Genomics Center (BMGC) using an Illumina Highseq 2000 sequencer (Illumina). 3 μg of each total RNA sample was sent to BMGC in a 96 well plate on dry ice. Samples were quantified using fluorimetry (RiboGreen assay) and RIN determined. For the library creation, total RNA was enriched for polyadenylated RNA using oligo-dT purification, and the enriched polyA(+) RNA was converted to cDNA through reverse transcription. The cDNA was then fragmented, blunt-ended, and ligated to indexed (barcoded) adaptors. The fragmented cDNA library was size selected for 190-210 base-pair fractions, and size distribution was validated using capillary electrophoresis. The cDNA fragments were quantified using a fluorimetry (PicoGreen). The indexed libraries were then normalized, pooled, clustered on a flow cell, and loaded onto the Illumina Highseq 2000 instrument for paired-end sequencing. The resulting reads were then subjected to further analysis. Gene expression levels were calculated as fragments per kilobase of exon per million fragments mapped (FPKM).

Global Gene Expression Analysis

Differential gene expression heatmap. Differentially expressed genes showing fold change ≥ 2 and p value < 0.05 were used to generate a heat map by unsupervised hierarchical clustering. Extent of differential expression is shown as Z-value.

Ingenuity Pathways Analysis (IPA). To identify the gene networks and cellular

pathways associated with *CNOT1* knockdown, the dataset consisting of 266 differentially expressed genes (fold change ≥ 2, $p < 0.05$, Table 4) identified by Illumina HumanHT-12 v4 Expression Beadchips analysis were used as input for network analysis using Ingenuity Pathway Analysis software (Ingenuity Systems, Redwood CA). For this type of analysis, differentially expressed genes, which interact with other molecules in the Ingenuity Knowledge Base are designated "Network Eligible" molecules. "Network eligible" molecules are combined into networks that maximize connections based on known biological attributes. Functional categories are assigned based on overlap with known function categories in Ingenuity Database. Networks are then scored based on the percent of dataset molecules they contain. The score is calculated using the Fishers Exact Test to determine the likelihood of the network containing a given number of Network Eligible molecules by chance. The score = -log (Fisher's Exact test result).

Gene Set Enrichment Analysis (GSEA). GSEA was performed using GSEA v.2.0, (Broad Institute, MIT http://www.broad.mit.edu/gsea/). To identify pathways altered in human liver CRC metastasis samples expressing high levels of *CNOT1* a complete ranked dataset was generated in which genes were ranked according to ratio of expression in *CNOT1* high expressing (CNOT1-Hi) to *CNOT1* low expressing (CNOT1-Lo) samples. The ranked dataset was compared to genesets derived from Merlos-Suárez *et al*. characterizing gene expression in sub-popμlations of the intestinal crypt epithelium (Merlos-Suárez *et al*., 2011). The complete group of genesets tested consisted of: ISC Signature (EphB2), Proliferation Signature, Late TA Signature and Lgr5-defined Signature. This dataset was also compared to genesets of candidate CRC cancer genes identified by *SB* screens. These genesets were derived from reports in Starr *et al*. papers (Starr *et al*., 2009, Starr *et al*., 2011, Starr T.K., unpublished reports of a p53 mutant screen) as well as a report from March *et al*. (March *et al*., 2011). To identify pathways altered in *CNOT1*-depleted SW480 cells a complete ranked dataset was generated in which genes were ranked according to ratio of expression in *CNOT1*-depleted to control treated cells. This dataset was compared to genesets characterizing gene expression in adaptive vs. terminal UPR. The complete group consisted of Han *et al*. paper supplemental table 1 (representing both adaptive and terminal responses) and

supplemental table 2 (representing the terminal response) (Han *et al*., 2009), and So *et al*. paper supplementary table 1 (So *et al*., 2012). This table was split into two genesets, one consisting of adaptive response genes activated by sXBP1 and a separate geneset consisting of RIDD genes. This dataset was also compared to the MSigDB C5 CC collection. In all the comparisons, normalized gene expression data was ranked using the Signal2Noise metric, which represents a Z value. An enrichment score (ES) was calculated that reflects the degree to which a geneset is overrepresented at the extremes (top or bottom) of the entire ranked differentially expressed geneset using a running-sum statistic. The statistical significance (nominal *p* value) of the ES was estimated by using an empirical phenotype-based permutation test procedure. GSEA was performed against 1000 random gene set permutations. The ES for each gene set was then normalized to account for the size of the set, yielding a normalized enrichment score (NES). The false positives were controlled by calculating the false discovery rate (FDR) corresponding to each NES, which is the estimated probability that a set with a given NES represents a false positive finding. The proportion of false positives was controlled for by calculating the false discovery rate (FDR) corresponding to each NES.

Assessment of Cell Function

Cell viability assay. Cell viability was determined using a 3-(4,5-dimethylthiazol-2-yl)-2,5 diphenyltetrazolium bromide (MTT) assay (Cell Viability Kit 1, Roche Applied Sciences) in which absorbance at 595 nm is proportional to viable cell number. Cells were plated into 96 well plates at indicated cell densities in triplicate in DMEM medium. At each time point 100 μl fresh media was added with 10 μl MTT reagent. After 4 hour incubation, 100 μl of lysis buffer was added. After overnight incubation, absorbance at 595 nm was read using a plate reader. Cell viability was determined on days 2-6 after the second siRNA transfection or 1-4 days after plasmids transfection unless otherwise indicated.

Apoptosis assay. Apoptosis was determined using an Annexin V fluorescein isothiocyanate (AV-FITC) and propidium iodide (PI) double staining flow cytometry assay. AV-FITC binds to phosphatidylserine which translocates to the outer layer of the

plasma membrane lipid bilayer during the early stages of apoptosis. PI is a vital stain, which can only enter the cell when the membrane loses integrity during late apoptosis and cell death. Thus AV-FITC- PI- staining identifies live healthy cells; AV-FITC+ PI- identifies early apoptotic cells; and AV-FITC+ PI+ identifies late apoptotic and dying cells. For this assay 1 X 10^6 cells were washed twice with cold PBS and resuspended in 400 µl of 1 X Annexin V binding buffer (10 mM HEPES, pH 7.4, 140 mM NaOH, 2.5 mM $CaCl_2$). Suspension was divided into 4 x 100 µl aliquots to be stained with: no dye, 5 µl of Annexin V–FITC, 5 µl of PI, and 5 µl of Annexin V–FITC plus 5 µl of PI, respectively. Cells were stained for 15 minutes at room temperature in the dark. Then, flow cytometric analysis was conducted using a Becton-Dickinson FACScan cytofluorometry (Becton-Dickinson) and data analysis were performed with FlowJo software (Tree Star, Inc.).

mRNA stability assay. SW480 cells were plated at 7.5 X 10^5/dish in 6 cm dishes and transfected once with *CNOT1* siRNA or with a non-targeting control siRNA. 48 hours after transfection, cells were treated with actinomycin D at 5 µg/ml final concentration and total RNA was extracted at indicated intervals from 0 to 120 minutes. *TXNIP* and *CNOT1* mRNA levels were then measured by qRT-PCR. Values represent mean ± SD of three independent experiments. The best-fit lines, determined by least-squares methods, are shown as dotted lines.

Analysis of unfolded protein response (UPR). Tunicamycin is a pharmacological agent which blocks the first step in the synthesis of N-linked glycoproteins and thus causes accumulation of unprocessed proteins in the ER and induction of the UPR. In order to study factors affecting the UPR, SW480 cells were treated with tunicamycin under conditions described in results.

Statistics

All data were analyzed by comparing means with Student's *t*-test or One-Way ANOVA method as indicated using SPSS (Version 19.0). Data is shown as mean ± SD and $p < 0.05$ is considered as statistically significant difference.

Bibliography

Adair-Kirk TL, AtkinsonJJ, GriffinGL, WatsonMA, KelleyDG, DeMello D, Senior RM, and Betsuyaku T. Distal airways in mice exposed to cigarette smoke: Nrf2-regulated genes are increased in Clara cells. *Am J Respir Cell MolBiol* 39: 400-411, 2008.

Akiva P, Toporik A, Edelheit S, Peretz Y, Diber A, Shemesh R, Novik A, Sorek R: Transcription-mediated gene fusion in the human genome. *Genome Res* 2006, 16:30-36.

Ammar,I., Gogol-Doring,A., Miskey,C., Chen,W., Cathomen,T., Izsvak,Z. and Ivics,Z. (2012) Retargeting transposon insertions by the adeno-associated virus Rep protein. *Nucleic Acids Res*., 40, 6693-6712.

Anderson AM, Staley JP. Long-distance splicing. *Proc Natl Acad Sci U S A*. 2008 May 13;105(19):6793-4.

André T, Boni C, Mounedji-Boudiaf L, *et al*. Multicenter International Study of Oxaliplatin/5-Fluorouracil/Leucovorin in the Adjuvant Treatment of Colon Cancer (MOSAIC) Investigators. Oxaliplatin, fluorouracil, and leucovorin as adjuvant treatment for colon cancer. *N Engl J Med*, 2004. 350 (23): p2343-51.

Angus-Hill ML, Elbert KM, Hidalgo J, Capecchi MR. T-cell factor 4 functions as a tumor suppressor whose disruption modulates colon cell proliferation and tumorigenesis. *Proc Natl Acad Sci U S A*. 2011 Mar 22;108(12):4914-9.

Artale S, Sartore-Bianchi A, Veronese SM, Gambi V, Sarnataro CS, Gambacorta M, *et al*. Mutations of *KRAS* and *BRAF* in primary and matched metastatic sites of colorectal cancer. *J Clin Oncol* 2008;26:4217-4219.

Aslam A, Mittal S, Koch F, Andrau JC, Winkler GS. The Ccr4-NOT deadenylase subunits CNOT7 and CNOT8 have overlapping roles and modulate cell proliferation. *Mol Biol Cell*. 2009 Sep; 20(17): 3840-50.

Asmann YW, Necela BM, Kalari KR, *et al*. Detection of redundant fusion transcripts as biomarkers or disease-specific therapeutic targets in breast cancer. *Cancer Res.* 2012 Apr 15;72(8):1921-8.

Baker SJ, Preisinger AC, Jessup JM, Paraskeva C, Markowitz S, *et al*. 1990. *p53* gene mutations occur incombination with 17p allelic deletions as late events in colorectal tumorigenesis. *Cancer Res*. 50:7717-22

Balatsos, N. A., Nilsson, P., Mazza, C., Cusack, S. & Virtanen, A. Inhibition of mRNA deadenylation by the nuclear cap binding complex (CBC). *J. Biol. Chem*. 281, 4517-4522 (2006).

Barreau C, Paillard L, Osborne HB. AU-rich elements and associated factors: are there unifying principles? *Nucleic Acids Res* 2006; 33:7138-50.

Bartel, D. P. MicroRNAs: target recognition and regulatory functions. *Cell* 136, 215-233 (2009).

Mark Bartlam and Tadashi Yamamoto. The structural basis for deadenylation by the CCR4-NOT complex. *Protein Cell* 2010, 1(5): 443-452.

Bass AJ, Lawrence MS, Brace LE, Ramos AH, Drier Y, *et al*. (2011) Genomic sequencing of colorectal adenocarcinomas identifies a recurrent *VTI1A-TCF7L2* fusion. *Nat Genet* 43: 964–968.

Beerenwinkel, N. *et al*. Genetic progression and the waiting time to cancer. *PLoS Comput. Biol*. 3, e225 (2007).

Belt EJT, Fijneman RJA, van den Berg EG, Bril H, Delis-van Diemen PM, Tijssen M, *et al*. Loss of lamin A/C expression in stage II and III colon cancer is associated with disease recurrence. *Eur J Cancer* 2011; 47: 1837–1845.

Benedix, F., Kube, R., Meyer, F., Schmidt, U., Gastinger, I., and Lippert, H. (2010). Comparison of 17,641 patients with right- and left-sided colon cancer: differences in epidemiology, perioperative course, histology, and survival. *Dis Colon Rectum* 53, 57-64.

Bergemann TL, Starr TK, Yu H, Steinbach M, Erdmann J, Chen Y, Cormier RT, Largaespada DA, Silverstein KA. New methods for finding common insertion sites and co-occurring common insertion sites in transposon- and virus-based genetic screens. *Nucleic acids research*. 40, 3822-3833 (2012).

Bertolotti, A., Zhang, Y., Hendershot, L., Harding, H. and Ron, D. (2000). Dynamic interaction of BiP and the ER stress transducers in the unfolded protein response. *Nature Cell Biol*. 2, 326-332.

Boivin GP, Washington K, Yang K, *et al*. (2003) Pathology of mouse models of intestinal cancer: Consensus report and recommendations. *Gastroenterology* 124:762-777.

Andreas Boland, Ying Chen, Tobias Raisch, Stefanie Jonas, DuyguKuzuoğlu-Öztürk, Lara Wohlbold, Oliver Weichenrieder, Elisa Izaurralde. Structure and assembly of the NOT module of the human CCR4-NOT complex. *nature structural & molecular biology* advance online publication Oct.13 2013.

Brady CA, Jiang D, Mello SS, *et al*. Distinct p53 transcriptional programs dictate acute DNA-damage responses and tumor suppression. *Cell* 145, 571–583.

Burger-van Paassen N, Loonen LM, Witte-Bouma J, Korteland-van Male AM, de Bruijn AC, van der Sluis M *et al*. Mucin Muc2 deficiency and weaning influences the expression of the innate defense genes *Reg3b, Reg3g* and *angiogenin-4*. *PLoS One* 2012; 7: e38798.

Randall W. Burt. Colon Cancer Screening. *GASTROENTEROLOGY* 2000;119:837-853.

Cadenas C, Franckenstein D, Schmidt M, *et al*. Role of thioredoxinreductase 1 and thioredoxin interacting protein in prognosis of breast cancer. *Breast Cancer Res* 12: R44, 2010.

Cadigan KM, Waterman ML. TCF/LEFs and Wnt signaling in the nucleus. *Cold Spring Harb Perspect Biol*. 2012 Nov 1;4(11).

Calfon M, Zeng H, Urano F, Till JH, Hubbard SR, Harding HP, Clark SG, Ron D. IRE1 couples endoplasmic reticulum load to secretory capacity by processing the *XBP-1* mRNA. *Nature*. 2002 Jan 3;415(6867):92-6.

Cancer Genome Atlas Network. Comprehensive molecular characterization of human colon and rectal cancer. *Nature*. 2012 Jul 18;487(7407):330-7.

Carin G. M. Zwartjes, Sandrine Jayne, Debbie L. C. van den Berg, and H. T. Marc Timmers. Repression of promoter activity by Cnot2, a subunit of the transcription regulatory Ccr4-Not Complex. *The Journal of Biological Chemistry*. (2004) 279, (12) 10848-10854.

Casimiro MC, Knollmann BC, Ebert SN, Vary Jr JC, Greene AE, Franz MR *et al*. Targeted disruption of the *Kcnq1* gene produces a mouse model of Jervell and Lange–Nielsen Syndrome. *Proc Natl Acad Sci USA* 2001; 98: 2526–2531.

Casimiro MC, Knollmann BC, Yamoah EN, Nie L, Vary Jr JC, Sirenko SG *et al*. Targeted point mutagenesis of mouse *Kcnq1*: phenotypic analysis of mice with point mutations that cause Romano–Ward syndrome in humans. *Genomics* 2004; 84: 555–564.

Chalhoub N, Baker SJ. 2009. PTEN and the PI3-kinase pathway in cancer. *Annu. Rev. Pathol. Mech. Dis*. 4:127-50.

de la Chapelle A: Genetic predisposition to colorectal cancer. *Nat Rev Cancer* 4:769-80, 2004.

Cheadle C, Fan J, Cho-Chung YS, Werner T, Ray J, Do L, Gorospe M, Becker KG. Control of gene expression during T cell activation: alternate regulation of mRNA transcription and mRNA stability. *BMC Genomics* 6, 75 (2005).

Chen C, Ito K, Takahashi A, Wang G, Suzuki T, Nakazawa T, Yamamoto T, Yokoyama K. Distinct expression patterns of the subunits of the CCR4-NOT deadenylase complex during neural development. *BiochemBiophys Res Commun*. 2011 Jul 29;411(2):360-4.

Chen, C.Y., Zheng, D., Xia, Z., and Shyu, A.B. (2009). Ago-TNRC6 triggers microRNA-mediated decay by promoting two deadenylation steps. *Nat. Struct. Mol. Biol*. 16, 1160-1166.

Chen KS and DeLuca HF. Cloning of the human 1 alpha, 25-dihydroxyvitamin D-3 24-hydroxylase gene promoter and identification of two vitamin D-responsive elements. *BiochimBiophysActa* 1263: 1-9, 1995.

Cheng H, Leblond CP. Origin, differentiation and renewal of the four main epithelial cell types in the mouse small intestine V. Unitarian theory of the origin of the four epithelial cell types. *Am J Anat*. 1974 Dec; 141(4):537-61.

Cho NL, Javid SH, Carothers AM, Redston M, Bertagnolli MM. Estrogen receptors alpha and beta are inhibitory modifiers of Apc-dependent tumorigenesis in the proximal colon of Min/+ mice. *Cancer Res*. 2007;67:2366–2372.

Chu D, Zhang Z, Zhou Y, Wang W, Li Y, *et al*. (2011) Notch1 and Notch2 have opposite prognostic effects on patients with colorectal cancer. *Annals of oncology: official journal of the European Society for Medical Oncology/ESMO* 22: 2440–2447.

Church GM (January 2006). "Genomes for all". *Sci. Am*. 294 (1): 46–54.

Cleveland AG, Oikarinen SI, Bynoté KK, Marttinen M, Rafter JJ, Gustafsson JA, Roy SK, Pitot HC, Korach KS, Lubahn DB, Mutanen M, Gould KA. Disruption of estrogen receptor signaling enhances intestinal neoplasia in *Apc*$^{(Min/+)}$ mice. *Carcinogenesis*. 2009;30:1581–1590.

Clevers, H. Wnt/beta-Catenin signaling in development and disease. *Cell* 127, 469–480 (2006).

Hans Clevers. The intestinal crypt, a prototype stem cell compartment. *Cell*. 2013 Jul 18; 154(2):274-84.

Cloonan N, Forrest AR, Kolle G, *et al*. Stem cell transcriptome profiling via massive-scale mRNA sequencing. *Nature Methods*. 2008;5:613–619.

Coller, J. M.; Gray, N. K.; Wickens, M. P. (1998). "mRNA stabilization by poly(A) binding protein is independent of poly(A) and requires translation". *Genes & Development* 12 (20): 3226-35.

Collart, M.A. and Timmers, H.T. The eukaryotic Ccr4-notcomplex: A regulatory platform integrating mRNA metabolismwith cellular signaling pathways? *Prog. Nucleic Acid Res*. *Mol. Biol*. 2004, 77: 289-322.

Collart, M.A., Panasenko, O.O. The Ccr4-Not complex. *Gene* 492, 42-53 (2012).

Collier LS, Carlson CM, Ravimohan S, Dupuy AJ, Largaespada DA. Cancer gene discovery using *Sleeping Beauty* transposon-based somatic mutagenesis in the mouse. *Nature*. 2005; 436:272–276.

Cooke, A., Prigge, A. &Wickens, M. Translational repression by deadenylases. *J. Biol. Chem*. 285, 28506-28513 (2010).

Cormier RT, Hong KH, Halberg RB, *et al*. Secretory phospholipase Pla2g2a confers resistance to intestinal tumorigenesis. *Nat Genet*. 1997;17:88–91.

Crosnier C, Stamataki D, Lewis J. Organizing cell renewal in the intestine: stem cells, signals and combinatorial control. *Nat Rev Genet*. 2006 May;7(5):349-59.

Cully M, You H, Levine AJ, Mak TW. Beyond PTEN mutations: the PI3K pathway as an integrator of multiple inputs during tumorigenesis. *Nat Rev Cancer*. 2006;6:184-92.

De Lisle RC, Mueller R, Boyd M. Impaired mucosal barrier function in the small intestine of the cystic fibrosis mouse. *J Pediatr Gastroenterol Nutr* 2011; 53: 371–379.

Dean JL, Sully G, Clark AR, Saklatvala J. The involvement of AU-rich element-binding proteins in p38 mitogen-activated protein kinase pathway-mediated mRNA stabilization. *Cell Signal* 2004; 16:1113-21.

DeBerardinis RJ, Lum JJ, Hatzivassiliou G, Thompson CB. The biology of cancer: metabolic reprogramming fuels cell growth and proliferation. *Cell Metab* 2008; 7: 11–20.

Decker, C.J. and Parker, R. 1993. A turnover pathway for both stable and unstable mRNAs in yeast. *Genes & Dev*. 7: 1632-1643.

Dedek K, Waldegger S. Colocalization of KCNQ1/KCNE channel subunits in the mouse gastrointestinal tract. *Pflugers Arch* 2001; 442: 896–902.

Deininger, M., Buchdunger, E., and Druker, B. J. (2005). The development of imatinib as a therapeutic agent for chronic myeloid leukemia. *Blood* 105, 2640–2653.

Demolombe S, Franco D, de Boer P, Kuperschmidt S, Roden D, Pereon Y *et al*. Differential expression of KvLQT1 and its regulator IsK in mouse epithelia. *Am J Physiol Cell Physiol* 2001; 280: C359–C372.

Derks S, Postma C, Carvalho B, *et al*. (2008) Integrated analysis of chromosomal, microsatellite and epigenetic instability in colorectal cancer identifies specific associations between promoter methylation of pivotal tumour suppressor and DNA repair genes and specific chromosomal alterations. *Carcinogenesis*. 29:434–439.

R. Derynck, Y.E. Zhang. Smad-dependent and Smad-independent pathways in TGF-beta family signaling. *Nature*, 425 (2003), pp. 577-584.

Dews M, Fox JL, Hultine S, Sundaram P, Wang W, Liu YY, Furth E, Enders GH, El-Deiry W, Schelter JM, Cleary MA, Thomas-Tikhonenko A. The myc-*miR-17*~92 axis blunts TGF{beta} signaling and production of multiple TGF{beta}-dependent antiangiogenic factors. *Cancer Res*. 2010 Oct 15;70(20):8233-46.

Dietrich WF, Lander ES, Smith JS, *et al*. (1993) Genetic identification of Mom-1, a major modifier locus affecting Min-induced intestinal neoplasia in the mouse. *Cell* 75:631–639.

Ding L, Getz G, Wheeler DA, Mardis ER, McLellan MD, *et al*. (2008) Somatic mutations affect key pathways in lung adenocarcinoma. *Nature* 455: 1069-1075.

Doak TG, Doerder FP, Jahn CL, Herrick G. "A proposed superfamily of transposase genes: transposon-like elements in ciliated protozoa and a common "D35E" motif". *Proc. Natl. Acad. Sci. U.S.A*. 1994 Feb, 1;91(3):942-6.

Duerkop BA, Vaishnava S, Hooper LV. Immune responses to the microbiota at the intestinal mucosal surface. *Immunity* 2009; 31: 368–376.

Dupuy AJ, Rogers LM, Kim J, Nannapaneni K, Starr TK, *et al*. (2009) A modified *sleeping beauty* transposon system that can be used to model a wide variety of human cancers in mice. *Cancer Res* 69: 8150-8156.

Dutta KK, Nishinaka Y, Masutani H, Akatsuka S, Aung TT, Shirase T, Lee WH, Yamada Y, Hiai H, Yodoi J, and Toyokuni S. Two distinct mechanisms for loss of thioredoxin-binding protein-2 in oxidative stress-induced renal carcinogenesis. *Lab Invest* 85: 798-807, 2005.

Dziarski R, Gupta D. Review: mammalian peptidoglycan recognition proteins (PGRPs) in innate immunity. *Innate Immun* 2010; 16: 168–174.

Edge *et al*. (2009) American Joint Committee on Cancer: AJCC Cancer Staging Manual, 7th edn (New York, Springer).

Edgren H, Murumagi A, Kangaspeska S, *et al*. Identification of fusion genes in breast cancer by paired-end RNA-sequencing. *Genome Biol.* 2011;12(1):R6.

el Marjou F, Janssen KP, Chang BH, Li M, Hindie V, Chan L, Louvard D, Chambon P, Metzger D, Robine S. Tissue-specific and inducible Cre-mediated recombination in the gut epithelium. *Genesis*. 2004;39:186–193.

Elso CM, Lu X, Culiat CT, Rutledge JC, Cacheiro NL, Generoso WM *et al*. Heightened susceptibility to chronic gastritis, hyperplasia and metaplasia in *Kcnq1* mutant mice. *Hum Mol Genet* 2004; 13: 2813–2821.

Espinoza I, Pochampally R, Xing F, Watabe K, Miele L. Notch signaling: targeting cancer stem cells and epithelial-to-mesenchymal transition. *Onco Targets Ther*. 2013 Sep 6;6:1249-1259.

Eulalio, A., Tritschler, F. &Izaurralde, E. The GW182 protein family in animal cells: new insights into domains required for miRNA-mediated gene silencing. *RNA* 15, 1433-1442 (2009).

Fabian MR, Mathonnet G, Sundermeier T, Mathys H, Zipprich JT, Svitkin YV, *et al*. Mammalian miRNA RISC recruits CAF1 and PABP to affect PABP-dependent deadenylation. *Mol Cell* 2009; 35:868-80; PMID: 19716330.

Fabian MR, Cieplak MK, Frank F, Morita M, Green J, Srikumar T, Nagar B, Yamamoto T, Raught B, Duchaine TF, Sonenberg N. miRNA-mediated deadenylation is orchestrated by GW182 through two conserved motifs that interact with CCR4-NOT. *Nat Struct Mol Biol*. 2011 Oct 7;18(11):1211-7.

Fabian MR, Frank F, Rouya C, Siddiqui N, Lai WS, Karetnikov A, Blackshear PJ, Nagar B, Sonenberg N. Structural basis for the recruitment of the human CCR4-NOT deadenylase complex by tristetraprolin. *Nat Struct Mol Biol*. 2013 Jun;20(6):735-9.

Falini B, Pileri S, Zinzani PL, *et al*. ALK-positive lymphoma: Clinico-pathological findings and outcome. *Blood* 93.2697,1999

Fan J, Yang X, Wang W, Wood WH 3rd, Becker KG, Gorospe M. Global analysis of stress-regulated mRNA turnover by using cDNA arrays. *Proc. Natl Acad. Sci. USA* 2002 Aug 6;99(16):10611-6.

Fan XC, Steitz JA. Overexpression of HuR, a nuclear-cytoplasmic shuttling protein, increases the in vivo stability of ARE-containing mRNAs. *EMBO J* 1998; 17:3448-60.

Faustino, N. A., and Cooper, T. A. (2003). Pre-mRNA splicing and human disease. *Genes Dev*. 17: 419-437.

Fearon ER, Vogelstein B. 1990. A genetic model for colorectal tumorigenesis. *Cell* 61:759-67.

Fearon, E.R. (2011). Molecular genetics of colorectal cancer. *Annu Rev Pathol* 6, 479-507.

Fenger-Gron, M., Fillman, C., Norrild, B., Lykke-Andersen, J. Multiple processing body factors and the ARE-binding protein TTP activate mRNA decapping. *Mol. Cell* 20, 905-915 (2005).

Ferlay J, Shin HR, Bray F, Forman D, Mathers C and Parkin DM. GLOBOCAN 2008 v2.0, Cancer Incidence and Mortality Worldwide: IARC Cancer Base No. 10. Lyon, France: International Agency for Research on Cancer; 2010.

Fijneman RJA, Anderson R, Richards E, Liu J, Tijssen M, Meijer GA *et al*. *Runx1* is a tumor suppressor gene in the mouse gastrointestinal tract. *Cancer Sci* 2012; 103: 593–92011.

Fodde R, Smits R. Disease model: Familial adenomatous polyposis. *Trends Mol Med*. 2001;7:369–373.

Fodde R. The APC gene in colorectal cancer. *Eur J Cancer.* 2002;38:867–871.

Fong Y, Fortner J, Sun RL, Brennan MF, Blumgart LH. Clinical score for predicting recurrence after hepatic resection for metastatic colorectal cancer: analysis of 1001 consecutive cases. *Ann Surg* 1999; 230: 309–318.

Forbes S, *et al*. COSMIC 2005. *Br J Cancer*. 2006;94:318–322.

Friedman RC, Farh KK, Burge CB, Bartel DP. "Most mammalian mRNAs are conserved targets of microRNAs". *Genome Res*. 2009 Jan;19(1):92-105.

Frolov, M.V., Benevolenskaya, E.V., Birchler, J.A. (1998) Regena (Rga), a Drosophila homolog of the global negative transcriptional regulator CDC36 (NOT2) from yeast, modifies gene expression and suppresses position effect variegation. *Genetics* 148, 317–329.

Futreal PA, Coin L, Marshall M, Down T, Hubbard T, Wooster R, Rahman N, Stratton MR. A census of human cancer genes. *Nat Rev Cancer*. 2004 Mar;4(3):177-83.

Garcia-Blanco, M. A. (2003). Messenger RNA reprogramming by spliceosome-mediated RNA trans-splicing. *J. Clin. Invest*. 112: 474-480.

Garneau NL, Wilusz J, Wilusz CJ. The highways and byways of mRNA decay. *Nat Rev Mol Cell Biol*. 2007 Feb;8(2):113-26.

Geurts AM, Hackett CS, Bell JB, Bergemann TL, Collier LS, *et al*. (2006) Structure-based prediction of insertion-site preferences of transposons into chromosomes. *Nucleic Acids Res* 34: 2803-2811.

Gilmartin GM. Eukaryotic mRNA 3' processing: A common means to different ends. *Genes Dev* 2005; 19:2517-21.

Goldberg SF, Miele ME, Hatta N, *et al*. Melanoma metastasis suppression by chromosome 6: evidence for a pathway regulated by CRSP3 and TXNIP. *Cancer Res*. 2003;63:432-440.

Grabundzija,I., Irgang,M., Mates,L., Belay,E., Matrai,J., Gogol-Doring,A., Kawakami,K., Chen,W., Ruiz,P., Chuah,M.K. *et al*. (2010) Comparative analysis of transposable element vector systems in human cells. *Mol. Ther*., 18, 1200-1209.

Grady WM, Markowitz SD. Genetic and epigenetic alterations in colon cancer. *Annu Rev Genomics Hum Genet*. 2002;3:101–128.

Grady WM, Pritchard CC. Molecular Alterations and Biomarkers in Colorectal Cancer. *Toxicol Patho*l. 2013 Oct 31.

Grahammer F, Herling AW, Lang HJ, Schmitt-Graff A, Wittekindt OH, Nitschke R *et al*. The cardiac $K^þ$ channel KCNQ1 is essential for gastric acid secretion. *Gastroenterology* 2001; 120: 1363–1371.

Greenman C, Stephens P, Smith R, *et al*. Patterns of somatic mutation in human cancer genomes. *Nature*. 2007 Mar 8;446(7132):153-8.

Guerra E, Trerotola M, Dell' Arciprete R, Bonasera V, Palombo B, El-Sewedy T, *et al*. A bicistronic *CYCLIN D1-TROP2* mRNA chimera demonstrates a novel oncogenic mechanism in human cancer. *Cancer Res* 2008; 68:8113-21.

Habermann JK, Paulsen U, Roblick UJ, *et al*. (2007) Stage-specific alterations of the genome, transcriptome, and proteome during colorectal carcinogenesis. *Genes Chromosomes Cancer* 46:10-26.

Hackett PB, Largaespada DA, Switzer KC, Cooper LJ. Evaluating risks of insertional mutagenesis by DNA transposons in gene therapy. *Transl Res*. 2013 Apr;161(4):265-83.

Haigis KM, Caya JG, Reichelderfer M, Dove WF. Intestinal adenomas can develop with a stable karyotype and stable microsatellites. *Proc Natl Acad Sci USA*. 2002;99:8927–8931.

Haigis KM, Dove WF. A Robertsonian translocation suppresses a somatic recombination pathway to loss of heterozygosity. *Nat Genet*. 2003;33:33–39.

Hall N (May 2007). "Advanced sequencing technologies and their wider impact in microbiology". *J. Exp. Biol*. 210 (Pt 9): 1518–25.

Han D, Lerner AG, Vande Walle L, Upton JP, Xu W, Hagen A, Backes BJ, Oakes SA, Papa FR. IRE1alpha kinase activation modes control alternate endoribonuclease outputs to determine divergent cell fates. *Cell*. 2009 Aug 7;138(3):562-75.

Han SH, Jeon JH, Ju HR, *et al*. VDUP1 upregulated by TGF-beta1 and 1,25-dihydorxyvitamin D3 inhibits tumor cell growth by blocking cell-cycle progression. *Oncogene* 2003;22(26):4035-4046.

Han SW, Kim HP, Shin JY, Jeong EG, Lee WC, Lee KH, Won JK, Kim TY, Oh DY, Im SA, Bang YJ, Jeong SY, Park KJ, Park JG, Kang GH, Seo JS, Kim JI, Kim TY. Targeted sequencing of cancer-related genes in colorectal cancer using next-generation sequencing. *PLoS One*. 2013 May 21;8(5):e64271.

Hashimoto T, Perlot T, Rehman A, Trichereau J, Ishiguro H, Paolino M *et al*. ACE2 links amino acid malnutrition to microbial ecology and intestinal inflammation. *Nature* 2012; 487: 477-481.

He XC, Zhang J, Tong WG, Tawfik O, Ross J, Scoville DH, Tian Q, Zeng X, He X, Wiedemann LM, Mishina Y, Li L. BMP signaling inhibits intestinal stem cell self-renewal through suppression of Wnt-beta-catenin signaling. *Nat. Genet*. 36 (2004), pp.1117-1121.

Heath JK. Transcriptional networksand signaling pathways that govern vertebrate intestinal development. *Curr Top Dev Biol*. 2010;90:159-92.

Heijmans J, van Lidth de Jeude JF, Koo BK, *et al*. ER stress causes rapid loss of intestinal epithelial stemness through activation of the unfolded protein response. *Cell Rep.* 2013 Apr 25;3(4):1128-39.

Hernández-Sánchez C, Bártulos O, Valenciano AI, Mansilla A, de Pablo F. The regulated expression of chimeric tyrosine hydroxylase-insulin transcripts during early development. *Nucleic Acids Res*. 2006 Jul 13;34(12):3455-64.

Hobert JA, Eng C. 2009. PTEN hamartoma tumor syndrome: an overview. *Genet. Med*. 11:687-94.

Hollien J., Lin J.H., Li H., Stevens N., Walter P., Weissman J.S. Regulated Ire1-dependent decay of messenger RNAs in mammalian cells (2009) *Journal of Cell Biology*, 186 (3), pp. 323-331.

Hosoi T, Ozawa K. Endoplasmic reticulum stress in disease: mechanisms and therapeutic opportunities. *Clin Sci* (*Lond*) 118: 19-29, 2010.

Subramanian A, Tamayo P, Mootha VK, Mukherjee S, Ebert BL, Gillette MA *et al*. Gene set enrichment analysis: a knowledge-based approach for interpreting genome-wide expression profiles. *Proc Natl Acad Sci USA* 2005; 102: 15545-15550.

Ishkanian AS, Mallof CA, Ho J, *et al*. High-resolution array CGH identifies novel regions of genomic alteration in intermediate-risk prostate cancer. *Prostate* 2009;69:1091 e 1100.

Ito K, Inoue T, Yokoyama K, Morita M, Suzuki T, Yamamoto T. CNOT2 depletion disrupts and inhibits the CCR4-NOT deadenylase complex and induces apoptotic cell death. *Genes Cells*. 2011 Apr;16(4):368-79.

Ito K, Takahashi A, Morita M, Suzuki T, Yamamoto T. The role of the CNOT1 subunit of the CCR4-NOT complex in mRNA deadenylation and cell viability. *Protein Cell*. 2011 Sep;2(9):755-63.

Itoh, S., Itoh, F., Goumans, M.J., Ten Dijke, P. Signaling of transforming growth factor-beta family members through Smad proteins. *Eur. J. Biochem*. 267, 6954−6967 (2000).

Ivics Z, Hackett PB, Plasterk RH, Izsvák Z. "Molecular reconstruction of Sleeping Beauty, a Tc1-like transposon from fish, and its transposition in human cells". *Cell*. 1997 Nov 14;91(4):501-10.

Jass JR. 2007. Classification of colorectal cancer based on correlation of clinical, morphological and molecular features. *Hisopathology* 50:113-30

Jensen, J., Pedersen, E. E., Galante, P., Hald, J., Heller, R. S., Ishibashi, M., Kageyama, R., Guillemot, F., Serup, P. and Madsen, O. D. (2000). Control of endodermal endocrine development by Hes-1. *Nat. Genet*. 24, 36-44.

Jeon JH, Lee KN, Hwang CY, Kwon KS, You KH, Choi I. Tumor suppressor *VDUP1* increases p27(kip1) stability by inhibiting JAB1. *Cancer Res* 2005;65(11):4485-4489.

Jessurun J, Romero-Guadarrama M, Manivel JC. Medullary adenocarcinoma of the colon: clinicopathologic study of 11 cases. *Hum Pathol.* 1999 Jul;30(7):843-8.

Jin LH, Shao QJ, Luo W, Ye ZY, Li Q, Lin SC. Detection of point mutations of the *Axin1* gene in colorectal cancers. *Int J Cancer*. 2003 Dec 10;107(5):696-9.

Jones S, Zhang X, Parsons DW, Lin JC, Leary RJ, *et al*. (2008) Core signaling pathways in human pancreatic cancers revealed by global genomic analyses. *Science* 321: 1801-1806.

Junn E, Han SH, Im JY, *et al*. Vitamin D3 up-regulated protein 1 mediates oxidative stress via suppressing the thioredoxin function. *J Immunol*. 2000;164:6287-6295.

Kaler P, Augenlicht L, Klampfer L. Activating mutations in *β-Catenin* in colon cancer cells alter their interaction with macrophages; the role of snail. *PLoS ONE*. 2012;7(9):e45462.

Kang S, Okuno T, Takegahara N, Takamatsu H, Nojima S, Kimura T., *et al*. Intestinal epithelial cell-derived semaphorin 7A negatively regulates development of colitis via avb1 integrin. *J Immunol* 2012; 188: 1108-1116.

Kaserer, K., Schmaus, J., Bethge, U., Migschitz, B., Fasching, S., Walch, A., Herbst, F., Teleky, B., Wrba, F. (2000). Staining patterns of p53 immunohistochemistry and their biological significance in colorectal cancer. *J Pathol*, 190, 450-6.

Kemp Z, *et al*. Colorectal tumour Gene Identification (CoRGI) Study Consortium. Evidence for a colorectal cancer susceptibility locus on chromosome 3q21-q24 from a high-density SNP genome-wide linkage scan. *Hum Mol Genet*. 2006;15:2903–2910.

Keng VW, Villanueva A, Chiang DY, *et al*. A conditional transposon-based insertional mutagenesis screen for genes associated with mouse hepatocellular carcinoma. *Nat Biotechnol.* 2009;27:264–274.

Kent WJ, Sugnet CW, Furey TS, Roskin KM, Pringle TH, Zahler AM, Haussler D. (2002) The human genome browser at UCSC. *Genome Res* 12:996–1006.

Khabar, K. S. The AU-rich transcriptome: more than interferons and cytokines, and its role in disease. *J. Interferon Cytokine Res*. 2005 Jan;25(1):1-10.

Kinzler KW, Vogelstein B. Lessons from hereditary colorectal cancer. *Cell. 1996 Oct 18;87 (2): 159-70.*

Kim, E.C. & Lance, P. Colorectal polyps and their relationship to cancer. *Gastroenterol Clin North Am*, 1997 Mar;26(1):1-17.

Knobloch M, Braun SM, Zurkirchen L, von Schoultz C, Zamboni N, Arauzo-Bravo MJ., *et al*. Metabolic control of adult neural stem cell activity by Fasn-dependent lipogenesis. *Nature* 2013; 493: 226–230.

Yuko Komiya and Raymond Habas. Wnt signal transduction pathways. *Organogenesis*. 2008 Apr-Jun; 4(2): 68-75.

Korinek V, Barker N, Moerer P, van Donselaar E, Huls G., *et al*. Depletion of epithelial stem-cell compartments in the small intestine of mice lacking Tcf-4. *Nat Genet*. 1998 Aug;19(4):379-83.

Körner CG, Wormington M, Muckenthaler M, Schneider S, Dehlin E, Wahle E. The deadenylating nuclease (DAN) is involved in poly(A) tail removal during the meiotic maturation of Xenopus oocytes. *EMBO J*. 17, 5427-5437 (1998).

Koso H, Takeda H, Yew CC, Ward JM, Nariai N, Ueno K, Nagasaki M, Watanabe S, Rust AG, Adams DJ, Copeland NG, Jenkins NA. Transposon mutagenesis identifies genes that transform neural stem cells into glioma-initiating cells. *Proc Natl Acad Sci USA*. 2012 Oct 30;109(44): E2998-3007.

Kreykenbohm V, Wenzel D, Antonin W, Atlachkine V, von Mollard GF. The SNAREs vti1a and vti1b have distinct localization and SNARE complex partners. *Eur. J. Cell Biol*. 81, 273–280 (2002).

Kristi D. Viles, Bruce A. Sullenger. Proximity-dependent and proximity-independent trans-splicing in mammalian cells. *RNA*. 2008 June; 14(6): 1081–1094.

Kurashina K, Yamashita Y, Ueno T, *et al*. (2008) Chromosome copy number analysis in screening for prognosis-related genomic regions in colorectal carcinoma. *Cancer Sci* 99:1835–1840.

Lang F, Shumilina E. Regulation of ion channels by the serum- and glucocorticoid-inducible kinase SGK1. *FASEB J* 2013; 27: 3–12.

Lassmann S, Weis R, Makowiec F, Roth J, Danciu M, Hopt U, Werner M. (2007) Array CGH identifies distinct DNA copy number profiles of oncogenes and tumor suppressor genes in chromosomal- and microsatellite-unstable sporadic colorectal carcinomas. *J Mol Med* 85:293-304.

Lau NC, Kolkman A, van Schaik FM, Mulder KW, Pijnappel WW, Heck AJ, Timmers HT. Human Ccr4-Not complexes contain variable deadenylase subunits. *Biochem. J*. 2009 Aug 27;422(3): 443-53.

Laurent-Puig P, Cayre A, Manceau G, Buc E, Bachet JB, *et al*. 2009. Analysis of PTEN, BRAF, and EGFR status in determining benefit from cetuximab therapy in wild-type KRAS metastatic colon cancer. *J. Clin. Oncol*. 27:5924-30.

Lee L, Jannapureddy M, Albo D, *et al.* Outcomes of Veterans Affairs patients older than age 80 after surgical procedures for colon malignancies. *Am J Surg*, 2007.194(5): p646-51.

Lee MP, Ravenel JD, Hu RJ, Lustig LR, Tomaselli G, Berger RD, *et al*. Targeted disruption of the Kvlqt1 gene causes deafness and gastric hyperplasia in mice. *J Clin Invest* 2000; 106:1447-1455.

Lee Y, Kim M, Han J, Yeom KH, Lee S, Baek SH, Kim VN (October 2004). "MicroRNA genes are transcribed by RNA polymerase II". *EMBO J*. 23 (20): 4051-60.

Lerner AG, Upton JP, Praveen PV, Ghosh R, Nakagawa Y, Igbaria A, Shen S, Nguyen V, Backes BJ, Heiman M, Heintz N, Greengard P, Hui S, Tang Q, Trusina A, Oakes SA, Papa FR. IRE1α induces thioredoxin-interacting protein to activate the NLRP3 inflammasome and promote programmed cell death under irremediable ER stress. *Cell Metab*. 2012 Aug 8;16(2):250-64.

Levy DB, Smith KJ, Beazer-Barclay Y, Hamilton SR, Vogelstein B, Kinzler KW. Inactivation of both APC alleles in human and mouse tumors. *Cancer Res*. 1994;54:5953–5958.

Li H, Wang J, Mor G, Sklar J. A neoplastic gene fusion mimics trans-splicing of RNAs in normal human cells. *Science.* 2008 Sep 5;321(5894):1357-61.

Li H, Bian C, Liao L, Li J, Zhao RC (2011) *miR-17*-5p promotes human breast cancer cell migration and invasion through suppression of HBP1. *Breast Cancer Res Treat* 126: 565-575.

Lin C, Yang L, Rosenfeld MG. Molecular logic underlying chromosomal translocations, random or non-random? *Adv Cancer Res*. 2012;113:241-79.

Lin E, Li L, Guan Y, Soriano R, Rivers CS, Mohan S, Pandita A, Tang J, Modrusan Z. Exon array profiling detects EML4-ALK fusion in breast, colorectal, and non-small cell lung cancers. *Mol Cancer Res*. 2009 Sep;7(9):1466-76.

Lin WJ, Duffy A, Chen CY. Localization of AU-rich element-containing mRNA in cytoplasmic granules containing exosome subunits. *J Biol Chem* 2007; 282:19958-68.

Loupakis F, Pollina L, Stasi I, *et al*. PTEN expression and KRAS mutations on primary tumors and metastases in the prediction of benefit from cetuximab plus irinotecan for patients with metastatic CRC. *J Clin Oncol*. 2009;27:2622-9.

Lund E, Dahlberg JE. "Substrate selectivity of exportin 5 and Dicer in the biogenesis of microRNAs". *Cold Spring Harb.Symp. Quant. Biol*. 2006;71:59-66.

Luo B, Lee AS. "The critical roles of endoplasmic reticulum chaperones and unfolded protein response in tumorigenesis and anticancer therapies," *Oncogene*. 2013 Feb 14;32(7):805-18.

Luongo C, Moser AR, Gledhill S, Dove WF. Loss of Apc^{+} in intestinal adenomas from Min mice. *Cancer Res*. 1994;54:5947–5952.

Lynch HT, de la Chapelle A. Hereditary colorectal cancer. *N Engl J Med* 2003;348:919-932.

Maher CA, Kumar-Sinha C, Cao X, Kalyana-Sundaram S, Han B, *et al*. (2009) Transcriptome sequencing to detect gene fusions in cancer. *Nature* 458: 97–101.

Maisonneuve P, FitzSimmons SC, Neglia JP, Campbell III PW, Lowenfels AB. Cancer risk in nontransplanted and transplanted cystic fibrosis patients: a 10-year study. *J Natl Cancer Inst.* 2003; 95: 381–387.

Malumbres M, Barbacid M. *RAS* oncogenes: the first 30 years. *Nat. Rev. Cancer* 2003, 3:459-65.

Mandel CR, Bai Y, Tong L. Protein factors in pre-mRNA 3'-end processing. *Cell Mol Life Sci* 2008; 65:1099-122.

Mann KM, Ward JM, Yew CC, Kovochich A, Dawson DW, Black MA, *et al*. *Sleeping Beauty* mutagenesis reveals cooperating mutations and pathways in pancreatic adenocarcinoma. *Proc Natl Acad Sci USA* 2012; 109: 5934–5941.

Mansfield, S. G., Chao, H., and Walsh, C. E. (2004). RNA repair using spliceosome-mediated RNA trans-splicing. *Trends Mol. Med.* 10: 263 – 268.

Mansilla A, López-Sánchez C, de la Rosa EJ, García-Martínez V, Martínez-Salas E, de Pablo F, Hernández-Sánchez C. (2005) Developmental regulation of a proinsulin messenger RNA generated by intron retention. *EMBO Rep*., 6, 1182-1187.

March HN, Rust AG, Wright NA, ten Hoeve J, de Ridder J, Eldridge M, van der Weyden L, Berns A, Gadiot J, Uren A, Kemp R, Arends MJ, Wessels LF, Winton DJ, Adams DJ. Insertional mutagenesis identifies multiple networks of cooperating genes driving intestinal tumorigenesis. *Nat Genet*. 2011 Nov 6;43(12):1202-9.

Marchese FP, Aubareda A, Tudor C, *et al*. MAPKAP kinase 2 blocks tristetraprolin-directed mRNA decay by inhibiting CAF1 deadenylase recruitment. *J Biol Chem*. 2010 Sep 3;285(36): 27590-600.

Martin JA, Wang Z. Next-generation transcriptome assembly. *Nat Rev Genet.* 2011 Sep 7;12(10):671-82.

Mates,L., Chuah,M.K., Belay,E., Jerchow,B., Manoj,N., Acosta-Sanchez,A., Grzela,D.P., Schmitt,A., Becker,K., Matrai,J. *et al.* (2009) Molecular evolution of a novel hyperactive Sleeping Beauty transposase enables robust stable gene transfer in vertebrates. *Nat. Genet*., 41, 753-761.

May WA, Lessnick SL, Braun BS, *et al*. The Ewing's sarcoma *EWS/FLI-1* fusion gene encodes a more potent transcriptional activator and is a more powerful transforming gene than *FLI-1*. *Mol Cell Biol*. 1993 Dec;13(12):7393-8.

McAlpine CA, Barak Y, Matise I, Cormier RT. Intestinal-specific PPARgamma deficiency enhances tumorigenesis in $Apc^{Min/+}$ mice. Int J Cancer. 2006;119:2339–2346.

Medema JP, Vermeulen L. Microenvironmental regulation of stem cells in intestinal homeostasis and cancer. *Nat Rev* 2011; Vol 474: 318-326.

Merlos-Suárez A, Barriga FM, Jung P, Iglesias M, Céspedes MV, Rossell D, Sevillano M, Hernando-Momblona X, da Silva-Diz V, Muñoz P, Clevers H, Sancho E, Mangues R, Batlle E. The intestinal stem cell signature identifies colorectal cancer stem cells and predicts disease relapse. *Cell Stem Cell*. 2011 May 6;8(5):511-24.

Miller MA, Olivas WM. Roles of Puf proteins in mRNA degradation and translation. *Wiley Interdiscip Rev RNA*. 2011 Jul-Aug;2(4):471-92.

Mitelman F, Johansson B, Mertens F. The impact of translocations and gene fusions on cancer causation. *Nat. Rev. Cancer*. 2007;7:233–245.

Moldt,B., Yant,S.R., Andersen,P.R., Kay,M.A. and Mikkelsen,J.G. Cis-acting gene regulatory activities in the terminal regions of sleeping beauty DNA transposon-based vectors. Hum. *Gene Ther*. 2007 Dec;18(12):1193-204.

Mootha VK, Lindgren CM, Eriksson KF, Subramanian A, Sihag S, Lehar J, *et al*. PGC-1 alpha-responsive genes involved in oxidative phosphorylation are coordinately downregulated in human diabetes. *Nat Genet* 2003; 34: 267-273.

Morita, M., Suzuki, T., Nakamura, T., Yokoyama, K., Miyasaka, T., and Yamamoto, T. Depletion of mammalian CCR4b deadenylase triggers elevation of the $p27^{Kip1}$ mRNA level and impairs cell growth. *Mol Cell Biol* 2007 27, 4980-4990.

Moser AR, Pitot HC, Dove WF. A dominant mutation that predisposes to multiple intestinal neoplasia in the mouse. *Science*. 1990;247:322–324.

Mueller PR, Wold B. In vivo footprinting of a muscle specific enhancer by ligation mediated PCR. *Science*. 1989;246:780–786.

Mulder, K. W., Winkler, G. S. and Timmers, H. T. DNA damage and replication stress induced transcription of RNR genes is dependent on the Ccr4-Not complex. *Nucleic Acids Res*. 2005, 33, 6384-6392

Mulder, K. W., Brenkman, A. B., Inagaki, A., van den Broek, N. J. and Timmers, H. T. Regulation of histone H3K4 tri-methylation and PAF complex recruitment by the Ccr4-Not complex. *Nucleic Acids Res*. 2007,35, 2428-2439.

Mullighan CG, Phillips LA, Su X, Ma J, Miller CB, Shurtleff SA, Downing JR. Genomic analysis of the clonal origins of relapsed acute lymphoblastic leukemia. *Science* 322, 1377-1380 (2008).

Muñoz J, Stange DE, Schepers AG, *et al*. The Lgr5 intestinal stem cell signature: robust expression of proposed quiescent '+4' cell markers. *EMBO J* 2012; 31: 3079–3091.

Nakao K, Mehta KR, Fridlyand J, Moore DH, Jain AN, Lafuente A, Wiencke JW, Terdiman JP, Waldman FM. High-resolution analysis of DNA copy number alterations in colorectal cancer by array-based comparative genomic hybridization. *Carcinogenesis* 2004 Aug;25(8):1345-57.

National Comprehensive Cancer Network. 2012. NCCN Clinical Practice Guidelines in Oncology. Colon cancer. Version 3.2012.

Neklason DW, Kerber RA, Nilson DB, *et al*. Common familial colorectal cancer linked to chromosome 7q31: A genome-wide analysis. *Cancer Res*. 2008 Nov 1;68(21):8993-7.

Newman JC, Bailey AD, Fan HY, Pavelitz T, Weiner AM. An abundant evolutionarily conserved CSB-PiggyBac fusion protein expressed in Cockayne syndrome. *PLoS Genet*. 2008 Mar 21;4(3):e1000031.

Nikou GC, Toubanakis C, Moulakakis KG, Pavlatos S, Kosmidis C, Mallas E, *et al*. Carcinoid tumors of the duodenum and the ampulla of Vater: current diagnostic and therapeutic approach in a series of 8 patients. Case series. *Int J Surg* 2011; 9: 248-253.

Nishisho I, Nakamura Y, Miyoshi Y, Miki Y, Ando H, Horii A, Koyama K, Utsunomiya J, Baba S, Hedge P. Mutations of chromosome 5q21 genes in FAP and colorectal cancer patients. *Science*. 1991 Aug 9;253(5020):665-9.

Norkina O, Kaur S, Ziemer D, De Lisle RC. Inflammation of the cystic fibrosis mouse small intestine. *Am J Physiol Gastrointest Liver Physiol* 2004; 286: G1032–G1041.

Nowell PC. Discovery of the Philadelphia chromosome: a personal perspective. *J. Clin. Invest.* 2007 Aug;117(8):2033-5.

O'Donnell KA, Keng VW, York B, Reineke EL, Seo D, Fan D, Silverstein KA, Schrum CT, Xie WR, Mularoni L, Wheelan SJ, Torbenson MS, O'Malley BW, Largaespada DA, Boeke JD. A *Sleeping Beauty* mutagenesis screen reveals a tumor suppressor role for Ncoa2/Src-2 in liver cancer. *Proc Natl Acad Sci U S A*. 2012 May 22;109(21):E1377-86.

Odorizzi G. The multiple personalities of Alix. *J Cell Sci*. 2006;119:3025–3032.

Oslowski CM, Hara T, O'Sullivan-Murphy B, Kanekura K, Lu S, Hara M, Ishigaki S, Zhu LJ, Hayashi E, Hui ST, Greiner D, Kaufman RJ, Bortell R, Urano F. Thioredoxin-interacting protein mediates ER stress-induced β cell death through initiation of the inflammasome. *Cell Metab.* 2012 Aug 8;16(2):265-73.

Parkin DM. (2001) Global cancer statistics in the year 2000. *Lancet Oncol* 2:533-543.

Parra G, Reymond A, Dabbouseh N, Dermitzakis ET, Castelo R, Thomson TM, Antonarakis SE, Guigo R. Tandem chimerism as a means to increase protein complexity in the human genome. *Genome Res* 2006, 16:37-44.

Pasquinelli AE. MicroRNAs and their targets: recognition, regulation and an emerging reciprocal relationship. *Nat Rev Genet*. 2012 Mar 13;13(4):271-82.

Patwari P, Chutkow WA, Cummings K, Verstraeten VL, Lammerding J, Schreiter ER, and Lee RT. Thioredoxin-independent regulation of metabolism by the alpha-arrestin proteins. *J Biol Chem* 284: 24996-25003, 2009.

Pérez-Mancera PA, Rust AG, van der Weyden L, *et al*. The deubiquitinase USP9X suppresses pancreatic ductal adenocarcinoma. *Nature*. 2012 Apr 29;486(7402):266-70.

Pérez-Mancera PA, Rust AG, van der Weyden L, *et al*. What we have learned about pancreatic cancer from mouse models. *Gastroenterology*. 2012 May;142(5):1079-92.

Peroz D, Rodriguez N, Choveau F, Baro I, Merot J, Loussouarn G. Kv7.1 (KCNQ1) properties and channelopathies. *J Physiol* 2008; 586: 1785–1789.

Petit AP, Wohlbold L, Bawankar P, Huntzinger E, Schmidt S, Izaurralde E, Weichenrieder O. The structural basis for the interaction between the CAF1 nuclease and the NOT1 scaffold of the human CCR4-NOT deadenylase complex. *Nucleic Acids Res*. 2012 Nov;40(21):11058-72.

Pfaffl MW. (2001) A new mathematical model for relative quantification in real-time RT-PCR. *Nucleic Acids Res* 29:2003–2007.

Piao, X., Zhang, X., Wu, L., and Belasco, J.G. CCR4-NOT deadenylates mRNA associated with RNA-induced silencing complexes in human cells. *Mol. Cell. Biol*. 2010, 30, 1486-1494.

Plesec TP, Hunt JL. *KRAS* mutation testing in colorectal cancer. *Adv Anat Pathol*. 2009 Jul;16(4): 196-203.

Polakis P. The many ways of Wnt in cancer. *Curr. Opin.Genet*. Dev. 2007 Feb;17(1):45-51.

Powell SM, Zilz N, Beazer-Barclay Y, Bryan TM, Hamilton SR, Thibodeau SN, Vogelstein B, Kinzler KW: *APC* mutations occur early during colorectal tumorigenesis. *Nature* 1992;359:235-237.

Preston P, Wartosch L, Gunzel D, Fromm M, Kongsuphol P, Ousingsawat J., *et al*. Disruption of the K^+ channel beta-subunit KCNE3 reveals an important role in intestinal and tracheal Cl^- transport. *J Biol Chem* 2010; 285: 7165-7175.

Quintana RM, Dupuy AJ, Bravo A, Casanova ML, Alameda JP, Page A, Sánchez-Viera M, Ramírez A, Navarro M. A transposon-based analysis of gene mutations related to skin cancer development. *J Invest Dermatol*. 2013 Jan;133(1):239-48.

Radice AD, Bugaj B, Fitch DH, Emmons SW. "Widespread occurrence of the Tc1 transposon family: Tc1-like transposons from teleost fish". *Mol. Gen. Gene*t. 1994 Sep 28;244(6):606-12.

Rahrmann EP, Watson AL, Keng VW, Choi K, Moriarity BS, Beckmann DA, Wolf NK, Sarver A, Collins MH, Moertel CL, Wallace MR, Gel B, Serra E, Ratner N, Largaespada DA. Forward genetic screen for malignant peripheral nerve sheath tumor formation identifies new genes and pathways driving tumorigenesis. *Nat Genet*. 2013 Jul;45(7):756-66.

Reya T, Clevers H. Wnt signalling in stem cells and cancer. *Nature*. 2005 Apr 14;434(7035):843-50.

Riccio, O., van Gijn, M. E., Bezdek, A. C., Pellegrinet, L., van Es, J. H., Zimber-Strobl, U., Strobl, L. J., Honjo, T., Clevers, H. and Radtke, F. Loss of intestinal crypt progenitor cells owing to inactivation of both Notch1 and Notch2 is accompanied by derepression of CDK inhibitors p27Kip1 and p57Kip2. *EMBO Rep*. 2008, 9, 377-383.

Rice KS, Dickson G, Lane M, Crawford J, Chung SK, Rees MI, *et al*. Elevated serum gastrin levels in Jervell and Lange–Nielsen syndrome: a marker of severe KCNQ1 dysfunction? *Heart Rhythm* 2011; 8: 551–554.

Rice P, Longden I, Bleasby A (2000) EMBOSS: The European Molecular Biology Open Software Suite. *Trends Genet* 16:276–277.

Ried T, Knutzen R, Steinbeck R, Blegen H, Schröck E, Heselmeyer K, du Manoir S, Auer G. (1996) Comparative genomic hybridization reveals a specific pattern of chromosomal gains and losses during the genesis of colorectal tumors. *Genes Chromosomes Cancer* 15:234–245.

Roche-Lestienne C, Soenen-Cornu V, Grardel-Duflos N, Laï JL, Philippe N, Facon T, Fenaux P, Preudhomme C. Several types of mutations of the Abl gene can be found in chronic myeloid

leukemia patients resistant to STI571, and they can pre-exist to the onset of treatment. *Blood*. 2002 Aug 1;100(3):1014-8.

Ron D, Walter P. Signal integration in the endoplasmic reticulum unfolded protein response. *Nat Rev Mol Cell Biol*. 2007 Jul;8(7):519-29.

Russell P, Benson JD, Denis CL. Characterization of mutations in NOT2 indicates that it plays an important role in maintaining the integrity of the CCR4-NOT complex. *J Mol Biol*. 2002 Sep 6;322(1):27-39.

Rustgi, A.K. The genetics of hereditary colon cancer. *Genes Dev*. 2007 Oct 15;21(20):2525-38.

Saad S, Stanners SR, Yong R, Tang O, Pollock CA. Notch mediated epithelial to mesenchymal transformation is associated with increased expression of the Snail transcription factor. *Int. J. Biochem.Cell Biol*., 2010 Jul;42(7):1115-22.

Saandi T, Baraille F, Derbal-Wolfrom L, Cattin AL, Benahmed F, Martin E, Cardot P, Duclos B, Ribeiro A, Freund JN, Duluc I. Regulation of the tumor suppressor homeogene Cdx2 by HNF4α in intestinal cancer. *Oncogene* 2013 Aug 8;32(32):3782-8.

Saitoh M, Nishitoh H, Fujii M, *et al*. Mammalian thioredoxin is a direct inhibitor of apoptosis signal-regulating kinase (ASK) 1. *EMBO J*. 1998;17:2596-2606.

Sandberg R, Neilson JR, Sarma A, Sharp PA, Burge CB. Proliferating cells express mRNAs with shortened 3' untranslated regions and fewer microRNA target sites. *Science* 2008; 320:1643-7.

Sandler H, Kreth J, Timmers HT, Stoecklin G. Not1 mediates recruitment of the deadenylase Caf1 to mRNAs targeted for degradation by tristetraprolin. *Nucleic Acids Res*. 2011 May;39(10): 4373-86.

Saif MW and Chu E. Biology of colorectal cancer. *Cancer J*. 2010 May-Jun;16(3):196- 201.

Sato, T., van Es, J.H., Snippert, H.J., Stange, D.E., Vries, R.G., van den Born, M., Barker, N., Shroyer, N.F., van de Wetering, M., and Clevers, H. Paneth cells constitute the niche for Lgr5 stem cells in intestinal crypts. *Nature* 2011, 469, 415-418.

Sato T, Stange DE, Ferrante M, Vries RG, Van Es JH, Van den Brink S, Van Houdt WJ, Pronk A, Van Gorp J, Siersema PD, Clevers H. Long-term expansion of epithelial organoids from human colon, adenoma, adenocarcinoma, and Barrett's epithelium. *Gastroenterology* Nov 2011; 141: 1762-17772.

Schee K, Lorenz S, Worren MM, Günther CC, Holden M, Hovig E, Fodstad O, Meza-Zepeda LA, Flatmark K. Deep sequencing the microrna transcriptome in colorectal cancer. *PLoS One*. 2013 Jun 18;8(6):e66165.

Schinzel AC, Hahn WC. Oncogenic transformation and experimental models of human cancer. *Front. Biosci*. 13, 71-84 (2008).

Schmidt MH, Hoeller D, Yu J, Furnari FB, Cavenee WK, Dikic I, Bögler O. Alix/AIP1 antagonizes epidermal growth factor receptor downregulation by the Cbl-SETA/CIN85 complex. *Mol Cell Biol*. 2004;24:8981-8993.

Schönthal AH, Chen TC, Hofman FM, Louie SG, Petasis NA. "Preclinical development of novel antitumor drugs targeting the endoplasmic reticulum stress response," *Current Pharmaceutical Design*. 2011;17(23):2428-38.

Seber GAF (2002) The Estimation of Animal Abundance and Related Parameters (Blackburn, Caldwell, *NJ*) Ed 2.

Segditsas S, Tomlinson I. Colorectal cancer and genetic alterations in the Wnt pathway. *Oncogene* 2006, 25:7531-37.

Seshagiri S, Stawiski EW, Durinck S, *et al*. Recurrent R-spondin fusions in colon cancer. *Nature*. 2012 Aug 30;488(7413):660-4.

Shalapour S, Deiser K, Sercan O, Tuckermann J, Minnich K, Willimsky G, *et al*. Commensal microflora and interferon-gamma promote steady-state interleukin-7 production in vivo. *Eur J Immunol* 2010; 40: 2391–2400.

Sheth SS, Bodnar JS, Ghazalpour A, Thipphavong CK, Tsutsumi S, Tward AD, Demant P, Kodama T, Aburatani H, Lusis AJ. Hepatocellular carcinoma in *Txnip*-deficient mice. *Oncogene*. 2006 Jun 15;25 (25):3528-36.

Shih IM, Zhou W, Goodman SN, Lengauer C, Kinzler KW, Vogelstein B. (2001) Evidence that genetic instability occurs at an early stage of colorectal tumorigenesis. *Cancer Res* 61:818-822.

Shyu, A.B., Belasco, J.G., and Greenberg, M.E. Two distinct destabilizing elements in the *c-fos* message trigger deadenylation as a first step in rapid mRNA decay. *Genes & Dev*. 1991 Feb;5(2):221-31.

Rebecca Siegel, Deepa Naishadham, Ahmedin Jemal. Cancer Statistics, 2013. *CA CANCER J CLIN* 2013; 63:11-30.

Simon R, Mirlacher M, Sauter G. Tissue microarrays. *Biotechniques* 2004; 36: 98–105.

So JS, Hur KY, Tarrio M, Ruda V, Frank-Kamenetsky M, Fitzgerald K, Koteliansky V, Lichtman AH, Iwawaki T, Glimcher LH, Lee AH. Silencing of lipid metabolism genes through IRE1α-mediated mRNA decay lowers plasma lipids in mice. *Cell Metab.* 2012 Oct 3;16(4):487-99.

Soda M, Choi YL, Enomoto M, Takada S, Yamashita Y, Ishikawa S, Fujiwara S, Watanabe H, Kurashina K, Hatanaka H, Bando M, Ohno S, Ishikawa Y, Aburatani H, Niki T, Sohara Y, Sugiyama Y, Mano H. Identification of the transforming *EML4-ALK* fusion gene in non-small-cell lung cancer. *Nature* 448 (7153) (2007) 561-566.

Sonnichsen, B., Koski, L.B., Walsh, A., Marschall, P., Neumann, B. Full-genome RNAi profiling of early embryogenesis in *Caenorhabditis elegans*. *Nature* 2005 Mar 24;434(7032):462-9.

Stabenau A, McVicker G, Melsopp C, Proctor G, Clamp M, Birney E. (2004) The Ensembl core software libraries. *Genome Res* 14: 929-933.

Starr TK, Allaei R, Silverstein KA, Staggs RA, Sarver AL, *et al*. (2009) A transposon-based genetic screen in mice identifies genes altered in colorectal cancer. *Science* 323:1747-1750.

Starr TK, Scott PM, Marsh BM, Zhao L, Than BL, O'Sullivan MG, Sarver AL, Dupuy AJ, Largaespada DA, Cormier RT. A *Sleeping Beauty* transposon-mediated screen identifies murine susceptibility genes for adenomatous polyposis coli (*Apc*)-dependent intestinal tumorigenesis. *Proc Natl Acad Sci U S A*. 2011 Apr 5;108(14):5765-70.

Stichting FMWV Rotterdam: Code Goed Gebruik van lichaamsmateriaal 2011, *ISBN* 978-90-817510-0-1.

Stoecklin G, Lu M, Rattenbacher B, Moroni C. A constitutive decay element promotes tumor necrosis factor α mRNA degradation via an AU-rich element-independent pathway. *Mol. Cell Biol*. 23, 3506-3515 (2003).

Stratton MR, Campbell PJ, Futreal PA. The cancer genome. *Nature*. 2009 Apr 9;458(7239):719-24.

Su LK, Kinzler KW, Vogelstein B, Preisinger AC, Moser AR, Luongo C, Gould KA, Dove WF. Multiple intestinal neoplasia caused by a mutation in the murine homolog of the *APC* gene. *Science*. 1992;256:668–670.

Subramanian A, Tamayo P, Mootha VK, Mukherjee S, Ebert BL, Gillette MA, Paulovich A, Pomeroy SL, Golub TR, Lander ES, Mesirov JP. Gene set enrichment analysis: a knowledge-based approach for interpreting genome-wide expression profiles. *Proc Natl Acad Sci U S A*. 2005 Oct 25;102(43):15545-50.

Suzuki A, Igarashi K, Aisaki K, Kanno J, Saga Y. NANOS2 interacts with the CCR4-NOT deadenylation complex and leads to suppression of specific RNAs. *Proc Natl Acad Sci U S A*. 2010 Feb 23;107(8):3594-9.

Tabas I, Ron D. Integrating the mechanisms of apoptosis induced by endoplasmic reticulum stress. *Nat Cell Biol*. 2011 Mar;13(3):184-90.

Takahashi Y, Nagata T, Ishii Y, Ikarashi M, Ishikawa K, and Asai S. Up-regulation of *vitamin D3 up-regulated protein 1* gene in response to 5-fluorouracil in colon carcinoma SW620. *Oncol Rep* 9: 75-79, 2002.

Takagi T, Nishio H, Yagi T, Kuwahara M, Tsubone H, Tanigawa N, *et al*. Phenotypic analysis of vertigo 2 Jackson mice with a Kcnq1 potassium channel mutation. *Exp Anim* 2007; 56: 295–300.

Takayama T, Miyanishi K, Hayashi T, Sato Y, Niitsu Y. Colorectal cancer: Genetics of development and metastasis. *J Gastroenterol*. 2006;41:185–192.

Takimoto, K., Wakiyama, M. & Yokoyama, S. Mammalian GW182 contains multiple Argonaute-binding sites and functions in microRNA-mediated translational repression. *RNA* 15, 1078-1089 (2009).

Tam AB, Mercado EL, Hoffmann A, Niwa M (2012) ER Stress Activates NF-κB by Integrating Functions of Basal IKK Activity, IRE1 and PERK. *PLoS ONE* 7(10): e45078.

Taylor BS, Schultz N, Hieronymus H, *et al*. Integrative genomic profiling of human prostate cancer. *Cancer Cell* 2010;18: 11 e 22.

Temme, C., Zaessinger, S., Meyer, S., Simonelig, M., Wahle, E. (2004) A complex containing the CCR4 and CAF1 proteins is involved in mRNA deadenylation in Drosophila. *EMBO J*.23, 2862-2871.

Tobiume K, Matsuzawa A, Takahashi T, *et al*. ASK1 is required for sustained activations of JNK/p38 MAP kinases and apoptosis. *EMBO Rep*. 2001;2:222-228.

Tomlins SA, Rhodes DR, Perner S, Dhanasekaran SM, Mehra R, Sun XW, Varambally S, Cao X, Tchinda J, Kuefer R, Lee C, Montie JE, Shah RB, Pienta KJ, Rubin MA, Chinnaiyan AM. Recurrent fusion of TMPRSS2 and ETS transcription factor genes in prostate cancer. *Science* 2005;310:644-8.

Yien Che Tsai and Allan M. Weissman. The Unfolded Protein Response, Degradation from the Endoplasmic Reticulum, and Cancer. *Genes Cancer*. 2010 July; 1(7): 764-778.

Uchida, N., Hoshino, S., and Katada, T. 2004. Identification of a human cytoplasmic poly(A) nuclease complex stimulated by poly(A)-binding protein. *J. Biol. Chem*. 279: 1383-1391.

Ueo T, Imayoshi I, Kobayashi T, Ohtsuka T, Seno H, Nakase H, Chiba T, Kageyama R. The role of *Hes* genes in intestinal development, homeostasis and tumor formation. *Development*. 2012 Mar;139(6):1071-82.

Unneberg P, Claverie J-M (2007) Tentative Mapping of Transcription-Induced Interchromosomal Interaction using Chimeric EST and mRNA Data. *PLoS ONE* 2(2): e254.

Unoki H, Takahashi A, Kawaguchi T, Hara K, Horikoshi M, Andersen G, *et al*. SNPs in *KCNQ1* are associated with susceptibility to type 2 diabetes in East Asian and European populations. *Nat Genet* 2008; 40: 1098-1102.

Vaishnava S, Yamamoto M, Severson KM, Ruhn KA, Yu X, Koren O, *et al*. The antibacterial lectin RegIIIgamma promotes the spatial segregation of microbiota and host in the intestine. *Science* 2011; 334: 255–258.

Vallon V, Grahammer F, Volkl H, Sandu CD, Richter K, Rexhepaj R, *et al*. KCNQ1-dependent transport in renal and gastrointestinal epithelia. *Proc Natl Acad Sci USA* 2005; 102:17864-17869.

VanDussen KL, Samuelson LC. Mouse atonal homolog 1 directs intestinal progenitors to secretory cell rather than absorptive cell fate. *Dev Biol*. 2010 Oct 15;346(2):215-23.

VanDussen KL, Carulli AJ, Keeley TM, Patel SR, Puthoff BJ, Magness ST, Tran IT, Maillard I, Siebel C, Kolterud Å, Grosse AS, Gumucio DL, Ernst SA, Tsai YH, Dempsey PJ, Samuelson LC. Notch signaling modulates proliferation and differentiation of intestinal crypt base columnar stem cells. *Development*. 2012 Feb;139(3):488-97.

Van Etten J, Schagat TL, Hrit J, Weidmann CA, Brumbaugh J, Coon JJ, Goldstrohm AC.Human Pumilio proteins recruit multiple deadenylases to efficiently repress messenger RNAs. *J Biol Chem*. 2012 Oct 19; 287(43): 36370-83.

Vito P, Lacanà E, D'Adamio L. Interfering with apoptosis: $Ca^{(2+)}$-binding protein ALG-2 and Alzheimer's disease gene ALG-3. *Science*. 1996;271:521-525.

Voidonikolas G, Kreml SS, Chen C, Fisher WE, Brunicardi FC, Gibbs RA, Gingras MC: Basic principles and technologies for deciphering the genetic map of cancer. *World J Surg* 2009, 33:615-29.

Vogelstein B, Fearon ER, Hamilton SR, Kern SE, Preisinger AC, *et al*. Genetic alterations during colorectal-tumor development. *N. Engl. J. Med*. 1988 Sep 1;319(9):525-32.

Vogelstein B, Fearon ER, Kern SE, Hamilton SR, Preisinger AC, Nakamura Y, White R. Allelotype of colorectal carcinomas. *Science* 1989 Apr 14;244(4901):207-11.

Vousden KH, Prives C. 2009. Blinded by the light: the growing complexity of p53. *Cell* 137:413-31.

Wahle, E. & Winkler, G.S. RNA decay machines: deadenylation by the Ccr4-Not and Pan2-Pan3 complexes. *Biochim. Biophys. Acta* 1829, 561-570 (2013).

Walisko O, Schorn A, Rolfs F, Devaraj A, Miskey C, Izsvák Z, Ivics Z. (2008) Transcriptional activities of the Sleeping Beauty transposon and shielding its genetic cargo with insulators. *Mol. Ther*., 16, 359-369.

Walther A, Johnstone E, Swanton C, Midgley R, Tomlinson I, Kerr D. Genetic prognostic and predictive markers in colorectal cancer. *Nat Rev Cancer*. 2009 Jul;9(7):489-99.

Wang K, Ubriaco G, Sutherland LC. *RBM6-RBM5* transcription-induced chimeras are differentially expressed in tumours. *BMC Genomics*. 2007 Oct 1;8:348.

Wang Y, De Keulenaer GW, Lee RT. *Vitamin D3-up-regulated protein-1* is a stress-responsive gene that regulates cardiomyocyte viability through interaction with thioredoxin. *J Biol Chem*. 2002;277:26496-26500.

Warth R, Garcia Alzamora M, Kim JK, Zdebik A, Nitschke R, Bleich M, *et al*. The role of KCNQ1/KCNE1 K(+) channels in intestine and pancreas: lessons from the KCNE1 knockout mouse. *Pflugers Arch* 2002; 443: 822–828.

Waterman, M.L. Lymphoid enhancer factor/T cell factor expression in colorectal cancer. *Cancer Metastasis Rev*. 23, 41-52 (2004).

Winbo A, Sandstrom O, Palmqvist R, Rydberg A. Iron-deficiency anaemia, gastric hyperplasia, and elevated gastrin levels due to potassium channel dysfunction in the Jervell and Lange–Nielsen Syndrome. *Cardiol Young* 2012; 18: 1-10.

Winkler GS, Mulder KW, Bardwell VJ, Kalkhoven E, Timmers HT. Human Ccr4-Not complex is a ligand-dependent repressor of nuclear receptor-mediated transcription. *EMBO J.* 2006 Jul 12;25(13):3089-99.

Winter J, Jung S, Keller S, Gregory RI, Diederichs S. Many roads to maturity: microRNA biogenesis pathways and their regulation. *Nat Cell Biol*. 2009 Mar;11(3):228-34.

Wold B, Myers RM. Sequence census methods for functional genomics. *Nature Methods* 2008 Jan;5(1):19-21.

Wong S, Witte ON. The BCR-ABL story: bench to bedside and back. *Annu. Rev. Immunol.* 2004;22:247-306.

Wood LD, Parsons DW, Jones S, Lin J, Sjoblom T, *et al*. (2007) The genomic landscapes of human breast and colorectal cancers. *Science* 318: 1108-1113.

Wu L, Fan J, Belasco JG. MicroRNAs direct rapid deadenylation of mRNA. *Proc Natl Acad Sci USA* 2006; 103:4034-9.

Wu X, Li Y, Crise B, Burgess SM. (2003) Transcription start regions in the human genome are favored targets for MLV integration. *Science* 300:1749-1751.

Wu X, Northcott PA, Dubuc A, *et al*. Clonal selection drives genetic divergence of metastatic medulloblastoma. *Nature*. 2012 Feb 15;482(7386):529-33.

Wu Y, Wang X, Wu F, Huang R, Xue F, *et al*. (2012) Transcriptome profiling of the cancer, adjacent non-tumor and distant normal tissues from a colorectal cancer patient by deep sequencing. *PLoS ONE* 7(8): e41001.

Wulff H, Castle NA, Pardo LA. Voltage-gated potassium channels as therapeutic targets. *Nat Rev Drug Discovery* 2009; 8: 982-1001.

Xiong Q, Gao Z, Wang W, Li M. Activation of Kv7 (KCNQ) voltage-gated potassium channels by synthetic compounds. *Trends Pharmacol Sci* 2008; 29: 99–107.

Yamashita A, Chang TC, Yamashita Y, Zhu W, Zhong Z, Chen CY, Shyu AB. Concerted action of poly(A) nucleases and decapping enzyme in mammalian mRNA turnover. *Nat. Struct. Mol. Biol*. 2005 Dec;12(12):1054-63.

Yang K, Popova NV, Yang W, Lozonschi I, Tadesse S, Kent S, *et al*. Interaction of Muc2 and Apc on Wnt signaling and in intestinal tumorigenesis: potential role of chronic inflammation. *Cancer Res* 2008; 68: 7313-7322.

Yasuda K, Miyake K, Horikawa Y, Hara K, Osawa H, Furuta H, *et al*. Variants in *KCNQ1* are associated with susceptibility to type 2 diabetes mellitus. *Nat Genet* 2008; 40: 1092-1097.

Yekta S, Shih IH, Bartel DP. MicroRNA-directed cleavage of *HOXB8* mRNA. *Science* 2004 Apr 23;304(5670):594-6.

Yoon, JK., Lee, JS. Cellular signaling and biological functions of R-spondins. *Cell. Signal.* 24, 369-377 (2012).

Zambrowicz BP, Imamoto A, Fiering S, Herzenberg LA, Kerr WG, Soriano P. Disruption of overlapping transcripts in the ROSA beta geo 26 gene trap strain leads to widespread expression of beta-galactosidase in mouse embryos and hematopoietic cells. *Proc Natl Acad Sci USA*. 1997;94:3789-3794.

Zhao L, Vogt PK. 2008. Class I PI3K in oncogenic cellular transformation. *Oncogene* 27:5486-96.

Zheng X, Dumitru R, Lackford BL, *et al*. Cnot1, Cnot2, and Cnot3 maintain mouse and human ESC identity and inhibit extraembryonic differentiation. *Stem Cells*. 2012 May;30(5):910-22.

Zhou J, Bi C, Cheong LL, Mahara S, Liu SC, Tay KG, Koh TL, Yu Q, Chng WJ. The histone methyltransferase inhibitor, DZNep, up-regulates TXNIP, increases ROS production, and targets leukemia cells in AML. *Blood*. 2011 Sep 8;118(10):2830-9.

Zhou R, Tardivel A, Thorens B, Choi I, Tschopp J. Thioredoxin-interacting protein links oxidative stress to inflammasome activation. *Nat Immunol* 11: 136-140, 2010.

Zhou R, Yazdi AS, Menu P, *et al*. A role for mitochondria in NLRP3 inflammasome activation. *Nature* 2011; 469: 221-225.

Zinszner, H., Kuroda, M., Wang, X., Batchvarova, N., Lightfoot, R. T., Remotti, H., Stevens, J. L., and Ron, D. (1998). CHOP is implicated in programmed cell death in response to impaired function of the endoplasmic reticulum. *Genes Dev*. 12, 982-995.

Zlobec I, Steele R, Terracciano L, Jass JR, Lugli A. Selecting immunohistochemical cut-off scores for novel biomarkers of progression and survival in colorectal cancer. *J Clin Pathol* 2007; 60: 1112-1116.

Zong WX, Lindsten T, Ross AJ, MacGregor GR, Thompson CB. BH3-only proteins that bind pro-survival Bcl-2 family members fail to induce apoptosis in the absence of Bax and Bak. *Genes Dev*. 2001 Jun 15;15(12):1481-6.

APPENDIX 1

A *Sleeping Beauty* transposon-mediated screen identifies murine susceptibility genes for adenomatous polyposis coli (*Apc*)-dependent intestinal tumorigenesis

Timothy K. Starr[a], Patricia M. Scott[b], Benjamin M. Marsh[b], Lei Zhao[b], Bich L. N. Than[b], M. Gerard O'Sullivan[a,c], Aaron L. Sarver[d], Adam J. Dupuy[e], David A. Largaespada[a], and Robert T. Cormier[b]

[a]Department of Genetics, Cell Biology and Development, Center for Genome Engineering, Masonic Cancer Center, University of Minnesota, Minneapolis, MN 55455; [b]Department of Biochemistry and Molecular Biology, University of Minnesota Medical School, Duluth, MN 55812; [c]Department of Veterinary Population Medicine, College of Veterinary Medicine, University of Minnesota, St. Paul, MN 55108; [d]Department of Biostatistics and Informatics, Masonic Cancer Center, University of Minnesota, Minneapolis, MN 55455; and [e]Department of Anatomy and Cell Biology, University of Iowa, Iowa City, IA 52242

Starr TK, Scott PM, Marsh BM, Zhao L, Than BL, O'Sullivan MG et al. A Sleeping Beauty transposon-mediated screen identifies murine susceptibility genes for adenomatous polyposis coli (Apc)-dependent intestinal tumorigenesis. *Proc Natl Acad Sci USA* 2011; 108: 5765–5770.

Abstract

It is proposed that a progressive series of mutations and epigenetic events leads to human colorectal cancer (CRC) and metastasis. Furthermore, data from resequencing of the coding regions of human CRC suggests that a relatively large number of mutations occur in individual human CRC, most at low frequency. The functional role of these low-frequency mutations in CRC, and specifically how they may cooperate with high-frequency mutations, is not well understood. One of the most common rate-limiting mutations in human CRC occurs in the adenomatouspolyposis coli (*APC*) gene. To identify mutations that cooperate with mutant *APC*, we performed a forward genetic screen in mice carrying a mutant allele of *Apc* (Apc^{Min}) using *Sleeping Beauty (SB)* transposon-mediated mutagenesis. Apc^{Min} *SB*-mutagenized mice developed three times as many polyps as mice with the Apc^{Min} allele alone. Analysis of transposon common

insertion sites (CIS) identified the Apc locus as a major target of *SB*-induced mutagenesis, suggesting that *SB* insertions provide an efficient route to biallelic Apc inactivation. We also identified an additional 32 CIS genes/loci that may represent modifiers of the Apc^{Min} phenotype. Five CIS genes tested for their role in proliferation caused a significant change in cell viability when message levels were reduced in human CRC cells. These findings demonstrate the utility of using transposon mutagenesis to identify low-frequency and cooperating cancer genes; this approach will aid in the development of combinatorial therapies targeting this deadly disease.

Human colorectal cancers (CRC) generally can be divided into two classes based on whether they display chromosomal instability (CIN) or microsatellite instability (MSI). The majority of CRC (~80–90%) have a CIN phenotype; the remaining cases are characterized by MSI (Grady and Markowitz 2002). CRC displaying CIN frequently harbor allelic losses or mutations in adenomatous polyposis coli (*APC*), v-Ki-ras2 Kirsten rat sarcoma viral oncogene homolog (*KRAS*), SMAD family member 4 (*SMAD4*), and tumor protein p53 (*TP53*), whereas MSI-type CRC usually have a mutation in one of six DNA mismatch repair genes (Takayama *et al.* 2007). In both CIN and MSI CRC complete functional loss of a gatekeeper tumor suppressor gene typically is the rate-limiting event in intestinal cell transformation. For CIN CRC, *APC* plays the key gate-keeping role, and its loss underlies the great majority of CIN CRC and >80% of all CRC. Although both classes of CRC are characterized by high-frequency mutations, such as those in *APC*, it is evident that many more low-frequency mutations are required for CRC development, and the majority of these low-frequency mutations are unknown (Wood *et al.,* 2007).

To identify these low-frequency mutations, we performed a forward genetic screen in mice using the *Sleeping Beauty (SB*) DNA transposon as a mutagen in intestinal epithelial cells. To focus on mutations that contribute to the CIN phenotype, we conducted the screen in mice carrying the Apc^{Min} allele. Apc^{Min} mice harbor a T→A nonsense mutation in the *Apc* gene (Moser *et al.,* 1990, Su *et al.,* 1992) that results in a truncated protein product that is unable to bind β-catenin and promote its degradation,

thus leading to abnormal levels of β-catenin protein and up-regulation of β-catenin target genes such as cyclin D1 (*Ccnd1*) and myelocytomatosis oncogene (*C-Myc*). The *Min* mutation corresponds to a mutational hotspot in the human *APC* ortholog, and these mutations similarly result in dysregulation of the WNT/β-catenin signaling pathway. There is strong evidence that β-catenin dysregulation is a common transformative event in tumorigenesis in the Apc^{Min} mouse and in both the inherited form of *APC*-deficient CRC (familial adenomatous polyposis, FAP) and in sporadic CRC (Fodde R 2002). Thus, the Apc^{Min} mouse is an informative genetic model for *APC*-deficient intestinal cancer. Apc^{Min} mice on the C57BL/6J background strain rarely survive beyond 120 d and can develop >100 tumors throughout the small and large intestine, with the phenotype dependent on diet, mouse strain, and other environmental factors (Dietrich *et al.,* 1993, Cormier *et al.,* 1997).

As in human CRC patients, loss of heterozygosity (LOH) leading to inactivation of both alleles of *Apc* is necessary for tumorigenesis to commence in Apc^{Min} mice (Levy *et al.,* 1994, Luongo *et al.*, 1994). However, in contrast to LOH events in many human CRC, LOH in Apc^{Min} tumors occurs predominantly by homologous somatic recombination (Haigis and Dove 2003). In this study we screened for mutations that cooperate with the Apc^{Min} mutation by randomly mutating genes through selective activation of SB transposition in intestinal cells of Apc^{Min} mice. The results of our screen support the importance of the loss of the second allele of *Apc*, because the great majority of tumors analyzed contained a transposon insertion in *Apc*, in particular in tumors in which there was maintenance of heterozygosity (MOH) for the *Min* allele. In addition to *Apc*, we identified 32 other genes and loci that probably facilitate the development of intestinal cancer in an Apc^{Min} model. The function of these additional mutations could be to remove the requirement for *Apc* LOH, or they may function in some other manner. The majority of these genes have not been associated with CRC previously. To confirm that these genes play a causal role in tumor development, we used siRNA to knock down message levels of nine of the candidate genes in human colon cancer cell lines and demonstrated that five of these genes affected the growth rate of these cells.

Results

Design of a Forward Genetic Screen for CRC Genes. In a previous study we demonstrated that *SB* transposon-mediated mutagenesis in the intestinal tract of C57BL/6J $Apc^{+/+}$ mice resulted in polyp formation (Starr *et al.,* 2009). By mapping transposon insertions in DNA extracted from these tumors, we were able to identify 77 genetic loci which probably harbored genes that, when mutated, contributed to tumor development. Because *APC* loss is rate limiting in the development of most human CRC (Powell *et al.,* 1992), we reasoned that *SB* mutagenesis in a mouse already harboring a mutation in *Apc* might generate more tumors with a shorter latency and reveal mutations that cooperate with *Apc* during tumor development.

To identify these genes, we performed a forward genetic screen using *SB* transposon-mediated mutagenesis in Apc^{Min} mice. The screen consisted of a cohort of Apc^{Min} SB transgenic test mice along with three groups of Apc^{Min} control mice. The Apc^{Min} SB test mice harbored three transgenes required for targeting *SB* mutagenesis to the gastrointestinal tract (Figure 35). The first transgene was a concatamer of oncogenic transposons (T2/Onc) that were resident on chromosome 1 (Collier *et al.,* 2005). To enhance the mutagenic potential of the transposon, T2/Onc contains a strong viral promoter, splice acceptors in both orientations, and a bidirectional polyA signal. The second transgene was a conditionally expressed knockin SB11 transposase allele downstream of the Rosa26 promoter (Rosa26-LsL-SB11) (Zambrowics *et al.,* 1997, Dupuy *et al.,* 2009). Because of the presence of a floxed stop cassette, the transposase allele is not expressed unless Cre recombinase protein is present. The third transgene was Cre recombinase driven by the gastrointestinal tract-specific Villin promoter (Vil-Cre) (el Marjou *et al.,* 2004). We have shown previously that these three transgenes effectively limit SB mutagenesis to the intestinal tract (Starr *et al.,* 2009). All mice were heterozygous for the Apc^{Min} allele, and all the transgenes were fully congenic on the C57BL/6J genetic background. The first control group contained Rosa26-LsL-SB11 and either Vil-Cre or T2/Onc; the second control group contained T2/Onc and/or Vil-Cre but

not Rosa26-LsL-SB11; and the third control group harbored only the *Apc*^{Min} allele. Mice were killed when moribund or at 120 d.

Intestinal Tumorigenesis Is Enhanced Significantly in *Apc*^{Min} SB Test Mice. *Apc*^{Min} mice that harbored all three transgenes (Rosa26-LsL-SB11, T2/Onc, and Vil-Cre) developed an average of 360 polyps (test mice, Table 9). In contrast, mice carrying the *Apc*^{Min} allele alone developed an average of 112 polyps (control group 3, Table 9), a result that is consistent with the phenotype of *Apc*^{Min} mice in our colony (McAlpine *et al.,* 2006). Surprisingly, we also observed an enhanced rate of polyp development in control group 1 that carried the Rosa-26-LsL-SB11 allele but not the complete combination of alleles required for transposition. This control group developed an average of 182 polyps (control group 1, Table 9), a result that was unexpected based on previous screens. It is possible that the increased polyp number in these animals is caused by one or more modifiers linked to the Rosa26-LsL-SB11 transgene, because strain-specific modifiers are known to exist (Fodde and Smits 2001). Control animals carrying the *Apc*^{Min} allele, T2/Onc, and/or Vil-Cre, but not Rosa26-LsL-SB11 (control group 2, Table 9) developed the same number of polyps as the control mice carrying the *Apc*^{Min} allele alone. Although the Rosa26-LsL-SB11 allele alone contributes to polyp formation, the effect of active *SB* transposition was much greater, resulting in twice as many polyps in the test mice. In addition, the tumor burden was so extensive that *Apc*^{Min} SB test mice became moribund earlier than any of the three control groups (Table 9). Indeed, in a subset of *Apc*^{Min} SB test mice the tumor load was very severe, with some animals developing as many as 700 tumors.

		Average no. polyps per mouse†			
Group*	Number per group	Large intestine	Small intestine	Total	Date of death‡
Test	38	14.7	345	360	85
Control 1	57	4.2	178	182	110
Control 2	9	2.4	113	115	120+
Control 3	100	2	110	112	120+

*Groups: Test = Apc^{Min} × Rosa26-LsL-SB11 × T2/Onc × Vil-Cre; Control 1 = littermates harboring either Apc^{Min} × Rosa26-LsL-SB11 or Apc^{Min} × Rosa26-LsL-SB11 × T2/Onc or Apc^{Min} × Rosa26-LsL-SB11 × Vil-Cre; Control 2 = littermates harboring either Apc^{Min} × T2/Onc or Apc^{Min} × Vil-Cre or Apc^{Min} × T2/Onc × Vil-Cre; Control 3 = contemporaneous mice harboring Apc^{Min} only.

†Average number of polyps per mouse by large intestine, small intestine, and total.

‡Control groups 2 and 3 were killed at 120 d whether they were moribund or not.

Table 9. Polyp number and age of death for transgenic mice.

Although polyp number was greatly increased by *SB* mutagenesis, there was no evidence of local or systemic metastasis in experimental or control mice. We performed histopathologic analysis of tumors collected from 10 animals. These analyses identified numerous microadenomas and adenomas in the small intestine and a much smaller number of these lesions in the large intestines. No adenocarcinomas were identified, perhaps because of the short lifespan of Apc^{Min} SB test mice. Immunohistochemistry for β-catenin was performed on 24 adenomas from seven animals. There was increased expression of β-catenin in all tumors compared with the adjacent normal mucosa epithelium (Figure. 34).

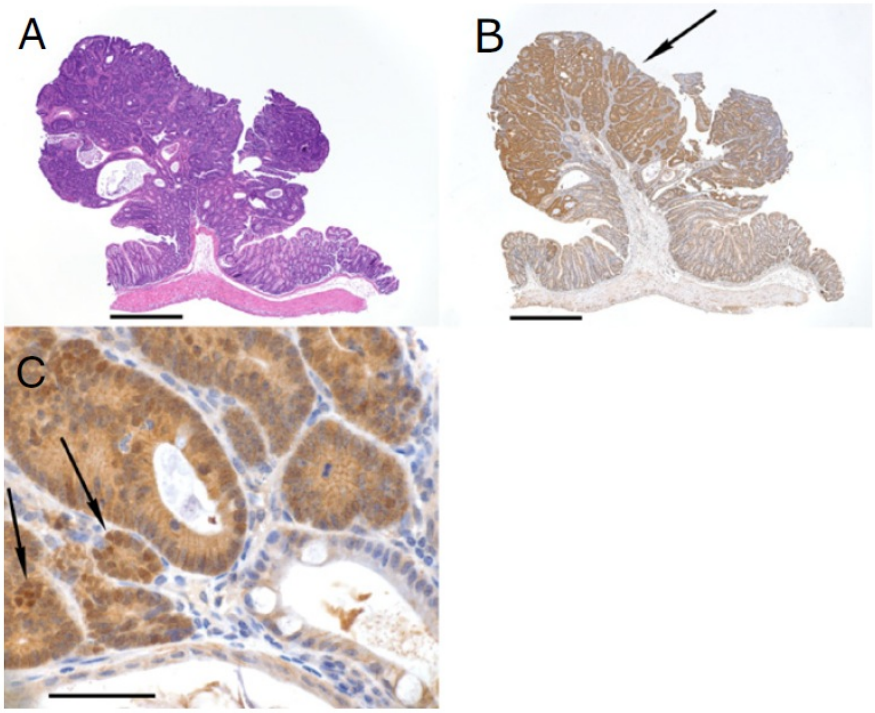

Figure 34. A pedunculated adenoma stained with H&E (A) or immunostained for β-catenin (B and C). (B) There is increased staining for β-catenin (arrow) in the adenoma. **(C)** Higher-power magnification of a different section showing increased cytoplasmic and nuclear (arrows) staining for β-catenin in tumor cells compared with adjacent normal tissue seen in lower right and bottom of picture. (Scale bars: A and B, 500 μm; C, 50 μm.)

Analysis of Common Insertion Sites Identifies 30 Candidate Cancer Genes. To identify genes that contribute to tumor initiation and development in Apc^{Min} mice, we analyzed transposon insertions in 96 polyps, representing all regions of the intestines, from 12 mice to find common insertion sites (CIS). A CIS is defined by analyzing transposon insertions in many tumors and identifying genomic loci that contain transposon insertions at a higher rate than would be expected by chance (SI Materials and Methods). The presence of a CIS indicates that a transposon-mediated mutation in that locus probably has contributed to tumor development. By analyzing the genes within the CIS, one can identify candidate cancer genes. To map transposon insertions, we isolated DNA from the 96 tumors, digested the DNA with restriction enzymes, and performed ligation-mediated PCR (LM-PCR) to amplify transposon-genomic fragments specifically (Mueller and Wold 1989). Barcodes and fusion sequences were attached to the LM-PCR primers to enable pooling of the amplicons, which then were sequenced using the Roche GS FLX pyrosequencing machine. Six separate sequencing runs produced 347,993 sequence reads, 93% of which contained a barcode, the transposon sequence, and sufficient genomic sequence (>16 bp) for BLAST analysis. We were able to map more than half of these sequences (53%) unambiguously to the mouse genome. Of the 173,101 mapped sequences, 100,171 (67%) were redundant, leaving 72,930 nonredundant mapped insertions. Roughly half of the nonredundant insertions mapped to the same chromosome as the donor transposon concatamer (Chr 1), as expected because of the phenomenon of local hopping seen in other SB screens (Starr *et al.* 2009, Collier *et al.* 2005, Keng *et al.* 2009). To eliminate statistical bias in the dataset, these sequences were eliminated along with a smaller number of insertions that probably represent PCR artifacts (SI Materials and Methods). The remaining 30,088 insertions (Table 15) weranalyzed to determine CIS. We used Monte Carlo simulations to find insertion rates in a given genomic window size that would not be expected to occur by chance (Starr *et al.,* 2009). For example, based on a random assignment of 30,088 insertions to the mouse genome, one would not expect to find five or more insertions within a 12-kb window. Using these Monte Carlodefined parameters, we identified 37 CIS. Two of these CIS were removed from further analysis because all the tumors contributing to these two CIS

originated from a single mouse, indicating the tumors may be clonally related. Two more CIS were removed because they also were identified in a control dataset of tail-snip DNA from mice harboring unselected SB insertions and may represent hotspots for SB insertions (Starr *et al.,* 2009) Because this control dataset was generated from tail snips, it is possible that other hotspots exist in other types of cells. After removal of these possible artifacts, 33 CIS remained (Table 10).

We assigned a candidate gene to each CIS if the majority of the insertions were in or near a single gene (Table 10). Four of the 33 CIS did not have an annotated gene within 40 kb and were not assigned a candidate gene. Another CIS contained two overlapping genes, SET domain-containing 5 (*Setd5*) and lipoma HMGIC fusion partner-like 4 (*Lhfpl4*), and all insertions in this CIS were in both genes. Notably, this CIS is located adjacent to the Rosa26 locus where the conditional SB11 knockin is located, and eight of nine insertions in this CIS are oriented with the internal promoter in the direction that would cause overexpression of the transgene. Rather than tagging an endogenous cancer gene, this CIS could represent selective pressure for increased mutagenesis via overexpression of SB11 transposase. Whether the transposon insertion caused a gain- or loss-of-function mutation sometimes can be predicted by analyzing the location and orientation of the insertions in all the tumors that comprise a single CIS. If all the tumors in a single CIS have transposon insertions in the same intron, and all the transposons are oriented in the direction of transcription, we predict the insertion causes a gain-of-function mutation. If the distribution of transposon insertions in all the tumors of a CIS is apparently random, and there is no bias in orientation, we predict a loss-of-function effect. Table 10 lists the predictions for the CIS. In total we identified 30 genes and four genomic loci with no annotated genes that probably contribute to intestinal tract cancer when mutated.

Candidate gene	Chromosome	Start address*	End address*	Number of insertions†	Tumors with insertions‡	Predicted effect on gene§
4930422G04Rik	3	127241424	127431287	23	12	NP
AC115907.7	3	127697338	127730035	8	8	NP
AC131780.5	9	3001410	3030207	7	7	NP
Adamts6	13	105093822	105104050	5	3	NP
Ap1ar	3	127454370	127633377	17	10	NP
Apc	18	34324389	34514767	185	72	Loss
Atf2	2	73708689	73773260	9	9	NP
Atl2	17	80239637	80306988	10	7	Loss
Cnot1	8	98254541	98300340	8	8	Loss
Csnk1a1	18	61726208	61750047	7	6	Loss
Elac1	18	73903365	73913215	5	3	Gain
Emcn	3	136918543	137092521	17	9	NP
Esco1	18	10578932	10773953	15	11	Loss
Fnbp1l	3	122217801	122319064	11	11	Loss
Itgam	7	135180978	135240752	11	10	NP
Myo5b	18	74613029	74796289	18	17	Gain
No Gene 16	16	29019897	29031672	5	3	NP
No Gene 18	18	26169184	26282443	12	7	NP
No Gene 4	4	131170124	131238909	12	8	NP
No Gene Y	Y	2781406	2897989	16	15	NP
Nsd1	13	55352993	55372133	6	6	Gain
Pdcd6ip	9	113560446	113723693	14	14	Loss
Pde4dip	3	97593369	97718572	14	11	NP
Pigl	11	62203495	62369763	16	16	NP
Setd5 or Lhfpl4	6	113039133	113100176	9	9	NP
Sfi1	11	3004743	3179859	21	19	Loss
Snx24	18	53440600	53638364	19	12	Loss
Srfbp1	18	52654288	52675270	6	5	NP
Stag1	9	100583003	100698850	12	12	Loss
Tmem132b	5	126077980	126153976	11	4	Loss
Wac	18	7855248	8046126	17	15	Loss
Zfp397	18	24110107	24157877	8	7	NP
Zfp609	9	65561432	65607064	8	8	Loss

*Genomic address based on National Center for Biotechnology Information Mouse genome Build 37.

†Number of nonredundant *SB* transposon insertions within the locus.

‡Number of independent tumors with an insertion within the locus.

§Predicted effect is based on an analysis of the location and orientation of SB transposon insertions in all tumors in a single CIS (see text for discussion). Gain, gain of function; Loss, loss of function; NP, no prediction.

Table 10. List of 33 CIS.

Transposon Insertions Implicated in LOH of the Wild-Type Allele of *Apc*. The most commonly mutated gene in this study was *Apc* (in 72 of 96 tumors), reflecting the strong selective pressure for loss of the wild-type allele in Apc^{Min} mice. Previous studies have demonstrated that loss of the Apc^{+} allele is an early event that occurs in almost every adenoma in Apc^{Min} mice (Levy *et al.,* 1994, Luongo *et al.,* 1994). In addition, inactivation of the wild-type *Apc* allele is caused predominantly by homologous somatic recombination events, leading to the replacement of the *Apc* wild-type allele with a second Apc^{Min} allele. We reasoned that in our transgenic model LOH could be accomplished by an inactivating transposon insertion, as opposed to duplication of the *Min* allele. To test this hypothesis, we performed PCR on DNA from tumors to amplify the region surrounding the *Min* mutation (T2860A). By sequencing the PCR amplicon, LOH can be ascertained in Apc^{Min} mice by measuring the ratio of the T:A trace peak heights at the location of the *Min* mutation. In heterozygous tissue the T:A ratio is between 0.8 and 1.2, which is considered MOH, but in tissue that has lost the wildtype allele the ratio drops below 0.5 (Figure 36). Ratios between 0.5-0.8 and >1.2 are considered uninformative, most likely caused by contamination from nontumor tissue. Of the 96 tumors tested, 47 gave informative results (Table 11). Of these 47 tumors, 32 had an identified transposon insertion in the *Apc* locus, and 15 did not. The majority (73%) of tumors lacking a transposon insertion in *Apc* had T:A ratios < 0.5, indicating LOH probably caused by loss of the entire allele. In support of our hypothesis, 53% of the tumors that had a transposon insertion in the *Apc* locus had T:A ratios between 0.8 and 1.2, indicating maintenance of the wild-type *Apc* locus at the site of the *Min* mutation. This result suggests that in these tumors the wild-type *Apc* allele is inactivated by the transposon more frequently than by duplication of the *Min* allele.

Set of CIS Identified in Apc^{Min} Mice Differs Significantly from Those Found in *Apc* Wild-Type Mice. We compared the list of genes identified in this study with the 77 genes identified in the screen we performed on an *Apc* wild-type background (Starr *et al.,* 2009). Surprisingly, only four genes were identified in both studies: *Apc*, nuclear receptor binding SET domain protein 1 (*Nsd1*), Sfi1 homolog, spindle assembly associated (*Sfi1*), and WW domain containing adaptor with coiled-coil (*Wac*). There are several reasons

that could explain why the overlap between the two studies was low. First, the total number of genes that could contribute to tumor formation may be large enough that the size of these two studies is not sufficient to saturate the candidate genes. Second, because we use a statistical method to identify cancer genes, it is likely that transposon insertions contributed to carcinogenesis in some of the tumors, but the insertions did not occur at a rate high enough to qualify as a CIS. In support of this hypothesis, 70% of the loci identified as CIS in this study (23 of 33) also had one or more insertions in the same locus in the previous study. Third, the overlap may be small because selection pressure for specific genetic mutations in cells that already have an Apc mutation is biased toward a different set of cancer genes than in cells with a different initial mutation. Fourth, because of technical limitations, our method of amplifying and sequencing transposon insertions does not identify all transposon insertions, so a portion of driver mutations will not be identified. For example, analysis of replicate sequencing runs indicates that 20–40% of the PCR amplicons in a given library are not sequenced in a given GS FLX sequencing run (SI Materials and Methods and Table 12).

Relevance to Human Disease. To determine the relevance of these findings to human cancers, we analyzed the regions of human orthology to the CIS loci and the orthologous human genes. Of the 30 candidate mouse genes associated with a CIS, 28 had human orthologs. We queried the literature for mutations and recurrent copy number changes in these genes in human CRC. Three of the genes, *APC, NSD1*, and phosphodiesterase 4D interacting protein (*PDE4DIP*), are considered bona fide cancer genes based on the cancer gene census maintained by the Wellcome Trust Sanger Institute (Futreal *et al.* 2004). Eight genes, *APC*, activating transcription factor-2 (*ATF2*), atlastin GTPase 2 (*ATL2*), casein kinase 1, alpha 1 (*CSNK1A1*), integrin, alpha M (*ITGAM*), programmed cell death 6-interacting protein (*PDCD6IP*), and *WAC*, have documented mutations in human cancers cataloged in the COSMIC database (Forbes *et al.,* 2006).

We found strong concordance between the CIS mouse loci and orthologous regions in the human genome showing recurrent chromosomal losses and gains in human CRC (Vogelstein *et al.,* 1989, Reid *et al.,* 1996, Nakao *et al.,* 2004, Habermann *et al.,* 2007, Lassmann *et al.,* 2007, Shih *et al.,* 2001, Derks *et al.,* 2008, Kurashina *et al.,* 2008).

Of the 33 identified CIS, 31 can be mapped to an orthologous human locus. Of these 31 candidate cancer loci, 24 are found in regions that commonly are lost or gained in human CRC (Table 13), including several of the CIS that are orthologous to human chromosomal arms 18q, 17p, 5q, and 4q. Interestingly, one CIS that has no annotated genes nearby (CIS No gene 16) is in an orthologous region (3q21–24) that is associated with CRC based on genome-wide linkage analyses (Kemp *et al.,* 2006, Neklason *et al.,* 2008). To determine the significance of this overlap, we performed the analysis using randomly generated CIS lists and a single dataset of regions that are lost recurrently in human CRC (Nakao *et al.,* 2004). Roughly 250 genomic regions in this dataset were lost in > 5% of the human samples tested, and 22 of the 31 CIS were located within these regions. In 10,000 simulations using equivalent-sized randomly generated CIS lists, we find an overlap of this magnitude < 0.3% of the time. These results suggest that our *SB* screen may be capable of pinpointing the affected genes in these regions.

Candidate Genes Regulate Proliferation of Human CRC Cell Lines. We tested nine genes [CCR4-NOT transcription complex, subunit 1 (*CNOT1*), *PDE4DIP*, *PDCD6IP*, *ATF2, SFI1*, *formin-binding protein 1-like (FNBP1L*), *myosin VB (MYO5B), sorting nexin 24 (SNX24)*, and *stromal antigen 1 (STAG1)*] for their effect on proliferation of the human CRC cell line SW480 by knocking down message levels using siRNA. We used the SW480 line because it has an APC gene-truncation mutation similar to the ApcMin mutation (Nishisho *et al.,* 1991). Cells were transfected two times at 48-h intervals with siRNA targeting the human genes. Knockdown efficiency was at least 50% for all nine genes as measured by quantitative real-time PCR. Cell proliferation was measured using a tetrazolium-based colorimetric assay on days two and six after the second transfection. Depletion of five (*CNOT1, PDE4DIP, PDCD6IP, ATF2*, and *SFI1*) of the nine genes tested resulted in a significant decrease in cell viability compared with a control siRNA of at least 33% at day six after transfection (Table 14).

Discussion

Using a transposon-based forward genetic screen in mice, we identified 33 genomic loci that probably cooperate with a germline mutation in the *Apc* gene to cause

intestinal tumorigenesis. The most frequently mutated locus was the *Apc* locus, a result that supports the hypothesis that there is strong selective pressure to lose the wild-type copy during tumor formation. *SB* insertions in *Apc* were found in 72 of 96 tumors (75%), suggesting that 75% of the tumors in Apc^{Min} SB test mice undergo LOH at the *Apc* locus via *SB* insertional mutagenesis. This hypothesis is supported by sequencing of the region spanning the 1-bp *Min* mutation, which indicated that the majority of tumors containing *SB* insertions at the *Apc* locus maintained heterozygosity at the location of the T:A *Min* mutation. In contrast, the majority of tumors lacking a transposon insertion in *Apc* showed loss of the wild-type sequence at the *Min* mutation site. These results suggest that the majority of tumors underwent biallelic loss of *Apc* activity through transposon insertion or somatic recombination. However, it also is possible that in some cases activity was lost through other mechanisms of *Apc* inactivation or through transposon insertion substituting for loss of the wildtype allele.

Although LOH at the *Apc* locus is the rate-limiting event in tumor initiation in the Apc^{Min} mouse and in familial and sporadic *APC*-deficient CRC, loss of *APC* probably is insufficient for the survival and growth of transformed cells into adenomas and, eventually, adenocarcinomas. SB-mutagenized animals showed increased polyp number but no evidence of adenocarcinoma or metastasis. Thus, it is likely that the CIS candidate genes identified in this *SB* screen contribute in a diverse fashion to initiation, establishment, and survival of adenomas. Moreover, depending on the complexity of the mechanism or pathway, the CIS candidates discovered in our screen, like the relatively large number of genes reported to be mutant in individual human CRC (Wood *et al.,* 2007), might be expected to occur at a low frequency if mutations at any one of multiple genes in a complex pathway can contribute equally to tumorigenesis.

Aside from *Apc*, only a few of the remaining 28 known genes that we identified as CIS in our screen have been implicated directly in CRC development, although > 90% are located in genomic regions that are lost or gained in human CRC. To eliminate false positives, we removed CIS that also were identified in a control dataset of unselected transposon insertions mapped in tail snips. However, it is possible that other tissuespecific hotspots could result in false positives. Nevertheless, the known functions

of several of the CIS candidate genes make them plausible candidates for drivers of human CRC. For example, *CNOT1* is a member of the Ccr4-Not complex, which is implicated in mRNA decay and transcriptional repression. In human cells, CNOT1 has been reported to be a repressor of nuclear receptor-mediated transcription (Winkler *et al.,* 2006). One target of CNOT1 repression appears to be estrogen receptor alpha (ERα), via interactions between CNOT1 and the ligand-binding domain of ERα. Inhibition of CNOT1 caused an increase in the expression of ERα target genes in breast cancer cells, and *ERα* has been shown to be a tumor suppressor gene in the intestinal tract (Cho *et al.,* 2007); in particular, knockout of *ERα* in Apc^{Min} mice caused a significant increase in intestinal tumorigenesis (Cleveland *et al.,* 2009).

Another gene identified in this study, *Pdcd6ip* (also known as ALG-2 interacting protein X, Alix) is involved in membrane trafficking and apoptosis (Odorizzi G 2006). *Pdcd6ip* produces a protein that binds to the protein product of *Pdcd6*, a proapoptotic gene involved in T-cell receptor–, Fas-, and glucocorticoid-induced cell death (Vito *et al.,* 1996). *Pdcd6ip* also can block down-regulation of the EGF receptor (EGFR), thereby having a positive effect on growth factor signaling (Schmidt *et al.,* 2004). These contradictory roles could explain why loss of *Pdcd6ip* in the mouse tumors promoted growth (via the loss of the proapoptotic function) but the loss of *Pdcd6ip* in SW480 cells caused decreased proliferation (via increased down-regulation of EGFR). Further functional studies are required to elucidate the role of this adaptor protein.

In summary, our approach identified 30 genes that probably modify tumorigenesis in the Apc^{Min} model of human CRC. Further functional analysis of these CIS candidate genes may provide insights into the etiology and treatment of human CRC, especially those cancers arising downstream of *APC* deficiency.

Materials and Methods (Detailed protocols are given in SI Materials and Methods.)

Mice. Mice containing Apc^{Min}, Rosa26-LsL-SB11, Villin-Cre, and T2/Onc were reared using Institutional Animal Care and Use Committee-approved protocols. All mice were

on an isogenic C57BL/6J background. Mice were monitored daily and killed and necropsied when moribund or after 120 d.

Histopathology and Immunohistochemistry. Formalin-fixed tissues were embedded in paraffin, and standard techniques were used to stain tissue sections with H&E. Standard immunohistochemistry techniques were used to detect β-catenin.

Linker-Mediated PCR. Linkers [described previously (Wu *et al.* 2003)] were ligated to NlaIII- (right-side) or BfaI- (left side) digested genomic DNA using T4 DNA ligase. A secondary digest (XhoI, right side; BamHI, left side) was performed to destroy concatamer-generated products. Primary and secondary PCR was performed using primers specific for linker and SB transposon sequences along with Fusion and barcode sequences. PCR amplicons were sequenced using the GS FLX (Roche).

Sequence Analysis. Sequences were analyzed for the presence of the barcode, inverted repeat/direct repeat (IR/DR) sequences required for transposition, and linker sequences. Genomic sequence was blasted against the mouse genome using BLASTN at 95% stringency and requiring a single match. Of the 324,898 sequences analyzed, 53% could be uniquely mapped to the mouse genome. Sequences were removed if they were redundant, on the donor concatamer resident chromosome (Chr 1), in the En2 gene (because the En2 sequence is present in the transposon), and when a single TA dinucleotide contained multiple insertions from several tumors from multiple mice (because of the possibility of a PCR artifact). The remaining 30,088 nonredundant sequences were used to identify CIS. A CIS was defined by Monte Carlo simulations using a random dataset of 30,088 insertions.

***Apc* LOH Analysis**. To measure LOH for the Apc^{Min} mutation, DNA was isolated from individual polyps, and PCR was performed using primers that flank the mutation (sense primer: CGGAGTAAGCAGAGACACAA; antisense primer: GGGAGGTATGAATGGCTGAT). The PCR product was purified using Qiagen 96 MinElute vacuum purification plates per the manufacturer's protocol and was sequenced using the sense primer as the sequencing primer. Trace peak heights at the location of the mutation were measured for each tumor, and the ratio of the T peak to the A peak was calculated.

Comparisons with Human Data. Eight publicly available studies measuring DNA copy number in CRC compared with normal tissue were analyzed. Mutations in human tumors were examined using the Catalog of Somatic Mutations in Cancer database (Forbes *et al.* 2006), and cancer gene status was based on the Census of Human Cancer Genes maintained by the Wellcome Trust Sanger Institute (Futreal *et al.* 2004).

Knockdown of CIS Candidate Genes using siRNA in SW480 Cells. SW480 cells were obtained from ATCC (catalog no. CCL-228) and were cultured under recommended conditions. Transient siRNA transfection was used to deplete expression of *Min* CIS genes.

Cell Viability Assay. Viability of siRNA-treated SW480 cells was determined using a 3-(4,5-dimethylthiazol-2-yl)-2,5-diphenyltetrazolium bromide (MTT) assay (Cell Viability Kit 1; Roche Applied Sciences).

Supporting Information

SI Materials and Methods

Mice. Apc^{Min} mice (C57BL/6J-ApcMin /J), which harbor a T→A nonsense mutation in the *Apc* gene that results in a truncated protein product, were obtained from a breeding colony at the University of Minnesota Medical School Animal Services facility. Rosa26-LsL-SB11 mice (backcrossed to C57BL/6J) were a generous gift from Adam Dupuy (University of Iowa, Iowa City, IA). Villin-Cre mice [B6.D2-Tg(Vil-Cre)20Syr], strain 01XE7, were purchased from the National Cancer Institute Mouse Repository. T2/Onc mice (mixture of C57BL/6J and FVB) were described previously (Collier *et al.* 2005). Mice were necropsied, and both normal and tumor tissues were collected by snap-freezing in liquid nitrogen or overnight fixation in 10% buffered formalin followed by 70% ethanol. PCR primer sequences were as follows: T2/Onc forward: CGCTTCTCGCTTCTGTTCGC, T2/Onc reverse: CCACCCCCAGCATTCTAGTT; Villin-Cre forward: CAAGCCTGGCTCGACGGCC, Villin-Cre reverse: CGCGAACATCTTCAGGTTCT; Rosa26-lox-stop-lox-SB11 and Rosa26-SB11 knock-in3- primer: wild-type forward: CTGTTTTGGAGGCAGGAA, wildtype reverse:

CCCCAGATGACTACCTATCCTCCC, knock-in reverse: CTAAAAGGCCTATCACAAAC. *Apc*^{Min} mice were genotyped as described previously (Dietrich *et al.* 1993).

Histopathology and Immunohistochemistry. Histopathological analysis of tumors and adjoining normal tissue was performed on tissues that were fixed in 10% neutral buffered formalin, routinely processed into paraffin, sectioned at a thickness of 4μm, and stained with H&E. Multiple H&E sections were obtained from tumors from the colon and duodenum. All tissues were analyzed by an American College of Veterinary Pathologists-certified veterinary pathologist (M.G.O.) from the University of Minnesota Masonic Cancer Comparative Pathology Shared Resources facility and using the standardized nomenclature of the 2003 Consensus Report and Recommendations for pathology of mouse models of intestinal cancer (Boivin *et al.* 2003). Immunohistochemistry was performed on 4-μm formalin-fixed, paraffin-embedded sections of small intestine which were deparaffinized and rehydrated, followed by antigen retrieval using 10 mM citrate buffer, pH 6.0, in a steamer. Staining for β-catenin was performed on a Dako Autostainer using a goat anti-human β-catenin polyclonal antibody (catalog no. sc-1496; Santa Cruz) as primary antibody (after blocking endogenous peroxidase and application of a protein block), with detection by a biotinylated donkey anti-goat antibody (Jackson ImmunoResearch Laboratories) and streptavidin-linked horseradish peroxidase (Dako) using diaminobenzidine (Dako) as the chromogen. Mayer's hematoxylin (Dako) was used as the counterstain. Small intestinal adenomas from *Apc*$^{Min/+}$ mice were used as a positive control tissue, and for negative control slides the primary antibody was substituted with Super Sensitive Goat Negative Serum (Biogenex).

Linker-Mediated PCR. Linkers used to sequence insertions weredescribed previously (Wu *et al.* 2003). Genomic DNA was digested with NlaIII (for sequencing from the right side of T2/Onc) or BfaI (for sequencing from the left side of T2/Onc) and ligated to the linker using T4 DNA ligase. A secondary digestion was performed to destroy concatamer-generated products (XhoI for right-side cloning and BamHI for left-side cloning). These two enzymes do not cut the transposon distal to the NlaIII or BfaI sites

but do cut the plasmid backbone present in the transgene concatamer, effectively destroying concatamer linker amplicons. Primary PCR was performed using primers that flank the inverted repeat/di direct repeat (IR/DR) sequences and the linker. Primer sequences are listed below. Primary PCR products were diluted 1:75 and used in a secondary PCR with nested primers. Secondary PCR was performed using FusA+BC+Left2°Primer or FusA+BC+ Right2°Primer and FusB+linker2°Primer primers (see below). FusA and FusB are sequences required for pyrosequencing using the 454 GSFlex machine (BC, barcode). PCR products were quantified using QuantIT picogreen assay (Invitrogen) and diluted to a concentration of 200,000 molecules/μL. All tumor samples were combined and diluted by the number of samples added, for a final concentration of 200,000 molecules/μL. Samples were sequenced using the Roche Genome Sequencer FLX using 454 pyrosequencing technology (Roche Applied Science) by the University of Minnesota Biomedical Genomics Center. Sequences (all sequences are listed in the 5′ → 3′ direction) used were

Left linker+: GTAATACGACTCACTATAGGGCTCCGCTTAAGGGAC

Left linker−: TAGTCCCTTAAGCGGAG

Right linker+: GTAATACGACTCACTATAGGGCTCCGCTTAAGGGACCATG

Right linker−: GTCCCTTAAGCGGAGCC

Linker 1°Primer: GTAATACGACTCACTATAGGGC

Linker 2°Primer: AGGGCTCCGCTTAAGGGAC

(Note, linker primers work for both the Left linker and the Right linker)

Left 1°Primer: CTGGAATTTTCCAAGCTGTTTAAAGGCACAGTCAAC

Left 2°Primer: GGACATCTACTTTGTGCATGACACAAGTC

Right 1°Primer: GCTTGTGGAAGGCTACTCGAAATGTTTGACCC

Right 2°Primer: CCACTGGGAATGTGATGAAAGAAATAAAAGC

FusA+BC+Left2°Primer:

GCCTCCCTCGCGCCATCAGAATGCCGCATTTAAGTGTATGTAAACTTC

Fusion A: GCCTCCCTCGCGCCATCAG

Example barcode (each tumor is different): AATGCCGCAT.

FusA+BC+Right2°Primer:
GCCTCCCTCGCGCCATCAGAATGCCGCATTAAGGTGTATGTAAACTTC
FusB+linker2°Primer: GCCTTGCCAGCCCGCTCAGAGGGCTCCGCTTAAGGGAC
Fusion B: GCCTTGCCAGCCCGCTCAG
A full list of barcodes is available upon request.

Processing of Sequence Files. PCR amplicons were generated so that the 10-bp library-identifying barcode always appeared in the beginning of the sequence in the sense orientation. Sequence quality was outstanding even up to the first base. Using a custom Perl script, we scanned positions 1–12 of all reads for the presence of the library barcode, allowing 0 or 1 mismatch. We typically found perfect matches to a single barcode at positions 1–11, with matches at 2–12 occurring rarely. We did not find barcode sequences (0–1 mismatch) anywhere else in the read sequences. We successfully assigned 98% of all sequence reads to a library barcode. All barcodes differed by at least 2 bp, and no sequence read matched two or more barcodes in a given region. This process was carried out separately for each of the six 454 pyrosequencing regions used in these analyses. Following barcode identification, the data for each of the six runs were merged to allow uniform handling of the entire dataset. Note that we did not attempt to assemble reads into contigs for several reasons: (i) The read quality was outstanding, matching the consensus with >99.9% accuracy when assembly was performed; (ii) the contigs tended not to tile at all, because the reads all were primed at the same location and are of similar length, conferring little advantage to using contigs; and (iii) assembly might introduce chimeric artifacts, particularly when two relatively closely spaced insertion sequences appeared on opposite strands.

To identify and remove IR/DR and linker sequences from each read, we applied EMBOSS Vectorstrip (Rice *et al.* 2000) with custom-designed modifications for pipeline application and assessed the best mismatch parameters to use. We sequentially attempted to match both construct elements (IR/DR and linker) in sense and antisense orientations with four successively less stringent parameter sets:

i) 10% mismatch allowed, long-construct elements (17–32 bp)

ii) 10% mismatch allowed, short-construct elements (<26 bp)

iii) 15% mismatch allowed, short-construct elements (<26 bp)

iv) 20% mismatch allowed, short-construct elements (<26 bp)

Note that the short-construct elements affect only the IR/ DR sequence, because the linker element already is shorter than 26 bp. As we reduced the stringency, more construct elements could be detected, but the risk of finding spurious chance matches increased. To guard against the introduction of spurious matches, we used generic scripts to assign a label to each recognized construct that was encountered from the 5′end to the 3′ end. We assigned the following labels: Ideal: a construct with both IR/DR and linker elements in the same orientation

No-linker: a construct with an IR/DR but missing a linker

No-IR/DR: a construct missing the IR/DR

Bad: a construct with no recognizable elements or multiple IR/DRs

Unknown: anything else

For example, an ideal construct might look like 11-[+IR/DR]- 42-[+linker]-4, where, in this case, the 42-bp insertion is in the sense orientation (as indicated by the + signs for IR/DR and linker). The numbers between elements in this representation indicate the number of base pairs between elements. Insertions < 16 bp were considered empty or unmappable. Ideal and nearly ideal construct configuration counts were monitored as the stringency parameters were relaxed. We expected the number of ideal configurations detected to increase and the unknown count to remain steady until we hit a parameter set that was too lax. We started with the strictest set of parameters (stringency level 0) and collected all ideal configurations. Then we took all sequences with nonideal configurations through stringency levels 1–3 to see if we could move them into the ideal category. In our final merged summary sequence table, the best status (ideal > no-linker > no-IR/DR > bad) was reported for each sequence along with the data for the most stringent run level (0–3) where it achieved this label.

Mapping Insertion Sequences. To map sequences to the mouse genome [National Center for Biotechnology Information (NCBI) Build 37], we used BLASTN (DeCypher's TeraBLASTN, Active Motif, http://timelogic.com), requiring query sequences to align within 1 bp of the start of right-IR/DR sequences or within 1 bp of the end of left-IR/DR

sequences (i.e., within 1 bp of the transposon insertion site with both types of reads). Additionally, the query was required to match with at least 95% identity. Lower thresholds of 90% and 85% identity were tested but failed to yield sufficiently higher percentages of newly mappable insertions to warrant lowering the matching stringency. Because we were most interested in the IR/DR position, we were careful to ensure that the query matched within 1 bp of the IR/DR insertion site, but we did not require the 3′ end of the query to match, in case cloning artifacts had altered that end of the sequence. If secondary genome hits were found that were at least 95% as long as the first match, their count was recorded, and the insertion location was considered ambiguous. However, if all secondary hits appeared within 5,000 bp of the primary hit on the same chromosome, we considered the insertion to be uniquely mappable to that locus. Of the 324,898 sequences analyzed by BLASTN, 173,101 (53%) could be uniquely mapped to the mouse genome. We removed redundant sequences that arose from the same tumor and mapped to the same TA dinucleotide insertion site in the genome. Of the 173,101 mapped sequences, 100,171 (67%) were redundant, leaving 72,930 nonredundant mapped insertions. Three more filtering steps were performed:

i) To avoid the bias of "local hopping," all nonredundant insertions mapping to the chromosome containing the transposon donor concatamer (Chr 1) were removed.

ii) The T2/Onc transposon contains sequence from an intron and splice acceptor of the murine En2 gene. Any insertions mapping to this sequence were removed because they might represent a transposition event back into the concatamer and not an insertion into the genomic En2 locus.

iii) Three-primer PCR was used to validate a sampling of nonredundant mapped insertions. We were successful in validating mapped insertions except in one circumstance. When a single TA dinucleotide contained multiple insertions from several tumors from multiple mice, we could not validate the insertions with three-primer PCR in some cases. We hypothesize that some of these TA dinucleotides are neasequences that cause PCR artifacts and do not represent true transposon insertions. We chose to adopt a conservative approach to avoid these artifacts, so we eliminated all insertions in TA dinucleotides containing insertions from two or more tumors from two or more different

mice. These three filtering steps removed 42,842 (59%) insertions, leaving a total of 30,088 nonredundant mapped insertions. This set was used to determine CIS.

Statistics Used to Identify CIS. To identify CIS, nonredundant insertions were assigned to clusters if the local density of insertions in a given window size exceeded that which would be expected by chance. Window sizes were determined by exact Monte Carlo simulation (see below). Based on a dataset of 30,088 insertions, the significance thresholds obtained are:

Five or more insertions within 12,000 bp
Six or more insertions within 22,000 bp
Seven or more insertions within 34,000 bp
Eight or more insertions within 50,000 bp,
Nine or more insertions within 65,000 bp
Ten or more insertions within 82,000 bp
Eleven or more insertions within 105,000 bp
Twelve or more insertions within 124,000 bp
Thirteen or more insertions within 150,000 bp
Fourteen or more insertions within 175,000 bp
Fifteen or more insertions within 200,000 bp

The assumption of standard Poisson statistics that potential insertion sites are randomly distributed throughout the genome is not strictly correct, because (i) TA dinucleotides are naturally clustered in genomes, and (ii) numerous unfinished regions in the mouse genome are "off-limits" because they are long tracts of Ns. For example, the initial telomeric region of every chromosome except Y is padded with 3 million consecutive Ns. Both these factors lead standard analytical approaches to underestimate\ the size and number of clusters that actually would be encountered by simply picking randomly chosen real TA sites. In other words, by ignoring the natural clustering of TA sites in the genome, the number of false-positive CIS that will be predicted is increased systematically. The magnitude of deviation gets larger as more and more insertion sites are scattered about the genome, as one would expect intuitively. Hence, we wrote a program to compute exactly the expected number of CIS of a given size in a specified

window across all the chromosomes that one would encounter by chance via Monte Carlo simulation. The observed number of unambiguous mappable nonredundant insertions was used for each chromosome separately as input. For example if chromosomes 1 and 2 had 2,100 and 1,420 insertions, respectively, then we randomly distributed 2,100 insertions among the real TA dinucleotide sites on mouse chromosome 1 and another 1,420 among the TA sites of chromosome 2. Once the total count of insertions was distributed randomly among the real TA sites across the whole genome, a tally of the number of CIS of size ≥3, ≥4, . . ., ≥15 was recorded within windows of 10,000 bp, 20,000 bp, . . . 150,000 bp. This process was repeated 100 times, and the average counts over those 100 iterations were computed. Four independent simulations of 100 iterations each were performed, yielding SE bars between simulations of < 1%, indicating sufficient convergence. The values obtained can be interpreted as expected values (E-values), because they indicate the expected number of CIS of a given number of insertions that would be observed within a given window size merely by chance. We chose a threshold with an E-value < 1. Thus, finding 11 CIS of ≥ 15 insertions within 200,000 bp, when not even a single CIS was expected, is highly significant. We compared the thresholds obtained by this method with the thresholds obtained using standard Poisson statistics with the assumption of random insertion in the genome. We found our method was uniformly more stringent and yielded fewer false positives than the standard Poisson statistics. A modified Poisson model that takes into account the local density of TA sites in the genome yielded excellent agreement with the Monte Carlo calculations.

Annotation and Sequence Information Management.We created two primary annotation files: one outlining details of each unique insertion, and one describing each CIS. These files provide information on the chromosomal mapping position of each insertion or CIS, redundancy information on each insertion, and characteristics of the nearest EnsEMBL gene that flanks the insertion. EnsEMBL mappings were identified by a custom Perl script that uses the published Application Programmer Interface (Stabenau *et al.* 2004). To facilitate the management of all sequence information, an MySQL relational database was constructed to store (i) genotypic and phenotypic information on all mice and tumors from which the insertion sequences were derived; (ii)

metainformation on the sequencing runs themselves; (iii) raw read sequences; (iv) construct element matching characteristics; (v) final processed insertion sequences; (vi) mapping information for each processed insert sequence to the mouse genome; (vii) clustering assignments of inserts into CIS; and (viii) annotation information on all mapped inserts and CIS. SQL queries were performed to facilitate the merging of distinct gastrointestinal tract tumor datasets and the annotation process.

Analysis of Replicate Sequencing Runs to Determine Percentage of Library Capture. To estimate the extent of undersampling of transposon insertions in our study, we analyzed the GS FLX sequencing replicates separately. Using a four-region plate, one sequencing run of the GS FLX machine can sequence four separate samples. In one of the sequencing runs we ran two aliquots of the left-side ligation-mediated (LM)-PCR pool in separate regions (1 and 4) and two aliquots of the right-side LMPCR in separate regions (2 and 3). We analyzed the sequence reads by custom Perl script to determine the extent of overlap (Table 12). For example, region 1 returned 68,371 total reads, of which 56,435 contained a perfect match to a barcode, the transposon-specific sequence, and a genomic TA dinucleotide along with at least 16 bases of genomic DNA. When duplicate sequences were combined, 20,654 unique transposon insertion reads remained. Region 4, which was a replicate, had 18,863 unique reads. The overlap between these two regions was 10,448 reads, a little more than 50%. Because this process is similar to a mark-recapture experiment, one can use the Lincoln–Peterson method (Seber GAF 2002) to estimate the number of amplicons in the total population (see below). Based on the overlap between the replicates sampled in regions 1 and 4, we estimate that there were 37,289 unique amplicons in the original pool. As a rough approximation, our protocol sampled about 78% of the amplicons present in the original left-side LM-PCR pool. If we apply the same analysis to the right-side LM-PCR pool, where the overlap was lower (~35%), we estimate that we sampled only 58% of the amplicons in the original right-side LM-PCR pool. In either case, it is apparent that by increasing the number of sequencing runs, or perhaps by using a different sequencing platform, we could find more transposon insertions and perhaps more candidate cancer genes.

Lincoln–Peterson Method to Estimate Total Population in a Mark-and- Recapture Experiment. A mark-and-recapture experiment can be used to estimate population size in an ecological setting where the researcher marks all animals captured during a first visit. The researcher then returns and makes a second capture, noting how many of the animals in the second capture were marked in the first capture. To use the Lincoln–Peterson method (Seber GAF 2002) in our study, we assume that the duplicate pools of amplicons contain equal numbers of the same amplicons. This assumption could be invalid, because the concentration in the amplicon pool is very small (~200,000 molecules/μL). Randomly removing a small volume could result in the two volumes containing different amplicons. Another caveat to using the Lincoln–Peterson method is that our use of unique reads instead of actual reads is not directly analogous to a mark-and-recapture experiment. Nevertheless, if we assume the aliquots are similar, then the number of reads in the first region (M) is analogous to the number of animals caught and marked in the first capture of a mark-andrecapture experiment. The number of reads in the second region (C) is analogous to the number of animals caught in the second capture, and the number that overlaps (R) is analogous to the number of animals marked in the first capture that are caught in the second capture. To estimate the total population (N), the Lincoln–Peterson method states that the proportion of marked individuals in the second capture to the number in the first capture (R/M) should equal the proportion of the number of animals in the second capture to the total population (C/N). Rearrangement of this equation gives n = (M × C)/R. Using the number of unique reads in regions 1 and 4 (Table 12) equates to (20,654 × 18,863)/10,448 = 37,289. The total number of unique reads we captured in both sequencing regions (20,654 + 18,863 − 10,448 = 29,069) represents 78% of the estimated total population of 37,289. Using the same analysis of the unique reads in region 2 and 3 (Table 12) equates to an estimated total populationof (25,753 × 25,804)/9,079 = 73,194. In this case, we have sampled only (25,753 + 25,804 − 9,079 = 42,478) 58% of the total population.

***Apc* Loss of Heterozygosity Analysis**. To measure loss of heterozygosity (LOH) for the ApcMin mutation, DNA was isolated from individual polyps, and PCR was performed

using primers that flank the mutation (sense primer: CGGAGTAAGCAGAGACACAA; antisense primer: GGGAGGTATGAATGGCTGAT). The PCR product was purified using Qiagen 96 MinElute vacuum purification plates according to the manufacturer's protocol and was sequenced using the sense primer as the sequencing primer. Trace peak heights at the location of the mutation were measured for each tumor. Wild-type DNA will only have a single peak, representing thymidine, whereas ApcMin nontumor DNA will have two peaks of equal height representing the wild-type thymidine base and the mutant adenine base. If significant LOH has occurred, the ratio of the height of the thymidine peak to the adenine peak will be < 0.5, whereas a ratio > 0.8 indicates maintenance of heterozygosity. Ratios between 0.5 and 0.8 and ratios > 1.2 are considered to be contaminated with nontumor tissue.

Chromosomal Copy Number Analysis. Eight studies measuring DNA copy number in CRC compared with normal tissue were analyzed (Vogelstein *et al.* 1989, Ried *et al.* 1996, Nakao *et al.* 2004, Habermann *et al.* 2007, Lassmann *et al.* 2007, Shih *et al.* 2001, Derks *et al.* 2008, Kurashina *et al.* 2008). Of the 33 CIS loci, 31 were mapped to the homologous human region using the Batch Coordinate Conversion (Lift- Over) utility from the University of California, Santa Cruz (UCSC) genome browser (Kent *et al.* 2002). The genome build appropriate to each study was analyzed. A CIS locus was determined to be lost or gained recurrently based on the individual study methodology. To determine the chances of this overlap occurring randomly, we ran 10,000 simulations using randomly generatedCIS listscompared with the recurrently lost regions in Nakao *et al*. (Nakao *et al.* 2004). In this study they hybridized genomic DNA from 135 human CRC along with normal lymphocytic DNA to a BAC array (HumArray1.14, University of California San Francisco; UCSF) and used Spot/Sproc analysis software (UCSF) to determine log2 ratios. They published an Excel file with the log2 ratios for each BAC clone for each human sample. Chromosomal losses were based on a log2 ratio lower than −0.225. The genomic coordinates of the BAC clones were downloaded from the UCSF website(http://cancer.ucsf.edu/_docs/cores/array/analysis/HA1.14_clonepos_May04.20060811.txt) and were mapped to the Human genome build HG19 using the Batch Coordinate Conversion utility from the UCSC genome browser

(http://genome.ucsc.edu/cgi-bin/hgLiftOver). After BAC clones that did not have at least 65% of samples giving a reading and positions that did not map to the HG19 build were removed, log2 ratios for 2,075 BAC clones remained. We selected the subset of these clones that had log2 ratios lower than −0.225 in at least 5% of the samples. Genomic regions recurrently lost were defined based on the genome coordinates of consecutive BAC clones that had log2ratios lower than −0.225. For example, if three adjacent clones all showed a loss, we assigned the region based on the start coordinate of the first clone and the end coordinate of the last clone. If the neighboring clones on both sides of a BAC were not decreased, the region was defined as the coordinates of the single BAC. Next, we wrote a Perl script that created 10,000 random sets of 31 CIS using the UCSC Golden Path coordinates. Each set of 31 CIS contained 31 randomly generated genomic regions that were the same length as the actual Apc^{Min} dataset CIS. The Perl script then counted the overlap between the random CIS list and the Nakao recurrently lost regions, and the process was repeated 10,000 times. In 10,000 simulations, only three random CIS lists had an overlap of 22 regions or more.

Knockdown of CIS Genes Using siRNA in SW480 Cells. SW480 cells were purchased from American Type Culture Collection. Cells were maintained in DMEM supplemented with 10% FBS, 2 mmol/L glutamine, 100 U/mL penicillin, and 100 μg/mL streptomycin and were incubated in a humidified atmosphere of 95% air and 5% CO2 at 37 °C. Cells were switched to antibiotic-free medium before siRNA transfection. Cells at 70% confluence were transfected twice, 48 h apart, with siRNA oligonucleotides (siRNA oligos) targeting the human ortholog of the CIS candidate gene (CIS siRNA) or with a nontargeting control (control siRNA), at a final concentration of 50 nmol/L, using Lipofectamine 2000 transfection reagent. Oligos targeting CIS genes were obtained from Qiagen (Hs_*ATF2*_3, Hs_*PDCD6IP*_5 Hs_*SFI1*_7, and Hs_ *PDE4DIP*_15) and from Dharmacon (*CNOT1* On-TARGETplus SMARTPool). The control siRNA oligo (OnTARGETplus Nontargeting siRNA#3) was obtained from Dharmacon. Total RNA was harvested fromCIS siRNA- and control siRNA-treated cells 2 or 3 d after the second siRNA transfection using the RNeasy kit (Qiagen). For each experimental sample, 1.5 μg RNA was converted to cDNA with random nonomer primers (Integrated DNA

Technologies) and recombinant Omniscript Reverse Transcriptase using the Omniscript RT kit (Qiagen) according to manufacturer's instructions. CIS cDNA and 18S ribosomal cDNA (used as internal control) were amplified from total cDNA by PCR. PCR was carried out in 10 μL using 2 μL cDNA from a 10× dilution of the 20 μL RT reaction (equivalent to 15 ng reversetranscribed RNA) for CIS genes and a 100× dilution for 18S rRNA, 500 nM of each primer, and 5 μL LightCycler 480 SYBR Green 1 Master Mix (Roche Applied Science). PCR was performed on a LightCycler 480 System (Roche Diagnostics) in96-well plates using the amplification protocol: one cycle of preincubation, 5 m at 95 °C; 45 cycles of amplification each consisting of denaturation at 95 °C for 5 s, annealing at 60 °C for 5 s, and elongation at 72 °C for 10 s; one cycle melting at 95 °C for 5 s, 65 °C for 1 m, heating to 97 °C; one cycle cooling at 40 °C for 30 s. Water was used as a template for negative control amplifications for each PCR run. All reactions were performed in duplicate. Standards were generated by reverse transcription of total RNA from untreated cells followed by PCR amplification to generate template DNA of the same sequence as the predicted CIS gene or 18S gene PCR product. Serial dilutions of template DNA were amplified in parallel with experimental samples and used to generate a standard curve for each gene. Data were analyzed using Roche LightCycler 480 software, and crossing points (CPs) were calculated using the absolute quantification-second derivative maximum method. The standard curve was used to determine efficiency of PCR amplification (E) for each gene. Relative mRNA levels represent the expression of the CIS gene in CIS siRNA-treated cells relative to expression in control siRNAtreated cells. CIS gene expression was normalized to 18S rRNA levels, and relative mRNA levels were calculated as described by Pfaffl (Pfaffl MW 2001): relative mRNA levels = ([Etarget] ΔCPtarget(control-treated))/[Eref] ΔCPref(control-treated)) × 100, where E is real-time PCR efficiency and CP is defined as the point at which fluorescence rises appreciably above background.

Primer sequences are as follows: activating transcription factor-2 (*ATF2*), 5′-TGACCGAAAGGATCATGAACTA-3′ and 5′-GCAGTCCTTTCTCAAGTTTCCA-3′; CCR4-NOT transcription complex, subunit 1 (*CNOT1*), 5′ CTTTCAACCCCCAATCAGACC-3′ and 5′-AGGTTTCATCTTACTCTGCTGGA-3′;

programmed cell death 6-interacting protein (*PDCD6IP*), 5′ AGGTGTTCCCTGTCTTGGCTGC-3′ and 5′ TTCATCATAGCGAGATGCCACTGTTT-3′; phosphodiesterase 4D-interacting protein (*PDE4DIP*), 5′-GAGAACTCCAGGACAAGAAACAGCAT-3′ and 5′-GGATTCCTCCTGCAGAAGCTGG-3′; Sfi1 homolog, spindle assembly associated (*SFI1*), 5′-AGCAGCAGGAGATGAGGAACAAG-3′ and 5′-CGAACAACCACGTAGATCAACCAG-3′.

Cell Viability Assay. Viability of siRNA-treated SW480 cells was determined using a 3-(4,5-dimethylthiazol-2-yl)-2,5-diphenyltetrazolium bromide (MTT) assay (Cell Viability Kit 1; Roche Applied Sciences) in which absorbance at 595 nm is proportional to viable cell number. One day after the second siRNA transfection, cells were replated into 96-well plates at 1,250 cells per well (*ATF2, PDCD6IP*, and *PDE4IP*) or 5,000 cells per well (*CNOT1*) in triplicate in regular growth medium. Cell viability was determined on days 2–6 after the second transfection. Day 6 A595 values for each treatment were normalized to day 2 values for the same treatment to correct for differences in plating. Relative cell viability represents the ratio of normalized absorbance at 595 nm of cells treated with CIS siRNA to absorbance of cells treated with control siRNA on day 6. Results shown for mRNA and cell viability are the mean ± SD of at least two experiments.

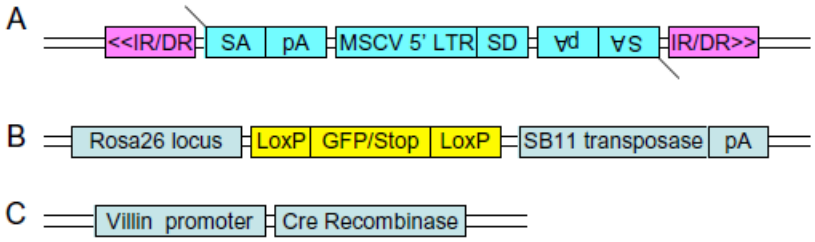

Figure 35. Three alleles used to target SB mutagenesis to the intestinal tract. (A) T2/Onc transposon. IR/DR, inverted repeat/direct repeat sequences required for transposition; MSCV 5′ LTR, murine stem cell virus 5′ long terminal repeat; SA pA, splice acceptor with a polyA signal. **(B)** Conditional SB allele. Rosa26 locus, endogenous Rosa26 locus [Gt(Rosa)26Sor]; LoxP-GFP/Stop-LoxP, GFP cDNA flanked by LoxP sites; SB11 transposase pA, SB11 transposase cDNA with polyA signal. **(C)** Cre recombinase cDNA driven by the Villin promoter.

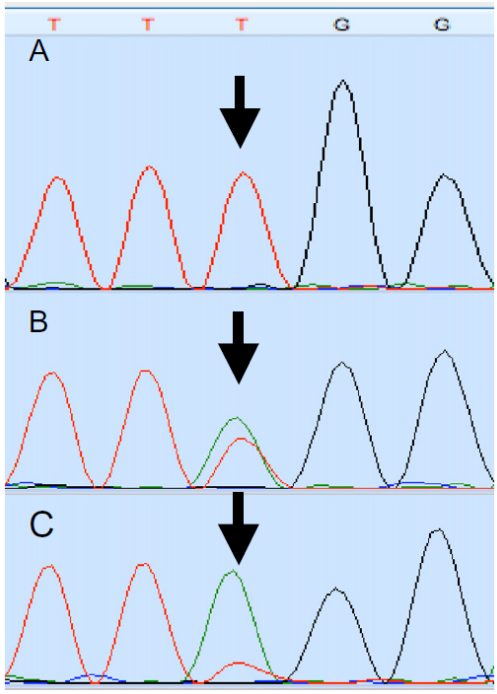

Figure 36. PCR technique for detecting *Apc* LOH. Trace peak heights of the T→A *Min* mutation in **(A)** wild-type mice, **(B)** heterozygous Apc^{Min} mice, and **(C)** an adenoma with LOH. Arrows indicate *Min* mutation. Red peaks = T; green peaks = A.

Table 11. LOH and MOH in Apc^{Min} tumors based on the ratio of T:A trace peaks.

Transposon insertion in *Apc*	Number of informative tumors*	% tumors with T:A ratio <0.5 (LOH)	% tumors with T:A ratio between 0.8–1.2 (MOH)
Yes†	32	47	53
No	15	73	27

MOH, maintenance of heterozygosity.
*To qualify as an informative tumor, the peak height ratio T:A must be <0.5 or between 0.8–1.2.
†Yes indicates the tumors had a mapped *SB* transposon insertion in the *Apc* gene.

Table 12. Sequence read overlap between duplicate regions of a single GS FLX sequencing run.

	Region 1 (left)†	Region 4 (left)†	Region 2 (right)†	Region 3 (right)†
Average read length (bases)	95	94	94	94
Total no. reads	68,371	59,228	54,405	113,982
No. reads with a perfect barcode‡	66,607	57,631	53,168	111,016
No. reads with IR/DR+TA match§	56,435	49,006	49,531	102,534
No. reads with unique 16 bases after TA¶	20,654	18,863	25,753	25,804
No. unique reads that overlap	10,448	10,448	9,079	9,079
Percent unique reads that overlap	51	55	35	35

*A four-region plate was used in the sequencing run.
†Left-side LM-PCR duplicate aliquots were run in regions 1 and 4; right-side duplicates were in regions 2 and 3.
‡The first 10 bases of the read perfectly matched one of the 96 barcodes.
§The bases immediately following the barcode perfectly matched the nested primer, the remainder of the IR/DR, and a TA dinucleotide.
¶The 16 bases immediately following the TA dinucleotide were unique compared with all other sequence reads.

Table 13. Human orthologous regions to the mouse CIS with recurrent chromosomal copy number changes based on published data.

Mouse address*	Mouse gene	Mouse Entrez ID	Human address†	Human gene	Human Entrez ID	Human band	In region of loss/gain‡
chr9:3001410–3030207	AC131780.5	114673?	Deleted in humans	No homology	N/A	N/A	N/A
chrY:2781406–2897989	No Gene Y	N/A	Deleted in humans	No homology	N/A	N/A	N/A
chr3:127241424–127431287	4930422G04Rik	71643	chr4:113299994–113576517	C4orf21	55345	4q25	Yes
chr3:127697338–127730035	AC115907.7	100043382	chr4:112926160–112964108	No Gene 3	N/A	4q25	Yes
chr13:105093822–105104050	Adamts6	108154	chr5:64747713–64758225	ADAMTS6	11174	5q12.3	Yes
chr3:127454370–127633377	Ap1ar	211556	chr4:113034449–113260728	AP1AR	55435	4q25	Yes
chr18:34324389–34514767	Apc	11789	chr5:111979623–112236985	APC	324	5q22.2	Yes
chr17:80239637–80306988	Atl2	56298	chr2:38501789–38613026	ATL2	64225	2p22.2–22.1	Yes
chr18:61726208–61750047	Csnk1a1	93687	chr5:148873515–148912809	CSNK1A1	1452	5q32	Yes
chr18:73903365–73913215	Elac1	114615	chr18:48495579–48509486	ELAC1	55520	18q21.2	Yes
chr3:136918543–137092521	Emcn	59308	chr4:101323972–101541428	EMCN	51705	4q24	Yes
chr18:10578932–10773953	Esco1	77805	chr18:19121974–19393499	ESCO1	114799	18q11.2	Yes
chr3:122217801–122319064	Fnbp1l	214459	chr1:93916974–94045997	FNBP1L	54874	1p22.1	Yes
chr7:135180978–135240752	Itgam	16409	chr16:31267174–31289751	ITGAM	3684	16p11.2	Yes
chr18:74613029–74796289	Myo5b	17919	chr18:47508944–47707289	MYO5B	4645	18q21.1	Yes
chr18:26169184–26282443	No Gene 18	N/A	chr18:35353815–35494000	No Gene 18	N/A	18q12.2	Yes
chr4:131170124–131238909	No Gene-4	N/A	chr1:29768033–29870348	No Gene 4	N/A	1p35.3	Yes
chr13:55352993–55372133	Nsd1	18193	chr5:176657455–176671302	NSD1	64324	5q35.3	Yes
chr3:97593369–97718572	Pde4dip	83679	chr1:144945932–145112522	PDE4DIP	9659	1q21.1	Yes
chr11:62203495–62369763	Pigl	327942	chr17:16040912–16299937	PIGL	9487	17p11.2	Yes
chr6:113039133–113100176	Setd5/Lhfpl4	72895/269788	chr3:9450610–9516832	SETD5 LHFPL4	55209 375323	3p25.3	Yes
chr11:3004743–3179859	Sfi1	78887	chr22:31790517–32022116	SFI1	9814	22q12.2	Yes
chr18:53440600–53638364	Snx24	69226	chr5:122221887–122440150	SNX24	28966	5q23.2	Yes
chr18:52654288–52675270	Srfbp1	67222	chr5:121370968–121397902	SRFBP1	153443	5q23.1	Yes
chr18:24110107–24157877	Zfp397	69256	chr18:32819631–32871403	ZNF397	84307	18q12.2	Yes
chr9:65561432–65607064	Zfp609	214812	chr15:64859323–64946983	ZNF609	23060	15q22.31	Yes
chr2:73708689–73773260	Atf2	11909	chr2:175997880–176076969	ATF2	1386	2q31.1	No
chr8:98254541–98300340	Cnot1	234594	chr16:58568279–58622838	CNOT1	23019	16q21	No
chr16:29019897–29031672	No Gene 16	N/A	chr3:192750830–192764409	No Gene 16	N/A	3q29	No
chr9:113560446–113723693	Pdcd6ip	18571	chr3:33684948–33911522	PDCD6IP	10015	3p22.3	No
chr9:100583003–100698850	Stag1	20842	chr3:136220568–136384331	STAG1	10274	3q22.3	No
chr5:126077980–126153976	Tmem132b	208151	chr12:125776600–125970181	TMEM132B	114795	12q24.31–24.32	No
chr18:7855248–8046126	Wac	225131	chr10:28820138–28913566	WAC	51322	10p12.1	No

*Based on mouse July 2007 Assembly (mm9) UCSC genome browser.

†Based on human GRCh37 Assembly (hg19) UCSC genome browser.

‡Region was identified in one of the following studies: Nakao *et al.,* 2004; Derks *et al.,* 2008; Lassmann *et al.,* 2007; Habermann *et al.,* 2007; Ried *et al.,* 1996; Vogelstein *et al.,* 1989; Shih *et al.,* 2001.

Table 14. Knockdown of *Apc*^{Min} CIS candidate genes affects viability of human colon cancer cells.

Gene	Relative mRNA levels of cells depleted for CIS gene*	Relative cell viability of cells depleted for CIS gene†
ATF2	17.2 ± 5.6%	61.0 ± 1.5%
CNOT1	13.7 ± 7.4%	18.5 ± 16%
PDCD6IP	10.5 ± 2.6%	64.2 ± 28%
PDE4DIP	27.9 ± 10%	55.0 ± 19%
SFI1	40.4 ± 13.2%	60.0 ± 14%

*Relative mRNA levels calculated using the ΔΔCt method (1) and represent levels of CIS mRNA in CIS siRNA-treated cells relative to levels in control, nontargeting siRNA-treated cells. 18S RNA was used as a housekeeping control. Results shown are the mean ± SD of at least two experiments.

†Relative cell viability represents the ratio of absorbance at 595 nm of cells treated with the indicated CIS gene siRNA to absorbance of cells treated with nontargeting control siRNA. Results shown are the mean ± SD of at least two experiments.

Table 15. Mapped transposon insertions in 96 tumors. Please see the weblink: http://www.pnas.org/lookup/suppl/doi:10.1073/pnas.1018012108/-/DCSupplemental/sd01.xls

Personal Contribution. Lei Zhao performed MTT experiments analyzed data to determine the knockdown effect of the following genes on proliferation of human (SW480) CRC cells: *CNOT1, PDCD6IP*, *PDE4DIP* and *SFI1*.

APPENDIX 2

The role of KCNQ1 in mouse and human gastrointestinal cancers

BLN Than[1,2], JACM Goos[3], AL Sarver[4], MG O'Sullivan[5], A Rod[1], TK Starr[6,7],RJA Fijneman[3], GA Meijer[3], L Zhao[1], Y Zhang[8], DA Largaespada[7], PM Scott[1] and RT Cormier[1]

[1]Department of Biomedical Sciences, University of Minnesota Medical School, Duluth, MN, USA; [2]Toxicology Graduate Program, University of Minnesota, Duluth, MN, USA; [3]Department of Pathology, VU University Medical Center, Amsterdam, The Netherlands; [4]Department of Biostatistics and Informatics, Masonic Cancer Center, University of Minnesota, Minneapolis, MN, USA; [5]College of Veterinary Medicine, University of Minnesota, St Paul, MN, USA; [6]Department of Genetics, Cell Biology and Development, Center for Genome Engineering, Masonic Cancer Center, University of Minnesota, Minneapolis, MN, USA; [7]Department of Obstetrics, Gynecology and Women's Health, Masonic Cancer Center, University of Minnesota Medical School, Minneapolis, MN, USA and [8]University of Minnesota Supercomputing Institute, Minneapolis, MN, USA.

Oncogene advance online publication 26 August 2013;doi: 10.1038/onc.2013.350

Abstract. *Kcnq1*, which encodes for the pore-forming a-subunit of a voltage-gated potassium channel, was identified as a gastrointestinal (GI) tract cancer susceptibility gene in multiple Sleeping Beauty DNA transposon-based forward genetic screens in mice. To confirm that *Kcnq1* has a functional role in GI tract cancer, we created Apc^{Min} mice that carried a targeted deletion mutation in *Kcnq1*. Results demonstrated that *Kcnq1* is a tumor suppressor gene as *Kcnq1* mutant mice developed significantly more intestinal tumors, especially in the proximal small intestine and colon, and some of these tumors progressed to become aggressive adenocarcinomas. Gross tissue abnormalities were also observed in the rectum, pancreas and stomach. Colon organoid formation was

significantly increased in organoids created from *Kcnq1* mutant mice compared with wild-type littermate controls, suggesting a role for *Kcnq1* in the regulation of the intestinal crypt stem cell compartment. To identify gene expression changes due to loss of *Kcnq1*, we carried out microarray studies in the colon and proximal small intestine. We identified altered genes involved in innate immune responses, goblet and Paneth cell function, ion channels, intestinal stem cells, epidermal growth factor receptor and other growth regulatory signaling pathways. We also found genes implicated in inflammation and in cellular detoxification. Pathway analysis using Ingenuity Pathway Analysis and Gene Set Enrichment Analysis confirmed the importance of these gene clusters and further identified significant overlap with genes regulated by MUC2 and CFTR, two important regulators of intestinal homeostasis. To investigate the role of KCNQ1 in human colorectal cancer (CRC), we measured protein levels of KCNQ1 by immunohistochemistry in tissue microarrays containing samples from CRC patients with liver metastases who had undergone hepatic resection. Results showed that low expression of KCNQ1 expression was significantly associated with poor overall survival.

INTRODUCTION

The *KCNQ1* gene encodes for the pore-forming a-subunit of a voltage-gated potassium channel that enables a K^+ current after electrical depolarization of the cell membrane. KCNQ1 is predominantly expressed in the myocardium, inner ear, stomach, intestine and pancreas, tissues in which KCNQ1 expression is critical for ion homeostasis (Peroz *et al.,* 2008). Inherited mutations in *KCNQ1* underlie several human disease syndromes. For example, mutations in *KCNQ1* are associated with congenital long QT syndrome, a disorder caused by abnormal ventricular repolarization that increases the risk of sudden death from cardiac arrhythmias. Jervell and Lange–Nielson syndrome is a rare autosomal disorder characterized by deafness in addition to long QT syndrome. Recent reports indicate that Jervell and Lange–Nielson syndrome patients can also be susceptible to GI defects, including iron-deficiency anemia, gastric and duodenal hyperplasia, elevated gastrin levels and, more rarely, gastric adenocarcinoma (Winbo *et al.,* 2012, Grahammer *et al.,* 2001, Rice *et al.,* 2011, Nikou *et al.,* 2011). Variants in *KCNQ1* are

also associated withenhanced risk for type 2 diabetes (Unoki *et al.,* 2008, Yasuda *et al.,* 2008).

Relatively little is known about the role of *KCNQ1* in cancer, but a potential role in GI tract cancers was indicated by its identification as a high-frequency common insertion site locus in Sleeping Beauty DNA transposon-based forward mutagenesis genetic screens for intestinal (Starr *et al.,* 2009, March *et al.,* 2011) and pancreatic cancer (Mann *et al*., 2011, Perez-Mancera *et al*., 2012). In our forward genetic screen in *Apc* wild-type mice, we found *Kcnq1* mutations in 18 intestinal tumors (13%) (Starr *et al.,* 2009) ranking it among the top 10 common insertion site genes. In this study, while transposon insertions in *Kcnq1* were found in tumors from all regions of the intestine, approximately two-thirds (64%) were located in the duodenum and jejunum, with 26% in the ileum and 10% in the colon. Furthermore, transposon insertions in *Kcnq1* were observed equally in both the forward and reverse strand orientation, consistent with a model whereby the transposon is acting to disrupt gene function. We performed a second forward genetic screen in Apc^{Min} mice and found *Kcnq1* transposon insertions in 13 intestinal tumors (14%) (Starr *et al.,* 2011). Another screen in Apc^{Min} mice found *Kcnq1* transposon mutations in 120 intestinal tumors (27%), ranking it no. 15 out of 641 common insertion site genes (120 kb window) (March *et al.,* 2011). We have also conducted a screen using p53R270H mutant mice and identified insertions in *Kcnq1* in 15 intestinal tumors (23%) (TK Starr, personal communication). Six mutant mouse alleles of *Kcnq1* have been created that partially model human disorders arising from inherited mutations in *KCNQ1*, especially Jervell and Lange–Nielson syndrome (Lee *et al.,* 2000, Casimiro *et al.,* 2001, Casimiro *et al.,* 2004, Takagi *et al.,* 2007, Elso *et al.,* 2004). These mutant alleles share similar but not identical phenotypes, including bilateral deafness from birth, gastric hyperplasia, gastric achlorhydria, elevated serum gastrin, headbobbing, bidirectional circling, ataxia, body tremor and hyperactivity with a consequent significant decrease in body weight. Conflicting results were reported regarding a cardiac phenotype in these models. In mouse small intestine, *Kcnq1* expression is strongest in the duodenum and proximal jejunum and decreases towards the ileum (Demolombe *et al.,* 2001, Dedek *et al.,* 2001). In the large intestine, *Kcnq1* expression is strongest in the distal colon

(Vallon *et al*., 2005, Warth *et al.,* 2002). To further investigate the role of *Kcnq1* in GI tract cancers, we measured GI cancer phenotypes following introgression of a targeted knockout (KO) allele of *Kcnq1* (Casimiro *et al.,* 2001) into the Apc^{Min} model of intestinal tumorigenesis. We then investigated the role of KCNQ1 in progression of human colorectal cancer (CRC) by measuring KCNQ1 protein levels in tissue microarrays containing samples from more than 500 CRC patients with liver metastases. Results from both of these studies indicate that *Kcnq1* is a tumor suppressor.

RESULTS

Loss of *Kcnq1* enhances tumor multiplicity in Apc^{Min} mice.

Haploinsufficiency for *Kcnq1* significantly enhanced Apc^{Min} intestinal tumor multiplicity overall, in both males and females, by ~40% (Table 16), with the phenotype strongest in the proximal small intestine and colon, where tumors increased 2-fold. $Kcnq1^{-/-}$ mice in our study manifested a range of previously reported phenotypes: rapid bidirectional circling, ataxia, tremor, head bobbing and they were smaller (~ 25%, body weight) and leaner than littermate *Kcnq1* wild-type and heterozygous mice. Less than half of the expected number of Apc^{Min} $Kcnq1^{-/-}$ mice survived until weaning (23 vs ~60). Survivor Apc^{Min} $Kcnq1^{-/-}$ mice demonstrated a very strong increase in tumors in the proximal half of the small intestine (B3-fold), especially in the proximal quarter of the small intestine containing the duodenum and proximal jejunum (Table 17), the region exhibiting strongest expression of *Kcnq1* in the intestine. Apc^{Min} $Kcnq1^{-/-}$ mice developed B2-fold increase in colon tumors but no increase in the distal small intestine of males, and a decrease in females. No significant differences between *Kcnq1* genotypes in tumor sizes were observed.

Table 1. Loss of *Kcnq1* enhances tumor multiplicity in Apc^{Min} mice

	N	Colon	Proximal SI	Distal SI
Males				
$Kcnq1^{+/+}$	30	1.8 ± 1.7	11 ± 8	56 ± 41
$Kcnq1^{+/-}$	34	3.8 ± 2.3*	18 ± 13*	76 ± 38*
$Kcnq1^{-/-}$	10	2.6 ± 2.8	36 ± 16*	52 ± 43
Females				
$Kcnq1^{+/+}$	26	1.2 ± 1.7	14 ± 9	58 ± 25*
$Kcnq1^{+/-}$	46	2.5 ± 2.2*	20 ± 12	84 ± 37*
$Kcnq1^{-/-}$	13	2.1 ± 2.0	22 ± 11*	30 ± 16

Abbreviation: SI, small intestine. Apc^{Min} $Kcnq1^{+/+}$, Apc^{Min} $Kcnq1^{+/-}$ and $Apc^{Min}Kcnq1^{-/-}$ mice were killed at 120 days of age and tumors counted and measured. *P-values: <0.05; two-sided P-values for tumor counts were determined by use of the Wilcoxon rank-sum test comparing gender- and age-matched classes produced in the same genetic crosses.

Table 16. Loss of *Kcnq1* enhances tumor multiplicity in *Apc* ^{Min} mice.

Table 2. Apc^{Min} $Kcnq1^{-/-}$ tumor phenotype is strongest in the proximal quarter of the small intestine

Males	*Tumors*	*Females*	*Tumors*
$Kcnq1^{+/+}$	4 ± 2	$Kcnq1^{+/+}$	5 ± 3
$Kcnq1^{+/-}$	6 ± 3	$Kcnq1^{+/-}$	8 ± 4
$Kcnq1^{-/-}$	21 ± 11*	$Kcnq1^{-/-}$	15 ± 9*

Mice and tissues are the same as Table 1. *P-values: <0.05; two-sided P-values for tumor counts were determined by use of the Wilcoxon rank-sum test comparing gender- and age-matched classes produced in the same genetic crosses.

Table 17. *Apc* ^{Min} *Kcnq1* $^{-/-}$ tumor phenotype is strongest in the proximal quarter of the small intestine.

Loss of *Kcnq1* promotes tumor progression

Tumors in Apc^{Min} mice are invariably benign adenomas that usually vary in size between 0.3 and ~5 mm. Adenocarcinomas are extremely rare. In Apc^{Min} mice carrying

either heterozygous or homozygous mutations in *Kcnq1* development of adenocarcinomas occurred at a frequency of ~10–15%. These adenocarcinomas appeared as large lesions (some >20 mm), located in the proximal small intestine in a region approximate with the duodenal–jejunal flexure at the head of the pancreas. In almost all cases, there was buckling of the intestinal tube, in two cases there was a pronounced intussusception of the tissue and in two cases the tumors extended across the entire inner surface of the intestinal lumen. Six of these large tumors were analyzed by histopathology and all were found to be invasive adenocarcinomas (Figure 37). Figure 37a depicts a lesion of > 2 cm in length from the duodenum of an Apc^{Min} $Kcnq1^{+/-}$ mouse, which when sectioned regionally revealed adenocarcinoma tissue in each section. No adenocarcinomas were detected in the remainder of the small intestine or in the large intestine, and no putative adenocarcinomas were detected in Apc^{Min} $Kcnq1^{+/+}$ mice.

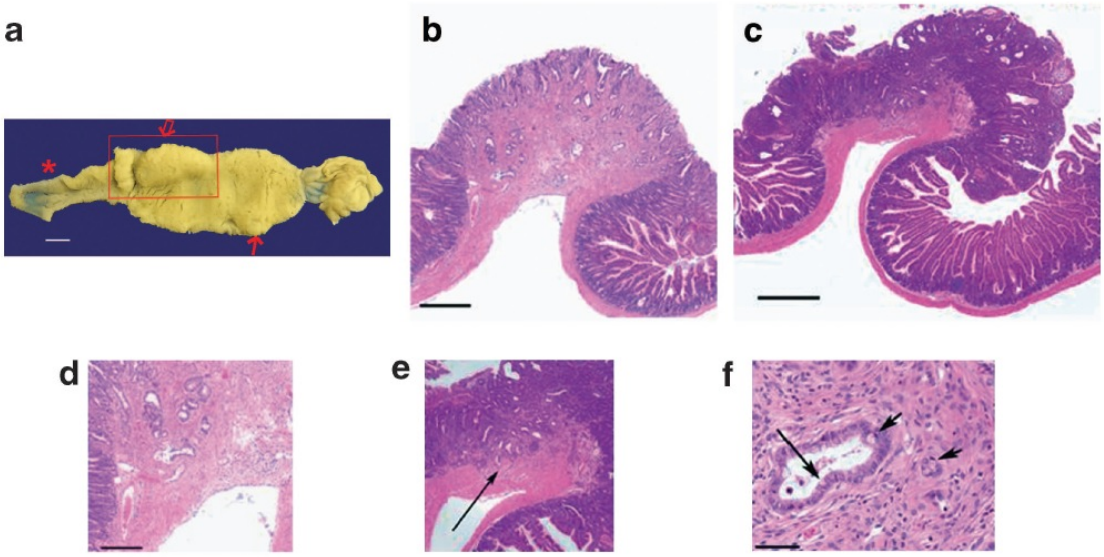

Figure 37. Loss of *Kcnq1* promotes tumor progression. (a) Duodenum from Apc^{Min} $Kcnq1^{+/-}$ mouse with stomach at right. Bar = 5 mm. Broad area of hyperplastic tissue with embedded tumors extends from pylorus–dudoenum juncture past the ampulla to a region approximate with the duodenal jejunal flexure. Asterisk indicates area of normal duodenum–proximal jejunum. Box encloses a region of adenocarcinoma tissue of > 2 cm. Sections from this lesion were taken from various regions and all showed evidence of invasion. Two of these adenocarcinoma sections are

depicted in **(b–f).** Smaller arrow depicts normal large adenoma of ~5mm that is embedded in hyperplastic tissue. **(b** and **c)** Bars = 500 μm; invasion into muscularis mucosa, **(d** and **e**) bar = 250 μm; prominent scirrhous response to invading tubules that exhibit differentiated goblet cells (long arrow) and signet ring cells (short arrows) **(f)**, bar = 50 μm.

Loss of *Kcnq1* is associated with other pathologies in the GI tract.

Rectal prolapse was evident in ~10% of Apc^{Min} $Kcnq1^{+/-}$ and Apc^{Min} $Kcnq1^{-/-}$ mice and in several cases the rectal prolapses were associated with enlarged rectums characterized by diffused severe crypt hyperplasia (Figure 44). In addition, $Kcnq1^{-/-}$ mice developed severe gastric hyperplasia that was characterized by mucosal hyperplasia, with parietal cells increased in size and crypt dilation with extensive cellular debris (Figure 45). Hyperplastic adenomas in the pylorus were also present in Apc^{Min} *Kcnq1* mutant mice. Although Apc^{Min} $Kcnq1^{+/-}$ mice showed an incidence of pyloric tumors of ~30%, the phenotype was much stronger in Apc^{Min} $Kcnq1^{-/-}$ mice where the incidence of pyloric tumors was ~90% (21/23). Furthermore, in Apc^{Min} $Kcnq1^{-/-}$ mice pyloric tumor multiplicity was much larger, with some mice developing as many as a dozen tumors. No pyloric tumors were observed in Apc^{Min} $Kcnq1^{+/+}$ mice. Finally, roughly one-third of Apc^{Min} $Kcnq1^{-/-}$ mice developed grossly and severely enlarged (~2- to 3-fold) pancreases, characterized by extra lobes. Histopathology of a matched pair of samples indicated that zymogen granules were less eosinophilic and less prominent, and that both exocrine cells and islets were smaller (Figure 46).

Loss of Kcnq1 has a strong effect on gene expression

We conducted cDNA microarray expression studies using tissue from distal colon and the proximal quarter of the small intestine of $Apc^{+/+}$ $Kcnq1^{+/+}$ and $Apc^{+/+}$ $Kcnq1^{-/-}$ mice. Overall, more than 400 genes showed a > 1.5-fold change in expression, and > 200 of these genes also had a P-value of < 0.05 (Tables 18 and 19). Expression of 20 genes was confirmed by reverse transcription–polymerase chain reaction (RT–PCR) (Figures 38 and 39).

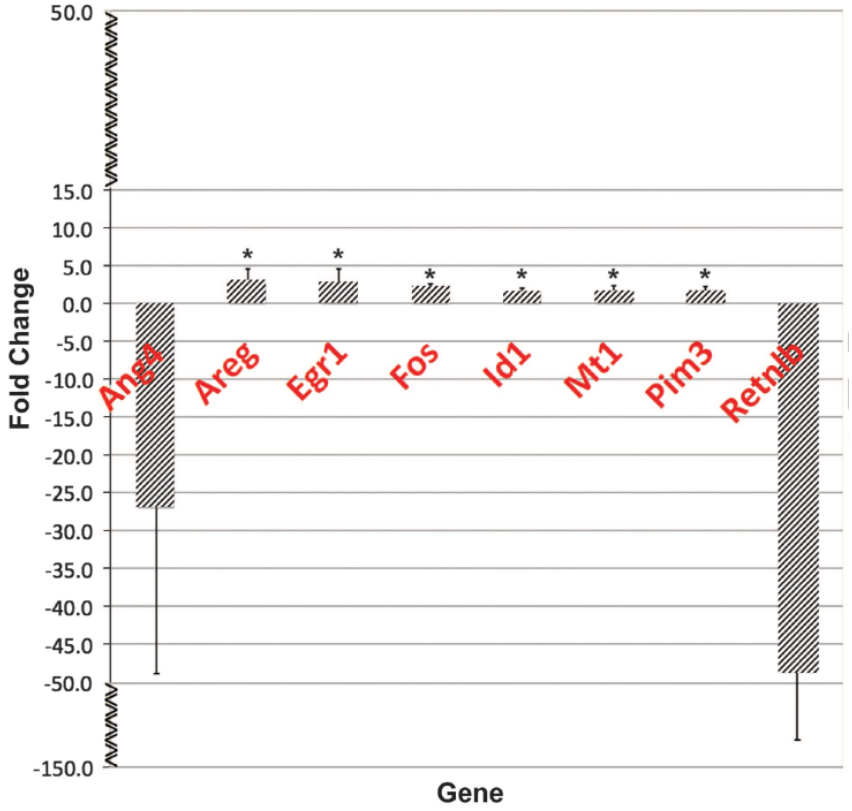

Figure 38. qRT–PCR gene expression analysis of mouse colon. Samples were analyzed in triplicate and normalized to 18S ribosomal RNA. Data are presented as the mean fold change ± s.d. Each bar represents the mean and s.d. of multiple experiments that measured fold differences in the mRNA expression of whole colon tissue isolated from adult (~100 days), littermate and gendermatched pairs of *Apc*$^{+/+}$ *Kcnq1*$^{+/+}$ and *Kcnq1*$^{-/-}$ mice. RNA was isolated from 1 cm sections from the same region of distal colon. At least two matched pairs of mRNAs were tested for each gene with most genes tested in at least three matched pairs of mRNAs. To be included in this figure, genes showed a mean fold difference of at least 1.5. In all cases, the direction in changes in gene expression confirmed microarray data. *P<0.05.

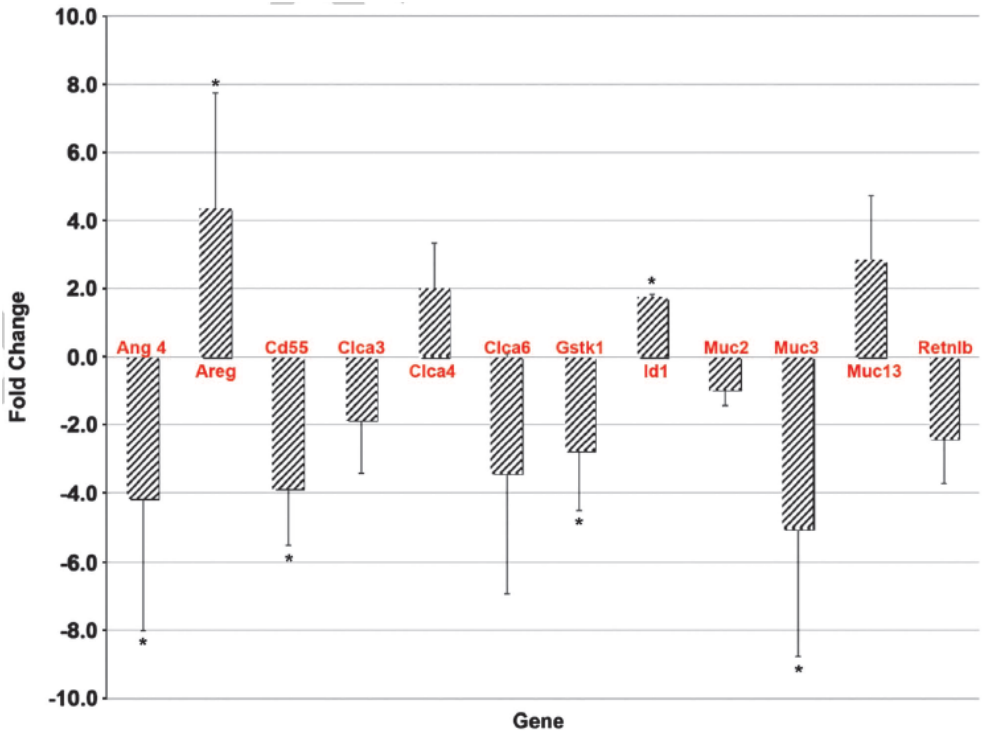

Figure 39. qRT–PCR gene expression analysis of mouse proximal small intestine. Each gene sample was run in triplicate and gene expression was normalized to the expression of 18S. Data are presented as the mean fold change ± s.d. Each bar represents the mean and s.d. of multiple experiments that measured fold differences in the mRNA expression in proximal small intestine tissue isolated from adult (~100 days), littermate and gendermatched pairs of $Apc^{+/+}$ $Kcnq1^{+/+}$ and $Kcnq1^{-/-}$ mice. mRNAs were isolated from 1 cm sections of proximal small intestine from the same region for all mice. At least two matched pairs of mRNAs were tested for each gene with most genes tested in at least three matched pairs of mRNAs. To be included in this figure, genes showed a mean fold difference of at least 1.5. In all cases, the direction of changes in gene expression confirmed microarray data. *P<0.05.

Target genes were clustered into several functional groups: innate immune response/goblet and Paneth cell function (*Ang4, Retnlb, Clps, Pnliprp2, Clca3, Muc2, Reg3a, Reg3b, Reg3g, Car1*), ion channels (*Trpv6, Slc12a8, Slc30a10, Aqp7, Aqp1, Aqp8, Aqp4, Clca3, Clca6*), mucins (*Muc2, Muc13, Muc4, Muc3*), growth regulatory signaling pathways (*Areg, Egr1, Fos, Ccdn1*), cancer cell migration (*Mmp9, Mmp15, S100a14, Mt1*), apoptosis (*Casp14, Casp2, Bcl6*) inflammation, mediated by mechanisms such as detoxification and stress responses (*Cyp2c55, Gstk1, Sirt1, Sirt3, Aldh1a1, Aldh1b1, Aldh2, Mt1, Gstm2*), the adaptive immune response and intestinal stem cell-

related genes (*Clca4, Aqp4, Aldh1a1, Olfm4*), consistent with a role for *Kcnq1* in the intestinal stem cell compartment (Munoz *et al.* 2012). Interestingly, while loss of *Kcnq1* showed a strong effect on colon secretory cell genes, there was no change in colon tissues in the secretory cell populations or cell proliferation (Figure 47).

***Kcnq1, Cftr* and *Muc2* share common genetic pathways in the GI tract**

Ingenuity Pathway Analysis (IPA) identified significant networks and functional groups altered in *Kcnq1* KO mice (see Figures 48A and B, and Table 20 (colon); and Figure 49 and Table 21 (proximal small intestine). In particular, IPA analysis identified Cftr as a top upstream regulator of *Kcnq1* KO dysregulated genes, indicating that genes differentially expressed in the *Kcnq1* KO mice overlap with targets of *Cftr* (overlap P-value of 5.81E-13, activation Z-score -2.722). Furthermore, the *Cftr* network is predicted to be downregulated in *Kcnq1* KO small intestine, suggesting that *Kcnq1* may be necessary for some aspects of Cftr function.

To identify common pathways and genes disrupted by *Kcnq1* and *Cftr* deficiencies, we used Gene Set Enrichment Analysis (GSEA). The entire ranked expression data set from the *Kcnq1* KO proximal small intestine array was compared with gene sets compiled from a microarray analysis of gene expression in the small intestine of *Cftr* KO mice (Norkina *et al.* 2004). *Cftr* gene sets consisted of all genes up- or downregulated by twofold in the *Cftr* KO mouse. GSEA revealed significant correlation, with overlap of gene identity and direction of regulation (Figure 40 and Table 20; normalized enrichment score (NES) for Cftr KO upregulated genes 1.97, $P < 0.001$; NES for *Cftr* KO downregulated genes -1.92, $P < 0.001$). These shared targets included a large subset of genes involved in lipid metabolism and, in particular, downregulation of genes involved in lipid oxidation. In support of the significance of this overlap, IPA analyses of *Kcnq1* KO and *Cftr* KO mice each identified lipid metabolism as a major functional category, with oxidation of lipids as the subcategory showing the most significant down regulation (*Kcnq1*, P-value 9.78E-06, activation Z-score, -2.26; *Cftr*, P-value 9.37E-09, Z-score, -3.62). Common targets included upregulation of *Idi1*, involved in cholesterol synthesis, and downregulation of *Hsd174b* and *Acaa1b*, both involved in

fatty acid beta oxidation. Inhibition of fatty acid oxidation is associated with a switch to lipogenesis and this switch is characteristic of metabolic remodeling that commonly occurs during oncogenesis (DeBerardinis *et al*. 2008). Also, fatty acid metabolism has recently been shown to have a key role in stem cell maintenance with lipogenesis associated with more highly proliferating stem cells (Knobloch *et al.* 2013). Thus, altered lipid metabolism may contribute to the development of CRC in *Kcnq1* and *Cftr* KO mice. A second group of genes dysregulated in both *Kcnq1* KO mice and *Cftr* KO mice is involved in inflammation. Because the intestinal epithelium is constantly exposed to flora and foreign substances, it must maintain protective and repair mechanisms. Disruption of these protective or homeostatic processes can result in inflammatory changes, which in turn are associated with inflammatory bowel disease and increased risk of CRC (Duerkop *et al.* 2009). Genes involved in inflammation are dysregulated in both *Kcnq1* KO mice and *Cftr* KO mice. These include upregulation of factors normally produced by intestinal epithelial cells to maintain immune homeostasis, including *Il7* (Shalapour *et al.* 2010), *Reg3g30* and *Pglryp1* (Vaishnava *et al.* 2011, Dziarski *et al.* 2010). In addition, a number of protective genes are downregulated including those involved in detoxification, *Gstt1, Cyp3a11, Cyp2b10*, and others involved in protective signaling, such as *Sema7a*, which promotes *Il10* signaling (Kang *et al.* 2012), and *Ace2*, which protects against inflammation-induced epithelial damage (Hashimoto *et al.* 2012). Further evidence of overlap between *KCNQ1* and *CFTR* was provided by analyzing RNA Seq data from 20 CRC liver metastases samples for concordance between expression levels of each gene. Using Pearson's correlation analysis of FPKM (fragments per kilobase pair of exon model per million fragments mapped) values in the 20 samples, it was found that *KCNQ1* and *CFTR* were significantly coexpressed, despite up to a 10-fold sample-to-sample FPKM variability for each gene (see Figures 40A and B). Finally, both *KCNQ1* and *CFTR* are regulated downstream of the serine threonine kinase gene *SGK1*, which is activated by factors including insulin, via the PI3K pathway, under conditions of osmotic stress (Lang *et al.* 2013). *SGK1* levels in turn appear to be influenced by the activity of both *KCNQ1* and *CFTR*, as *Sgk1* expression was upregulated by more than twofold in *Kcnq1* KO colon (Table 20) and was also upregulated by > 1.6-fold in *Cftr* KO colon

(BLN Than, personal communication). Of further interest, *Sgk1* expression levels were downregulated by 1.5-fold in the proximal small intestine of *Kcnq1* KO mice and downregulated by 5.5-fold in the small intestine of *Cftr* KO mice (Norkina *et al.* 2004).

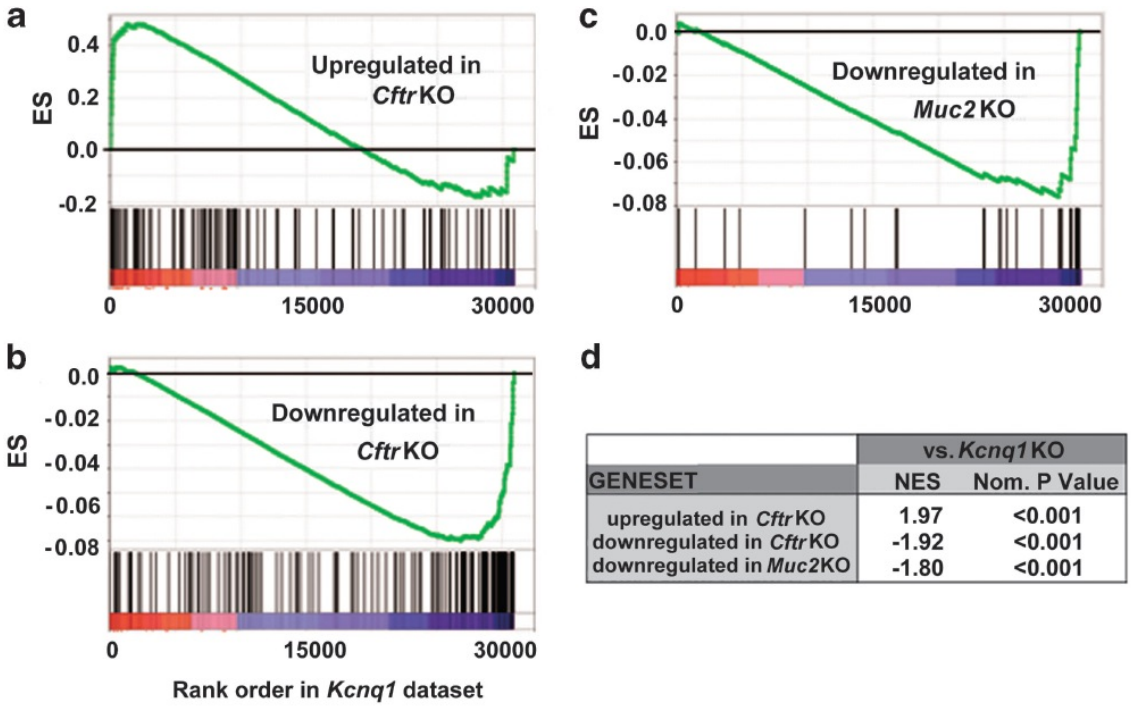

	vs. *Kcnq1* KO	
GENESET	NES	Nom. P Value
upregulated in *Cftr* KO	1.97	<0.001
downregulated in *Cftr* KO	-1.92	<0.001
downregulated in *Muc2* KO	-1.80	<0.001

Figure 40. Results of GSEA showing enrichment scores (ES) of *Cftr* and *Muc2* gene sets with respect to the ranked *Kcnq1* expression data set. Shown are enrichment plots for gene sets consisting of **(a)** genes upregulated in the small intestine of *Cftr* KO mice (Norkina *et al.* 2004); **(b)** genes downregulated in the small intestine of *Cftr* KO mice (Norkina *et al.* 2004); and **(c)** genes downregulated in the small intestine of *Muc2* KO mice (Yang *et al.* 2008); **(d)** NES and nominal P-value (nom. P-value) are shown for each comparison.

CFTR export of Cl^- and HCO_3^- maintains extracellular H2O homeostasis, which in turn is necessary for hydration and function of the protective lumenal mucin layer (De Lisle *et al.,* 2011). Another gene directly involved in maintenance of the mucin layer is MUC2, which encodes MUCIN2, one of the major glycoproteins making up this layer. As with *Kcnq1* and *Cftr*, *Muc2* deficiency is implicated in CRC (Yang *et al.,* 2008). To test if common pathways were disrupted by loss of *Kcnq1* and *Muc2*, we compared gene expression changes in the *Kcnq1* KO mouse with those reported for *Muc2* KO mice

(Yang *et al.,* 2008). GSEA identified significant overlap in gene expression, with genes downregulated in *Muc2* KO mice enriched in genes downregulated in *Kcnq1* KO mice (Figure 40 and Table 22, NES -1.80, $P < 0.001$). This group included a number of genes involved in detoxification, including cytochrome oxidase P450 enzymes and several glutathione S-transferases, *Gsta2, Gstm2, Gstm4, Gstm6* and *Gstt1*. Moreover, in a separate study (Burger-van Paassen *et al.,* 2012), deficiency for *Muc2* in the mouse intestine resulted in significant increases in the innate immune responders *Reg3g* and *Reg3b*, matching our findings in *Kcnq1* KO mice. Finally, we found that *Areg*, an epidermal growth factor receptor pathway gene that was upregulated in both the colon and proximal small intestine of *Kcnq1* KO mice, was also upregulated by >10-fold in the colon of *Muc2* KO mice (RTC and RJAF, unpublished microarray results) and in the colon of *Cftr* KO mice (BLNT, manuscript in preparation) (see Table 23).

Loss of *Kcnq1* promotes colon organoid development.

To investigate a role for *Kcnq1* in the intestinal stem cell compartment, we created intestinal organoids from the colons of a group of $Apc^{+/+}$ $Kcnq1^{+/+}$ and $Kcnq1^{-/-}$ age- and gendermatched littermate mice. At days 2–5, organoid growth was monitored and organoid number counted on day 5. Loss of *Kcnq1* increased the number of colon organoids by greater than threefold, confirming a potential regulatory effect of *Kcnq1* on the intestinal stem cell compartment (Munoz *et al.,* 2012) (Figure 41).

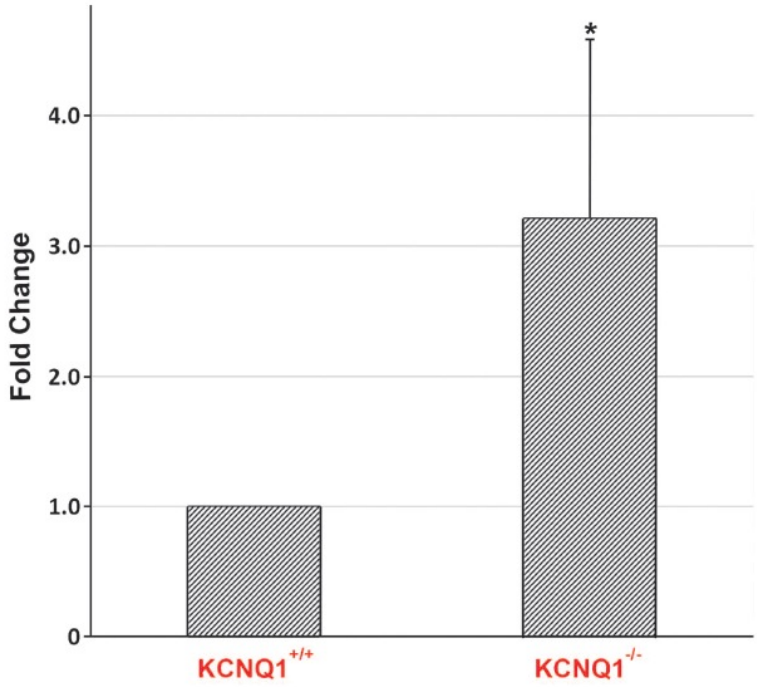

Figure 41. Colon organoids. Colon organoids were created from 500 crypt bottoms and plated in triplicate in 24-well plates. Crypt bottoms were isolated on separate days from 5 of each, age-, gender- and littermate-matched *Apc*$^{+/+}$ *Kcnq1*$^{+/+}$ and *Apc*$^{+/+}$ *Kcnq1*$^{-/-}$ mice (one matched pair per day). Organoids were examined daily and counted at 5 days post plating. *P < 0.05.

KCNQ1 expression is associated with good prognosis in late-stage human CRC.

On the basis of our finding that deficiency for *Kcnq1* drove the progression of intestinal tumors in mice, we tested the hypothesis that low levels of KCNQ1 in human CRC would correlate with a worse prognosis. To this end, we evaluated KCNQ1 protein expression in tissue microarrays containing samples from more than 500 stage IV CRC patients with liver metastases who had undergone hepatic resection. Immunohistochemical staining for KCNQ1 expression was evaluated for 311 patients. Membranes of neoplastic CRC liver metastasis (CRCLM) epithelium were scored for KCNQ1 staining intensity (Figure 42). We found that high KCNQ1 expression was related to improved overall survival (OS) (hazard rate ratio (HRR) 0.64; 95% confidence interval (CI): 0.45–0.92; P = 0.02). Median OS for patients with high KCNQ1 expression

was 60 months, whereas patients with low KCNQ1 levels had a median OS of 37 months, indicating a significant 23-month difference in survival (Figure 43).

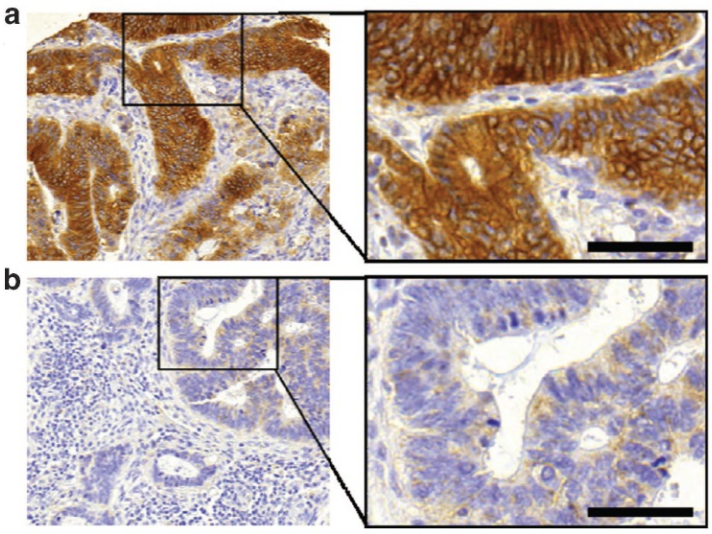

Figure 42. Representative human samples showing the expression pattern of KCNQ1 in the epithelium of CRCLM. Staining intensity was evaluated as **(a)** high or **(b)** low. Scale bars are 50 µm.

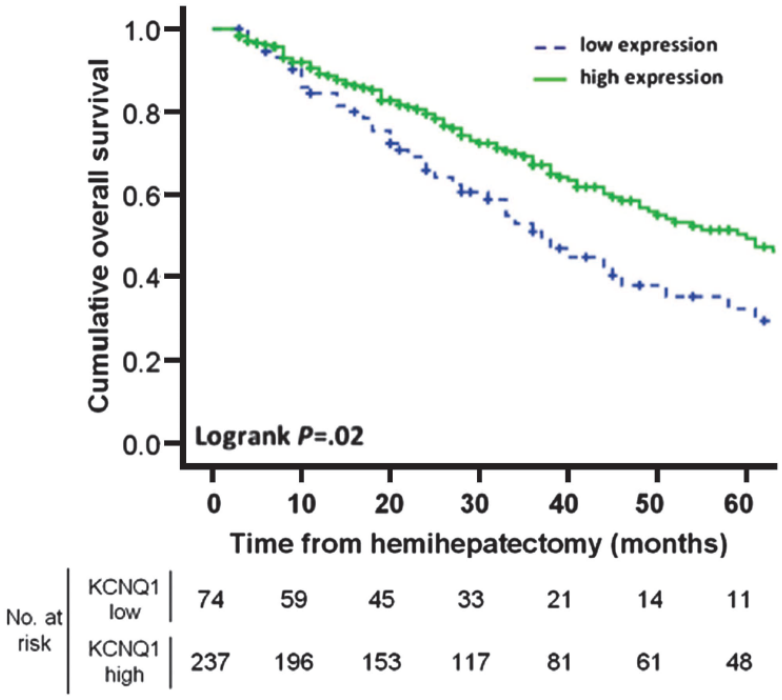

Figure 43. Kaplan–Meier graph depicting OS in months, stratified by intensity of KCNQ1 expression in CRCLMs. P-values were calculated using the log-rank statistic.

Next, we performed a multivariate analysis to evaluate whether the prognostic value of KCNQ1 protein expression was independent of established prognostic clinicopathological variables, that is, primary tumor-to-liver metastasis interval > 12 months, number of liver metastases > 1, maximal tumor diameter > 5.0 cm, lymph node positivity at the time of diagnosis of the primary tumor and serum carcinoembryonic level > 200 ng/ml. Upon stepwise backward Cox regression analysis with OS as the dependent variable, KCNQ1 expression (HRR, 0.49; 95%: 0.32–0.77; P = 0.002), lymph node positivity at the time of diagnosis of the primary tumor (HRR, 1.64; 95% CI: 1.08–2.48; P = 0.02) and maximal tumor diameter > 5.0 cm (HRR, 1.44; 95% CI: 0.96–2.16; P = 0.08) were retained as prognostic variables. Note that the association between maximal tumor diameter and survival was not significant; however, the variable was retained in the model because we only excluded variables when P > 0.1.

DISCUSSION

We first identified *Kcnq1* as a potential CRC driver gene in our forward genetic screens for GI tract cancer genes. Here, we have followed up with studies using a transgenic mouse model and analysis of human CRC tissues that support a tumor suppressor role for *Kcnq1*. We demonstrated the tumor suppressor function of *Kcnq1* in Apc^{Min} mice, where both hetero- and homozygous inactivation of *Kcnq1* resulted in significantly more adenomas and, importantly, progression to adenocarcinoma. This was especially evident in the proximal small intestine. Furthermore, *Kcnq1* deficiency caused rectal adenomatous hyperplasia, pyloric tumorigenesis, gastric hyperplasia and pancreatic abnormalities. Notably, in human CRC that had metastasized to the liver, low KCNQ1 protein expression correlated with significantly lower OS, by almost 2 years, compared to patients with high KCNQ1 expression. These findings suggest that KCNQ1 expression could be a biomarker to help determine eligibility for hepatic resection in CRC patients with liver metastases. In addition, newly developed small molecules that enhance K^+ ion

channel activity (Xiong *et al.,* 2008, Wulff *et al.,* 2009) could potentially be used to treat CRC patients with low levels of KCNQ1.

By what mechanism does loss of KCNQ1 influence cancer processes in the GI tract? A promising model is via KCNQ1's functional interactions with CFTR and MUC2. In the healthy intestinal epithelium, KCNQ1 is physiologically linked to the CFTR ion channel, with basolateral export of K^+ ions by KCNQ1 providing the electrochemical driving force for apical export of Cl^- ions by CFTR (Preston *et al.,* 2010). *Cftr* was identified as a CRC driver gene in two *Sleeping Beauty* GI tract forward genetic screens (Starr *et al.,* 2009, March *et al.,* 2011), and individuals with cystic fibrosis, caused by inactivating mutations in *CFTR*, are at increased risk for GI cancers including CRC (Maisonneuve *et al.,* 2003). To test if common pathways and genes are disrupted by loss of Kcnq1 and Cftr activity, we used GSEA to compare gene sets consisting of genes reported to be up- or downregulated in the small intestine of *Cftr* KO mice to the entire ranked *Kcnq1* expression data set and found significant correlation (Figure 40). Genes upregulated in common include several involved in immune responses and inflammation, whereas genes downregulated in common include a subset involved in fatty acid metabolism, in particular lipid oxidation. Further evidence of overlap between *KCNQ1* and *CFTR* was the finding of concordance between *KCNQ1* and *CFTR* expression in RNA Seq analysis of 20 CRC liver metastases (Figures 50A and B).

As with *Kcnq1* and *Cftr*, *Muc2* deficiency is implicated in CRC (Yang *et al.,* 2008). To test if common pathways were disrupted by loss of *Kcnq1* and *Muc2*, we compared gene expression changes in the *Kcnq1* KO mice with those reported for *Muc2* KO mice. GSEA identified significant overlap in gene expression with genes downregulated in *Muc2* KO mice enriched in genes downregulated in *Kcnq1* KO mice (Figure 40). This group included a number of genes involved in detoxification including cytochrome oxidase P450 enzymes and several glutathione S transferases, and genes involved inflammation.

These results point to common pathways (inflammation, lipid metabolism, detoxification and stress responses) disrupted by *Kcnq1, Cftr* and *Muc2* deficiencies. Therefore, we can hypothesize that KCNQ1, like MUC2 and CFTR, may act through one

or more of these pathways in preventing cancer in the GI tract. Moreover, precisely defining mechanisms of action for KCNQ1 can lead to its use as a prognostic predictor for CRC patients and potential therapeutic target.

MATERIALS AND METHODS

Mice

C57BL/6J mice and C57BL/6J-*Apc*^{Min} mice were obtained from the Jackson Laboratory (Bar Harbor, ME, USA). C57BL/6-*Kncq1* knockout mice were obtained from Dr Karl Pfeifer (NIH, Bethesda, MD, USA) (Casimiro *et al.,* 2001). Details of mouse husbandry are as described previously (Fijneman *et al.,* 2012). The genotype of the *Apc* and *Kcnq1* loci were determined by PCR assays as described previously (Casimiro *et al.,* 2001, Fijneman *et al.,* 2012).

Tumor analysis

Scoring of GI tumor tissues was performed as described previously (Fijneman *et al.,* 2012). Two-sided P-values for tumor counts were determined by use of the Wilcoxon rank-sum test comparing gender- and age-matched classes produced in the same genetic crosses.

Histopathology

Histopathological analysis of tumors and adjoining normal tissue was performed on formalin-fixed paraffin-embedded tissues by an ACVPcertifie veterinary pathologist (MGO0S) from the University of Minnesota Masonic Cancer Comparative Pathology Shared Resources facility using protocols as described previously (Fijneman *et al.,* 2012).

Organoid culture

Gender- and age-matched littermate C57Bl/6J *Kcnq1*$^{+/+}$ and *Kcnq1*$^{-/-}$ mice were killed between 8 and 12 weeks of age. Colons were removed, cut open and washed in cold phosphate-buffered saline. Colon organoids were then cultured using the protocol of Sato *et al*. (Sato *et al.,* 2013) following the plating of 500 crypt bottoms per well in triplicate per sample. Two-sample t-test was used to determine statistical significance.

RNA processing for Illumina bead arrays

Mouse intestinal tissues were removed, opened longitudinally and rinsed in phosphate-buffered saline. Colon tissues were processed in RNAlater (Qiagen, Valencia, CA, USA) as per the manufacturer's protocol. The distal quarter of the proximal quarter of the small intestine was flash frozen in liquid nitrogen. The tissue was then transferred from liquid nitrogen to precooled RNALaterIce (Ambion, Foster City, CA, USA) at -80^{o}C for 30 min, and later transferred to -20^{o}C for at least 48h. Immediately before RNA isolation, tissue in either RNALater or RNALaterIce was placed in 2–4 ml of RLT (guanidine thiocyanate buffer)/14.3 M b-mercaptoethanol buffer. The tissue was then homogenized using an IKA Ultra-Turrax T25 digital homogenizer (Fisher Scientific, Waltham, MA, USA). RNA isolation was then conducted using an RNeasy Mini Kit with an additional DNAse Digestion step (Qiagen). RNA sample concentrations were measured using a Nanodrop-1000 Spectrophotometer (Thermo Scientific, Rochester, NY, USA). RNA was stored at -80^{o}C.

Illumina bead microarray and data analysis

RNA labeling, microarray hybridization and scanning were performed at the University of Minnesota BioMedical Genomics Center using Illumina MouseWG-6 v.2.0 Expression BeadChips (Illumina, San Diego, CA, USA), according to the manufacturer's instructions. Differential expression of genes was quantified by the moderated t-statistic. Data were analyzed using GeneData Expressionist Software (GeneData Inc., San Francisco, CA, USA); genes that showed statistically significant differences in expression between groups were determined using the two-group t-test and analysis of variance. Gene expression data has been submitted to the Gene Expression Omnibus, and accession number is pending.

qRT–PCR

Quantitative RT–PCR was performed as described previously (Starr *et al.,* 2011). Significant differences in expression between groups were determined using the two-group t-test.

List of primers used:

All primers were designed using Primer-BLAST (National Center for Biotechnology Information) and obtained from Integrated DNA Technologies.

Mouse primers

Ang4: forward, 5'-AGCACACAGCTAGACTCGTCCC-3'; reverse, 5'-ACCAGAC CCAGCACGAAGACC-3'; *Areg*: forward, 5'-GGTCTTAGGCTCAGGCCATTA-3'; reverse, 5'-CGCTTATGGTGGAAACCTCTC-3'; *Cd55*: forward, 5'-GGGGCTATG ATCCGTGGGCG-3'; reverse, 5'-TGCCCAAGATTGGCCTGGCA-3'; *Clca3*: forward, 5'-CCACACCAAAACGAGAAGGC-3'; reverse, 5'-TGCTTCGGAGATTG CATCGT-3'; *Clca4*: forward, 5'-ACATGGACCGGCCTTTCTAC-3'; reverse, 5'-CG ACATCTCCTCGACACACA-3'; *Clca6*: forward, 5'-GTTCAATCAGAAAAGGCTT CCA-3'; reverse, 5'-ACTTCCCAAGTGCTTCTGTAATTG-3'; *Gstk1*: forward, 5'-TGGATGCGTGTATGGTCTCG-3'; reverse, 5'-CAGAAAGTGTTGGGCTTGCG-3'; *Egr1*: forward, 5'-CCTCAAGGGGAGCCGAGCG-3'; reverse, 5'-AACCGAGT CGTTTGGCTGGG-3'; *Fos*: forward, 5'-CGGGTTTCAACGCCGACTA-3'; reverse, 5'-TTGGCACTAGAGACGGACAGA-3'; *Id1*: forward, 5'-CTCAGCACCCTGAAC GGCGA-3'; reverse, 5'-CATCTGGTCCCTCAGTGCGCC-3'; *Muc2*: forward, 5'-AACGATGCCTACACCAAGGTC-3'; reverse, 5'-ACTGAACTGTATGCCTTCC TCA-3'; *Muc3*: forward, 5'-CACTACCACCCCAGCACCTA-3'; reverse, 5'-GCCT CCATTCTCGCAGTTGA-3'; *Muc13*: forward, 5'-TTTGGCTACAGCGGGAT GAA-3'; reverse, 5'-TCTTTGACCTCGCAGAGACG-3'; *Mt1*: forward, 5'-AAAC CCTTTGCGCCCGGACT-3'; reverse, 5'-AGCAGGAGCAGTTGGGGTCC-3'; *Pim3*: forward, 5'-GCTCATCGACTTCGGCTCGGG-3'; reverse, 5'-AGTGGCAGACCGC CCGTGATA-3'; and *Retnlb*: forward, 5'-AAGCCTACACTGTGTTTCCTTTT-3'; reverse, 5'-GCTTCCTTGATCCTTTGATCCAC-3'.

Pathway analysis

GSEA. GSEA v.2.0, http://www.broad.mit.edu/gsea/ (Subramanian *et al.,* 2005, Mootha *et al.,* 2003). Gene sets analyzed were obtained from published reports and the National Center for Biotechnology Information Gene Expression Omnibus database. GSEA compared the entire ranked *Kcnq1* proximal small intestine KO expression data set to *Cftr* KO25 (twofold change in expression, $t \leq 0.05$) and *Muc2* KO36 (1.5-fold change in the duodenum at 3 or 6 months of age).

IPA. Genes showing a 1.5-fold change in expression in whole colon (N = 89) and proximal small intestine (N = 345) microarrays were analyzed using IPA (IPA Ingenuity Systems).

Tissue microarrays

Patient study population. Patients who underwent liver resection with curative intent, sometimes with addition of RFA, in one of the seven Dutch hospitals affiliated with the DeCoDe PET group were identified by crossreferencing surgery and pathology databases using Dutch MeSH terms for 'colon', 'rectum', 'carcinoma', 'adenocarcinoma', 'colorectal neoplasms', 'liver', 'neoplasm metastasis' and '(hemi)hepatectomy'. Clinicopathological data from 507 patients that were operated on between 1990 and 2010 were extracted from these databases (see Supplementary Table 22; a manuscript describing the patient population in more detail is in preparation). Formalin-fixed paraffin-embedded tissue specimens were collected from one CRCLM sample and an adjacent control liver sample. Only specimens of patients with histologically confirmed CRCLM were included in the study, whereas tissue samples of patients with multiple primary tumors were excluded. Collection, storage and use of clinicopathological data and tissue specimens were performed in compliance with the 'Code for Proper Secondary Use of Human Tissue in The Netherlands', and approved in protocol 2011-03 of the Department of Pathology (Stichting FMWV Rotterdam 2011).

Tissue microarrays. A total of 21 tissue microarrays (TMAs) were generated as described previously (Simon *et al.,* 2004, Belt *et al.,* 2011). In brief, three tissue core biopsies of 0.6mm in diameter were punched from morphologically representative areas of all formalin-fixed paraffin-embedded donor blocks, and transferred into TMA recipient paraffin blocks using the 3DHISTECH TMA Master (v.1.14, 3DHISTECH Ltd, Budapest, Hungary).

Immunohistochemistry. Four-micrometer sections of TMAs were mounted on glass slides, deparaffinized by xylene and rehydrated with a decreasing alcohol series. Staining for KCNQ1 was performed upon antigen retrieval by microwave heating in citric acid (10mM, pH 6.0) and endogenous peroxidase neutralization in 0.3% hydrogen peroxide in methanol for 25 min. The primary rabbit polyclonal antibody directed against human

KCNQ1 (sc-20816; Santa Cruz Biotechnology Inc., Santa Cruz, CA, USA) was incubated overnight at a 1:200 dilution at 4^{o}C, followed by incubation with anti-rabbit secondary antibodies for 30 min at room temperature (Envision Plus; Dako, Heverlee, Belgium). Secondary antibodies were visualized by liquid diaminobenzidine substrate chromogen system. Slides were counterstained with Mayer's hematoxylin. Staining of formalin-fixed paraffin-embedded colon tissue was used as a positive control, and incubation without primary antibody as a negative control.

Evaluation of KCNQ1 protein expression. Immunohistochemical stainings were digitally captured using the Mirax slide scanner system equipped with a x20 objective with a numerical aperture of 0.75 (Carl Zeiss BV, Sliedrecht, The Netherlands) and a Sony DFW-X710 Fire Wire 1/3 in-type progressive SCAN IT CCD (pixel size 4.65 x 4.65 μm^2). Actual scan resolution at x 20 was 0.23 µm. Computer monitors were calibrated using Spyder2PRO software (v.1.0–16; Pantone Colorvision, Regensdorf, Switzerland). TMA core biopsies were scored for intensity of KCNQ1 protein expression on membranes of neoplastic epithelial cells (categories negative, weak, moderate, strong) using dedicated TMA scoring software (v.1.14.25.1; 3DHISTECH Ltd). For facilitating scoring, a chart with visual analogue scales of staining patterns was used. Intensity scores were dichotomized into low and high KCNQ1 intensities using receiver operating characteristic curve analysis (Zlobec *et al.,* 2007).

Statistical analysis of TMAs. OS was defined as the time in months after surgery until death in a follow-up period of 10 years. Patients were excluded from analysis if OS < 2 months (n = 72), if OS or survival status were unknown (n = 36) or if tissue cores could not be evaluated for technical reasons (n = 88). The relation between KCNQ1 expression and survival was studied using Kaplan–Meier curves and tested using log-rank statistics. HRR was calculated using Cox regression. Multivariate analysis was performed by inclusion of KCNQ1 protein expression in a proportional hazards (Cox regression) analysis together with established prognostic clinicopathological variables combined in the clinical risk score as defined by Fong *et al*. (Fong *et al*., 1999) primary tumor-to-liver metastasis interval > 12 months, number of liver metastases > 1, maximal tumor diameter > 5.0 cm, lymph node positivity at the time of diagnosis of the primary tumor, serum

carcinoembryonic level > 200 ng/ml. Stepwise backward regression was used to exclude variables from the model when P > 0.1. All statistical tests were two-sided and executed using IBM SPSS Statistics 20.0 software (SPSS Inc., Chicago, IL, USA). P-values < 0.05 were considered significant.

Supplemental Information:

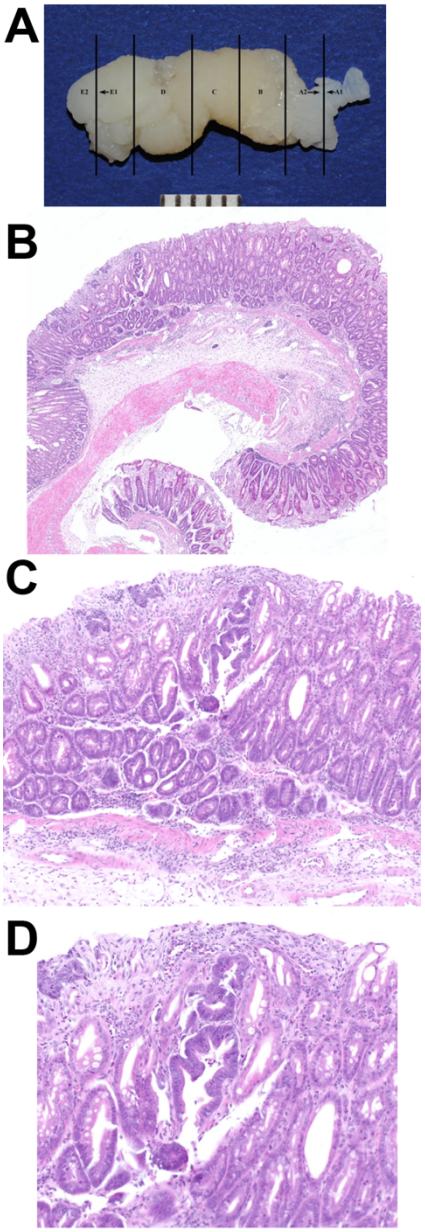

Figure 44. Rectal Adenomatous Hyperplasia. Panel A. Gross image of rectum. Lines represent locations of cross sections taken for histopathological analysis. Panels B, C & D, three cross sections of the same tissue showing diffuse crypt hyperplasia. The incidence of abnormal rectums was 10 out of 102 *Apc*^{Min} *Kcnq1*$^{+/-}$ (79) and *Apc*^{Min} *Kcnq1*$^{-/-}$ (23) mice and 0 out of 58 for *Apc*^{Min} *Kcnq1*$^{+/+}$ mice, a difference that is highly significant (p = 0.009, Fisher's Exact Test).

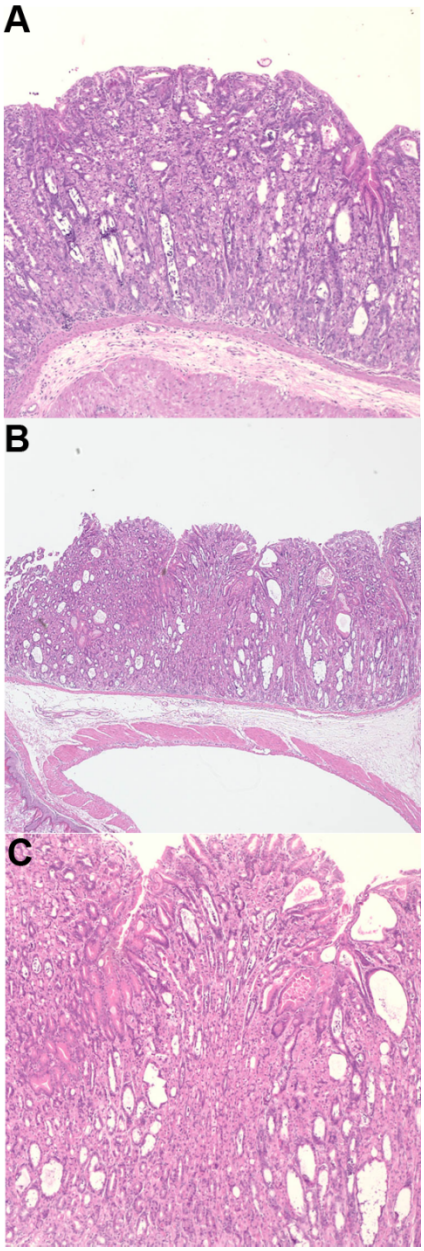

Figure 45. Stomach of *Apc*$^{+/+}$ *Kcnq1*$^{-/-}$ mice. Panels A & B, 10X; **Panel C**, 20X. Severe gastric hyperplasia that was characterized by mucosal hyperplasia, with parietal cells increased in size and crypt dilation with debris present. Hyperplastic adenomas developed in the pylorus (not shown). The incidence of pyloric tumors was 21 out of 23 *Apc*^{Min} *Kcnq1*$^{-/-}$ mice and 0 out of 58 *Apc*^{Min} *Kcnq1*$^{+/+}$ mice, a difference that is highly significant ($p < 2.2e-16$, Fisher's Exact Test).

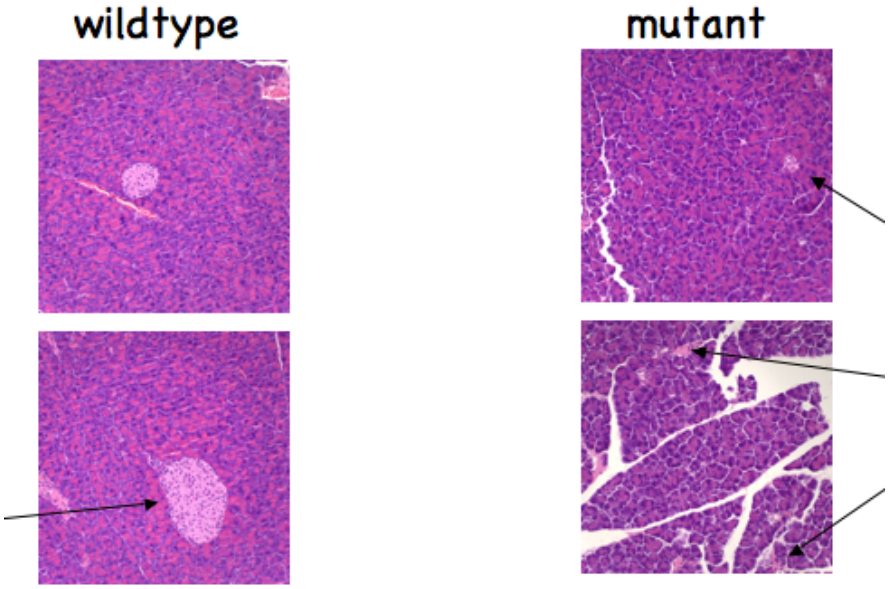

Figure 46. Pancreas. 20X. ***Kcnq1* Wildtype, left panels**; ***Apc*^{Min} *Kcnq1*$^{-/-}$ right panels**. Zymogen granules were less eosinophilic and less prominent. Exocrine cells seemed to be smaller and islets appeared to be less prominent (arrows). The incidence of enlarged pancreases was 8 out of 23 *Apc*^{Min} *Kcnq1*$^{-/-}$ mice and 0 out of 58 in *Apc*^{Min} *Kcnq1*$^{+/+}$ mice, a difference that was high significant ($p = 1.52e-05$, Fisher's Exact Test). The maximum diameter of a total of 56 pancreatic islets was measured, 28 from *Apc*^{Min} *Kcnq1*$^{-/-}$ mice and 28 from *Apc*^{Min} *Kcnq1*$^{+/+}$ mice. The mean diameter of islets from *Apc*^{Min} *Kcnq1*$^{-/-}$ mice was 100 microns and the mean diameter of islets from *Apc*^{Min} *Kcnq1*$^{+/+}$ mice was 118 microns. While the difference in means was not significant, when the 56 islet diameters were ranked in size the top 7 islets were all from the *Kcnq1*$^{+/+}$ group (246, 242, 212, 210, 199, 184, and 181 microns), while the largest islet from the *Kcnq1*$^{-/-}$ group was 173 microns.

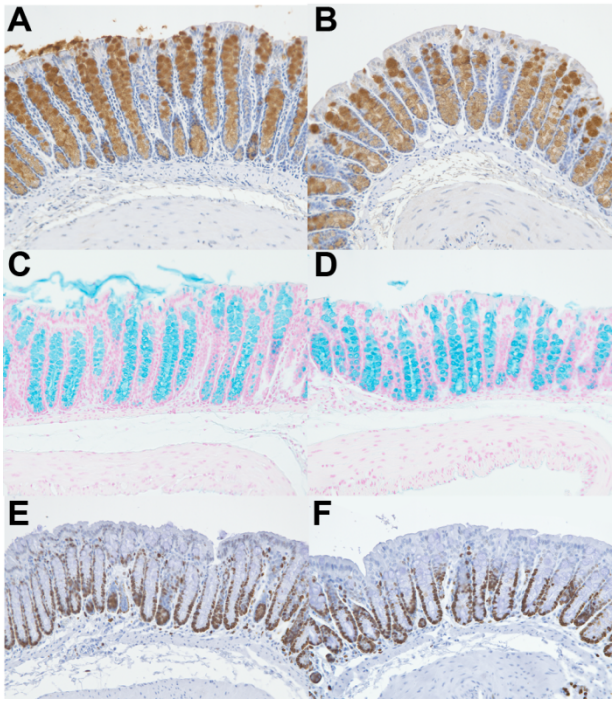

Figure 47. Immunohistochemistry for cellular markers in mouse colon. Age and gender matched *Kcnq1*$^{+/+}$ and *Kcnq1*$^{-/-}$ adult littermate mice were sacrificed and FFPE tissues processed as previously described (Fijneman *et al.*, 2012). Multiple sections were examined by immunostaining for the goblet cell markers Mucin2 and alcian blue (for detection of acidic mucopolysaccharides), and the proliferation marker Ki67. No significant differences were detected between genotypes. Representative colon section is shown above. Mucin2: Panel A (*Kcnq1*$^{+/+}$), Panel B (*Kcnq1*$^{-/-}$); Alcian Blue: Panel C (*Kcnq1*$^{+/+}$), Panel D (*Kcnq1*$^{-/-}$); Ki67: Panel E (*Kcnq1*$^{+/+}$), Panel F (*Kcnq1*$^{-/-}$). *Methods.* 4 µm formalin-fixed, paraffin-embedded sections of small intestine were deparaffinized and rehydrated, followed by antigen retrieval using 10mM Citrate buffer pH 6.0 in a steamer. A rabbit polyclonal antibody was used for Mucin 2, Catalog number: SC15334, (Santa Cruz Biotechnology). A rabbit monoclonal antibody was used for Ki-67, Catalog number: CRM325, clone SP6, (Biocare Medical). Detection was achieved using a rabbit EnVision™+ Kit (catalog K4011, Dako) with DAB as chromogen. Alcian blue staining was performed using a standard protocol.

Figure 48. Colon Microarray - Top Functional Networks Identified by IPA

A. Cancer, Cellular Function and Maintenance, Molecular Transport

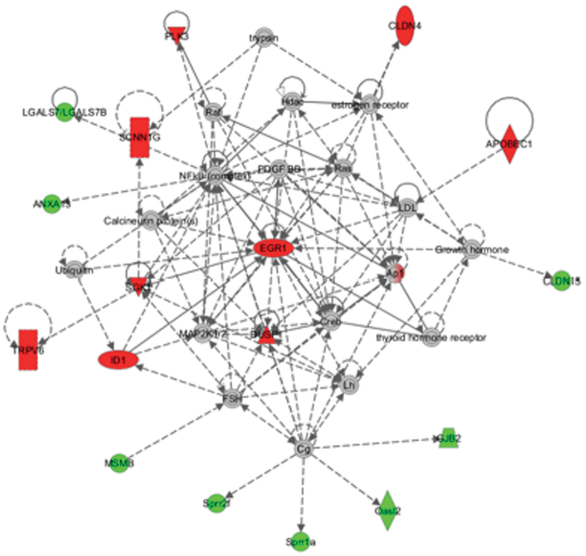

B. Immunology & Inflammatory Disease

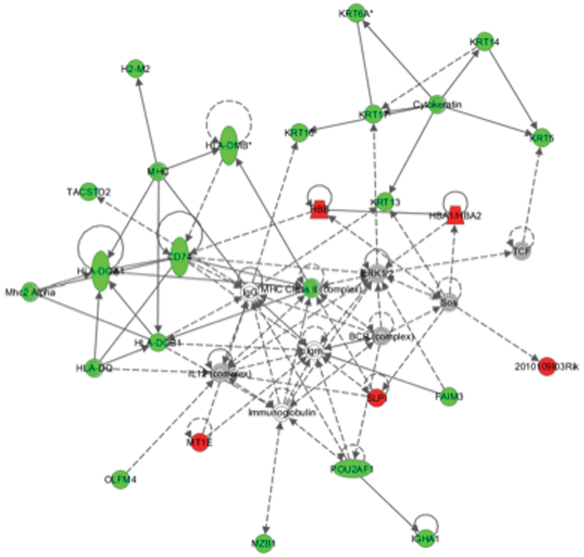

Figure 49. Proximal Small Intestine Microarray - Top Gene Networks Identified by IPA.

A. Molecular Transport, Cell Death and Survival, Cellular Assembly and Organization

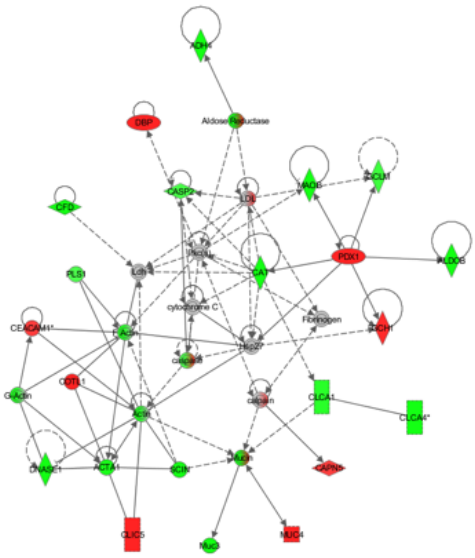

Figure 50. Concordance between expression of *KCNQ1* and *CFTR* in colorectal cancer liver metastases. Twenty stage IV CRC liver metastases were analyzed by RNA seq, followed by Pearson's Correlation analysis to determine concordance between the expression levels of *KCNQ1* and *CFTR*. Panel A. Using all twenty samples. Panel B. removal of two top and bottom outliers, N = 18.

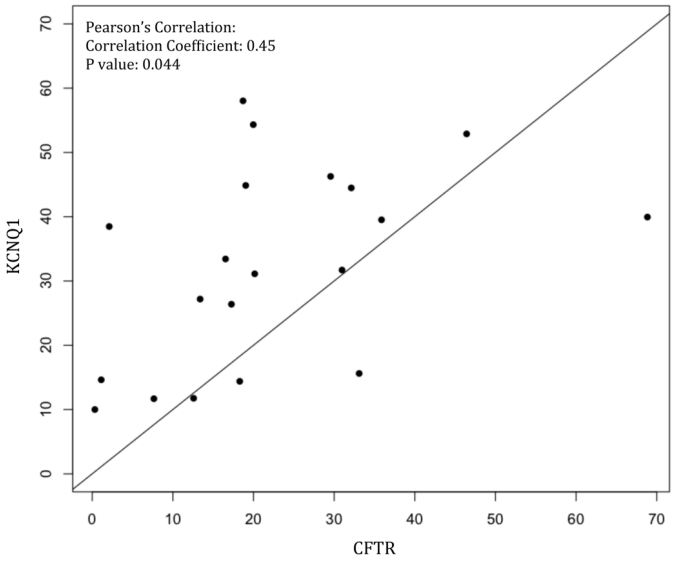

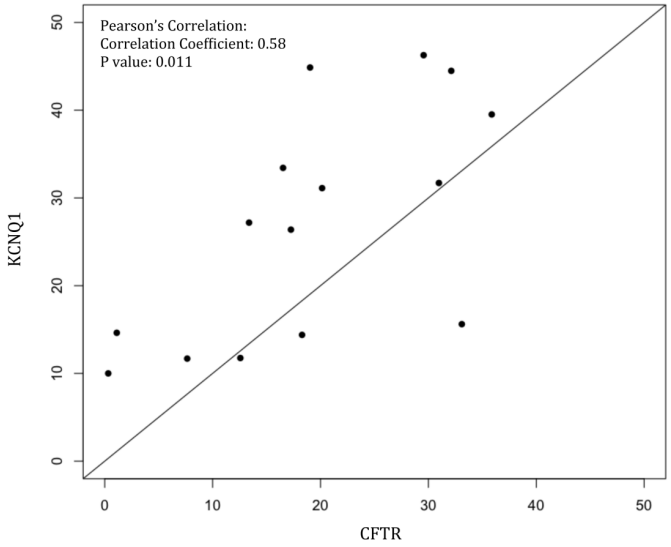

RNA Seq analysis. Twenty fresh frozen stage IV CRC LM samples were obtained from the University of Minnesota BioNet Tissue Procurement facility. The samples were from 9 males and 11 females, average age 64 years. RNA was isolated using RNA LaterICE (Invitrogen) and Qiagen RNAEasy kits, and quantified using a Nanodrop-1000 Spectrophotometer (Thermo Scientific), and quantity and quality were confirmed using The extracted RNA-samples were sent to the University of Minnesota Genomics Center (UMGC) for sequencing. All raw reads that passed the CASAVA 1.8 P/F filter were directly deposited at the Minnesota Supercomputing Institute, where the data were

analyzed. Sequence quality was assessed via fastqc (http://www.bioinformatics.babraham.ac.uk/projects/fastqc/). Since the raw sequence reads were of sufficient quality, no data trimming or filtering was necessary. Hence, the raw paired-end reads were mapped to human genome (hg19 assembly) using Tophat 2.0.6 with the iGenomes reference (UCSC human hg19 annotation, downloaded from http://cufflinks.cbcb.umd.edu/igenomes.html March 9, 2012). Final mapping percentages of the 20 samples range from 92% to 94%. The mapped samples were then analyzed via Cuffdiff (default parameters using the iGenomes UCSC hg19 GTF file previously mentioned) to quantify the expression level of each known gene in units of FPKM (Fragment mapped per kilobase of exons per million mapped reads). Additional statistical test of Pearson's correlation from R/Bioconductor was applied to selected gene pairs to check for expression concordance.

Table 18. List of top known genes 1.5 fold (A) up-regulated and (B) down-regulated in *Kcnq1* $^{-/-}$ mouse colons, represented as fold change vs control *Kcnq1*$^{+/+}$. The asterisk in the Fold Change column indicates a P value of 0.05 or less.

Table 19. List of top known genes 1.5 fold (A) up-regulated and (B) down-regulated in *Kcnq1*$^{-/-}$ mouse small intestines, represented as fold change vs control *Kcnq1*$^{+/+}$. The asterisk in the Fold Change column indicates a P value of 0.05 or less.

Table 20. IPA Analysis of Colon Microarray.

Table 21. IPA Analysis of Proximal Small Intestine Microarray.

Table 22. Core genes enriched in *Kcnq1* KO.

Table 23. Expression of *Areg*.

Table 18-23 can be found in the supplemental tables. Please see the weblink: http://www.nature.com/onc/journal/vaop/ncurrent/full/onc2013350a.html

CONFLICT OF INTEREST

The authors declare no conflict of interest.

ACKNOWLEDGEMENTS

We thank Dr Karl Pfeifer at the NIH for generously providing *Kcnq1* mutant mice and reviewing the manuscript. Research was supported by a grant to RC and DL (NCI R01 CA134759-01A1) and to JG and RF (Center for Translational Molecular Medicine, DeCoDe project grant 03O-101) and to TKS (NCI R00 4R00CA151672-02).

Personal Contribution. Lei Zhao isolated RNA samples for Illumina RNA Sequencing and analyzed data.

APPENDIX 3

The roles of *CNOT1* and *CNOT2* in regulating mRNA levels of $p27^{kip}$ and *CDX2*

Introduction

Sleeping Beauty (SB) transposon-based screens have identified *Cnot1* and *Cnot2*, two subunits of the CNOT complex, as candidate CRC genes (Starr *et al*., 2009). (See introduction for discussion of *CNOT1*). The TCGA project identified 48 somatic mutations in *CNOT2* in different types of cancers and 3 of them were discovered in CRC. In addition, 47 somatic mutations in *CNOT2* were documented in the COSMIC database and 76% of them were missense mutations. The presence of somatic DNA mutations in *CNOT2* provided evidence for a correlation between genetic alterations in *CNOT2* and CRC. The biological importance of *CNOT2* has been reported in several model animals. It is critical for yeast survival (Russell *et al*., 2002). Apoptosis may be occurring in *CNOT2*-depleted *C. elegans* and *D. melanogaster* during early embryonic stages (Frolov *et al*., 1998; Sonnichsen *et al*., 2005). In Hela cells *CNOT2* depletion caused apoptotic cell death in a caspase-dependent manner (Ito *et al*., 2011). As for the molecular function of *CNOT2*, accumulating results suggest that it plays a role in regulation of deadenylation as a component of the CNOT deadenylase complex and/or in transcriptional regulation (Zwartjes *et al*., 2004). CNOT2 plays an important role in maintaining the integrity of the CNOT complex, supported by the fact that CNOT2 mutations affect the structural integrity of the complex in yeast (Russell *et al*., 2002). Mammalian *CNOT2* depletion also destabilized the CNOT complex and impaired its deadenylase activity. Ito *et al* showed that the disruption of the CNOT complex induced by *CNOT2* depletion is accompanied by a loss of deadenylase activities (Ito *et al*., 2011). Furthermore, knockdown of *CNOT2* inhibits mRNA decay in Drosophila S2 cells (Temme *et al*. 2004). These results suggest that the structural integrity of the complex is apparently important

for full deadenylase activity. However, the exact mechanism by which CNOT2 contributes to the regulation of the deadenylase activity of the CNOT complex remains obscure. CNOT2 also acts as a transcriptional repressor of Estrogen Receptor (ER)-mediated gene expression through direct repression of pol II transcription. The major repressive function of CNOT2 is localized in the Not-Box repression domain in the C-terminus of CNOT2 (Zwartjes *et al.*, 2004). Depletion of deadenylase subunits of the CNOT complex was reported to affect cell viability (Ito *et al*., 2011; Morita *et al*., 2007), suggesting that the deadenylase activity of the CNOT complex is important for regulation of cell viability. Thus attenuated deadenylation activity of the CNOT complex may contribute to the decreased cell viability caused by *CNOT2* depletion.

Cyclin-dependent kinase inhibitor 1B (CDKN1B, $p27^{Kip}$) is a well-known cell cycle inhibitor which prevents the activation of cyclin E-CDK2 or cyclin D-CDK4 complexes, and thus arrest cell cycle progression at G1. Cnot6L was shown to contribute to the deadenylation and degradation of $p27^{Kip1}$ mRNA through a 3'UTR ARE-mediated mechanism (Morita *et al*., 2007). The gut-specific homeotic transcription factor caudal type homeobox 2 (CDX2) is a crucial regulator of intestinal development and homeostasis, which exhibits a tumor suppressor function in CRC (Saandi *et al*., 2013). *Cnot1* and *Cnot2* silencing was shown to lead to markedly increased expression of *Cdx2* in mouse embryonic stem cells (Zheng *et al*., 2012). These data suggest that $p27^{Kip1}$ and *CDX2* are potential target genes of CNOT1- and CNOT2-mediated deadenylation or transcriptional regulation.

In our study, to investigate the role of *CNOT1* and *CNOT2* in CRC, we measured cell viability following depletion of *CNOT1* and *CNOT2* in SW480 CRC cells. We then studied the role of CNOT1- and CNOT2-mediated deadenylation in regulating $p27^{kip}$ and *CDX2* mRNA levels and the contribution of these two genes to *CNOT1* and *CNOT2* depletion caused cell viability reduction.

Results

Depletion of the CNOT Complex Subunits Results in Reduced Cell Viability in SW480 Cells

As shown in Figure 24 D, depletion of *CNOT2* resulted in decreased cell viability in SW480 CRC cells, suggesting that *CNOT2* may function as an oncogene. In addition, cell viability assay revealed that depletion of *CNOT6L, CNOT7* and *CNOT8* caused significant decrease in cell viability (Figure 24 D), suggesting that CNOT1 and CNOT2's effects on cell viability may be mediated by deadenylation activity of these deadenylase subunits.

p27^{kip} and *CDX2* mRNA Levels Were Upregulated in SW480 Cells Depleted for *CNOT1* and *CNOT8*

The CNOT deadenylases were reported to mediate deadenylation and subsequent degradation of cell cycle inhibitor *p27^{kip}* and the intestinal differentiation factor *CDX2*. Consistent with published data, we found that *p27^{kip}* (Figure 51A) and *CDX2* (Figure 51B) mRNA levels were increased by 1.5 and 2.5-fold, respectively, in *CNOT1*-depleted but not changed in *CNOT2*-depleted cells. To determine which deadenylase subunit shares a common phenotype with CNOT1 we examined the effect of their depletion on levels of *p27^{kip}* (Figure 51A) and *CDX2* (Figure 51B) mRNA levels. Lack of *CNOT8* caused a 1.5- and 2-fold increase in *p27^{kip}* and *CDX2* mRNA levels, respectively. But depletion of other deadenylase subunits did not cause an obvious change in *p27^{kip}* mRNA levels. Interestingly, depletion of *CNOT6* and *6L* both caused decreased *CDX2* mRNA levels possibly through indirect mechanisms. These results suggest that CNOT1 and 8 may works in complexes to regulate the mRNA levels of *p27^{kip}* and *CDX2* through deadenylation.

A.

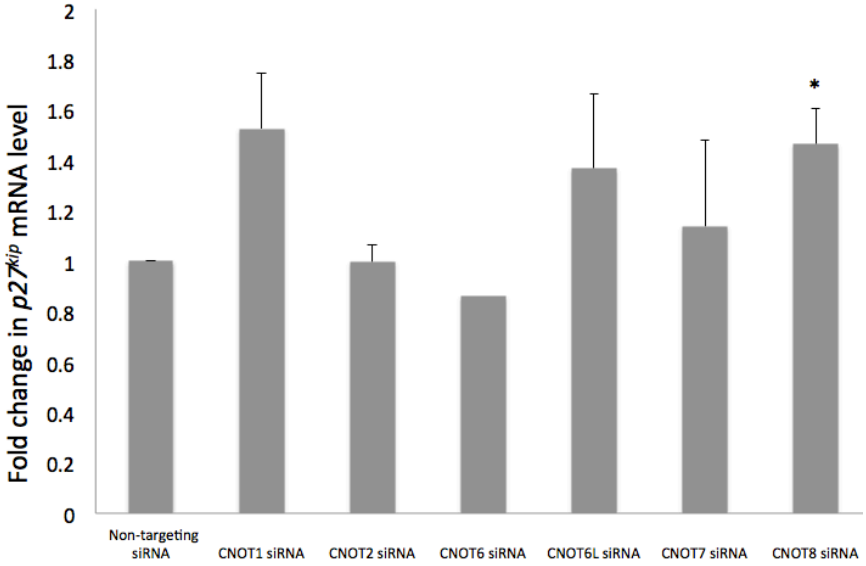

B.

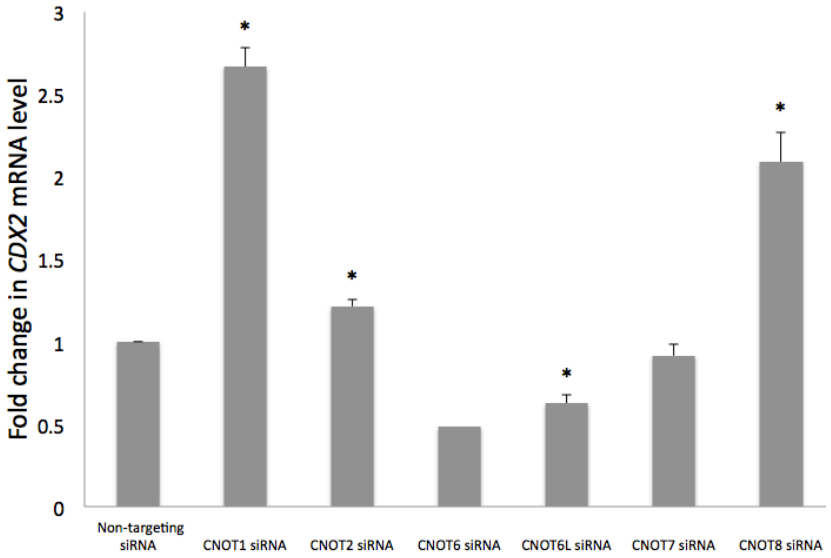

Figure 51. *p27^{kip}* and *CDX2* mRNA expression levels in SW480 cells depleted for CNOT subunits. SW480 cells were depleted for *CNOT1, 2, 6, 6L, 7* and *8*, respectively as described before. Total RNA was extracted at 48 hours after the second siRNA transfection. mRNA expression levels of *p27^{kip}* (A) and *CDX2* (B) were measured by qRT-PCR. Values represent the mean ± SD of at least two independent experiments except for CNOT6 (one experiment). Statistical significance was determined by a *t*-test. * = $p < 0.05$.

Effects of Depletion for RBPs on Cell Viability and *p27^{kip}* and *CDX2* mRNA Levels

To test if 3'UTR RNA binding proteins (RBPs) might mediate the phenotype shared by CNOT1 and CNOT8 we examined the effect of depletion of several RBPs on cell viability and *p27^{kip}* and *CDX2* mRNA levels, including *ZFP36, PUM1, PUM2* and *CELF1*. They were knocked down in SW480 cells by transfection of corresponding siRNA oligos, which was confirmed by qRT-PCR (Figure 52A). Cell viability was reduced in cells depleted for *ZFP36, PUM1* and *CELF1*, but not in cells depleted for *PUM2* (Figure 52A). mRNA levels of *p27^{kip}* were increased by 1.35 fold in *ZFP36*-depleted cells but not in other cells (Figure 52B). *CDX2* mRNA levels were increased by 1.5 fold in *ZFP36* and *CELF1*-depleted cells but not in other cells (Figure 52C). Together, these results suggest that ZFP36 and CELF1 may work with CNOT1 and 8 in complexes to regulate cell viability and mRNA levels of *p27^{kip}* and *CDX2* through deadenylation.

A.

Gene	mRNA levels	Cell viability
ZFP36	74.07±17.04%	57.14±9.21%
PUM1	60.03%	42.90%
PUM2	15.76%	92.67%
CELF1	46.16%	63.77%

B.

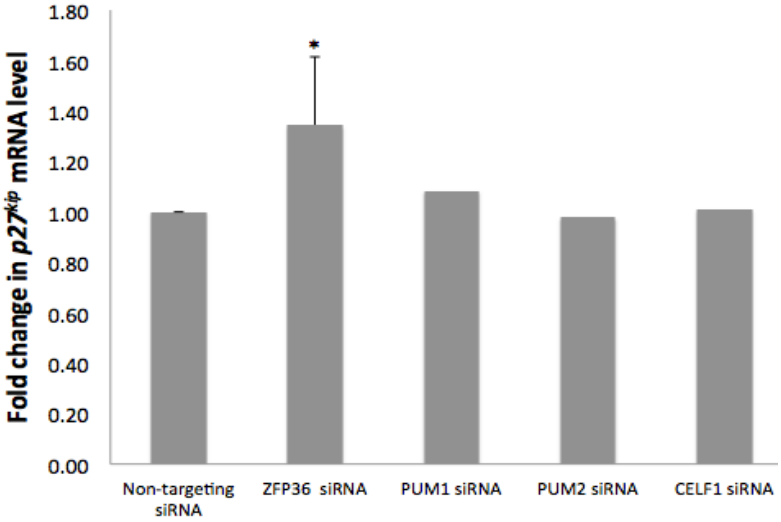

C.

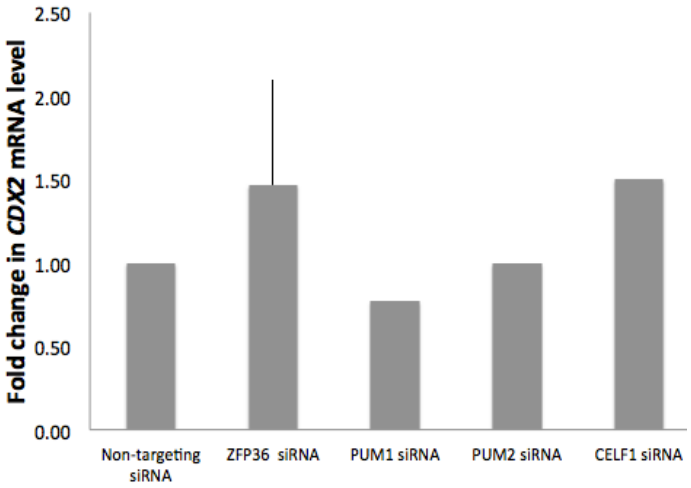

Figure 52. Cell viability and *p27^{kip}* and *CDX2* mRNA expression levels in SW480 cells depleted for RBPs. SW480 cells were depleted for *ZFP36, PUM1, PUM2* and *CELF1* by siRNA transfection as described before. (A) On day 1 after the second transfection SW480 cells were plated at 2,500 cells per well in triplicate in 96 well plates. Cell viability was measured by MTT assay on day 6 after the second transfection. Relative cell viability represents = absorbance at 595 nm of cells treated with indicated siRNA/cells treated with non-targeting control. Results represent one experiment except for ZFP36 (3 experiments). (B and C) Total RNA was extracted 48 hours after the second transfection and *p27^{kip}* (B) and *CDX2* (C) mRNA expression levels were determined by qRT-PCR. Values represent one experiment except for ZFP36 (mean ± SD of 3 experiments). Significance of difference was calculated by a *t*-test. * = $p < 0.05$.

Depletion of *CDX2* Did Not Result in Changes in Cell Viability in SW480 Cells

To initially investigate whether the decreased cell viability caused by knockdown of *CNOT1, CNOT8, ZFP36* and *CELF1* was due to increased levels of *CDX2*, we depleted *CDX2* by transfection of siRNA oligos targeting *CDX2* in SW480 cells and measured cell viability using the MTT assay. Knockdown of *CDX2* was confirmed by qRT-PCR (Figure 53A). No obvious difference in cell viability was observed in *CDX2* siRNA transfected cells comparing to control cells (Figure 53B). These results suggest that upregulated *CDX2* may not be the cause for the reduction in cell viability. However, this is the data from only one experiment which was performed in highly malignant SW480 cells. Therefore, more assays need to be performed, including overexpression of

CDX2 and knocking down *CDX2* in normal colon epithelial cell lines, before we can draw any conclusions.

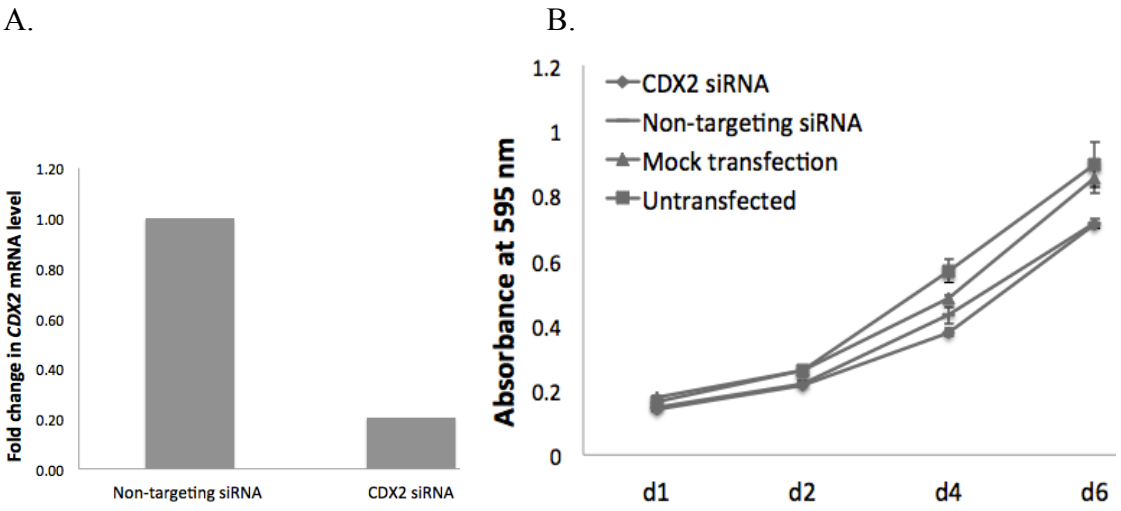

Figure 53. Depletion of *CDX2* did not result in changes in cell viability in SW480 cells. SW480 cells were depleted for *CDX2* by transfection of siRNA oligo targeting *CDX2* at 50 nM final concentration twice 48 hours apart. Knockdown of *CDX2* was confirmed by qRT-PCR (A) and cell viability (B) was measured by MTT assay. Data represents result of only one experiment. Each data point for MTT assay represents the mean ± SD of three replicates in one MTT assay. Significance of differences in cell viability on day 6 was determined by one-way ANOVA.

CNOT1 Does Not Regulate *p27^{kip}* and *CDX2* mRNA Levels Through 3'UTR-Mediated Deadenylation

To investigate whether CNOT1 regulates *p27^{kip}* and *CDX2* mRNA levels through 3'UTR-mediated deadenylation we performed a 3'UTR luciferase reporter assay in SW480 cells using a Dual-Glo reporter assay system (Promega). The 3'UTR of *p27^{kip}* and *CDX2* was cloned downstream of a sequence encoding renilla luciferase in a psi-Check2 vector where activity of renilla luciferase is indicative of 3'UTR mediated deadenylation. This vector also constitutively encodes the firefly luciferase to normalize cell number and transfection efficiency. Results revealed that transfection of *CNOT1* siRNA did not cause a change in luciferase activity of *p27^{kip}* (Figure. 54A) and *CDX2* (Figure 54B) 3′UTR reporter plasmids compared with cells transfected with control

siRNA. This result suggested that CNOT1 might regulate mRNA levels of these two genes through mechanisms other than deadenylation. However, the data represent the result of only one experiment. More replicates and more assays need to be done before we can draw any conclusions.

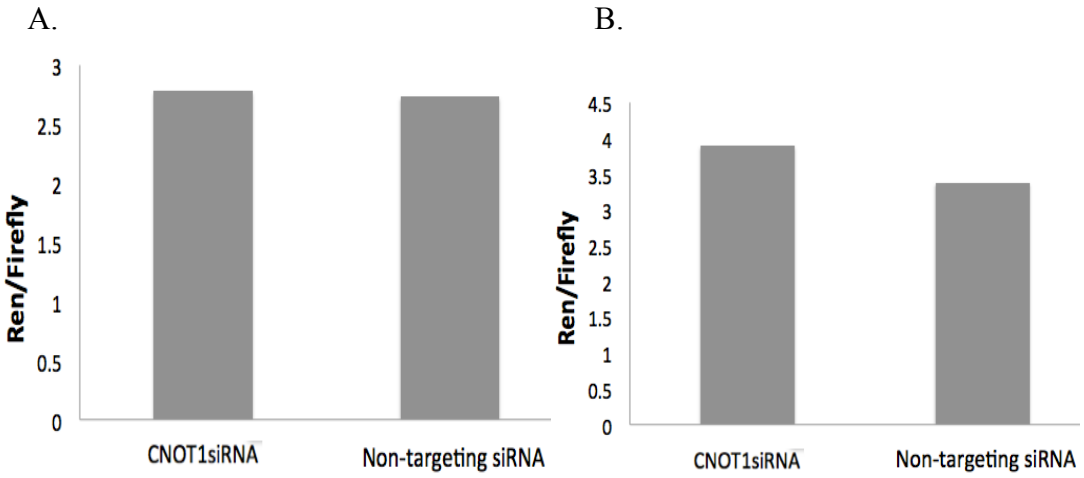

Figure 54. CNOT1 does not regulate *p27^{kip}* and *CDX2* mRNA levels through 3'UTR-mediated deadenylation. A luciferase reporter assay was performed in SW480 cells to investigate whether CNOT1 regulates *p27^{kip}* and *CDX2* level through 3'UTR-mediated deadenylation. SW480 cells were co-transfected with 50 ng of luciferase reporter plasmid containing either *p27^{kip}* or *CDX2* 3'UTR together with 50 nM *CNOT1* siRNA or control siRNA. Firefly and renilla luciferase activity was measured at 48 hours post-transfection using the Dual-Glo reporter assay system (Promega). Luciferase activity was analyzed by the ratio of renilla/firefly illuminance to normalize cell number and transfection efficiency. The luciferase activity of *p27^{kip}* (A) and *CDX2* (B) reporter was not obviously changed in *CNOT1* siRNA transfected cells comparing to control cells. The data represent the result of only one experiment in which each treatment was performed in duplicates.

Discussion

Consistent with published studies, knockdown of *CNOT1* and *CNOT2* in SW480 CRC cells highly reduced cell viability, suggesting that *CNOT1* and *2* may function as an oncogene in CRC and that the integrity of the CNOT complex is important in maintaining cell viability. It has been shown that the attenuated deadenylase activity of the CNOT complex could cause reduced cell viability (Ito *et al*., 2012; Morita *et al*., 2007).

Therefore, the suppression of deadenylation activity caused by *CNOT1* and *CNOT2* depletion might be responsible for the decreased cell viability. To test this hypothesis we depleted deadenylase subunits in SW480 cells and measured cell viability. We found that cell viabilities in *CNOT6L, 7* and *8*-depleted cells were highly reduced, suggesting that decreased cell viability induced by *CNOT1* and *2* depletion might be due to suppressed deadenylation.

$p27^{kip}$ and CDX2 are two well-known cell cycle inhibitors and are potential target genes of CNOT1 and 2 mediated deadenylation. We investigated the mRNA levels of these two genes in both *CNOT1*- and *CNOT2*-depleted SW480 cells. The results showed that mRNA levels of these two genes were upregulated in *CNOT1*-depleted cells but had no obvious change in *CNOT2*-depleted cells, suggesting that CNOT2 may not participate in regulation of these two genes. These results also revealed that CNOT1 and CNOT2 might have different roles in deadenylation mediated by the CNOT complex. Next, to initially study whether deadenylation contribute the regulation of $p27^{kip}$ and *CDX2* mRNA levels by CNOT1 we measured the mRNA levels of these two genes in SW480 cells depleted for deadenylase subunits. We found that lack of *CNOT8* caused an increase in $p27^{kip}$ and *CDX2* mRNA levels. But depletion of other deadenylase subunits did not result in obvious changes in $p27^{kip}$ mRNA levels. Interestingly, depletion of *CNOT6* and *6L* both caused decreased *CDX2* mRNA levels, suggesting an indirect effect. Together, these results suggest that CNOT1 and 8 may participate in a complex that regulates mRNA levels of $p27^{kip}$ and *CDX2* by deadenylation. These findings also revealed that deadenylase subunits have specificity in targets or that their distribution and abundance might be different in cell lines.

RNA binding proteins (RBPs) promote deadenylation of target RNA transcripts by binding to AREs in their 3'UTRs. They recruit the deadenylases to the target mRNAs through direct binding to CNOT1 that in turn provides a platform to recruit the deadenylases and thereby trigger decay of target mRNAs. *SB*-based screens have identified several RBPs as potential CRC cancer genes, including *Pum1*, *Pum2*, *Elavl1* and *Celf1*. To test if these RBPs might mediate the phenotype shared by CNOT1 and

CNOT8 we examined the effect of depletion of several RBPs on cell viability and $p27^{kip}$ and *CDX2* mRNA levels. Cell viability was reduced in cells depleted for *ZFP36, PUM1* and *CELF1* but not in cells depleted for *PUM2*. mRNA levels of $p27^{kip}$ were increased only in *ZFP36*-depleted cells. *CDX2* mRNA levels were increased by 1.5 fold in *ZFP36*, and *CELF1*-depleted cells. Together, these results suggest that ZFP36 and CELF1 may work with CNOT1 and 8 in complexes to regulate cell viability and mRNA levels of $p27^{kip}$ or *CDX2* through deadenylation.

Two important questions are whether CNOT1 regulates $p27^{kip}$ *and CDX2* mRNA levels through deadenylation and whether upregulated levels of these two genes were responsible for the reduced cell viability in *CNOT1* insufficient cells. To answer the first question we performed a 3'UTR luciferase reporter assay. The results revealed that lack of *CNOT1* did not result in a change in luciferase activity of $p27^{kip}$ and *CDX2* 3′UTR reporter plasmids. This result suggested that CNOT1 might regulate the mRNA levels of these two genes through mechanisms other than deadenylation. It is also possible that the assay was not able to detect the changes in deadenylation possibly due to the reporter plasmids, so we may need to construct new reporter plasmids, such as a plasmid containing concatemers of targeting sites of known microRNAs that destabilizes these two genes. To answer the second question we depleted *CDX2* in SW480 cells. But no obvious change in cell viability was observed. These results suggest that upregulated *CDX2* may not be the cause for reduction in cell viability caused by *CNOT1* depletion. However, this experiment was carried out in highly malignant SW480 cells. Therefore we need to knock down *CDX2* in a normal colon epithelial cell line and perform an overexpression study of *CDX2*, before we can draw any conclusions.

In this study we failed to provide evidence that CNOT1 and CNOT2 could regulate $p27^{kip}$ and *CDX2* mRNA levels through deadenylation and that upregulated *CDX2* levels could be responsible for decreased cell viability following *CNOT1* and *CNOT2* depletion. However, there were several obvious limitations in this study. Some of the experiments were performed only once, thus the results need to be confirmed by more replicates. Knockdown of *CDX2* was performed in a highly malignant CRC cell line, possibly making the acceleration in cell proliferation impossible to be observed.

Thus a less malignant cell line and overexpression studies are necessary. The 3'UTR reporter assay may not work for our purpose, so a new strategy to design reporter plasmids may be needed. It is also possible that upregulation of *p27^{kip}* and *CDX2* do not contribute to decreased cell viability caused by *CNOT1* and *CNOT2* depletion. Upregulation of other genes or a combination of other genes may be the reason.

Material and methods

siRNA transfection, MTT assay, RNA isolation, cDNA synthesis, qRT-PCR were performed as described in previous sections.

Luciferase Reporter Plasmids Construction and Luciferase Assay

Clones containing complete 3'UTR of *p27^{kip}* (clone ID: 3458141) and *CDX2* (clone ID: 4867859) were obtained from Openbiosystem. PCR primers containing restriction sites for XhoI and NotI were designed to amplify the complete 3'UTR of *p27^{kip}* and *CDX2*. *p27^{kip}*: forward, 5'- CAACTCGAGATGACCCACCGGGGTCTGCAG-3'; reverse, 5'-CAAGCGGCCGCATCTGGAAAGCTCATTTATCT-3'; *CDX2*: forward, 5'-CAACTCGAGATAAACAGCTCGAATTAAGAAT-3'; reverse, 5'-CAAGCGGCCGCATAGCTATGGAAGTTTTCTT-3'. PCR was carried out using a Phusion High-Fidelity DNA Polymerase (New England Biolabs) with the following reaction mix: 8 µl of 5 x Phusion HF buffer, 0.4 µl Phusion DNA Polymerase, 200 µM of each dNTP, 1 µl of each primer (final concentration 0.5 µM), 100 ng of DNA template, and corresponding amount of H_20 to make a 40 µl volume. Cycling conditions were 95°C for 5 minutes, then 35 cycles of 95°C for 30 seconds, 60°C for 30 seconds, 72°C for 30 seconds, and finally 72°C for 10 minutes. PCR products was digested with XhoI and NotI and inserted between the corresponding restriction sites on a psiCHECK-2 vector (Promega) to generate 3'UTR reporter plasmids. psiCHECK-2 vector contains both the synthetic firefly luciferase (Fluc) gene and the synthetic renilla luciferase (hRluc) gene, each with its own promoter and poly(A)-addition sites. The correctness of all constructs was confirmed by sequencing.

To perform luciferase reporter assays, SW480 cells were plated at 2 x 10^4/well on 96 well plates and co-transfected with 50 ng of 3'UTR luciferase reporter plasmids for

p27^{kip} or *CDX2* together with 50 nM *CNOT1* siRNA or a control siRNA. Firefly and renilla luciferase activities were measured at 48 hours post-transfection using a Dual-Glo reporter assay system (Promega) according to manufacturer's instructions. Briefly, 96 well plates was changed with 75 µl DMEM medium and then added with 75 µl of Dual-Glo luciferase reagent containing the firefly luciferase substrate. Incubate plates for 15 minutes to allow for cell lysis to occur, and then measure the firefly luminescence in a luminometer (Biotek). Add 75 µl of Dual-Glo Stop & Glo reagent that contains the inhibitor of firefly luciferase and substrate for renilla luciferase. Incubate for 15 minutes, and then measure renilla luminescence in the same plate order as the firefly luminescence. Total renilla luciferase activity was normalized to firefly luciferase activity in order to correct for differences in transfection efficiency.

APPENDIX 4

Construction of *CNOT1* mutant plasmids

As discussed in the introduction, multiple somatic mutations in *CNOT1* have been identified in various types of human cancers, in particular CRC that has the highest *CNOT1* mutation rate among cancers (~8%). Furthermore, several recurrent mutations also have been documented, for example, R1733H and R1640Q. These results suggest that genetic mutations in *CNOT1* may contribute to the development of CRC. To further study the potential contribution of *CNOT1* somatic mutations to CRC we have began to create constructs that contain the documented mutations in *CNOT1* to study their effects on CRC in cell culture as well as in mouse models. To start with we selected nine somatic mutations in CRC identified by the TCGA project (Table 24). Among these mutations, seven have been documented more than once in the COSMIC database and all of them are predicted to have a medium level impact on CNOT1 function. The distribution of these mutations in CNOT1 protein is illustrated (Figure 55).

AA change	Codon	Mutation	COSMIC	FIS
R369C	CGT	TGT	4	Medium
L484R	CTG	CGG	2	Medium
R499C	CGC	TGC	2	Medium
R499H	CGC	CAC	2	Medium
R591C	CGT	TGT	6	Medium
L1232F	TTG	TTC	1	Medium
R1394C	CGT	TGT	4	Medium
A1396T	GCA	ACA	1	Medium
R1446H	CGT	CAT	2	Medium

Table 24. The 9 selected mutations in *CNOT1*. COSMIC indicates the number of times this mutation has been documented in the COSMIC database. FIS (Functional Impact Score): the predicted functional impact for missense mutations calculated by Mutation Assessor.

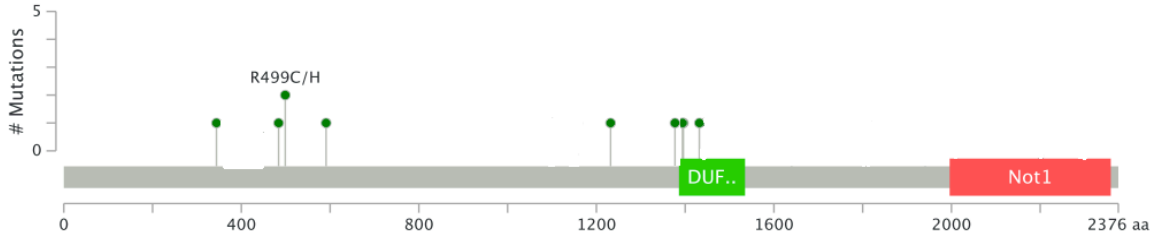

Figure 55. The distribution of selected mutations in the *CNOT1* protein. Each dot represents a mutation.

Clones encoding *CNOT1S* (NM_206999.2) ORF (BC040523) in a pBluescriptR vector were obtained from Open Biosystem (Clone Id: 5266600). The *CNOT1S* ORF was inserted between the Xho1 and BamH1 sites from 5' to 3' (Figure 57). These nine somatic mutations were introduced into the ORF of *CNOT1S* via using a Transformer Site-Directed Mutagenesis Kit (Clontech). The general procedure of this method is illustrated in Figure 56. The mutagenic primer introduces the desired mutation and the selection primer mutates a unique restriction site in the plasmid for selection of mutated plasmids. These two primers are simultaneously annealed to one strand of a denatured double-stranded template and both mutations are incorporated in the same newly synthesized strand after elongation by T4 DNA polymerase. The mixture of original and mutated DNA is then digested with a restriction enzyme that cuts at the original restriction site and is used to transform *E. coli.* BMH 71-18 *mut*S, which is mismatch repair deficient, to propagate the mutated plasmid. The uncut, mutated DNA has much higher transformation efficiency than linear DNA with no mutations, so the product of the first round of transformation will be mutated plasmids with the two mutations on one of the two strands. Then the DNA will be digested with the same restrictive enzyme again and used to transform a regular *E. coli.* strain. The final product will be a mixture of original plasmids and mutated plasmids with the two mutations on both strands. Two rounds of DNA digestion and transformation ensure that a very high frequency of transformants carry the mutated plasmid, which nearly always contains both mutations.

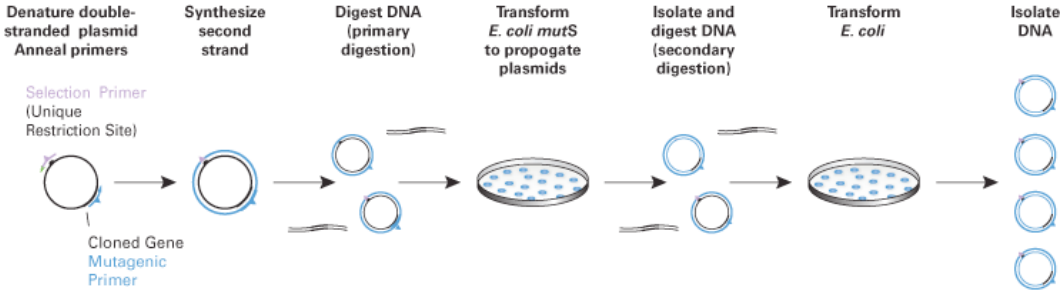

Figure 56. The general procedure of making site-directed mutations using a Transformer^{R} Site-Directed Mutagenesis Kit. (From Clontech website: http://www.clontech.com)

The nine *CNOT1* mutants were constructed following the protocol below.

A. Design selection and mutagenic primers (Table 25). The selection primer deletes the single Sca1 site on pBluescriptR-CNOT1s plasmid. And the mutagenic primers bear the nine desired point mutations in *CNOT1*.

Primer type		Change	Original	Mutated	Primer sequence
Selection primer		Delete Sca1	AGTACT	AATACT	5'p-GTGACTGGTGAATACTCAACCAAGTC-3'
Mutagenic primer	#1	R369C	CGT	TGT	5'p-CCTGGATTTCAAATTTGTGACAGTAAAGG-3'
	#2	L484R	CTG	CGG	5'p-CCAGACATGCGGGTATTGGC-3'
	#3	R499C	CGC	TGC	5'p-GGCATACCTTGTGCCATGAACTTATCTCC-3'
	#4	R499H	CGC	CAC	5'p-GGCATACCTTGCACCATGAACTTATCTCC-3'
	#5	R591C	CGT	TGT	5'p-GCACTTGCTTCATGTCGTGAATAC-3'
	#6	L1232F	TTG	TTC	5'p-GGACAACAAGAATTCCTCTATGTAGTGC-3'
	#7	R1394C	CGT	TGT	5'p-CAGTGTGTGTGTCAGGCAATTG-3'
	#8	A1396T	GCA	ACA	5'p-GTGCGTCAGACAATTGAACGGGCTGTCC-3'
	#9	R1446H	CGT	CAT	5'p-CACATGATGCATAACTTGACAGCTGG-3'

Table 25. The sequence of selection and mutagenic primers.

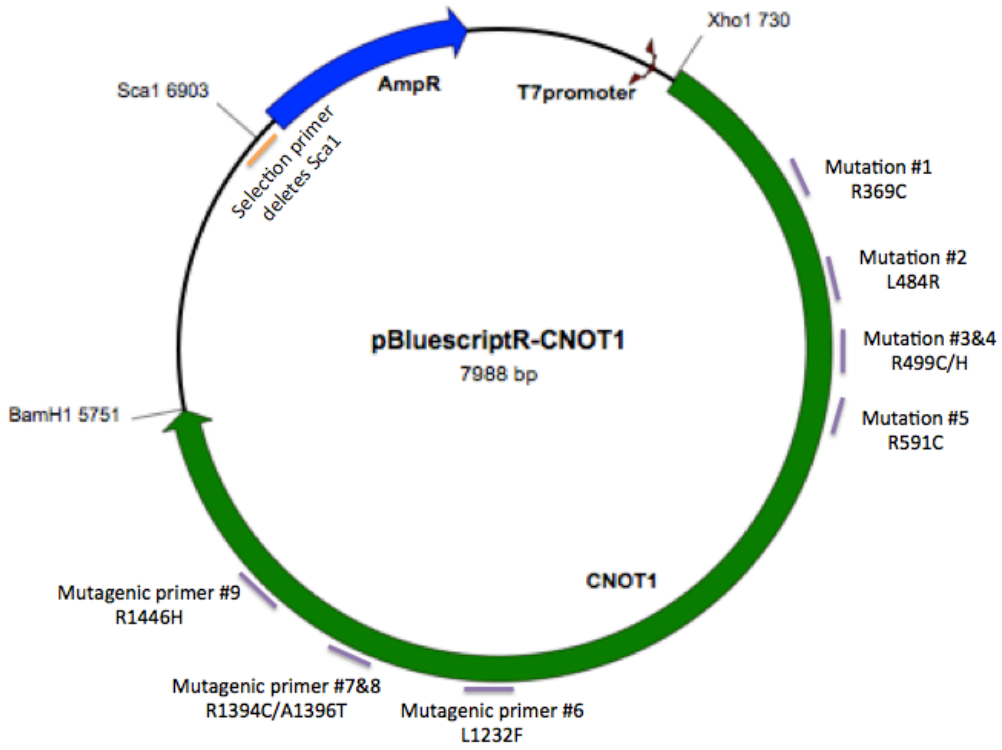

Figure 57. The map of pBluescriptR-CNOT1 plasmid and the location of mutagenic and selection primers on the plasmid.

B. Denaturation of plasmids and annealing of primers to the DNA template.

Set up the primer/plasmid reaction system in a 0.5 ml microcentrifuge tube, as follows:

10X Annealing Buffer	2.0 µl
pBluescriptR-CNOT1 (0.05 µg/µl)	2.0 µl
selection primer (0.05 µg/µl)	2.0 µl
mutagenic primer (0.05 µg/µl)	2.0 µl
H20	12.0 µl
Total	20 µl

Incubate at 100°C for 3 minutes.

Chill immediately in an ice and water bath (0°C) for 5 minutes.

C. Synthesis of the mutant DNA strands.

To the primer/plasmid annealing reaction from last step add:

10X Synthesis buffer	3.0 µl
T4 DNA polymerase (5 units/µl)	1.0 µl
T4 DNA ligase (2.84 WEISS units/µl)	1.0 µl
H2O	5.0 µl
Total	10 µl

Incubate at 37°C for 2 hours.

Heat the reaction at 70°C for 5 minutes to inactivate the enzymes.

D. Primary selection for mutant plasmids by restriction digestion. This step will selectively linearize the parental DNA to increases the percentage of mutant plasmids present in the pool of the first transformation.

Mixed plasmids from step B	30 µl
10X NEB buffer 4	3.5 µl
Sca1-HF	1.5 µl
Total	35 µl

Incubate at 37°C for 2 hours.

Heat the reaction at 70°C for 5 minutes to inactivate the enzymes.

E. First Transformation.

Transform the BMH 71-18 *mut*S cells with digest reaction from step D to propagate the heterozygous mutant plasmids.

BMH 71-18 *mut*S cells	100 µl
digested plasmids from step D	10 µl

Put on ice 30 minutes, incubate at 42°C for 1 minute, transfer to ice for 5 minutes.

Add 1 ml of S.O.C (with no antibiotic) to each tube. Incubate at 37°C for 60 minutes with shaking at 220 rpm to let cells recover.

Add 4 ml of LB medium containing ampicillin at 100 µg/ml to each tube.

Incubate the culture at 37°C overnight with shaking at 220 rpm.

F. Isolation of the mixed plasmid pool using a Qiagen Miniprep Kit.

Nanodrop the harvested plasmids and adjust the concentration to ≈ 100 ng/µl.

G. Selection of the mutant plasmids.

Mixed plasmids (≈100ng)	1.0 µl
10X NEB buffer 4	2.0 µl
Sca1-HF	1.0 µl
H20	16 µl
Total	20 µl

Incubate at 37°C for 2 hours.

Add an additional 0.5 µl Sca1-HF, and continue incubation at 37°C for another 1 hour.

Heat the reaction at 70°C for 5 minutes to inactivate the enzymes.

H. Final Transformation

Transform the NEB5α high efficiency cell with digest reaction from step G to propagate the final mutant plasmids.

Digested plasmids from step G	5 µl
NEB5α high efficiency cell	50 µl

Put on ice 30 minutes, incubate at 42°C for 1 minute, transfer to ice for 5 minutes.

Add 450 µl S.O.C medium (with no antibiotic) to each tube. Incubate at 37°C for 60 minutes with shaking at 220 rpm to let cell recover.

Use 50 µl, 100 µl and 350 µl cell suspension to streak three LB plates containing 50 µg/ml ampcillin for each mutant.

Incubate plate at 37°C overnight.

I. Propagate cells and harvest final plasmids.

Pick 3 clones from each plate and grow cells in 2.5 ml LB containing 100 µg/ml ampcillin at 37°C overnight with shaking at 220 rpm.

Isolate final plasmids from 4 clones for each mutant using a Qiagen Miniprep Kit (Qiagen).

J. Confirm the mutations by Sanger sequencing.

The sequencing primers for confirming introduced mutations are listed in table 26.

Mutant	AA change	Sequencing primer
#1	R369C	CAAGGGTTTTGGGAATGATG
#2	L484R	CCCTGTCATACTGTTGCCACT
#3	R499C	CCCTGTCATACTGTTGCCACT
#4	R499H	CCCTGTCATACTGTTGCCACT
#5	R591C	TCGAATACTTGATGTGGCCC
#6	L1232F	TGTTAAAGGACAACAAGAATTGC
#7	R1394C	CAGTACAGCTACCACGACATCA
#8	A1396T	CAGTACAGCTACCACGACATCA
#9	R1446H	CAGTACAGCTACCACGACATCA

Table 26. The sequencing primers used for validation of mutations.

Set up the reaction in a 0.5 ml eppendorf tube for Sanger sequencing as follows:

CNOT1 mutant	800 ng
Sequencing primer (2 µM)	1.6 µl
Add H20 to	12 µl

Send the tubes for sequencing to the University of Minnesota BioMedical Genomic Center. The sequencing results revealed that all nine mutations except for #6 were successfully introduced into the *CNOT1S* ORF in the pBluescriptR vector (Figure 58).

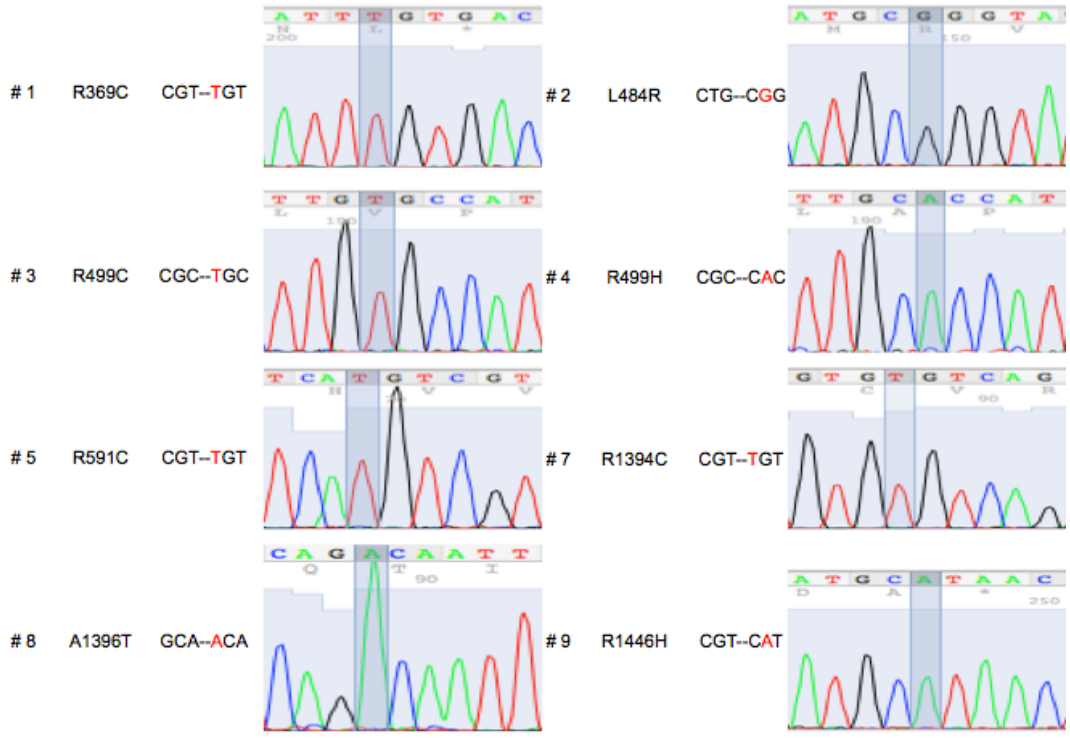

Figure 58. Validation of introduced mutations by Sanger sequencing. The mutated nucleic

acids were marked out in gray.

K. Construction of plasmids expressing *CNOT1* mutants.

The pBluescriptR vector is non-expressing. Therefore, to ectopically express the *CNOT1* mutants in cells we transferred the mutated *CNOT1* ORF into a pcDNA3 vector (Life Technologies) that can be expressed in mammalian cells. The eight *CNOT1* mutant constructs were digested with Apa1 and Not1 and inserted between the corresponding restriction sites on a pcDNA3 vector to generate pcDNA3-CNOT1SΔ. The final plasmids were propagated by transforming NEB5α cells and confirmed by restrictive digestion and agarose gel electrophoresis.

Discussion

Multiple somatic mutations in *CNOT1* have been documented in different types of cancers, in particular CRC. To characterize these mutations in CRC ectopic expression of *CNOT1* bearing these mutations in cell lines represents a direct means to test the function of these mutations *in vitro*. The CNOT1 mutations in CRC span the whole CNOT1 protein and no obvious cluster was discovered. Due to a lack of understanding of CNOT1 structure, it is difficult to predict which mutations may have more influence than others. Therefore, we selected 9 mutations spanning the short CNOT1 isoform to make *CNOT1* mutants. There are several methods in introducing a site-specific mutation into a construct. We employed Clontech's Transformer Site-Directed Mutagenesis method to introduce the 9 mutations into the *CNOT1S* ORF. Finally, we successfully constructed 8 *CNOT1* mutants, confirmed by Sanger sequencing. These results suggested that this method is an effective way to introduce a mutation into a plasmid construct of 8kb in length. We note that the short CNOT1 isoform lacks the amino acids after 1478 aa including part of the deadenylase binding domain and the NOT1 domain on the C-terminal region. Since long CNOT1 isoforms are the complete and predominant isoforms and may have different functions, we now need to make the mutated long CNOT1 isoforms bearing the same mutations in ways described in material and methods section. We also need to introduce the mutations discovered in the C-terminal region of CNOT1 into the construct for long CNOT1 isoforms. In the future, we will express these *CNOT1*

mutants in CRC and normal colon epithelial cells to study their effects on oncogenic phenotypes, assembly of the CNOT complex and deadenylation of target mRNA transcripts. If necessary, we can introduce another mutation to these *CNOT1* mutants to silence the sites targeted by siRNA oligos used to deplete endogenous *CNOT1*. Furthermore, we may carry out *in vivo* studies by producing transgenic mice bearing *CNOT1* mutations that show strong phenotypes in cell line based studies. These studies will be helpful in determining the role of *CNOT1* in CRC and in understanding the structure and functions of CNOT1.

APPENDIX 5

Identification of fusion mRNA transcripts in human colorectal cancer and normal colon epithelial tissues using RNA seq

Introduction

A gene fusion is formed by combining a part of one gene with a segment of another. Until recently, most fusion genes were discovered in neoplasms having hematopoietic and mesenchymal origins (Li *et al*., 2008), such as leukemia, lymphoma and sarcoma. Recurrent and characteristic gene fusions are a common feature of these neoplasms (Li *et al*., 2008) that together represent only 10% of all human cancers, such as *BCR-ABL1* in chronic myelogenous leukemia (CML) (Nowell *et al*, 2007), *NPM1-ALK* in lymphomas (Falini *et al*., 1999) and *EWS-FLI-1* in Ewing's sarcoma (May *et al*., 1993). Recurrent gene fusions are widely used for disease classification, diagnosis, and therapeutic targets. For example, treatment of CML with Gleevec, a tyrosine kinase inhibitor specifically targeting the BCR-ABL chimeric protein, has been proved to increase the survival rate of CML patients (Deininger *et al*., 2005).

However, detection of cancer-specific, recurrent gene fusions was rare in common types of epithelial carcinomas, which account for 80% of cancer-related deaths. This apparent discrepancy is mainly due to the inherent complexity of the solid cancer genome and technical limitations rather than fundamental genetic differences between hematological malignancies and solid cancers. With the application of new technological approaches, in particular the next-generation sequencing (NGS) techniques, and software for analyzing sequencing data, increasing numbers of gene fusions were being identified in solid tumors, such as *TMPRSS2-ERG* in prostate cancers (Taylor *et al*., 2010, Ishkanian *et al*., 2009), *EML4-ALK* in non-small cell lung cancer (NSCLC) (Soda *et al*., 2007) and *VAPB-IKZF3* in breast cancer cell lines (Edgren *et al*., 2011). These results

have changed our views regarding the presence and frequency of fusion genes in solid tumors, sparking a revitalization of the quest to identify novel gene fusions in epithelial malignancies.

The Mechanisms for Formation of Fusion Gene Transcripts

A fusion gene transcript is a chimeric RNA joining the transcripts of two or more different genes. The fusion transcripts can be produced by different mechanisms.

Chromosomal rearrangement is a most common cause of gene fusions, which can cause translocations, deletions and inversions. The best-known example of a gene fusion caused by chromosomal translocation is the *BCR-ABL* fusion gene in CML (Wong and Witte, 2004).

In addition to chromosomal rearrangements, fusion transcripts can also be produced due to aberrant RNA splicing at the transcript level, including transcription-induced chimeras (TICs) and *trans*-splicing (Figure 59).

A TIC is a specialized *cis*-splicing event that results from read-through transcription of two adjacent, independent genes that share the same orientation. In this process, RNA polymerase II keeps transcribing over multiple polyadenylation sites, where transcripts are normally cleaved and processed. Most of these fusion transcripts are generated from tandem genes that are physically located within ~50 kb of each other and the median distance is ~8.5 kb, indicating the spatial proximity might be a prerequisite for forming TICs (Akiva *et al*., 2006). TICs were previously reported in isolated cases and thought to be a rare event in mammals. Recent studies, however, incorporating systematic *in silico* analyses of ESTs and cDNAs in the NCBI databases, found that as much as 5% of the tandem gene pairs in the human genome is comprised of chimeric sequences, indicating TICs could be quite frequent. (Parra *et al*., 2006, Unneberg *et al*., 2007). Despite the prevalence, the regulation and function of most TIC-induced fusion transcripts remains largely uncharacterized (Wang *et al*., 2007, Akiva *et al*., 2006). Some of these chimeric transcripts are thought to be produced as ‘noise’ in the transcription process, while some could encode chimeric proteins or have a logical function inferred.

For example, the *RBM6-RBM5* TIC expression levels were associated with elevated levels of *RBM6* and *RBM5* mRNA, and with increased tumor size in breast tumor tissue (Wang *et al*., 2007). In addition, two tissue-specific TICs fusing tyrosine hydroxylase (*TH*) and insulin (*INS*) genes were reported to encode two TH protein isoforms whose functionality was somewhat diminished with respect to the canonical TH, providing an additional aspect in the control of *TH/insulin* gene expression. (Hernández-Sánchez *et al*., 2006, Mansilla *et al*., 2005).

Trans-splicing can generate chimeric mRNAs between pre-mRNAs originating from two different genes. It is a special form of RNA processing where exons from two different primary RNA transcripts are joined end to end and ligated (Figure 59). This process was found to follow similar mechanisms as *cis*-splicing of RNA, which is also catalyzed by the spliceosome (Faustino *et al*., 2003). Juxtaposition of the loci encoding the RNAs that participate in *trans*-splicing seems to be essential for some pre-mRNA substrates but not for some other ones (Kristi *et al*., 2008). Some resultant fusion transcripts may have functional effects. An example is the cyclin D1 (*CCND1*)-tumor-associated calcium signal transducer 2 (*TROP2*) fusion transcript detected in a variety of human cancers (Guerra *et al*., 2008). This RNA transcript did not encode a chimeric protein, but rather led to elevated levels of *CCND1* in that the 3' UTR in the *CCND1* mRNA was deleted due to *trans*-splicing with *TROP2* pre-RNA. Removal of the 3'UTR stabilizes the chimeric RNA transcript relative to normal *CCND1* mRNA. In addition, the chimeric RNA was reported to be oncogenic as it could transform primary cells in culture and induce aggressive tumor formation in cooperation with activated RAS in both cultured cells and transgenic mice. These findings have turned the view of *trans*-splicing in higher eukaryotes from a bizarre phenomenon to a biological event that is attaining stronger recognition (Mansfield *et al*., 2004, Garcia-Blanco *et al*., 2003).

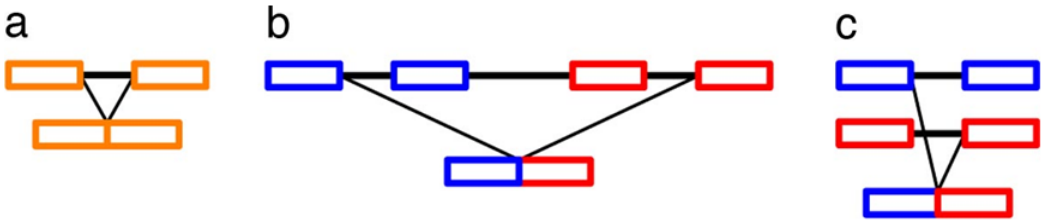

Figure 59. RNA splicing mechanisms in eukaryotes. (Anderson *et al*., 2008) (a) Canonical pre-mRNA *cis*-splicing yielding mRNA from pre-mRNA composed of two exons (orange boxes) and an intron (black line). (b) A transcription-induced chimera generated by read-through transcription from one gene (blue) into a downstream gene (red), followed by *cis*-splicing. (c) Trans-splicing of exons from two distinct pre-mRNAs (red and blue boxes).

The Biological Effects of Gene Fusions

Previous studies suggested that the consequence of gene fusions could be either generation of a truncated or chimeric protein with a different function or an alteration of gene expression (Tomlins *et al*., 2005). In most cases, gene fusions occur within introns, giving rise to the expression of truncated or chimeric proteins with a new or altered activity (Mitelman *et al*., 2007), such as BCR-ABL chimeric protein which has constitutive tyrosine kinase activity (Wong and Witte, 2004). Some of the resultant chimeric proteins are abnormal, tumor-specific products that may provide tumor cells with a growth and/or survival advantage (Li *et al*., 2008, Mitelman *et al*., 2007). Besides encoding chimeric proteins, formation of gene fusions can affect gene expression (Lin *et al*., 2012). In some cases, gene fusion occurs between the coding region of a gene and the transcriptionally active promoter or enhancer region of another gene, which may lead to upregulated expression of the former gene. Examples include *TMPRSS2-ERG* and *TMPRSS2-ETV1* gene fusions where expression of *ERG* or *ETV1* genes are dramatically up-regulated due to their repositioning after the *TMPRSS2* transcription start site which is actively transcribed in prostate cancer (Tomlins *et al*., 2005). Another type of gene fusion involves recombination between the coding region of one gene with the non-coding regulatory region, such as 3'UTR, of the second gene, which may alter the post-transcriptional regulation of the former gene. One example is the chimera between *CCND1* mRNA with *TROP2* pre-RNA, which led to the deletion of 3' UTR of *CCND1* mRNA transcript. The *CCND1-TROP2* fusion transcript stabilized *CCND1* mRNA levels and consequently resulted in elevated *CCND1* levels, promoting cells to pass the G1 phase of the cell cycle (Guerra *et al*., 2008).

Next Generation Sequencing and RNA Sequencing

Next generation sequencing (NGS) technology is a fundamentally novel approach to DNA sequencing, which can sequence the fragments of a DNA template in a massively parallel fashion, producing thousands or millions of sequences concurrently. This advance enables rapid sequencing of large stretches of DNA base pairs spanning entire genomes (Hall *et al*., 2007, Church *et al*., 2006). Whole-genome DNA sequencing can be used to identify potential fusion-gene-creating rearrangements. However, only a fraction of gene fusions predicted based on DNA sequencing is expected to generate an expressed fusion mRNA, making this approach tedious to discover activated, oncogenic fusion gene events. In contrast, RNA sequencing (RNA-seq) using next-generation sequencing instruments directly identifies only those fusion genes that are expressed, providing an efficient tool to identify candidate oncogenic fusions (Edgren *et al*., 2011). RNA-seq also facilitates comprehensive characterization of cellular transcriptomes.

In a standard RNA-seq procedure, RNA sample (total or polyA+ enriched) is converted to cDNA through reverse transcription, which is then broken into a library of small fragments. Oligonucleotide adapters are then attached to a cDNA library on one or both ends. Finally the adaptor-ligated cDNA library is sequenced on a high-throughput platform either single-ended (single-end sequencing) or pair-ended (pair-end sequencing) (Martin *et al*., 2011). This process usually generates millions of short (30-400 bp) reads which can be analyzed by a variety of bioinformatics tools. The methods for inferring the sequencing data are generally classified as two types. In one approach the reads are aligned and mapped to a reference genome either of the organism itself (whose transcriptome is being studied) or of a closely related species. The other approach, *de novo* transcriptome assembly, uses bioinformatics tools to assemble the transcriptome directly from short sequence reads without referring to a reference genome (Wang *et al*., 2009). Generally speaking, the results of RNA-Seq have shown high levels of reproducibility, for both technical and biological replicates (Cloonan *et al*., 2008). The general procedure of RNA sequencing is summarized in Figure 60. Paired-end RNA-seq, where 36 to 100 bp are sequenced from both ends of 200 to 500 bp long cDNA molecules, is especially suitable for identification of chimeric mRNA transcripts. The employment of the paired-end RNA-seq, combined with effective analytic pipelines

enable the discovery of fusion RNA transcripts in breast cancer (Edgren *et al*., 2011, Asmann *et al*., 2012), lung cancer (Lin *et al*., 2009), colon cancer (Chu *et al*., 2011), and other types of solid tumors with high confidence.

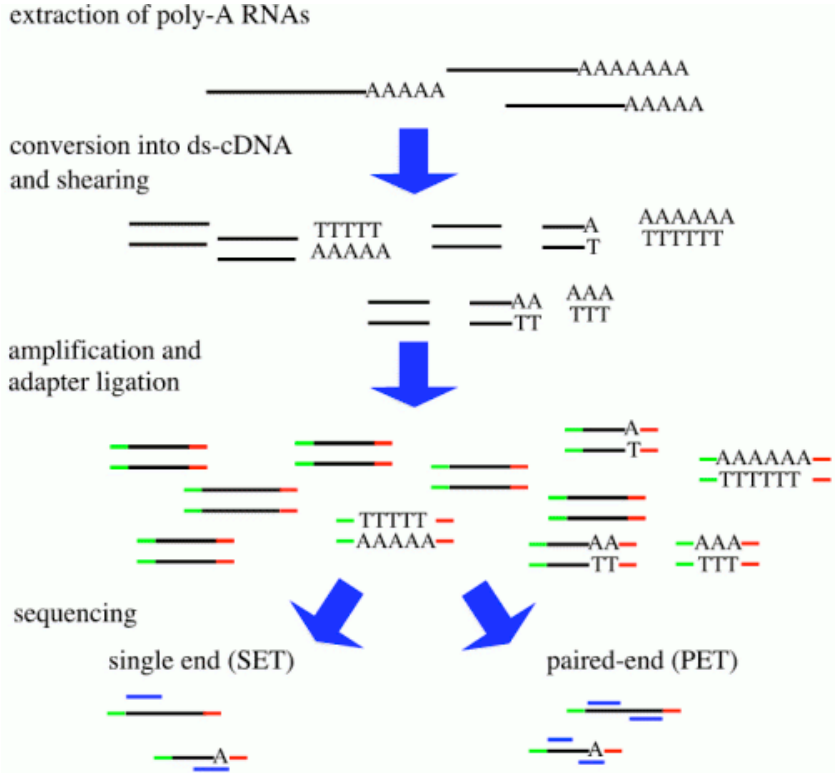

Figure 60. The procedure of RNA-seq. (Solar home http://cmb.molgen.mpg.de)

Fusion Genes in CRC

The first recurrent fusion gene in CRC was reported by Lin *et al* in 2009 (Lin *et al*., 2009). They performed an exon array for the global search of gene rearrangements in a large collection of breast cancer, CRC and non-small cell lung cancer (NSCLC) samples and identified the echinoderm microtubule associated protein like 4 (*EML4*)-anaplastic lymphoma receptor tyrosine kinase (*ALK*) fusion in multiple samples. An RT-PCR assay was then used to screen a collection of tumor samples for the presence of the *EML4-ALK* fusion transcript, leading to detection of the *EML4-ALK* fusion in 2.4% of breast cancer (5 of 209), 2.4% of CRC (2 of 83), and 11.3% of NSCLC (12 of 106), which was confirmed by subsequent sequencing of PCR products. The presence of *EML-ALK* rearrangement was further verified by identifying genomic fusion points in tumor

samples using long-range genomic PCR. A FISH assay was used to confirm the *EML4-ALK* translocation in tumor samples and tumor-derived cell lines positive for the fusion transcript. The functional role of the *EML4-ALK* fusion in cell growth and proliferation was assessed by measuring cell viability following siRNA-mediated silencing of *EML4* and *ALK*. Cell growth inhibition was not observed in control cell lines lacking the *EML4-ALK* fusion. On the contrary, significant growth inhibition was observed in lung and breast cancer cell lines but not in CRC cell lines harboring the *EML4-ALK* fusion, failing to show the functionality of this fusion in CRC (Lin *et al*., 2009).

Next generation sequencing provides the capacity for doing a deeper analysis of the entire genomes of CRC tumors. In the first study using NGS to discover gene fusions in CRC, Bass *et al* performed whole genome sequencing of 9 CRCs and paired non-neoplastic tissues (Bass *et al*., 2011). They found 11 chromosomal rearrangements that could give rise to in-frame fusion transcripts, including a fusion of vesicle transport through interaction with t-SNAREs 1A (*VTI1A*) and transcription factor 7-like 2 (*TCF7L2*). By screening cDNA from a panel of 97 primary CRCs, they found that the in-frame *VTI1A-TCF7L2* fusion was recurrently expressed in 3 of 97 cases. The *VTI1A-TCF7L2* chimeric transcript fuses the first three exons of *VTI1A* to the fourth exon of *TCF7L2*. *VTI1A* encodes a v-SNARE protein mediating fusion of intracellular vesicles within the Golgi complex 21 (Kreykenbohm *et al*., 2002). *TCF7L2* encodes a transcriptional factor belonging to the TCF/LEF family 4 (Clevers *et al*., 2006, Waterman *et al.,* 2004). TCF7L2 is known to have a significant role in CRC in collaboration with beta-catenin. To test the functional importance of the *VTI1A-TCF7L2* fusion gene in CRC, they knocked down the fusion gene through RNAi targeting the sequence spanning the fusion, which caused a dramatic reduction in the anchorage-independent growth of NCI-H508 cells, suggesting the fusion gene has a substantial role in cancer cell survival. This paper provides an excellent example of employment of NGS technology in identification of important genomic rearrangements and fusion events occurring in CRC.

Using RNA-seq, Wu *et al* profiled the whole transcriptomes of CRC tissue, adjacent non-tumor tissue and distant normal tissue from a stage III CRC patient (Wu *et*

al., 2012). They identified a cancer-specific gene fusion between the prostaglandin F2 receptor inhibitor (*PTGFRN*) and NOTCH2 (*NOTCH2*) using two algorithms, deFuse and TopHat-Fusion, which was confirmed by RT-PCR and Sanger sequencing. NOTCH2 is a homolog of NOTCH1 and plays a role in a variety of developmental processes by controlling cell fate decisions. *NOTCH2* expression has been shown to be a prognostic predictor and is related to tumor differentiation status in CRC (Chu *et al*., 2011). In the *PTGFRN-NOTCH2* gene fusion the first intron of *PTGFRN* is fused with the 3′ junction of the 17th exon of *NOTCH2*, thus the fusion gene is under the control of the promoter of *NOTCH2*. The predicted protein encodes the first 917 aa of NOTCH2, lacking some essential domains in NOTCH2, such as NOTCH domain, and appearing to act like a loss-of-function mutation. This study employed RNA-Seq to successfully identify the tumor-specific *PTGFRN-NOTCH2* fusion gene in CRC. However, this study only included one tumor sample and did not show the functional significance of the *PTGFRN-NOTCH2* gene fusion. Therefore, a study using RNA-seq in larger group of CRC samples is necessary to identify recurrent gene fusions in CRC.

In another large scale study of fusion genes in CRC, Seshagiri *et al* (Seshagiri *et al*., 2012) applied exome sequencing and RNA-seq to 70 pairs of primary human CRC and normal tissues to characterize their exomes, transcriptomes and copy-number alterations. 36 chromosomal rearrangements that result in gene fusions were identified using RNA-seq. Among these gene fusions, recurrent gene fusions involving R-spondin family members R-spondin 2 homolog (*RSPO2*) (3%; 2 out of 68) and R-spondin 3 homolog (*RSPO3*) (8%; 5 out of 68) were discovered. R-spondins are secreted proteins that can potentiate canonical WNT signaling (Yoon *et al*., 2012). The recurrent *RSPO2* fusion involves eukaryotic translation initiation factor 3, subunit E (*EIF3E*) exon 1 and *RSPO2* exon 2, which is expected to produce a functional RSPO2 protein driven by the *EIF3E* promoter. Two different *RSPO3* fusion variants were identified where either exon 1 or exon 7 of protein tyrosine phosphatase, receptor type, K (*PTPRK*) (5') was fused to exon 2 of *RSPO3* (3'). The *PTPRK* (e1)–*RSPO3* (e2) transcript found in four samples is an in-frame fusion that preserves the entire coding sequence of RSPO3 and replaces its secretion signal sequence with that of *PTPRK*. The *PTPRK* (e7)-*RSPO3* (e2) fusion,

detected in one sample, is also an in-frame fusion that potentially encodes a 70 kD protein consisting of the first 387 amino acids of PTPRK, including its secretion signal sequence, and the RSPO3 amino acids 34-272 lacking its native signal peptide. In studies of the biological activity of the *R-spondin* fusions, they showed that the RSPO fusion proteins were capable of potentiating WNT signaling in both 293T and HT-29 cells using a WNT-responsive luciferase reporter assay.

Furthermore, TCGA has comprehensively examined in genomic alterations in CRC, providing the most integrated view of CRC cancer genes to date (Cancer Genome Atlas Network, 2012). To identify new chromosomal translocations, they performed low-pass, paired-end, whole-genome sequencing on 97 tumors with matched normal samples. Despite the low genome coverage, they detected 250 candidate interchromosomal translocation events (0–10 per tumor). Among these events, 212 had one or both breakpoints in an intergenic region, whereas the remaining 38 juxtaposed coding regions of two genes in putative fusion events, of which 18 were predicted to code for in-frame events. They also found three separate cases (3%) in which the first two exons of the neuron navigator 2 (*NAV2*) gene are joined with the 3′ coding portion of transcription factor 7 like 1 (*TCF7L1*) through an interstitial deletion. *TCF7L1* encodes TCF3, a member of the TCF/LEF class of transcription factors that heterodimerize with nuclear β-catenin to enable β-catenin-mediated transcriptional regulation. However, the predicted NAV2–TCF7L1 fusion protein lacks the TCF3 β-catenin-binding domain, suggesting a loss of function truncation. They also observed 21 cases of translocation involving tetratricopeptide repeat domain 28 (*TTC28*) that was identified as a target of P53 and an inhibitor of tumor cell growth (Brady *et al*., 2011). In all cases the fusions are predicted to lead to inactivation of TTC28.

These studies provided examples for employment of next-generation sequencing and RNA-seq in identification of recurrent and functional gene fusions in CRC as well as other solid tumors. Identification of these genomic rearrangements and fusion events will be beneficial in further understanding the mechanisms of CRC formation and developing novel therapeutic strategies targeting these gene fusions or their product.

All the published studies in gene fusions in CRC were performed using primary CRC samples. To study the fusion transcripts that are associated with advanced stage CRC and potentially involved in cancer progression we studied the fusion transcripts in 20 liver metastasis of stage IV CRC and 5 normal colon samples using RNA-seq and analyzed the sequencing data via deFuse software.

Results

In the 20 CRC samples, we discovered 414 fusion transcripts involving 737 genes, among which 289 fusion transcripts were unique, 42 were in-frame fusions, and 137 occurred between adjacent genes, suggesting that these fusion transcripts were transcriptional read-throughs, also known as TICs, rather than actual genome rearrangements. In addition, the number and characteristics of fusion transcripts vary from sample to sample. On average, each CRC sample had 33 fusion transcripts (range 15-51), 0.7 in-frame fusions (range 0-3), 18 TICs (range 9-31), and 5 fusion transcripts (range 1-12) which had a predicted probability ≥ 0.85, suggesting the presence of these fusions are highly possible (Figure 61, table 27, 35 and 36, Sue Rathe, unpublished data). These results suggest that fusion transcripts and TICs are prevalent in CRC samples. However, the in-frame fusions that potentially encode chimeric proteins are rare.

In the 5 normal colon samples, 54 fusion events were discovered among which 37 were unique fusion transcripts, none was an in-frame fusion, and 24 were caused by TIC. On average, each normal colon sample had 10.8 fusion transcripts (range 9-14), no in-frame fusion, 7 TICs (range 6-8), and 1 fusion transcripts (0-2) having a predicted probability ≥ 0.85 (Figure 62, table 28, 37 and 38). These results suggest that fusion transcripts and TICs also exist in normal colon samples, while the numbers are lower than in CRCs.

We then compared the lists of fusion transcripts discovered in both CRC and normal samples to identify the fusions occurring in both types of samples. We found that 20 unique transcripts were discovered in both CRC and normal colon samples, among which 17 were the same fusion transcripts and 3 were formed by same partners but with

different breakpoints. None of these fusions were in-frame and 15 of them were TICs (Figure 63, Table 39).

Follow-up filtering using a stringent threshold for in-frame fusions resulted in a workable set of 12 fusion candidates that we are testing in *in vitro* assays. The criteria for selection of candidate fusion transcripts are: probability ≥ 0.85, in coding regions, and in-frame. All the 12 fusion transcripts were validated by RT-PCR followed by DNA sequencing except four which were validated by RT-PCR only. Interestingly, 6 of these fusion transcripts were also discovered in normal colon samples by RT-PCR, although none of them were predicted by the RNA seq data. In addition, 7 of the candidate fusion transcripts were TICs and 3 of them were found to be cancer-specific (Table 29).

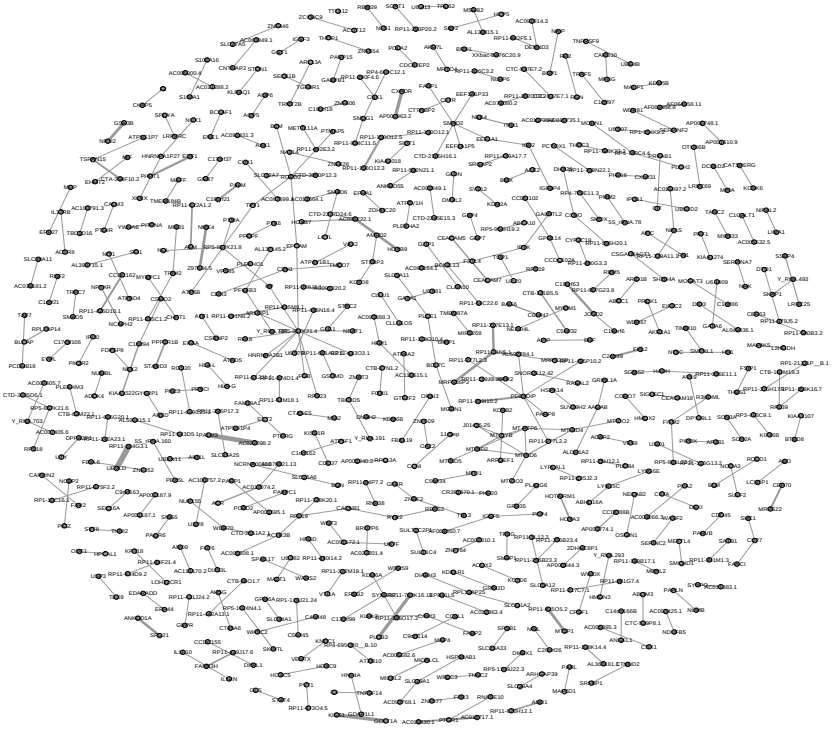

Figure 61. The map of fusion transcripts in 20 CRC liver metastasis. The thickness of the edges corresponds to the times that the same fusion was detected.

(A)

# fusions	414
# unique fusion transcripts	289

# in-frame	42
# TIC	137

(B)

Per sample	Range	Average
# fusions	15--51	33
# in-frame	0--3	0.7
# TIC	9--31	18
# prob≥0.85	1--12	5

Table 27. Summary of fusion transcripts discovered in 20 CRC samples. (A) Characteristics of fusion transcripts. (B) Fusion transcripts discovered in per sample. # in-frame: number of the fusion transcripts remaining an open reading frame; # TICs: number of fusion transcripts predicted to be TICs; # probability ≥ 0.85: number of fusions having predicted probability ≥ 0.85.

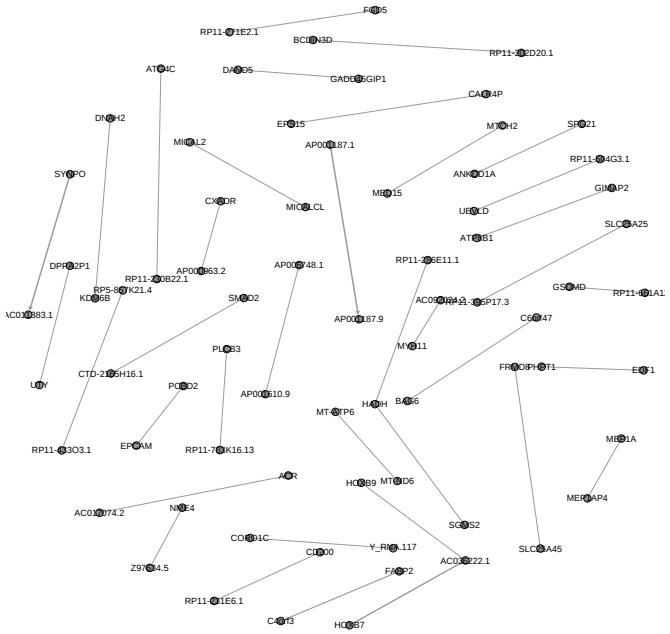

Figure 62. The map of fusion transcripts in 5 normal colon samples. The thickness of the edges corresponds to the times that the same fusion was detected.

(A)

# fusions	54
# unique fusion transcripts	37
# in-frame	0

# TIC	24

(B)

Per sample	Range	Average
# fusion	9--14	10.8
# in-frame	0	0
# TIC	6--8	7
# prob≥0.85	0--2	1

Table 28. Summary of fusion transcripts discovered in 5 normal colon samples. (A) Characteristics of fusion transcripts. (B) Fusion transcripts discovered in per sample. # in-frame: number of the fusion transcripts remaining an open reading frame; # TICs: number of fusion transcripts predicted to be TICs; # probability ≥ 0.85: number of fusions having predicted probability ≥ 0.85.

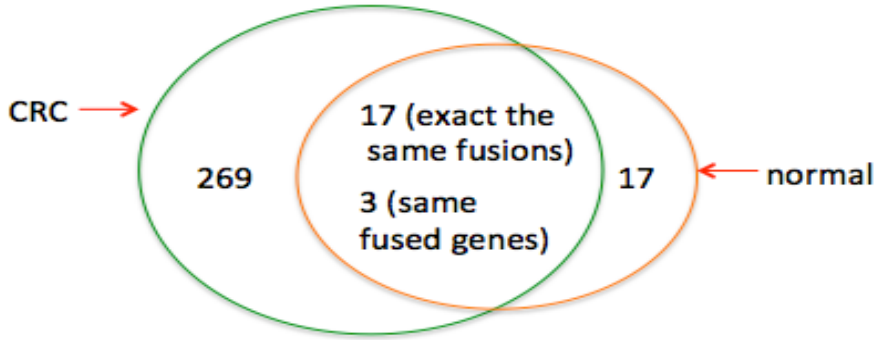

Figure 63. The overlapping fusion transcripts discovered in both CRC and normal samples.

Gene1	Gene2	#Sample	Probability	TIC	PCR	Sequencing	Cancer specific
KISS1	GOLT1A	13	0.978	Y	Y	Y	N
OSGIN1	NECAB2	2	0.971	Y	Y	Y	Y
CDH1	CDH3	1	0.965	N	Y	Y	N
IGSF5	PCP4	1	0.959	Y	Y	N	N
ADCK4	NUMBL	3	0.957	Y	Y	Y	N
GFER	ZNRF2	1	0.941	N	Y	Y	Y
UBXN11	AIM1L	1	0.929	Y	Y	N	Y
EHMT2	MIF	1	0.914	N	Y	Y	N
RGN	RP2	1	0.882	Y	Y	N	N
WFDC3	TNNC2	4	0.870	Y	Y	N	Y

NUP155	WDR70	1	0.854	N	Y	Y	Y
KDM2A	SYT12	1	0.854	N	Y	Y	Y

Table 29. Lists of the fusions that have been validated by PCR and Sanger Sequencing.

Discussion

Given that common gene fusions are rare in CRC (Bass *et al*., 2011), identifying case-specific gene fusions can help to understand the complexity of the molecular basis of CRC development. In addition, all the published studies of gene fusions in CRC were performed using primary CRC samples. Therefore, we used 20 liver metastasis of stage IV CRC to study the fusion transcripts in advanced stage CRC. Since only 1 of the 5 normal colon samples matches one of the CRC samples, we are not able to compare the fusions in paired samples to identify fusion transcripts potentially involved in CRC progression. However, the fusion transcripts discovered in CRC samples provide some candidate fusion transcripts for functional characterization. The RNA-seq dataset was analyzed for presence of fusion transcripts by using deFuse which is a bioinformatics tool for discovering fusion transcripts from RNA seq data. In the 20 CRC samples, we discovered 414 fusion events and 289 unique fusion transcripts. The majority of gene fusions were only found in a single patient, however, several were highly recurrent. The number of fusion genes varies from sample to sample (15 to 51 fusions per sample). Only 42 fusion transcripts retained an open reading frame, suggesting that majority of fusion transcripts do not encode chimeric proteins and they may function through other mechanisms. About half of the fusion transcripts (137/289) occured between adjacent genes, suggesting that these fusion transcripts were transcriptional read-throughs or TICs rather than actual genome rearrangements. This result suggested that TICs are an important mechanism in forming fusion transcripts in CRC. Together, these results indicated that fusion transcripts and TICs are prevalent in CRC samples, while the in-frame fusions that potentially encode chimeric proteins are rare. In the 5 normal colon samples, 54 fusion events were discovered and 37 were unique fusion transcripts. On average, each sample had 10.8 fusion transcripts that was a lower number than CRC samples. Among the 37 unique fusion transcripts 24 were caused by TICs, suggesting

that TICs are also widely involved in formation of fusion transcripts in normal colon tissues. In consistent with the low occurrence of in-frame fusions in CRC samples, none of these fusion transcripts was in-frame. These results suggest that fusion transcripts and TICs also exist in normal colon samples, while the numbers were lower than in CRCs.

12 fusion candidates that meet the criteria of probability ≥ 0.85, in coding regions, and in-frame were validated by RT-PCR followed by DNA sequencing, suggesting the predicted probability ≥ 0.85 is a good predictor for the presence of a fusion transcript. 6 of these fusion transcripts were also discovered in normal colon samples by RT-PCR, although none of them were predicted by the RNA-seq data. This result suggests that RNA-seq may not be able to pick all the fusion transcripts in a specific sample. 7 of these fusion transcripts were TICs consistent with RNA-seq data that about 50% fusions were formed by TICs, suggesting that TICs are an important mechanism in formation of fusion transcripts. We also found that 3 of these TICs were cancer-specific, which were reported for the first time.

In ongoing studies, we will functionally characterize some of the fusion transcripts, especially cancer-specific TICs, to reveal the influence of fusion transcripts in tumor formation and to identify potential targets for novel therapies.

Material and methods

Tumor and Normal Colon Samples

The liver metastasis of 20 stage IV colon cancer patients and 5 normal colon samples were obtained from the Biological Materials Procurement Network (BioNet) at the University of Minnesota. All tumor and normal tissues were snap frozen in liquid nitrogen at the time of surgical resection, and delivered to us on dry ice, and transferred into liquid nitrogen immediately upon they were received. The clinico-pathological profile of the 20 CRC (Table 30) and 5 normal colon samples (Table 31) are listed below.

Table 30. Summery of clinico-pathological profile of the 20 CRC patients

	Median	Range
Age,yr	59.5	(36-90)
Variable	n	%
Gender		
Male	11	55
Female	9	45
Histology		
AD	19	95
Adenocarcinoid	1	5
Differentiation*		
Well	2	25
Moderate	6	75
Poor	0	0
Stage		
IV	20	1

* Differentiation was not available for 12 cases.
Two patients received chemotherapy, but drugs were unknown.
AD = Adenocarcinoma.

Table 31. Summery of clinico-pathological profile of the 5 normal colon samples

	Median	Range
Age,yr	68	(49-77)
Variable	n	%
Gender		
Male	3	60
Female	2	40
Location		
Left colon	0	
Right colon	4	80
Rectum	1	20

RNA Isolation

Total RNA was isolated from 20 fresh frozen CRC samples and 5 fresh frozen normal colon tissues as described in chapter 4. RNA integrity was assessed by capillary electrophoresis and the RNA Integrity Number (RIN) for each sample is listed as below (Table 32).

Table 32. RIN of the total 25 RNA samples

	Sample name	RIN
Cancer samples	T980321	9.0
	T010314	8.9
	T001683	8.7
	T000418	8.1
	T970244	7.9
	T021380	7.8
	T021606	7.8
	T990569	7.8
	T970192	7.6
	T000447	7.5
	T010902	7.4
	T020556	7.3
	T980748	7.3
	T020193	7.2
	T980429	7.2
	T001090	7.1
	T010004	6.9
	T020201	6.8
	T990896	6.1
	T970854	5.8
Normal tissue	T022437	8.3
	T011145	7.3
	T020627	7.1
	T020613	7.0
	T020447	6.6

Experimental Validation of Fusion Transcripts

We used RT-PCR followed by DNA sequencing to validate the presence of fusion genes transcripts in RNA samples.

cDNA synthesis was performed as described before.

PCR. All standard PCR was carried out with HotStarTaq DNA Polymerase using a HotStarTaq Master Mix Kit (Qiagen) with the following reaction mix: 25 µl of 2 X HotStarTaq Master Mix (2.5 units HotStarTaq DNA Polymerase, 1 x PCR Buffer, 200 µM of each dNTP), 10 µl of each primer (final concentration 0.2 µM), and 5 µl of cDNA template in a 50 µl volume. Cycling conditions were 95°C for 5 minutes, then 35 cycles

of 95°C for 30 seconds, 60°C for 30 seconds, 72°C for 1 minute per kb of target, and finally 72°C for 10 minutes. The primers used for PCR are listed (Table 33).

Fusion	Forward primer	Reverse primer
KISS1-GOLT1A	GCAACTTAACCAAGGGTCAGC	GCAGTAGCTGCCAAGAAACC
OSGIN1-NECAB2	CAAGAAGGGTCTGGGGCATA	TCCACATGGTTGGTGTTGTCA
CDH1-CDH3	GTCTCCTCTTGGCTCTGCC	CTTTCCTGGACTGTCTCGCC
IGSF5-PCP4	AAAGACCACAGACACCGCTT	ACTGAGACTGAATGGCCACC
ADCK4-NUMBL	TACATCGAGGTGGTGAAGGC	GTAACTTGTTCATGGTGCCCG
GFER-ZNRF2	CTTACCAGCTCACCTCTCGC	CCAGCGCTCATCCACTTTTG
UBXN11-AIM1L	ACTGGAGACGATGTGTGTGC	TTTCATGTCCTCCACATGGTCC
EHMT2-MIF	CCAGAGTTTGGCTATGAGGCT	GCTTGCTGTAGGAGCGGTT
RP2-RGN	AATATCCCGGGGTCAGAGACA	TTGTGGTCTAGCGACCAATCC
WFDC3-TNNC2	CTTCCGCATCTTCGACAGGA	TCATCCATCACACAGCCAACA
NUP155-WDR70	TCCTTGTTCCTTCCTTGCTACA	TTTTTGCCTTGCATCGTCCG
KDM2A-SYT12	CAGCCCTGGAGTGGTTTCTT	GACTTCCGGAGGGTCCCATA

Table 33. List of primers used for validation of candidate fusion transcripts.

Gel extraction. PCR products were subjected to electrophorisis using a 1% low melting agarose (LMT) gel with 0.05% ethidium bromide. The desired bands on gel were excised from the gel using a sterile scalpel and the PCR products were then extracted from the gel slice using the QIAquick Gel extraction kit (Qiagen) following the manufacturer's instructions. The extracted DNA was quantified using Nanodrop.

Sanger sequencing. The reaction mix comprises 50 ng DNA extracted from LMT gel, 1.6 µl of 2 µM sequencing primer stock and H_20 to make a final volume of 12 µl. The reactions were sent to the University of Minnesota BioMedical Genomics Center for sequencing by using an ABI 3730 DNA sequencer (Applied Biosystems). Results were screened by eye using the Applied Biosystems software packages Sequence Scanner version 1.0 (Applied Biosystems). Sequencing results were compared with the RNA seq data to confirm the fusion transcripts. The sequencing primers are listed in Table 34.

Fusion	Sequencing primer
GOLT1A-KISS1	CAAGGGTCAGCTTCCCGT
OSGIN1-NECAB2	CTGGGGCATAACTTTGTGTC

CDH1-CDH3	CCTCTTGGCTCTGCCAGG
IGSF5-PCP4	ACCACAGACACCGCTTCTCT
ADCK4-NUMBL	TGTATGATGCCTCCAGCCA
GFRE-ZNRF2	ATCGGCTCCTTACCAGCTC
UBXN11-AIM1L	CAGTGACTATGGCCTGCAGT
EHMT2-MIF	TGAGTATGCCAGGAGCCC
RGN-RP2	TCCCGGGGTCAGAGACAG
WFDC3-TNNC2	CGCATCTTCGACAGGAATG
KDM2A-SYT12	GTTGCAATCTGGTTCCTAAGGA

Table 34. List of sequencing primers for validation of candidate fusion transcripts.

Illumina RNA-Sequencing was performed as described in chapter 4.

deFuse. Fusion transcript discovery was performed using deFuse (http://compbio.bccrc.ca). Briefly, deFuse identifies fusion transcripts by clustering discordantly aligning paired-end reads as potential evidence of reads that span a fusion breakpoint. Clusters of discordantly aligning reads are then used to inform a targeted search for reads split by fusion breakpoints. The results produced by deFuse are further filtered to reduce the number of false positives. After these series of filters are applied, a candidate list of fusions is carried forward for further analysis (McPherson *et al*., 2011).

Supplemental information

Table 35. Summary of fusion transcripts discovered in each CRC sample

Sample	# Fusions	# In Frame	# Adjacent	# prob≥0.85
T980429-5	51	3	31	7
T020556-4	49	2	25	11
T980321-1	49	8	26	8
T020201-4	48	8	20	4
T010314	45	5	29	12
T001683	42	3	15	8
T001090	38	2	26	10
T970192-5	35	0	17	5
T990896-2	33	2	16	3
T021380	32	2	22	12
T010004	31	2	19	2
T970854-6	29	3	14	3
T990569-2	26	3	13	5

T020193-2	25	2	13	1
T000418-2	24	4	12	3
T970244-7	22	1	14	1
T980748	22	0	10	6
T010902-3	21	4	14	3
T021606-3	16	1	9	1
T000447	15	0	12	3

Fusion number of gene fusions discovered in each sample
In-frame number of the fusion transcript remainning an open reading frame
Adjacent number of the two genes which are located in adjacent
Probability ≥ 0.85 number of fusions having predicted probability ≥ 0.85

Table 36. Summary of fusion transcripts discovered in the 20 CRC samples

Gene1	Gene2	#Sample (20 total)	In Frame	Adjacent	Probability ≥0.85
RP11-150O12.3	RP11-150O12.5	14	N	Y	0.35
GOLT1A	KISS1	13	0.23_Y	Y	0.67
MT1P1	RP11-435O5.2	13	N	Y	0.26
ANO1	RP11-626H12.1	12	N	N	0.4
NME4	Z97634.5	11	N	Y	0.67
AC036222.1	HOXB9	11	N	Y	0.57
AC022098.2	PALM3	11	N	Y	0.28
AL360181.1	RP11-108K14.4	10	N	Y	0.62
BAG6	C6orf47	10	N	Y	0.5
AC017074.2	ACR	10	N	N	0.46
PAQR6	SMG5	9	N	Y	0.36
PPP1R1B	STARD3	8	N	Y	0.67
GSK3B	NR1I2	8	N	Y	0.61
C19orf63	JOSD2	8	N	Y	0.44
C2orf49	FHL2	8	N	Y	0.15
AC007405.7	Y_RNA.703	7	N	Y	0.67
AC036222.1	HOXB7	7	N	Y	0.62
AC011383.1	SYNPO	7	N	Y	0.55
C5orf32	CTB-131B5.5	7	N	Y	0.36
MICAL2	MICALCL	6	N	Y	0.86
HOTAIRM1	HOXA3	6	N	N	0.5
AP003774.1	CCDC88B	6	N	Y	0.25
MRPS36P2	RP11-11N5.1	6	N	Y	0.2
AC036222.1	CTD-2377D24.6	5	N	N	0.44
TNNC2	WFDC3	4	Y	N	0.83
AKR1A1	PRDX1	4	N	N	0.67
CDC42EP2	POLA2	4	N	Y	0.5
MORN1	RP4-740C4.4	4	N	Y	0.5
AC018717.1	AC019330.1	4	N	Y	0.46
AC090425.1	NDUFB5	4	N	Y	0.43
CALM3	PTGIR	4	N	Y	0.4
HADH	RP11-286E11.1	4	N	Y	0.2
RP11-11N5.1	RP11-217E13.1	4	N	N	0.15

MIR633	TANC2	4	N	Y	1
RP11-191N8.2	RP11-815M8.1	3	N	Y	0.83
CLDN10	DZIP1	3	N	Y	0.67
CKAP5	F2	3	N	Y	0.6
ADCK4	NUMBL	3	Y	Y	0.5
AL049836.1	DIO3	3	N	Y	0.4
AC100791.3	TBC1D16	3	N	N	0.4
ARSD	GYG2P1	3	N	N	0.25
CARD10	MFNG	3	N	Y	1
RP1-10C16.1	RP11-375F2.2	2	N	N	0.8
NCBP2	PIGZ	2	N	Y	0.75
ATAD5	EIF5A	2	N	N	0.75
AFM	RP11-622A1.2	2	N	Y	0.71
ACOT12	ZCCHC9	2	N	Y	0.67
PFKFB3	Y_RNA.738	2	N	Y	0.67
AL137145.2	PFKFB3	2	0.33_Y	N	0.67
METTL11A	RP11-492E3.2	2	N	N	0.5
MAP6D1	PARL	2	N	Y	0.5
AC087699.1	CUX1	2	N	N	0.5
AC079080.2	RP11-162O12.2	2	N	Y	0.5
RP11-255B23.3	RP11-255B23.4	2	N	Y	0.5
AL139815.1	MSRB2	2	N	Y	0.5
DUS3L	FUT6	2	N	N	0.5
PITPNA	YWHAE	2	N	N	0.5
ACE2	BMX	2	N	Y	0.4
AC007405.6	Y_RNA.703	2	N	Y	0.33
TTLL12	TTLL12	2	Y	N	0.33
NECAB2	OSGIN1	2	0.33_Y	Y	1
TNFRSF9	UBE4B	2	N	N	1
TBC1D5	ZMAT3	1	N	N	0.8
CDH1	CDH3	1	0.40_Y	Y	0.8
NFS1	RBM39	1	N	Y	0.75
CEACAM7	RPS19	1	N	N	0.75
IGSF5	PCP4	1	0.50_Y	Y	0.75
SCN2A	SCN3A	1	N	Y	0.75
C17orf99	SYNGR2	1	0.25_Y	Y	0.75
CIITA	DEXI	1	N	Y	0.67
TBC1D5	Y_RNA.191	1	N	N	0.67
OAZ2	ZNF609	1	N	Y	0.67
ATXN10	RP4-695O20__B.10	1	N	N	0.67
RP11-142A23.1	RP11-656G20.1	1	N	Y	0.67
SLC25A33	SPSB1	1	N	N	0.67
DCBLD2	MINA	1	N	N	0.5
HSP90AB1	SLC29A1	1	Y	Y	0.5
AMPD2	STXBP3	1	Y	N	0.5
AQP5	AQP6	1	Y	Y	0.5
CAPRIN2	FAR2	1	N	N	0.5
SERINC2	WASF2	1	N	N	0.5

FAM19A1	PTPRG	1	N	N	0.5
TBL3	ZNRF2	1	Y	N	0.5
KIF16B	RP3-410C9.1	1	N	N	0.5
MND1	TRIM2	1	0.50_Y	Y	0.5
BLM	RCCD1	1	Y	N	0.5
SYT8	TNNI2	1	Y	Y	0.5
RP5-1024N4.1	SKINTL	1	N	Y	0.5
L2HGDH	MAP4K5	1	Y	N	0.5
EIF2C2	WDR67	1	Y	N	0.5
ACAP2	VPS8	1	Y	N	0.5
BCL2L13	RP11-14C22.6	1	N	N	0.5
C1orf21	RNF2	1	N	N	0.5
RGN	RP2	1	0.50_Y	N	0.5
PLCE1	SLC5A11	1	N	N	0.5
RP11-285C1.2	TRIM2	1	N	Y	0.5
BCLAF1	ENC1	1	N	N	0.5
SMTNL1	TIMM10	1	N	Y	0.5
RP4-610C12.1	SMUG1	1	N	N	0.5
AC093768.1	SLC29A1	1	N	N	0.5
GLG1	STAC2	1	Y	N	0.5
MYOM1	NEDD4L	1	N	N	0.5
NPR2	RP11-112J3.16	1	N	Y	0.5
AC005682.6	MAP4	1	N	N	0.5
CEP63	RP11-680B3.2	1	N	N	0.5
ATP6V1H	PLEKHA2	1	Y	N	0.5
AL591415.1	RP11-543D5.1	1	N	Y	0.5
DTD1	RP11-379J5.2	1	N	Y	0.5
CBX1	RP11-390F4.6	1	N	N	0.5
ATP5G1P7	TSPAN15	1	N	Y	0.5
AP001610.9	AP006748.1	1	N	Y	0.5
GGT1	IGSF3	1	N	N	0.5
TPD52	U6.413	1	N	N	0.5
AC091849.1	CTD-2245E15.3	1	N	Y	0.5
CACNB1	RPL19	1	N	Y	0.5
LRPPRC	SPDYA	1	Y	N	0.5
BCL7C	MGRN1	1	N	N	0.5
RP11-1L12.3	SLC5A12	1	N	N	0.5
CDC45	PARVB	1	Y	N	0.5
AF064860.7	IGSF5	1	N	Y	0.5
CTB-63M22.1	PLEKHM3	1	N	N	0.5
SPAG17	WARS2	1	N	N	0.5
BDP1	NAIP	1	Y	N	0.5
AC011897.2	NBAS	1	N	N	0.5
CTNND2	SRFBP1	1	N	N	0.5
C4orf3	FABP2	1	N	Y	0.5
AC019181.2	SLC38A11	1	N	N	0.5
GLS	STAT4	1	Y	Y	0.5
CDH1	TMCO7	1	Y	Y	0.5
NCAPH2	NPTXR	1	0.10_Y	N	0.2

C17orf37	GRB7	1	N	Y	0.17
PLEKHO1	VPS45	1	N	Y	1
RP11-439A17.7	SRGAP2	1	N	N	1
CDC37	KISS1R	1	Y	N	1
AIM1L	UBXN11	1	Y	Y	1
TEX9	USP3	1	N	N	1
HOXC5	HOXC9	1	N	Y	1
ATP6V1B1	VAX2	1	N	Y	1
RP1-154K9.2	U6.507	1	N	Y	1
SMAP1	TPBG	1	N	N	1
RP11-322M19.1	VTI1A	1	N	N	1
NUP155	WDR70	1	Y	N	1
THOP1	ZNF554	1	N	Y	1
KDM2A	SYT12	1	Y	N	1
ARFGEF1	KCNB2	1	N	N	1
5S_rRNA.78	PMM2	1	N	N	1
C1orf94	KIAA1522	1	N	N	1
GFER	ZNRF2	1	Y	N	1
AC004066.3	PPA2	1	N	N	1
C20orf26	NINL	1	N	N	1
CXorf31	PHF16	1	N	Y	1
CORO7	HMOX2	1	N	N	1
RNF38	RP11-84P7.2	4	N	N	0
AC005532.5	C1GALT1	3	N	Y	0
ATF1	CSRNP2	2	N	N	0
FGB	RP5-857K21.4	2	N	N	0
RP5-857K21.6	RPS18	2	N	N	0
ATIC	FN1	2	N	Y	0
FABP1	SMAD2	2	N	N	0
PPDPF	PTK6	1	N	Y	0
AC006008.1	ACTR3B	1	N	N	0
KRT18	LOH12CR1	1	N	N	0
BCL7C	PLCE1	1	N	N	0
SKAP1	Y_RNA.493	1	N	Y	0
METTL4	SMCHD1	1	N	N	0
AC091172.1	WNT3	1	N	N	0
FBXL6	ZNF252	1	N	N	0
ABLIM3	CTC-529P8.1	1	N	N	0
GSDMD	RP11-661A12.5	1	N	Y	0
RP11-113G13.2	USO1	1	N	N	0
C1orf94	CSMD2	1	N	Y	0
AC091320.2	RP11-328J2.1	1	N	N	0
EDARADD	ERP44	1	N	N	0
C9orf163	SEC16A	1	N	Y	0
CR381670.1	PHF20	1	N	N	0
NBAS	RP11-339A11.1	1	N	N	0
PTGR1	RNASE10	1	N	N	0
RGS20	RP11-419C23.1	1	N	N	0
GDAP1L1	HNF4A	1	Y	N	0

LIMA1	NIPAL2	1	N	N	0
MIR1268	TMEM87A	1	N	N	0
EFHA1	ZDHHC20	1	N	N	0
CPSF1	WWOX	1	N	N	0
RP11-504G3.1	UEVLD	20	N	N	0
C19orf21	PALM	17	N	Y	0
ANKDD1A	SPG21	16	N	Y	0
PLCB3	RP11-783K16.13	16	N	Y	0
AP000963.2	CXADR	13	N	Y	0
EDF1	PHPT1	12	N	Y	0
CCDC162	RP11-425D10.1	11	N	N	0
C4orf48	WHSC2	11	N	Y	0
AC016735.1	AC016735.2	10	N	Y	0
LRRC25	SSBP4	8	N	N	0
CTA-398F10.2	TSPAN15	7	N	N	0
GRIN2D	KDELR1	6	N	Y	0
PDE4DIP	RP11-289I10.2	6	N	N	0
BLCAP	RPL7AP14	6	N	Y	0
RP11-395P17.3	SLC25A25	5	N	Y	0
FAM83H	RP11-429J17.6	5	N	Y	0
AF064858.11	AF064858.8	5	N	Y	0
PLCH2	RP4-740C4.4	5	N	Y	0
CEACAM5	CEACAM7	5	0.12_Y	Y	0
CFTR	CTTNBP2	4	N	Y	0
ACTR8	IL17RB	4	N	Y	0
KIAA1274	PRF1	4	N	Y	0
NLRP6	RP11-326C3.2	4	N	Y	0
DPPA2P1	UTY	4	N	Y	0
MT-ATP6	MT-ND4	3	0.33_Y	N	0
GBP4	GBP7	3	N	Y	0
CTC-537E7.1	CTC-537E7.2	3	N	Y	0
CTAGE5	MIA2	3	Y	Y	0
GRPR	RP11-431J24.2	3	N	Y	0
ITIH1	NEK4	3	N	Y	0
RP5-857K21.8	TPT1	3	N	N	0
ATP5F1	C1orf162	3	N	Y	0
PDE4DIP	RP11-277L2.2	3	N	N	0
AHSG	CT45A6	3	N	N	0
AC012363.4	EPB41L5	2	N	Y	0
CATSPERG	KCNK6	2	N	Y	0
CTD-2165H16.1	SMAD2	2	N	N	0
DNAH2	KDM6B	2	N	Y	0
CCDC102A	GPR114	2	N	Y	0
CCNO	DHX29	2	N	Y	0
AC083849.1	CNTNAP2	2	N	Y	0
MT-ATP6	MT-CYB	2	0.50_Y	N	0
DMBX1	RP5-1109J22.3	2	N	Y	0
AC091814.3	DENND3	2	N	N	0
MT-ATP6	MT-ND6	2	N	N	0

FDPSP8	NEK2	2	N	Y	0
AC022201.4	BRD7P6	2	N	Y	0
KNDC1	VENTX	2	N	N	0
CTD-3035D6.1	RP5-857K21.6	2	N	N	0
FSIP1	THBS1	2	N	Y	0
NCRNA00106	SLC25A6	2	N	Y	0
MALT1	U6.282	2	N	Y	0
NCOA3	SULF2	2	N	Y	0
EPCAM	RP5-857K21.4	2	N	N	0
AP001187.1	AP001187.9	2	N	N	0
FPR3	ZNF577	2	N	Y	0
RP5-857K21.4	RPL8	2	N	N	0
MT-ND4	MT-ND6	2	N	N	0
AC006000.4	AC011288.2	2	N	Y	0
LYPLAL1	RP11-135J2.3	2	N	Y	0
MT-CYB	MT-ND2	2	0.40_Y	N	0
AVL9	DPY19L1	2	N	N	0
SERPINF2	WDR81	2	0.33_Y	Y	0
HPGD	RP11-440I14.2	1	N	Y	0
AAGAB	GRINL1A	1	N	N	0
AP2B1	PIPOX	1	N	N	0
RP11-434D9.2	RP11-44F21.4	1	N	N	0
AC013564.1	SMAD6	1	N	Y	0
J01415.25	MT-ND6	1	N	N	0
CTD-2151A2.1	WDR70	1	N	N	0
KDM6A	RP11-185O17.3	1	N	N	0
MT-ATP6	MT-ND2	1	N	N	0
ATPBD4	NIT1	1	N	N	0
AAK1	AC092431.3	1	N	Y	0
ACTR3B	RP11-728K20.1	1	N	N	0
KCTD8	STXBP3	1	N	N	0
HMGN3	Y_RNA.293	1	N	N	0
ERBB2	WDR59	1	N	N	0
ATP8A2	GTF2F2	1	N	N	0
BTBD8	KIAA1107	1	Y	Y	0
RP11-834C11.5	SMUG1	1	N	N	0
ABCC1	ARID1B	1	N	N	0
ARL13A	TRMT2B	1	N	N	0
5S_rRNA.160	PEX5L	1	N	Y	0
TOP1	U2.20	1	N	Y	0
KDM5B	MACF1	1	N	N	0
BGN	SLC25A6	1	N	N	0
CACNB1	RYR2	1	N	N	0
GATA1	U6.681	1	N	Y	0
HPCAL1	ODC1	1	N	Y	0
CEP70	MRPS22	1	N	N	0
GPR35	PLA2G6	1	Y	N	0
RP4-779E11.3	SMOX	1	N	Y	0
LCTL	SMAD6	1	N	N	0

PVT1	RP11-473O4.5	1	N	N	0
AL049836.1	AL049836.1	1	N	N	0
DIAPH3	RPL13AP25	1	N	N	0
HNRNPA1P27	NOX1	1	N	Y	0
HCP5	SBF2	1	N	N	0
NCL	RP5-857K21.8	1	N	N	0
MT-CO3	MT-ND6	1	N	N	0
RP11-391M1.3	SATB1	1	N	N	0
GABPB1	PARP15	1	N	N	0
HNRNPA1P27	XKRX	1	N	N	0
HP	RP5-857K21.8	1	N	N	0
HP	RP5-857K21.4	1	N	N	0

Samples number of samples this gene fusions has been discovered in
In-frame if the fusion transcript remains an open reading frame
Adjacent if the two genes are located in adjacent
Probability≥0.85 percentage of this fusions having predicted probability≥0.85

Table 37. Summary of fusion transcripts discovered in each normal sample

Sample	# Fusions	# In Frame	# Adjacent	# prob≥0.85
T011145-9	14	0	7	2
T020447-3	10	0	8	0
T020613-1	9	0	8	2
T020627-1	12	0	7	1
T022437-2	9	0	6	0

Fusion number of gene fusions discovered in each sample
In-frame number of the fusion transcript remainning an open reading frame
Adjacent number of the two genes which are located in adjacent
Probability ≥ 0.85 number of fusions having predicted probability ≥ 0.85

Table 38. Summary of fusion transcripts discovered in 5 normal samples

Gene1	Gene2	#Sample (5 total)	In Frame	Adjacent	Probability ≥0.85
AP001187.1	AP001187.9	3	N	N	0
SYNPO	AC011383.1	4	N	Y	0
FABP2	C4orf3	3	N	Y	0
AP001610.9	AP006748.1	1	N	Y	0.5
BAG6	C6orf47	2	N	Y	0
EPS15	CALR4P	2	N	Y	0
GIMAP2	ATP8B1	2	N	N	0
HOXB7	AC036222.1	3	N	Y	0.33
KDM6B	DNAH2	1	N	Y	0
RP11-286E11.1	HADH	2	N	Y	0
RP11-504G3.1	UEVLD	2	N	N	0
AC036222.1	HOXB9	1	N	Y	1

ACR	AC017074.2	1	N	N	0
ANKDD1A	SPG21	1	N	Y	0
AP000963.2	CXADR	1	N	Y	0
BCDIN3D	RP11-202D20.1	1	N	N	0
CD200	RP11-231E6.1	1	N	Y	0
CORO1C	Y_RNA.117	1	N	Y	0
CTD-2165H16.1	SMAD2	1	N	N	1
EDF1	PHPT1	1	N	Y	0
EPCAM	PCBD2	1	N	N	0
GADD45GIP1	DAND5	1	N	Y	0
GSDMD	RP11-661A12.5	1	N	Y	0
MEP1A	MEP1AP4	1	N	N	0
MICAL2	MICALCL	1	N	Y	1
MT-ATP6	MT-ND6	1	N	N	0
MTCH2	MED15	1	N	N	0
MYH11	AC092024.2	1	N	N	0
NME4	Z97634.5	1	N	Y	0
RP11-230B22.1	ATG4C	1	N	Y	0
RP11-271E2.1	FGD5	1	N	N	0
RP11-783K16.13	PLCB3	1	N	Y	0
RP5-857K21.4	RP11-433O3.1	1	N	N	0
SGMS2	HADH	1	N	Y	0
SLC25A25	RP11-395P17.3	1	N	Y	0
SLC25A45	FRMD8	1	N	Y	0
UTY	DPPA2P1	1	N	Y	0

Samples number of samples this gene fusions has been discovered in
In-frame if the fusion transcript remains an open reading frame
Adjacent if the two genes are located in adjacent
Probability ≥ 0.85 percentage of this fusions having predicted probability ≥ 0.85

Table 39. The overlapping fusion transcripts in CRC and normal samples

Gene1	Gene2	# In CRC	# In normal
AC011383.1	SYNPO	7	4
AC017074.2	ACR	10	1
AC036222.1	HOXB7	7	3
ANKDD1A	SPG21	16	1
AP000963.2	CXADR	13	1
AP001187.1	AP001187.9	2	3
BAG6	C6orf47	10	2
C4orf3	FABP2	1	3
CTD-2165H16.1	SMAD2	2	1
DNAH2	KDM6B	2	1

DPPA2P1	UTY	4	1
EDF1	PHPT1	12	1
GSDMD	RP11-661A12.5	1	1
HADH	RP11-286E11.1	4	2
MICAL2	MICALCL	6	1
MT-ATP6	MT-ND6	2	1
NME4	Z97634.5	11	1
PLCB3	RP11-783K16.13	16	1
RP11-395P17.3	SLC25A25	5	1
RP11-504G3.1	UEVLD	20	2

In CRC numer of CRC samples this fusion has been discovered in
In normal numer of normal samples this fusion has been discovered in